

# Phosphate based ceramic as solid-state electrolyte for lithium ion batteries

Zur Erlangung des akademischen Grades eines

**Doktors der Ingenieurwissenschaften**

der Fakultät für Maschinenbau des

Karlsruher Instituts für Technologie (KIT)

genehmigte

**Dissertation**

von

Dipl.-Ing. Yuantao Cui

Hauptreferent: Prof. Dr. Hans Jürgen Seifert

Korreferent: Prof. Dr.-Ing. habil. Torsten Markus

Tag der mündlichen Prüfung: 11.09.2018



# Kurzfassung

Lithiumaluminiumgermaniumphosphat (LAGP) und Lithiumaluminiumtitanphosphat (LATP) sind vielversprechende Feststoffelektrolytmaterialien für die zukünftigen Lithium-Ionen-Batterien. Sie verfügen über gute ionische Leitfähigkeit und hervorragende thermische Stabilität, die die Leistung und Sicherheit von Lithium-Ionen-Batterien stark verbessern kann. LAGP und LATP weisen eine sogenannte NaSICON-Struktur auf, deren Skelett aus eckenverknüpften  $\text{PO}_4$ -Tetraedern und  $\text{TiO}_6$ - bzw.  $\text{GeO}_6$ -Oktaedern besteht. Die NaSICON-Struktur ermöglicht eine leichte Migration von Li-Ionen durch das Kristallgitter.

Ein wichtiges Ziel dieser Arbeit war die Optimierung der ionischen Leitfähigkeit von LAGP und LATP. Dazu wurden LAGP Proben mit unterschiedlichen Zusammensetzungen mit Hilfe der Sintermethode bzw. der Wärmenachbehandlungsmethode präpariert. Die ionische Leitfähigkeit wurde mittels Impedanzspektroskopie und die thermische Leitfähigkeit mittels Laserflashmessungen gemessen. Die optimierte Sinter- bzw. Wärmebehandlungstemperatur wurden bei  $800^\circ\text{C}$  gefunden. Unter den Proben mit unterschiedlichen Zusammensetzungen zeigte das Li-reiche LAGP die höchste Leitfähigkeit. Die optimierte Sintertemperatur für die Proben von LATP wurde bei  $1000^\circ\text{C}$  gefunden. Bei LAGP wurde erstmals der Zusammenhang zwischen der thermischen und der ionischen Leitfähigkeit untersucht. Dabei ist nachgewiesen worden, dass für diese Materialien das Wiedemann-Franz-Gesetz nicht gilt.

Um das Verständnis über die Mechanismen des Ionentransports in polykristallinem LAGP/LATP zu erweitern, wurde das Gefüge der Proben untersucht. Die Phasentransformationen in LAGP wurden untersucht, um die Sinter- und Wärmebehandlungsvorgang zu folgen. Rasterelektronenmikroskopie (REM), DSC, Dilatometrie (DIL), thermogravimetrische Analyse (TGA), XRD und Hot-stage-XRD Messungen wurden ausgeführt.

Es wurden Li-Ionen-Zellen gebaut um die Funktionalität des LAGP/LATP Materials als Feststoffelektrolyte zu testen. Zellen mit unterschiedlichen Elektrodenkombinationen und Strukturen wurden getestet. LAGP und LATP zeigten beide eine Instabilität gegen Li-Metall- und Graphitanode. LAGP war nur stabil gegen eine  $\text{Li}_4\text{Ti}_5\text{O}_{12}$ -Anode. Daher wurden zusätzlich Zyklische Voltammetrie-Messungen ausgeführt, um die Reaktion bei LAGP genauer zu untersuchen. Eine Reduktionsreaktion findet an LAGP statt, wenn die Spannung an LAGP unter 1 V gegen Li/Li<sup>+</sup> fällt. Die Reaktion wirkte sich negativ auf die Beschaffenheit des LAGP Feststoffelektrolyten aus und verursachte das Versagen der Zelle. Verbesserungen und Modifikationen sind deswegen für die Anwendung von LAGP/LATP als Feststoffelektrolyte in Li-Ionen-Zellen notwendig.

# Abstract

Lithium aluminum germanium phosphate (LAGP) and lithium aluminum titanium phosphate (LATP) are promising solid-state electrolyte materials for future lithium ion batteries. They have good ionic conductivity and excellent thermal stability, which can improve the performance and safety of the lithium ion cells. The LAGP and LATP have the NaSICON structure, whose framework consists of corner connecting  $\text{PO}_4$ -tetrahedra and  $\text{TiO}_6$ - or  $\text{GeO}_6$ -octahedra, respectively. The NaSICON structure enables an easy migration of the  $\text{Li}^+$  ions through the lattice.

An important objective of this work was the optimization of the ionic conductivity of the LAGP and LATP solid-state electrolytes via different process routes. LAGP samples with different compositions were prepared via sintering method and heat-treating method, respectively. The ionic conductivities of the samples were measured with impedance spectroscopy and the thermal conductivity with Laser flash measurements. The optimized sintering/heat-treating temperature was found to be  $800^\circ\text{C}$  and the Li rich LAGP showed the highest ionic conductivity among the samples with different compositions. For LATP, the optimized sintering temperature was found to be  $1000^\circ\text{C}$ . For LAGP, the relation between the thermal conductivity and the ionic conductivity was investigated for the first time and it was revealed that these materials do not obey the Wiedemann-Franz law.

The microstructure of the samples was analyzed for a better understanding of the ion conducting mechanisms in the polycrystalline LAGP/LATP material. The phase transitions in LAGP were investigated for a better understanding of the sintering/heat-treating process. Scanning electron microscopy (SEM), DSC, Dilatometry (DIL), Thermal gravimetric analysis (TGA), XRD and hot stage XRD measurements were carried out.

Lithium ion cells were assembled in order to test the functionality of LAGP and LATP as solid-state electrolyte. Cells with different electrode combinations and different structures were tested. Instability of the LAGP and LATP solid-state electrolyte was observed vs lithium metal and graphite anode. On the other hand, LAGP was stable vs.  $\text{Li}_4\text{Ti}_5\text{O}_{12}$  anode. Thus cyclic voltammetry measurements were carried out in order to investigate the reaction for LAGP in more detail. It was shown that the LAGP is reduced at the voltage below 1 V vs  $\text{Li}/\text{Li}^+$ . This reaction caused damage of the LAGP electrolyte pellet and the failures of the test cells. Improvements and modifications are therefore required for the application of the LAGP and LATP as solid-state electrolyte in lithium ion batteries.

# Danksagung

An dieser Stelle möchte ich mich bei allen bedanken, die mich bei dieser Arbeit unterstützt haben.

Mein Dank gilt zunächst Herrn Prof. Dr. Hans J. Seifert für die Betreuung dieser Arbeit, die fachliche Diskussion und die freundliche Hilfe. Die Gespräche auf intellektueller und persönlicher Ebene werden mir immer als bereichernder und konstruktiver Austausch in Erinnerung bleiben.

Prof. Dr. Torsten Markus danke ich für seine Bereitschaft der Übernahme des Korreferats.

Mein außerordentlicher Dank gilt Dr. Magnus Rohde für die wertvollen Ratschläge, die vielen fachlichen Diskussionen und die mannigfachen Ideengebungen. Ohne seine mühevollen Betreuung und Hilfe in dieser beschwerlichen Zeit könnte ich meiner Arbeit niemals schaffen.

Ebenso bedanke ich mich bei Dr. Carlos Ziebert und Dr. Morsi Mahmoud für die hilfreichen Diskussionen und die wertvollen Unterstützungen.

Allen Mitarbeiterinnen und Mitarbeitern der IAM-AWP möchte ich für die Unterstützung danken. Frau Petra Lukits, Frau Judith Jung und Frau Petra Severloh danke ich für die Anweisung und Bedienung von verschiedenen Messgeräten. Bei Dr. Thomas Bergfeldt und Herrn Tobias Weigärtner möchte ich mich für die Durchführung der chemischen Analysen und der Augerelektronenspektroskopie bedanken. Bei Dr. Harald Leiste und Dr. Thomas Reichmann möchte ich mich für die Durchführung der XRD und die hilfreichen Diskussionen bedanken. Bei Dr. Wilhelm Pfleging möchte ich mich für die Durchführung der LIBS bedanken. Ich danke Dr. Julian Fischer für die Durchführung des RF-Magnetronsputters und Frau Melanie Mangang für die Hilfe beim Batterietest. Des Weiteren danke ich Frau Alexandra Reif und Dr. Damian Cupid für die TGA-Messungen.

Ich danke Dr. Günter Schell vom Institut für Angewandte Materialien – Keramik im Maschinenbau für die Durchführung von SPS-Sintern und Dr. Holger Geßwein vom Institut für Angewandte Materialien – Keramische Werkstoffe und Technologien für die Durchführung der Hot-stage-XRD.

Mein weiterer Dank gilt allen Projektpartnern der Helmholtz-Energie-Allianz "Stationäre elektrochemische Feststoff-Speicher und -Wandler". Insbesondere bedanke ich mich bei Dr. Frank Tietz für die fachliche Diskussion und Zusammenarbeit. Ich bedanke mich auch bei der Helmholtz-Gemeinschaft für die Finanzierung dieses Projekts von der Helmholtz-Energie-Allianz unter dem Förderkennzeichen HA-E-0002.

Nicht zuletzt gilt mein Dank meinen Freunden und meiner Familie für die warmherzigen Unterstützungen. Ich danke besonders meinen Eltern, dass sie mich ständig ermutigen und meinen Stress abbauen.

Karlsruhe, Juli 2018

Yuantao Cui

# Erklärung

Hiermit erkläre ich, dass ich die vorliegende Arbeit selbständig angefertigt und keine anderen als die angegebenen Quellen und Hilfsmittel benutzt sowie die wörtlich und inhaltlich übernommenen Stellen als solche kenntlich gemacht und die Satzung des KIT zur Sicherung guter wissenschaftlicher Praxis in der jeweils gültigen Fassung beachtet habe.

Yuantaο Cui

Karlsruhe 05. 07. 2018

# Index

1	Introduction.....	1
1.1	Motivation.....	1
1.2	Lithium ion battery.....	2
1.2.1	Electrode materials of Lithium ion battery .....	2
1.2.2	Liquid electrolytes in lithium ion cells.....	3
1.2.3	Safety concerns of lithium ion batteries .....	4
1.3	Solid-state electrolyte .....	5
1.4	NaSICON Super ionic conductor.....	8
1.5	Polycrystalline LAGP/LATP and Equivalent circuit model (ECM) .....	14
1.6	Ionic conductivity and complex impedance spectroscopy .....	16
1.6.1	The Nyquist-diagram .....	19
1.6.2	The conductivity spectrum:.....	21
1.7	Development of LAGP/LATP solid-state electrolytes.....	22
1.8	Objectives and experiments.....	24
2	Characterization of ceramic solid-state electrolytes.....	25
2.1	Experimental methods.....	26
2.1.1	Glass fabrication and sample preparation .....	26
2.1.2	Thermal analysis.....	28
2.1.3	Ionic conductivity measurement using electrical impedance spectroscopy .....	30
2.1.4	Scanning electron microscopy and energy-dispersive X-ray spectroscopy .....	31
2.1.5	Density measurement .....	32
2.1.6	X-ray diffraction (XRD).....	33
2.1.7	Spectroscopic analysis.....	34
2.2	LAGP solid-state electrolyte via sintering route.....	36
2.2.1	Sample characterization.....	37
2.2.2	Discussion.....	53
2.3	LAGP solid-state electrolyte via heat-treating route .....	56
2.3.1	Sample characterization.....	57
2.3.2	Optimized ionic conductivity.....	84

2.3.3	Phase transitions in LAGP .....	88
2.3.4	Thermal conductivity .....	94
2.4	LATP solid-state electrolyte through sintering route .....	106
2.4.1	Sample characterization .....	106
2.4.2	Discussion .....	113
3	Test of lithium ion cells with solid-state electrolyte.....	115
3.1	Lithium ion battery cell assembly and test.....	116
3.1.1	Hybrid cell with liquid and solid-state electrolyte.....	116
3.1.2	All solid state cell with LAGP solid-state electrolyte .....	117
3.1.3	Galvanostatic cycling with potential limitation .....	118
3.1.4	Cyclic voltammetry .....	118
3.1.5	Impedance spectroscopy on cell .....	119
3.2	Cell tests and post mortem investigation.....	120
3.2.1	Cells with hybrid solid + liquid electrolyte.....	120
3.2.2	All-solid-state cells with LAGP solid-state electrolyte .....	136
3.3	Stability of LAGP solid-state electrolyte .....	144
3.3.1	Cyclic voltammetry .....	144
3.3.2	Impedance spectroscopy.....	153
3.3.3	Laser-induced breakdown spectroscopy.....	155
4	Summary and conclusion.....	157
4.1	Material developments .....	157
4.2	Cell tests .....	158
	References.....	161
	Appendix.....	172
	Ionic conductivity of the LAGP and LATP samples .....	172
	Thermal diffusivity and thermal conductivity of the LAGP samples.....	181

# 1 Introduction

## 1.1 Motivation

Lithium ion battery is one of the most massively used battery types. Lithium ion batteries have the advantages of high energy density, high open circuit voltage, fast charge / discharge, no memory effect and low self-discharge, which make them the most suitable power source for portable electronic devices, which are fabricated in largest amount. Electrical vehicles are being intensively developed nowadays and many of them rely on lithium ion batteries. The battery system is an important limiting factor for the performance of an electrical vehicle. In addition, large lithium ion battery modules have the application as stationary energy storage systems, which are required for the renewable energy systems such as wind and solar in order to reduce the fluctuation of the output of wind and solar energy<sup>1</sup>.

For those applications (portable devices, electrical vehicles and stationary energy storage), larger capacity, longer lifetime and especially higher safety are required. However, the liquid electrolytes in lithium ion batteries raise safety issues such as decomposition, leakage and inflammation. The instability of the organic liquid electrolyte is also a limiting factor for the lifetime of lithium ion batteries.

Solid-state electrolytes have the potential to improve the performance of battery systems significantly. Glass and ceramic solid-state electrolytes have a good thermal stability. There would be no concerns about leakage of the electrolytes, when the liquid organic electrolytes are replaced with solid-state electrolyte. Better heat resistance and higher power density can be also achieved in lithium ion battery cells.

In addition, a number of solid-state electrolytes may offer a larger electrochemical stability window compared to liquid electrolytes, which enables the application of high voltage cathode and increases the energy density of the Lithium ion battery.

Moreover, the solid-state electrolytes are supposed to be able to suppress the growth of Li dendrites during cycling of the Lithium ion batteries, which improves the safety. It will be then possible to apply the Li metal as anode, which has a far higher capacity than other anode materials. The solid-state electrolyte material gives also more freedom of the battery geometry. Higher packing efficiency of the cells can be achieved with help of advanced processing techniques, which increases practical battery energy densities.

Phosphate based ceramics lithium aluminum germanium phosphate (LAGP) and lithium aluminum titanium phosphate (LATP) were reported to have a good ionic conductivity<sup>2</sup>. For the applications, their fabrication processes need to be optimized for the best conductivity. Tests in battery cells are also required. In addition, their thermophysical properties and electrochemical stability are of great importance for the application as solid-state electrolytes.

## 1. Introduction

### 1.2 Lithium ion battery

#### 1.2.1 Electrode materials of Lithium ion battery

A lithium ion battery consists of the anode, the cathode, the electrolyte, and the separator. Li ions are extracted from the cathode and transported to the anode. The electrons flow through the external circuit from cathode to the anode (Figure 1-1). The lithium ion battery was invented in 1970s. In 1979, John Goodenough and Koichi Mizushima demonstrated a rechargeable cell with a voltage around 4 V using lithium cobalt oxide (LiCoO<sub>2</sub>) as the cathode (positive electrode) and lithium metal as the anode (negative electrode).

The discovery of lithium cobalt oxide (LiCoO<sub>2</sub>, LCO) as a cathode material enabled the development of rechargeable lithium ion battery<sup>3</sup>. The LiCoO<sub>2</sub> has a layered structure: the cobalt atoms are octahedrally coordinated by oxygen atoms. The octahedra are connected with each other forming a planar structure. Li<sup>+</sup> ions are positioned between the cobalt-oxygen planar layers<sup>4</sup>. Cobalt ions are oxidized by charging (from Co<sup>3+</sup> to Co<sup>4+</sup>) and lithium ions are extracted from the layer structure of the LiCoO<sub>2</sub>. A half Li of each LiCoO<sub>2</sub> formula unit can be extracted while its layered structure is preserved, which corresponds to a capacity of 140 mAh/g and a voltage window of 3 V - 4.2 V vs Li/Li<sup>+</sup>. Cobalt ions are reduced by discharging and Li<sup>+</sup> ions intercalate again in the layer structure of Li<sub>1-x</sub>CoO<sub>2</sub>. The reaction on the cathode side is:

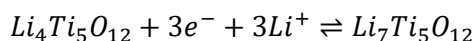


In the 1980s, the graphite was discovered as an anode material, which is less reactive than lithium metal and causes less safety problems (Li metal fails to be an appropriate anode due to the dendrite formation<sup>5</sup>). Graphite has a layered, planar structure. Individual layers are bound via weak van der Waals bonds, which allow them to be easily separated or to slide past each other. During charging and discharging, the Li<sup>+</sup> ions are intercalated into and extracted from the graphite, respectively. The potential of graphite lies at around 0.1 V vs Li/Li<sup>+</sup> (depending on the state of charge)<sup>6</sup>. The graphite is the most often used anode material for lithium ion batteries. The reaction on the anode side can be written as:



There are other cathode materials for lithium ion batteries. Lithium nickel manganese cobalt oxide (NMC) is one of the most successful cathode materials. These systems can be tailored to serve different requirements from high power to high capacity. There are different ratios of nickel, manganese and cobalt: from NMC 1:1:1 to NMC 5:3:2 to NMC 8:1:1<sup>7</sup>. Manganese spinels (Li<sub>1+x</sub>[Mn<sub>2</sub>]O<sub>4</sub>) are environmental friendly and less expensive<sup>8</sup>. Lithium iron phosphate (LiFePO<sub>4</sub>, LFP) has lower cost and no environmental harmful element. It has a good thermal stability, enhanced safety, better tolerance to abuse but lower voltage than LiCoO<sub>2</sub><sup>9</sup>.

Lithium titanate (Li<sub>4</sub>Ti<sub>5</sub>O<sub>12</sub>, LTO) is an electrode material with a potential of 1.5 V vs. Li/Li<sup>+</sup>. The LTO can work as cathode material vs. graphite and also as anode material vs. LiCoO<sub>2</sub>. The cell voltage lies at 1.5 V vs. Li/Li<sup>+</sup> and at 2.4 V vs LiCoO<sub>2</sub>. The reaction between LTO and e<sup>-</sup>, Li<sup>+</sup> is:



1-3

Both  $Li_4Ti_5O_{12}$  and  $Li_7Ti_5O_{12}$  have a cubic spinel structure with the space group of  $Fd\bar{3}m$ <sup>10</sup>. The lattice parameter exhibits less than 0.1% change during cycling<sup>11</sup>.

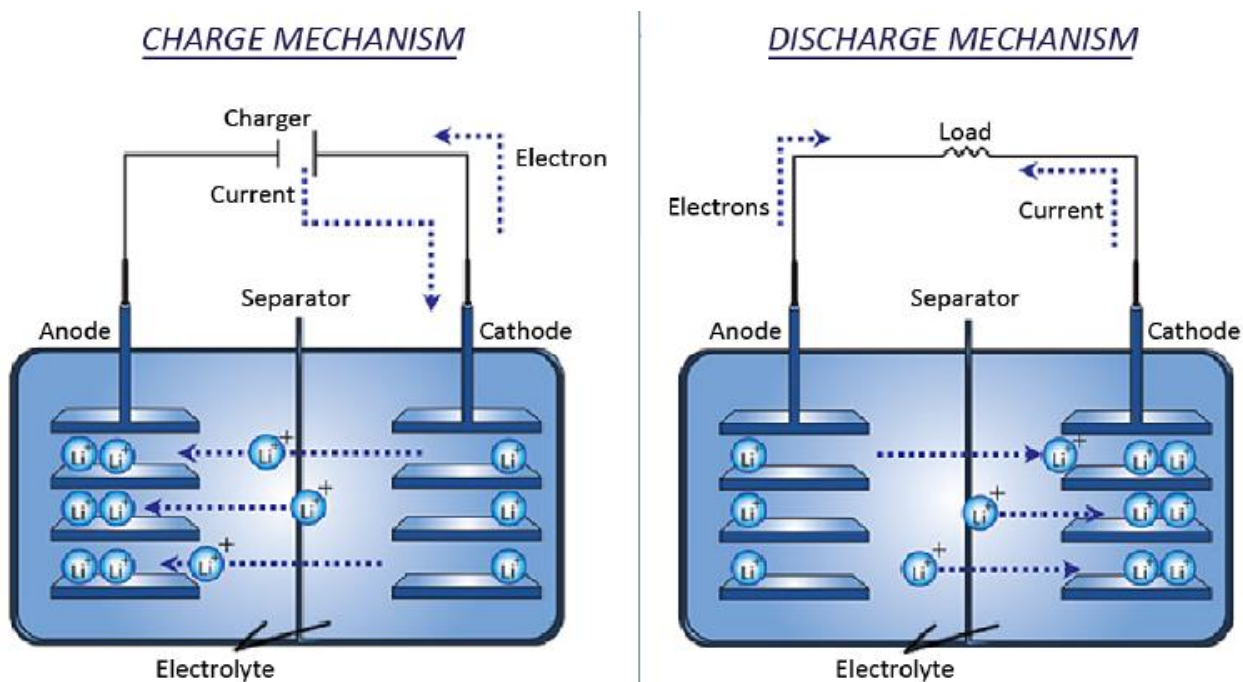


Figure 1-1: Charge and discharge process of secondary lithium-ion batteries<sup>12</sup>.

### 1.2.2 Liquid electrolytes in lithium ion cells

The electrolyte in lithium ion cells provides Lithium ion conduction between the cathode and the anode. Li ions dissolved in the electrolyte can migrate under external electric field. A good ionic conductivity, thermal and electrochemical stability are required for the electrolyte at its operating temperature<sup>13</sup>.

Aqueous solutions cannot be applied as electrolytes for lithium ion battery because  $H_2O$  can dissociate in  $H_3O^+$  and  $OH^-$ . The anode material in lithium ion battery (for example Li metal or Li in graphite) can reduce the  $H_3O^+$  cations and produce  $H_2$  gas.

Aprotic organic solvents are therefore applied for liquid electrolyte in lithium ion batteries. A sufficient solubility of lithium salts, an appropriate melting point and a good chemical stability are required for the organic solvents. Most of the lithium electrolytes are based on solutions of one or more lithium salts in two or more solvents.

Various solvents such as Ethylene carbonate (EC), propylene carbonate (PC), dimethyl carbonate (DMC), ethyl methyl carbonate (EMC), diethyl carbonate (DEC), propyl methyl carbonate (PMC), dimethoxyethane (DME) are applied for the mixed solvents. Most of the organic solvents are inflammable<sup>14, 15</sup>. A commonly used solvent mixture consists of ethylene carbonate (EC) and dimethyl carbonate (DMC). The dimethyl

## 1. Introduction

carbonate has the formula  $\text{OC}(\text{OCH}_3)_2$  and the ethylene carbonate has the formula  $(\text{CH}_2\text{O})_2\text{CO}$ <sup>16</sup>. The mixture is a colorless liquid at room temperature.

The organic solvents are not stable with respect to Li or graphite anodes. They decompose in contact with the anode material and form a passivation layer, the solid electrolyte interface (SEI) layer<sup>17</sup>. A huge variety of compounds has been observed in SEI layers.  $(\text{CH}_2\text{OCO}_2\text{Li})_2$ ,  $\text{Li}_2\text{CO}_3$ ,  $\text{LiF}$ , etc are proposed in different researches<sup>18</sup>. This SEI layer covers the anode surface and prevents the organic solvent from further decomposition. The SEI layer has also influence on the cell characteristics such as the cycle life, safety, and the self-discharge<sup>19</sup>.

The Li ions dissolved in the organic solvents are the charge carriers in the electrolyte. However, simple Li-salts such as  $\text{LiCl}$ ,  $\text{LiF}$  and  $\text{Li}_2\text{O}$  have poor solubility in an aprotic solvent. Because of their strong cation–anion interactions and high lattice energy, it is energetically unfavorable for such lithium salts to dissolve in those aprotic organic solvents. Therefore, Li-salts of weakly coordinating anions are applied. Via the electron-drawing substituents like  $-\text{F}$  or  $-\text{CF}_3$ , the negative charges are delocalized over the whole anion.  $\text{LiPF}_6$ ,  $\text{LiBF}_4$ ,  $\text{LiClO}_4$ , etc. are commonly applied for liquid electrolyte. Among them, the  $\text{LiPF}_6$  is the dominant salt in commercial lithium ion batteries due to its best balance of properties in different categories: the conductivity, the thermal stability, the sensitivity to hydrolysis and formation of proper SEI. The  $\text{LiPF}_6$  dissociates into  $\text{Li}^+$  and  $[\text{PF}_6]^-$  ions in solvent:



The  $\text{LiPF}_6$  could hydrolyze by the presence of small amounts of moisture:



and



These reactions take place at around  $80^\circ\text{C}$  and introduce impurities in the electrolyte. The hydrogen fluoride (HF) is very toxic and corrosive<sup>15, 20</sup>.

### 1.2.3 Safety concerns of lithium ion batteries

The reactive materials employed in lithium ion batteries (liquid electrolyte, anode material, polymer separator, e.g.) can bring safety risks, which lead to serious failure such as short circuit and inflammation of the batteries.

The cell temperature can rise dangerously high under abusive conditions, e.g. insufficient heat dissipation or short circuit. The SEI layer, which passivates the anode, begins to decompose at  $80^\circ\text{C}$  -  $120^\circ\text{C}$ . The electrolyte reacts then with the anode material and generates heat (self-heating). As the temperature further increases, the  $\text{LiCoO}_2$  cathode begins to evolve oxygen gas at the temperature higher than  $250^\circ\text{C}$ , which reacts violently with the anode and electrolyte, which would cause fire and explosion. Most of the cathode materials decompose and evolve oxygen at elevated temperature with the exception of  $\text{LiFePO}_4$

<sup>21-23</sup>. The separator and the battery case melt and fail at a temperature higher than 200°C. Melting of the separator can cause internal short circuit of the cell. Leakage of the battery case expose the cell components to the air and can cause inflammation.

Multiple safety devices are developed for the Lithium ion cells. A cell safety vent can release the gas if a certain pressure level is exceeded in the cell. A current limiting fuse controls the maximum current. A shut down separator stops the ionic transport when the cell temperature exceeds the temperature limit.

However, an internal short circuit is more difficult to handle. In that case, the anode and cathode get into direct contact and large current flows without passing the external circuit. The internal short circuit could be caused by foreign particles, by dendrites formation or by physical damage. Metallic foreign objects can fall between electrode sheets through failures in the manufacturing process and cause damage on the separator. Dendrites can be formed on the graphite anode by high charging current or low temperature, at which the  $\text{Li}^+$  ion cannot diffuse fast enough into the graphite matrix. Dendrites are needle-like lithium metal crystals, which can puncture the separator and cause internal short circuit. In addition, a mechanical impact can damage the cell structure and cause direct contact of the different electrodes.

One way to improve the battery safety is to use a more robust electrolyte. Solid-state electrolyte made of glass or ceramic material provides an alternative for the liquid electrolyte and the separator in lithium ion cells.

### 1.3 Solid-state electrolyte

Solid-state electrolyte refers to the solid-state material, which provides ionic conductivity and has negligible electronic conductivity.

Solid-state electrolytes made of glass and ceramic have the advantages of excellent thermal stability, good electrochemical stability and form stability. The risks of decomposition and leakage of the flammable liquid organic electrolytes can be eliminated in cells with solid-state electrolyte. The cells will become more robust vs. higher operation temperature, which increases both the safety and the performance of the lithium ion batteries. Materials with roughly twice the shear modulus of lithium can suppress dendrites<sup>24</sup>. A dense solid-state electrolyte with sufficient shear modulus can thus improve the cell safety with respect to dendrites formation and internal short circuit. It is then possible to use Li metal as anode material, which provides highest energy density. It is possible to produce multiple-layer-stacked cell using solid-state electrolyte, which can achieve a higher power density. Thin film lithium ion battery can be produced for special applications such as smart card or wearable devices.

In contrast to liquid electrolyte, a crystalline solid-state electrolyte has a lattice framework, which is immobile under external electric field. However, there are mobile ions in the lattice, which can migrate under external electric field. There is usually only one kind of mobile ions in solid-state electrolytes (e.g.  $\text{Li}^+$ ). The ion transport number (the fraction of the total electric current carried in an electrolyte by a given ionic species) of this ion is close to 1, which is significantly higher than the  $\text{Li}^+$  transport number in conventional liquid electrolytes (lower as 0.6)<sup>25</sup>.

## 1. Introduction

The ion transport in the solid-state electrolyte is conducted by jumping of the mobile ions from one lattice site to neighboring vacancies in the lattice. Alternatively, an ion can jump to an interstitial site and migrate via interstitial sites. The number of vacancies and interstitial defects are therefore important for the ionic conductivity of the crystalline solid-state electrolyte materials. Vacancies and interstitial atoms can be generated as Frenkel defect (An atom is displaced from its lattice position to an interstitial site) or Schottky defect (oppositely charged ions leave their lattice sites and create vacancies). These defects are formed via thermal activated process and called intrinsic defects. The ionic conductivity resulting from those defects is called intrinsic conductivity. The number of the intrinsic generated charge carriers have therefore strong temperature dependence.

On the other hand, defects could also be introduced into the crystal by doping with foreign atoms. One example is the yttria-stabilized zirconia (YSZ). The YSZ is produced by doping  $ZrO_2$  with the  $Y_2O_3$ . The addition of  $Y_2O_3$  stabilizes the zirconia cubic fluorite structure at room temperature and introduces oxygen vacancies into the lattice. The ionic conductivity of the YSZ depends therefore on the concentration of dopant. The ionic conductivity resulting from the introduced defects is called extrinsic conductivity.

The ionic conductivity of the solid-state electrolyte  $\sigma$  can be generally expressed as:

$$\sigma = nZe\mu \quad 1-7$$

with  $n$ : the volume density of the mobile ions,  $Z \cdot e$ : the charge, which is carried by one mobile ion and  $\mu$ : the mobility of the carrier<sup>26</sup>.

The “ $n$ ” refers to the concentration of interstitial defects when the ions migrate via interstitial sites in the solid-state electrolyte. It refers to the concentration of vacancies when the ions migrate via vacancies in the solid-state electrolyte. For extrinsic defects,  $n$  depends on the concentration of dopant. For intrinsic defects, the  $n$  obeys the Arrhenius equation.

Atoms need to overcome an energy barrier when they are jumping from one site to another site in the lattice (activation energy). The ionic conductivity obeys the Arrhenius equation:

$$\sigma = \sigma_0 \exp\left(-\frac{E_a}{kT}\right) \quad 1-8$$

with  $\sigma$ : the ionic conductivity,  $\sigma_0$ : the pre-exponential factor, which represents the vibration rate of the ions,  $T$ : the absolute temperature and  $k$ : the Boltzmann constant,  $E_a$ : the activation energy. For the solid-state electrolyte with dominating extrinsic conductivity, the activation energy  $E_a$  represents the activation energy for ion migration. For the solid-state electrolyte with dominating intrinsic conductivity, it includes the activation energy for ion migration and the energy for the defect formation. The ionic conductivity of solid-state electrolyte has therefore strong temperature dependence. The ionic conductivity increases exponentially with  $1/T$ .

A solid-state electrolyte is often called superionic conductor when it has a high ionic conductivity in the same order of magnitude as molten salts.

Silver iodide (AgI) is one of the earliest investigated superionic conductors. The AgI has a phase transition at 147°C from  $\beta$ -AgI to  $\alpha$ -AgI (wurtzite to body centered cubic). The ionic conductivity of the AgI jumps from  $10^{-4}$  S/cm to more than 1 S/cm in the phase transition. In the  $\alpha$ -AgI, the Ag sub lattice is highly disordered and has a quasi-molten state, while the iodide sub lattice remains solid. It allows the correlated motion of the silver ions, which largely enhances the ionic conductivity<sup>27-29</sup>.

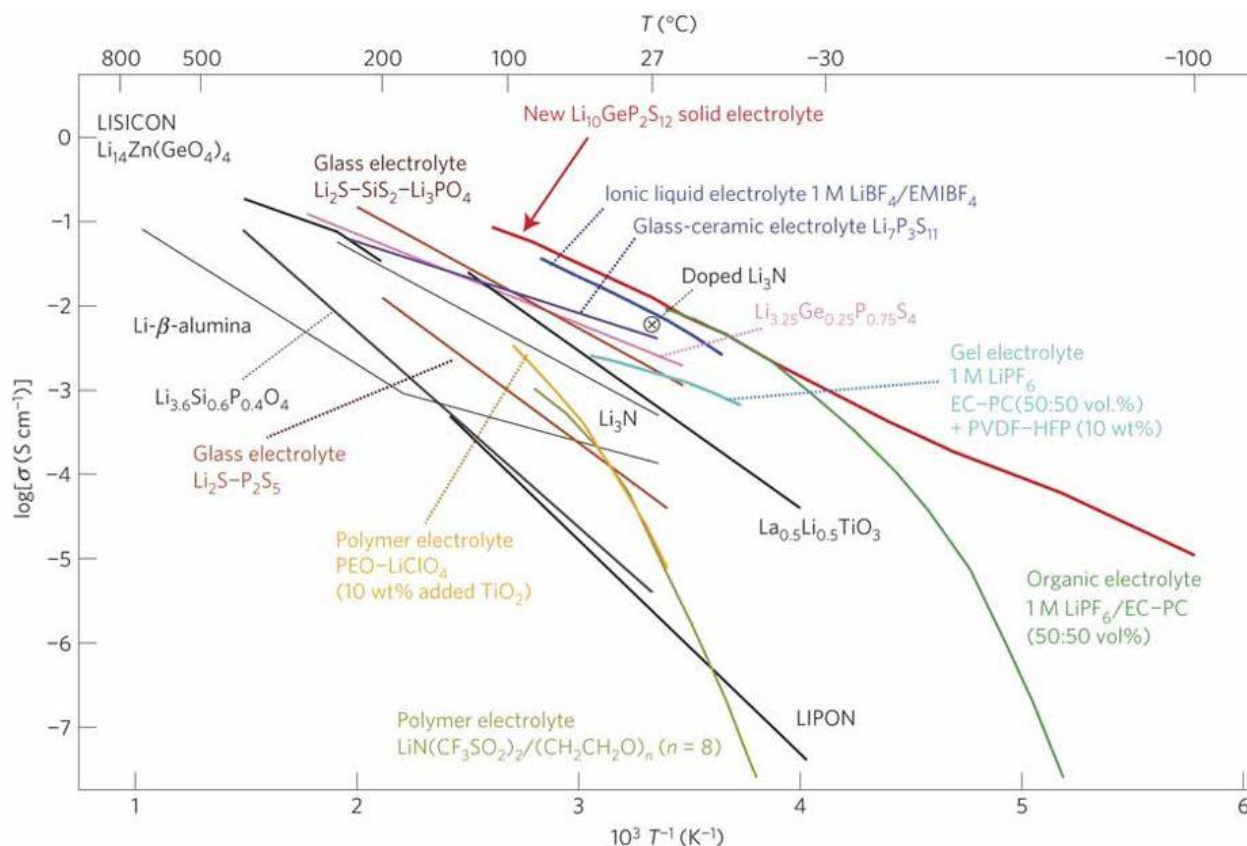


Figure 1-2: Ionic conductivity of different kinds of lithium solid electrolytes, organic liquid electrolytes, polymer electrolytes, ionic liquids and gel electrolytes<sup>30</sup>.

The lithium ion batteries are widely used. Solid-state electrolytes conducting  $\text{Li}^+$  ions gain therefore great interest. Different kinds of lithium superionic conductors were investigated in the past years. Many of them have a good ionic conductivity, which is comparable to that of polymer electrolytes (Figure 1-2). The Garnet-type Li-ionic conductors, Perovskite-type Li-ionic conductors, sulfide Li-ionic conductors and phosphate NaSICON Li-ionic conductors are the promising solid-state electrolyte materials<sup>31</sup>.

The garnet structure crystal has the general formula  $\text{X}_3\text{Y}_2\text{Z}_3\text{O}_{12}$ , where the X-sites are occupied by divalent cations, the Y-sites by trivalent cations and the Z-sites by tetravalent atoms. Each X-site is coordinated with eight oxygen atoms in a distorted cubic. The Y-site is 6-fold coordinated (octahedral) and the Z-site is 4-fold coordinated (tetrahedral). One example of the garnet type Li-ionic conductor is the  $\text{Li}_5\text{La}_3\text{Ta}_2\text{O}_{12}$ . Its stoichiometry can be modified by substitution of tetravalent atoms with pentavalent Ta. Extra  $\text{Li}^+$  ions are introduced into the crystal on the interstitial sites. Various kinds of elements are applied as dopant in garnet type Li-ionic conductor with the formula  $\text{Li}_6\text{Ala}_2\text{M}_2\text{O}_{12}$  (A = Ca, Sr, Ba; M = Nb, Ta). The Garnet-type

## 1. Introduction

Li-ionic conductors have good ionic conductivity (in the range of  $10^{-5} - 10^{-3}$  S/cm at room temperature) and good chemical stability<sup>32-34</sup>.

The perovskite structure crystal has the general formula of  $ABO_3$ , where A and B represent cations and O is oxygen. The B cation is tetravalent and coordinated with six oxygen atoms. The  $BO_6$ -octahedra share corners with each other and build a 3-dimensional framework. The divalent A cations occupy the holes created by eight  $BO_6$  octahedra, giving the A cations 12-fold oxygen coordination. The 3D structure of the perovskite structure allows good diffusion of the cations.  $Li_{3x}La_{2/3-x}TiO_3$  (LLTO) is one example of the Perovskite-type Li-ionic conductor. By substitution of the  $A^{2+}$  with the  $La^{3+}$  and  $Li^+$ , vacancies are generated in the crystal (when  $x < 1/6$ ). The LLTO has an ionic conductivity of  $10^{-4} - 10^{-3}$  S/cm at room temperature). However, the  $Ti^{4+}$  can be reduced by Li metal and lithium intercalation graphite anode, which makes the LLTO unstable in Li-ion cells<sup>35</sup>. Perovskite Li-ionic conductors with other elements such as  $Li_{2x-y}Sr_{1-x}Hf_{1-y}Nb_yO_3$  ( $x = 0.75y$ ) and  $Li_{3/8}Sr_{7/16}Hf_{1/4}Ta_{3/4}O_3$  are investigated in order to overcome this problem<sup>36</sup>.

The sulfide Li-ionic conductors involve a group of glass-ceramic sulfide materials such as  $Li_2S-SiS_2$ ,  $Li_2S-SiS_2-LiI$ ,  $Li_2S-P_2S_5$  and  $Li_2S-GeS_2-P_2S_5$ . A superionic  $Li_7P_3S_{11}$  phase is formed in the  $Li_2S-P_2S_5$  system, which improves the ionic conductivity<sup>37</sup>. In the  $Li_2S-GeS_2-P_2S_5$  System, the superionic  $Li_{4-x}Ge_{1-x}P_xS_4$  phase is formed<sup>38</sup>. Besides the high ionic conductivity of the crystal grains, the advantage of sulfide electrolytes is the low grain boundary resistance (The grain boundary resistance has the largest fraction of the total resistance in other Li-ionic conductors)<sup>39</sup>. The sulfide Li-ionic conductors have the ionic conductivity as high as  $10^{-2}$  S/cm at room temperature<sup>2</sup>. The main drawback of the sulfide electrolytes is their hydrolysis in air.  $H_2S$  is formed in this reaction and can induce security risks<sup>37</sup>.

There are other kinds of Li-ionic conductor such as  $Li_3N$ , Li- $\beta$ -alumina and  $Li_{2.88}PO_3.86N_{0.14}$  (LiPON)<sup>34, 40</sup>. However, none of the solid-state electrolyte mentioned above has replaced the liquid electrolyte applied in commercial Li-ion batteries. Research and development are required to improve the properties (ionic conductivity, chemical stability, production procedure, etc.) of the solid-state electrolytes.

### 1.4 NaSICON Super ionic conductor

The phosphate based solid ionic conductors lithium aluminum germanium phosphate  $Li_{1+x}Al_xGe_{2-x}(PO_4)_3$  ( $x = 0.3 - 0.7$ , LAGP) and lithium aluminum titanium phosphate  $Li_{1+x}Al_xTi_{2-x}(PO_4)_3$  ( $x = 0.3 - 0.7$ , LATP) are reported to have a ionic conductivity in the range of  $10^{-4} - 10^{-3}$   $Scm^{-1}$ <sup>2, 41-43</sup>. They are non-flammable, stable in air and water and have high melting points. The LAGP and LATP are therefore candidates for solid-state electrolytes in lithium ion batteries.

The LAGP and LATP possess a so-called NaSICON structure. This structure was proposed in 1976 by Hong and Goodenough et al. The structure has a suitable tunnel size for  $Na^+$  migration in the  $Na_{1+x}Zr_2Si_xP_{3-x}O_{12}$  ( $0 \leq x \leq 3$ ) framework and was named as Sodium (Na) Super (S) Ionic (I) Conductor (CON) (NaSICON)<sup>44, 45</sup>. The crystal with the composition  $NaZr_2P_3O_{12}$  has a rhombohedral space group  $R\bar{3}c$  (Space group No. 167) (Figure 1-3, Figure 1-4). A small distortion to monoclinic symmetry occurs at  $1.8 \leq x \leq 2.2$ . Consequently, the structure of  $Na_3Zr_2Si_2PO_{12}$  has the space group  $C2/c$  (Space group No. 15) (Figure 1-4).

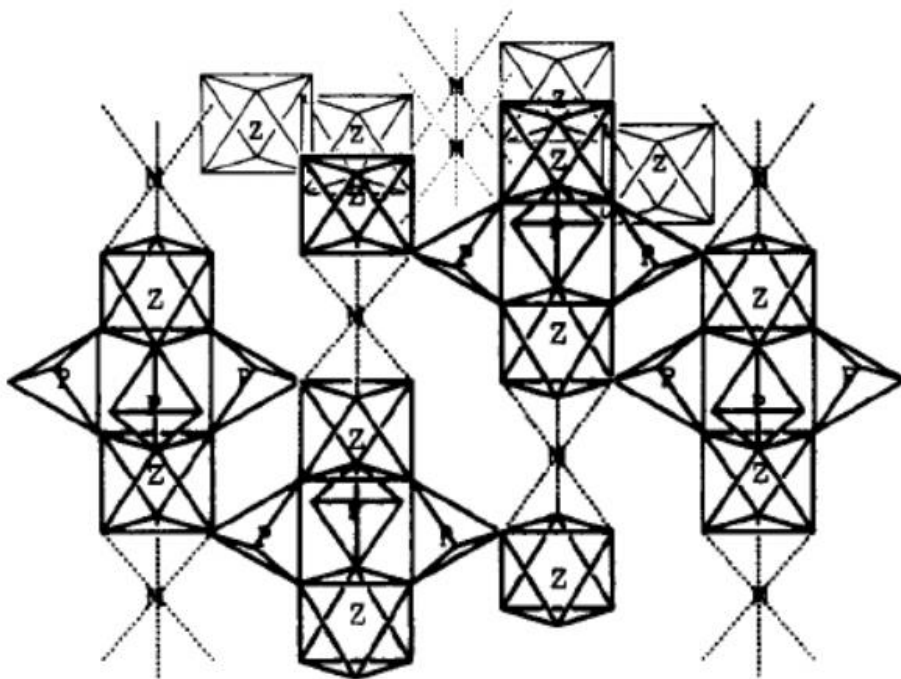


Figure 1-3: Rhombohedral  $R\bar{3}c$  structure of  $\text{NaZr}_2\text{P}_3\text{O}_{12}$ <sup>44</sup>. Z: Zirconium, P: Phosphorous, N: Sodium. Oxygen atoms are on the corner of each octahedra and tetrahedra.

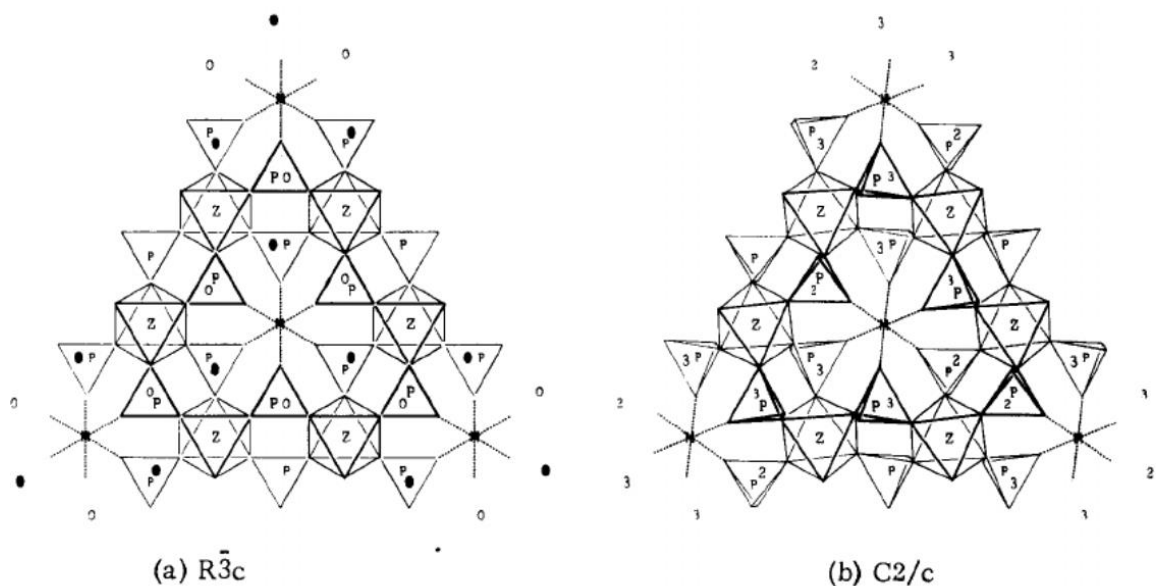


Figure 1-4: The  $a - b$  plane of the NaSICON structure with the space group (a)  $R\bar{3}c$  and (b)  $C2/c$ <sup>44</sup>.

In later publications, the NaSICON is referred to a class of structurally isomorphous 3D framework compounds with high conductivity. Generally, the NaSICON compounds have the formula  $\text{A}_x\text{M}_y\text{M}'_z\text{P}_3\text{O}_{12}$ . The A usually refers to an alkali ion ( $\text{Li}^+$ ,  $\text{Na}^+$  or  $\text{K}^+$ ). The M and M' refer to divalent ( $\text{Zn}^{2+}$ ,  $\text{Cd}^{2+}$ ,  $\text{Ni}^{2+}$ ,  $\text{Mn}^{2+}$ ,

## 1. Introduction

$\text{Co}^{2+}$ ), trivalent ( $\text{Fe}^{3+}$ ,  $\text{Sc}^{3+}$ ,  $\text{V}^{3+}$ ,  $\text{Cr}^{3+}$ ,  $\text{Al}^{3+}$ ,  $\text{In}^{3+}$ ,  $\text{Ga}^{3+}$ ,  $\text{Y}^{3+}$ ,  $\text{Lu}^{3+}$ ), tetravalent ( $\text{Ti}^{4+}$ ,  $\text{Zr}^{4+}$ ,  $\text{Hf}^{4+}$ ,  $\text{Sn}^{4+}$ ,  $\text{Si}^{4+}$ ,  $\text{Ge}^{4+}$ ) and pentavalent ( $\text{V}^{5+}$ ,  $\text{Nb}^{5+}$ ,  $\text{Ta}^{5+}$ ,  $\text{Sb}^{5+}$ ,  $\text{As}^{5+}$ ) transition metal ions<sup>46,47</sup>.

In the 3D framework of a NaSICON lattice, each M atom is octahedrally coordinated with six oxygen atoms (yellow octahedra in Figure 1-5). Each phosphorous atom is tetrahedrally coordinated with four oxygen atoms (purple tetrahedra in Figure 1-5). The  $\text{MO}_6$ -octahedra and  $\text{PO}_4$ -tetrahedra are connected with each other via their corners. I.e. each oxygen atom is bonded with phosphorous atom on one hand and with the M atom on the other hand.

The Wyckoff positions of the different atoms in the NaSICON structure are listed in Table 1-1. The exact atom coordinates vary between compounds with different elements and compositions. There are 72 oxygen atoms occupying two kinds of 36f positions in one elementary cell. There are 18 phosphorous atoms occupying the 18e positions and 12 M-atoms occupying the 12c positions. The alkali ions (e.g.  $\text{Na}^+$  or  $\text{Li}^+$ ) occupy the 6b positions (A1). There are other 18 interstitial positions (A2) in one unit cell, which have also the Wyckoff position  $18e^{48-50}$ . As shown on Figure 1-6, the A1 sites are between two  $\text{MO}_6$ -octahedra along the c-axis and the A2 sites are in distorted octahedra.

There are numerous options of substitution at various lattice sites. The tetravalent ions in the  $\text{MO}_6$ -octahedra can be substituted by trivalent ions. The phosphorous atoms in the  $\text{PO}_4$ -tetrahedra can be substituted by tetravalent ions. The charge deficiency is compensated by additional monovalent ions ( $\text{Na}^+$  or  $\text{Li}^+$ ) in the crystal. The charge compensating cations occupy vacancies A2, which is initially unoccupied without substitution (Li2 position on Figure 1-6).

The lithium aluminum germanium phosphate glass-ceramics (LAGP) and lithium aluminum titanium phosphate (LATP) have the NaSICON structure with the space group  $R\bar{3}c$ , which consists of corner connecting  $\text{PO}_4$ -tetrahedra and  $\text{GeO}_6$ - or  $\text{TiO}_6$ -octahedra, respectively<sup>51-53</sup>. Li-ions occupy the low energy site A1 between two  $\text{GeO}_6$ -octahedra/ $\text{TiO}_6$ -octahedra (Wyckoff position 6b) in the un-doped  $\text{LiGe}_2(\text{PO}_4)_3$  / $\text{LiTi}_2(\text{PO}_4)_3$  (LGP/LTP) lattice. The  $\text{Al}^{3+}$  ions occupy the  $\text{Ge}^{4+}/\text{Ti}^{4+}$  site (Wyckoff position 12c) when they are doped in LGP/LTP. The additional  $\text{Li}^+$  ions introduced by doping occupy the A2 sites with higher energy (Wyckoff position 18e).

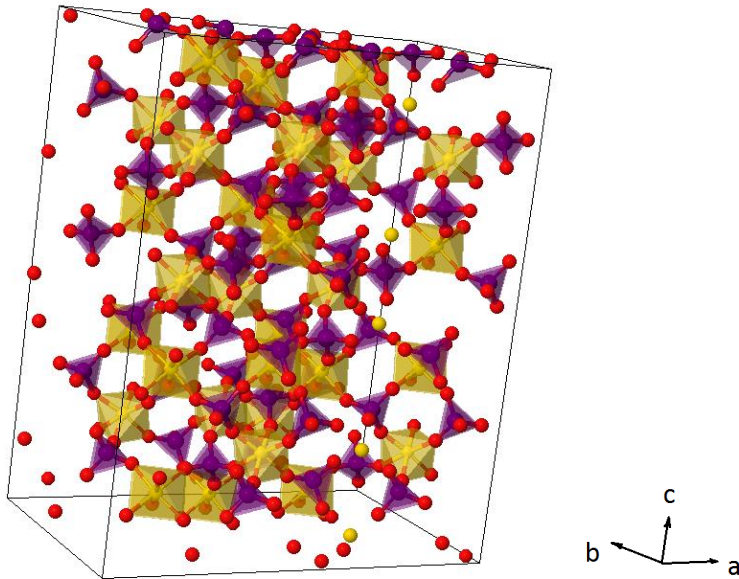


Figure 1-5: 3D crystal structure of NaSICON  $\text{Na}_{1+x}\text{Zr}_2\text{P}_{3-x}\text{Si}_x\text{O}_{12}$ . Sodium atoms are not shown. Red dots: Oxygen atoms, yellow octahedron:  $\text{ZrO}_6$  octahedron, purple tetrahedron:  $\text{PO}_4$  tetrahedron. (Generated by chemtube3d of University Liverpool. ChemTube3D by Nick Greeves is licensed under a Creative Commons Attribution-Noncommercial-Share Alike 2.0 UK: England & Wales License)

Table 1-1: Wyckoff positions of the atom sites in  $R\bar{3}c$  NaSICON structure with hexagonal axis.

Atom site	Wyckoff position
A1	6b
A2	18e
M	12c
P	18e
O	36f

## 1. Introduction

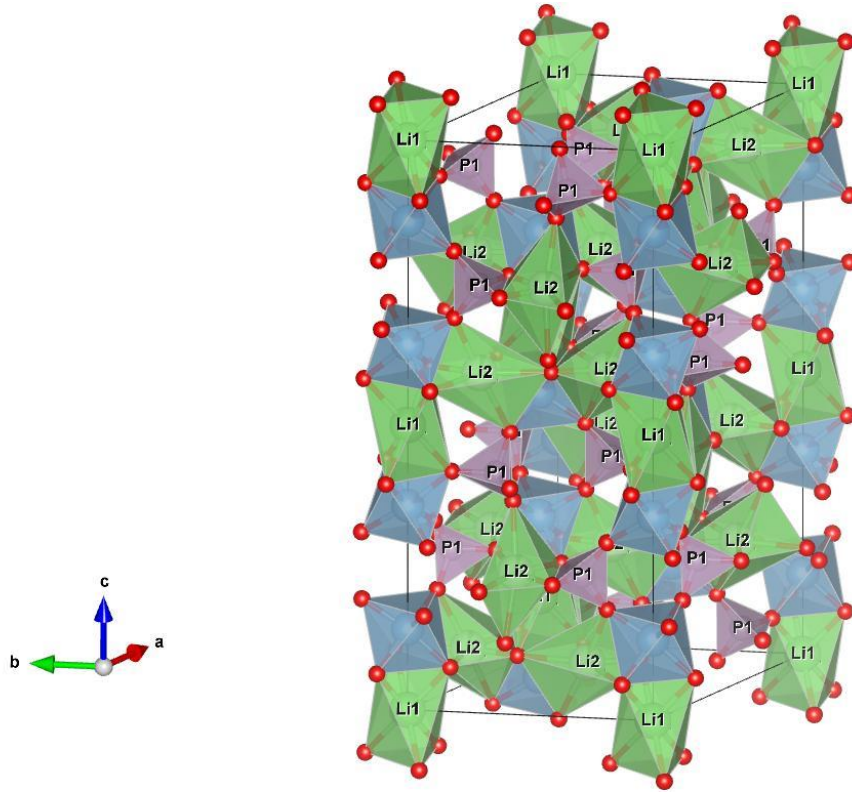
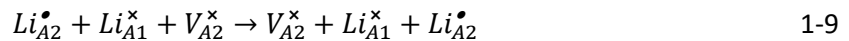


Figure 1-6: Structure of the  $Li_{1.2}(Al_{0.2}Ge_{0.2}Ti_{1.6})(PO_4)_3$  crystal with NaSICON structure<sup>54</sup>. The Li1 atoms occupy the A1 site, the Li2 atoms are on the A2 site.

The 3D-Framework of the crystal enables an easy migration of the monovalent ions ( $Li^+$ ,  $Na^+$  or  $K^+$ ). The A2 vacancies in the lattice are partially occupied by the monovalent ions ( $Na^+$  or  $Li^+$ ). The ions can jump between the A1 and A2 site. Ionic conduction occurs by correlated migrations of the monovalent ions:



where  $Li_{A1}^{\times}$  refers to the monovalent ion on A1 site with neutral charge relative to site that it occupies (a monovalent ion),  $Li_{A2}^{\bullet}$  refers to the monovalent ion on A2 site, which has a single positive charge relative to the site that it occupies (a vacancy), and  $V_{A2}^{\times}$  refers to a vacancy at the A2 site with neutral charge.

Figure 1-7 shows the migration path of  $Li^+$  ions in a  $LiTi_2(PO_4)_3$  crystal. The  $Li^+$  ion migrates along the A1-A2-A1 path. Figure 1-8 shows the simulated diffusion channel in the  $LiTi_2(PO_4)_3$  crystal (using energy minimization of Universal Force Field), through which the  $Li^+$  ions can migrate.

There are different mechanisms, which can enhance the ionic conductivity. The additional  $Li^+$  ions increase the concentration of the charge carriers and hence increase the ionic conductivity. The doped atoms and the extra  $Li^+$  ions enlarge the lattice volume. The enlarged lattice volume is correlated with a larger bottleneck width in the diffusion path, which reduces the activation energy of the ion migration. Moreover, new interstitial sites for  $Li^+$  ions can be created, which increases the probability of a successful jump. These mechanisms have a combined effect and increase the ionic conductivity of the crystal to the magnitude of  $10^{-4} - 10^{-3}$  S/cm at room temperature<sup>48, 55, 56</sup>.

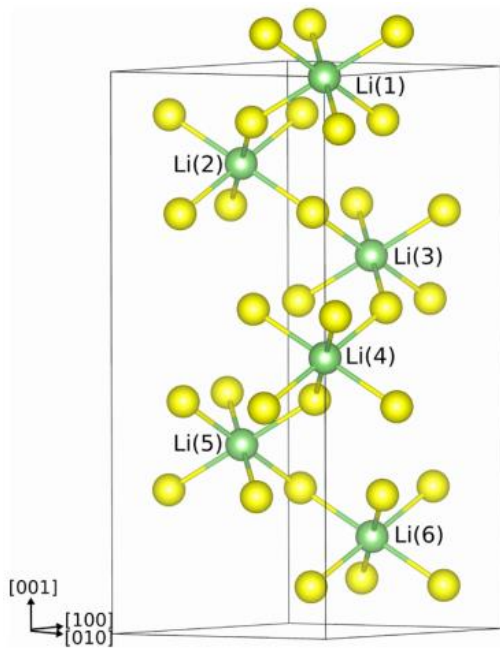


Figure 1-7: Migration path for Li ions in  $\text{LiTi}_2(\text{PO}_4)_3$  consisting of A1 (stable sites in green) and A2 (transition sites in yellow) positions <sup>57</sup>.

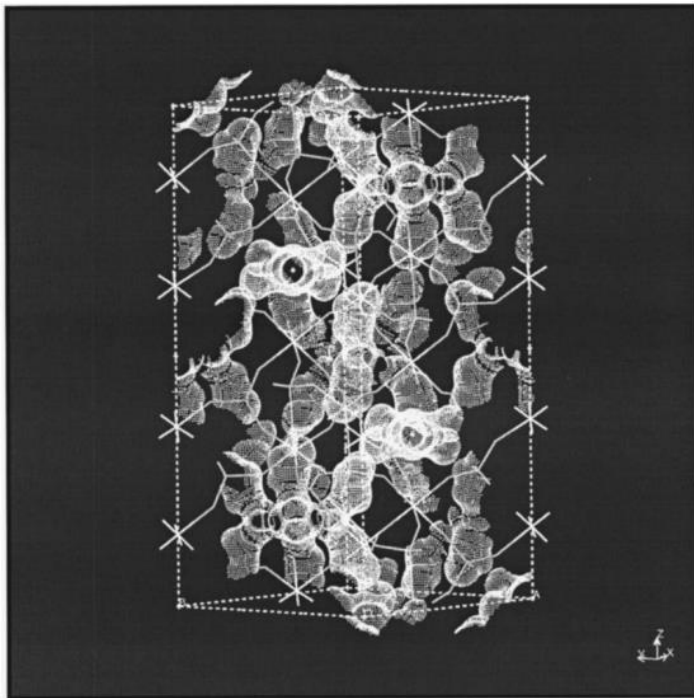


Figure 1-8 : Diffusion channels in the  $[\text{Ti}_2(\text{PO}_4)_3]$  framework <sup>55</sup>.

## 1. Introduction

### 1.5 Polycrystalline LAGP/LATP and Equivalent circuit model (ECM)

The LATP and LAGP solid-state electrolytes are usually fabricated as polycrystalline materials. The grain boundaries have significant influence on the ion transport in LAGP/LATP.

The grain boundary has a thickness of several atom layers. Atoms at the grain boundary have an irregular arrangement and a lower packing density. Since there are more defects at the grain boundary, diffusion is faster at grain boundary than in grains in conventional polycrystalline materials. However, due to its crystal structure and vacancy distribution, the grains of the NaSICON materials have a higher ionic conductivity and lower resistance as the grain boundary. Moreover, glassy or crystalline minor phases can be formed at the grain boundary and affect the ionic conductivity<sup>58, 59</sup>.

It was reported that the ratio of the grain boundary resistance and the grain resistance is about 10 ( $R_{gb}/R_g \approx 10$ ) in LATP solid-state electrolyte<sup>60</sup> and grain conductivity ( $10^{-2}$  S/cm at room temperature) is 3 - 5 orders of magnitude higher than the grain boundary conductivity (in the range of  $10^{-7} - 10^{-5}$  S/cm at room temperature)<sup>61</sup>. In LAGP solid state electrolyte, the grain boundary resistance is also higher than the grain conductivity and the conductivity ( $10^{-6}$  S/cm at  $-60^\circ\text{C}$ ) is 1 - 2 orders of magnitude higher than the grain boundary conductivity (in the range of  $10^{-8} - 10^{-7}$  S/cm at  $-60^\circ\text{C}$ )<sup>62, 63</sup>.

The arrangement of the grains can be described with the brick-layer model, where the “bricks” represent the grains (Figure 1-9). There are series as well as parallel connections between the grains and the grain boundary. The mobile ions migrate via the “grain - grain boundary - grain” route or via the parallel grain boundary. However, since the resistance of the grain boundary is larger than the resistance of the grain, the current flows mainly via the grains. The parallel grain boundary conduction is therefore negligible. On the other hand, the mobile ions need still to cross the grain boundary when they migrated via the “grain - grain boundary - grain” route. The series grain boundary resistance needs to be taken into account.

An equivalent circuit model can be used to describe the conduction mechanisms of a material. It is a simplified form of a more complex circuit in order to aid analysis and calculation. The equivalent circuit should preferably behave the same in an electric circuit as the real material.

For detailed investigation of the LAGP and LATP solid-state electrolyte, the equivalent circuit needs to contain components representing the grain and the grain boundary. The arrangement of the grains is described using the brick-model (Figure 1-9). The equivalent circuit can be simplified to a series connection of the grain and the grain boundary contribution as shown in Figure 1-10.  $R_{\text{grain}}$  and  $C_{\text{grain}}$  represent the resistance and capacitance of the grains and  $R_{\text{grain-boundary}}$  and  $C_{\text{grain-boundary}}$  represent the resistance and capacitance of the grain boundary, respectively.

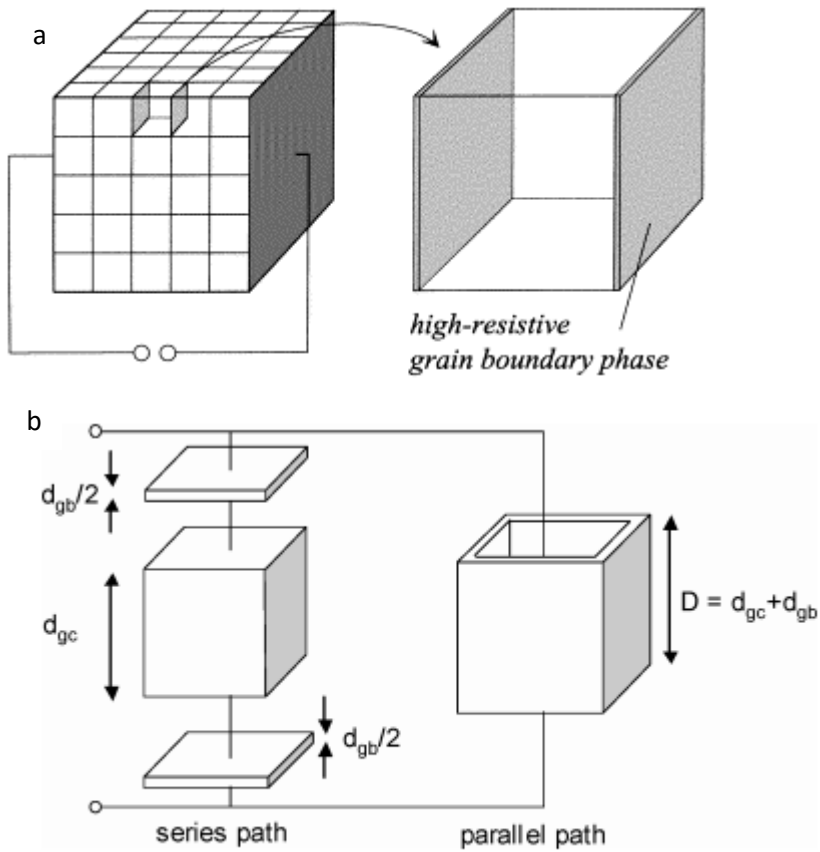


Figure 1-9: Brick-layer model for the ionic conduction in polycrystalline materials: (a) the material consists of the grains and the high resistive grain boundary phase. (b) Schematic representation of the serial path of grain core and capping grain boundary and the grain boundary path in parallel<sup>64,65</sup>.

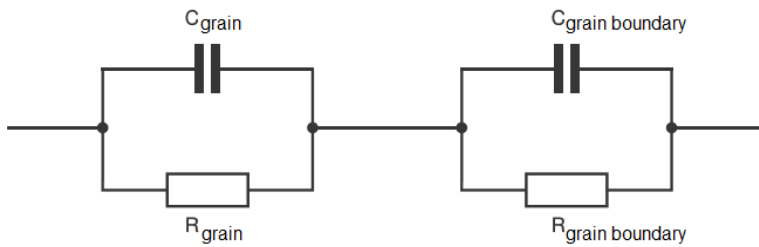


Figure 1-10 : The equivalent circuit model with grain and grain boundary contribution, which represents the ionic conduction in solid electrolytes.

## 1. Introduction

### 1.6 Ionic conductivity and complex impedance spectroscopy

Ionic conductivity represents the ability of a material to conduct ions. Analogous to the electrical conductivity, the ionic conductivity  $\sigma$  can be defined as:

$$\sigma = \frac{j}{E} = \frac{1}{\rho} \quad 1-10$$

with  $j$ : the ion current density in the ionic conductor (SI unit A/m<sup>2</sup>),  $E$ : the electric field intensity (V/m) and  $\rho$ : the resistivity of the ionic conductor. The ionic conductivity has the unit of A/(V·m) and S/m (The unit Siemens (S) is defined as 1/Ω). In the literature, the unit S/cm is most frequently used.

The ionic conductivity can be calculated using the resistance and the sample geometric parameters. The conductivity of a cylindrical sample can be calculated as:

$$\sigma = \frac{d}{R \cdot A} \quad 1-11$$

with  $R$ : the resistance of the sample,  $d$ : the height of the cylindrical sample and  $A$ : cross section area of the cylindrical sample.

A sample needs to be connected to the measuring circuit for the conductivity measurement by applying electrodes. When the solid-state electrolyte sample is connected on both sides with electrochemical active electrodes, for example Li metal, redox reactions take place and the ions migrate into and out of the sample. This kind of electrode is called a non-blocking electrode. When a DC voltage is applied on such electrodes, current can flow continuously. However, the resistance at the interface between the electrode and the sample needs to be taken into account for the conductivity measurement. The interface resistance contributes significantly to the total resistance of the measuring circuit and is also dependent on the interface property<sup>66</sup>. It is difficult to separate the resistance of the interface and of the sample. The DC method with non-blocking electrode is therefore not suitable for the ionic conductivity measurement.

When a solid-state electrolyte sample is connected on both sides with inert electrodes, such as gold or platinum, which are called blocking electrodes, the ions cannot migrate from the electrode into the solid-state electrolyte and vice versa. When DC voltage is applied to the sample, the Li<sup>+</sup> ions migrate to the negative pole due to the electrical field. The charge accumulates at the interface between the sample and the electrodes and forms a polarization layer. The electrical field of the polarization layer counteracts the external electrical field and achieves equilibrium in the ion conductor so that the current goes to zero.

The electrical impedance spectroscopy (EIS) is applied to measure the ionic conductivity. The electrical impedance spectroscopy uses an AC (alternating current) sinusoidal excitation potential. An AC current flows through the sample. By varying the frequency of the excitation potential, the measuring device scans a certain frequency range. For each frequency, the amplitude and the phase shift of the response signal is recorded and the electrical impedance is calculated.

Similar to the ohmic resistance, the electrical impedance is defined as the ratio of the voltage and current:

$$Z = \frac{V}{I} \quad 1-12$$

with  $Z$ : the electrical impedance,  $V$ : the voltage applied on the conductor,  $I$ : the current through the conductor.

In the case of AC measurement, the voltage and current can be presented as complex-valued functions:

$$V = V_0 e^{i\omega t} \quad 1-13$$

$$I = I_0 e^{i(\omega t - \phi)} \quad 1-14$$

with  $\phi$ : the phase shift between voltage and current,  $V_0$ : the amplitude of the voltage,  $I_0$ : the amplitude of the current,  $\omega$ : the angular frequency of the excitation potential (unit: radians per second).

According to the equation 1-12, the complex impedance equals:

$$Z = \frac{V_0}{I_0} e^{i\phi} = Z_0 e^{i\phi} \quad 1-15$$

with  $V_0$ : the amplitude of the voltage,  $I_0$ : the amplitude of the current,  $\omega$ : the angular frequency of the excitation potential (unit: radians per second),  $t$ : time,  $\phi$ : phase shift between voltage and current,  $Z_0$ : absolute value of the impedance.

The electrical impedances of common electrical elements (resistance, capacitance and inductance) are shown in Table 1-2.

*Table 1-2 : The electrical impedance of the common electrical elements*

Element	Electrical impedance	
Resistor	R	R=V/I
Capacitor	$(i\omega C)^{-1}$	C: capacity of the capacitor
Inductor	$i\omega L$	L: inductivity of the inductor

However, materials often show properties that the common electrical elements (resistor, capacitor and inductor) do not represent exactly. In AC (alternating current) measurements, materials show dispersive character, which means that the electric response of the material has a frequency dependence. The capacitive process in a real material may not behave exactly as an ideal capacitor, but with a phase angle different from  $90^\circ$ . In order to consider this effect, the constant phase element is introduced<sup>67-69</sup>.

The constant phase element (CPE) is defined to have the electrical impedance as follows:

$$Z_{CPE} = \frac{1}{Q} \cdot \frac{1}{(i\omega)^n} \quad 1-16$$

$Q$ : the amplitude of the constant phase element,  $n$ : the phase parameter ( $0 \leq n \leq 1$ ).

## 1. Introduction

For  $n = 1$ , the constant phase element is equivalent to a capacitor. For  $n = 0$ , the constant phase element becomes a resistor. For a certain value of the parameter  $n$  the CPE causes a constant phase shift between  $-90^\circ \leq \phi \leq 0^\circ$ .

There are various explanations of the CPE. The surface roughness at the interface between solid-state electrolyte and electrode is commonly considered as one reason for the CPE<sup>70, 71</sup>. There are also other explanations such as inhomogeneous reaction rates on a surface<sup>72</sup> and non-uniform current distribution<sup>73</sup>. With help of the constant phase element, equivalent circuit model can be better adapted to the real measurement. Figure 1-11 shows the equivalent circuit model of a solid-state electrolyte with CPE.

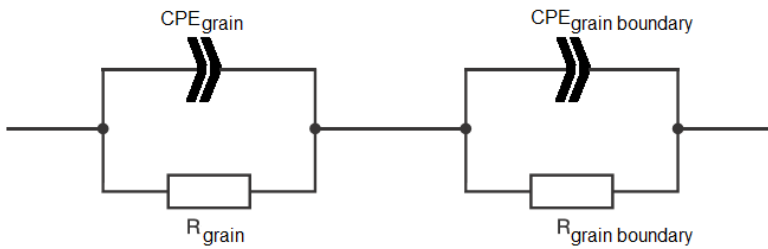


*Figure 1-11 : The equivalent circuit model with resistances and constant phase elements (CPE) of the grain and grain boundary.*

The complex impedance can be written in real part and imaginary part.

$$Z = Z' + iZ'' \quad 1-17$$

with  $Z$ : complex impedance,  $Z'$ : real part of the complex impedance,  $Z''$ : imaginary part of the complex impedance.

$$Z' = Z_0 \cos(\phi) \quad 1-18$$

$$Z'' = Z_0 \sin(\phi) \quad 1-19$$

with  $Z_0$ : the absolute value of the impedance  $\phi$ : the phase difference of the voltage and current.

Each complex impedance value corresponds to a frequency  $\nu$  at which it is measured. A complex impedance value has two variables ( $Z'$  and  $Z''$  or  $Z_0$  and  $\phi$ ). Together with the corresponding frequency  $\nu$ , the result of the impedance spectroscopy is a 3-variable data set ( $Z'$ ,  $Z''$ ,  $\nu$ ). There are different ways to present the data set in two-dimensional diagrams and calculate the ionic conductivity of the sample. The Nyquist-diagram and the conductivity spectrum are explained in the following.

### 1.6.1 The Nyquist-diagram

In a Nyquist-diagram, the real part of the complex impedance  $Z'$  is plotted vs the negative imaginary part of the complex impedance  $Z''$ . The frequency information is implicit and not directly readable. Figure 1-12 shows the Nyquist-diagram of a solid-state electrolyte sample with a part of a deformed semicircle in the high frequency range.

The measured diagram can be fitted using the equivalent circuit model. The equivalent circuit model for the fitting is shown on the inset of Figure 1-12. The  $R_1$ ,  $CPE_1$  and  $R_2$ ,  $CPE_2$  can be interpreted as resistance and capacitance of the grain and grain boundary of the sample, respectively. The  $CPE_3$  represents the effect of the blocking electrode<sup>69</sup>. The experimental data can be fitted using the parameters of the equivalent circuit model by the software EISSA.

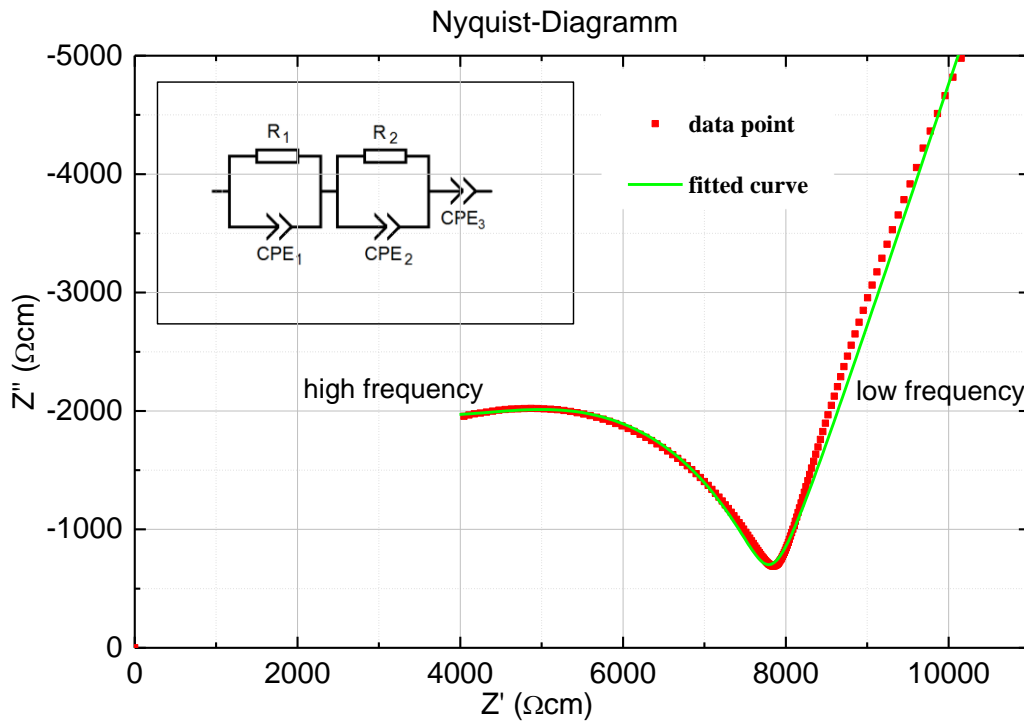


Figure 1-12 : Nyquist-diagram and the fitted curve of a LAGP sample. The fitted equivalent circuit model is given in the inset.

Figure 1-13 shows the Nyquist-diagram of different electronic elements and elements combinations. In reality, the measured data do not show the same behavior of standard electrical elements. The constant phase element (CPE) is therefore introduced. Figure 1-14 shows the Nyquist-diagram of the resistor-CPE circuit compared with that of a resistor-capacitor circuit.

# 1. Introduction

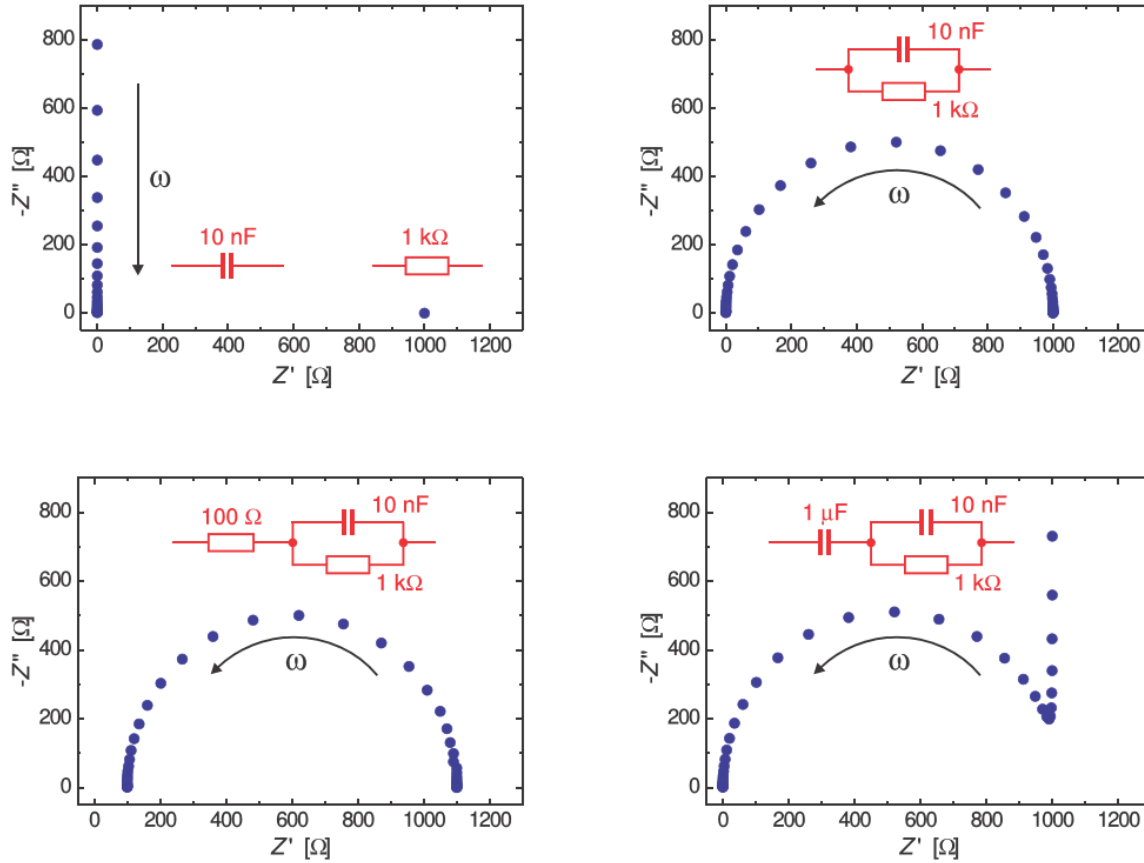


Figure 1-13: The Nyquist-diagrams of different electrical elements and elements combinations. The arrow shows the increasing angular frequency ( $\omega$ ). Top left: Pure capacitor has only imaginary impedance. Pure resistor has frequency independent real impedance. Top right: The parallel connection of a capacitor and a resistor shows a semicircle in the Nyquist-diagram. Bottom left: A series connected resistor shifts the semicircle. Bottom right: The series connected capacitor induces a spike in the high frequency side<sup>67</sup>.

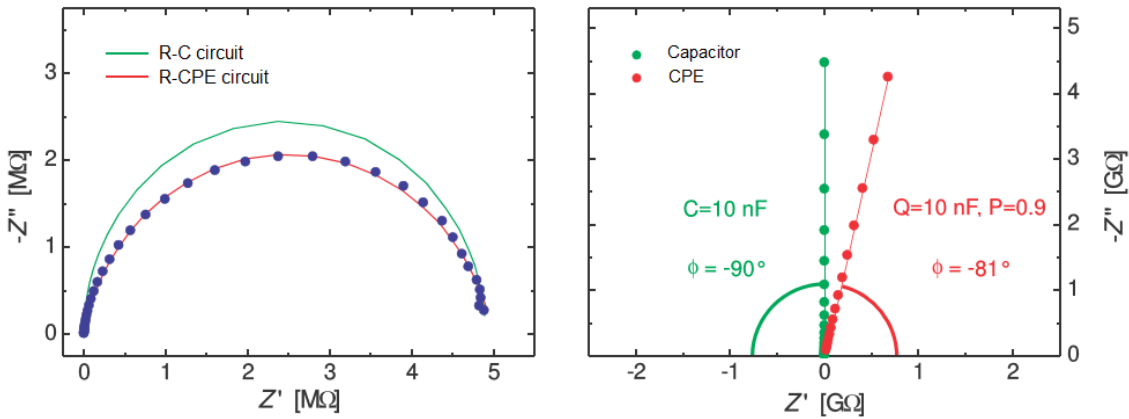


Figure 1-14 : Comparison of the Nyquist-diagram of resistor-capacitor circuit (R-C circuit) and resistor-CPE circuit (R-CPE circuit)<sup>67</sup>.

## 1.6.2 The conductivity spectrum:

The impedance measurement can be also presented in the conductivity spectrum. For a sample with a regular form, the complex conductivity  $\sigma$  can be calculated by:

$$\sigma = \frac{1}{Z} \cdot \frac{d}{A} \quad 1-20$$

with  $Z$ : the complex impedance,  $d$ : the thickness of the sample,  $A$ : the area of the parallel surface contacted with electrode.

The conductivity is a complex value:

$$\sigma = \frac{1}{Z' + iZ''} \cdot \frac{d}{A} = \frac{Z'}{Z'^2 + Z''^2} \cdot \frac{d}{A} + \frac{-iZ''}{Z'^2 + Z''^2} \cdot \frac{d}{A} \quad 1-21$$

The complex conductivity  $\sigma$  can be separated in real and imaginary part:

$$\sigma' = \frac{Z'}{Z'^2 + Z''^2} \cdot \frac{d}{A} \quad 1-22$$

$$\sigma'' = \frac{-iZ''}{Z'^2 + Z''^2} \cdot \frac{d}{A} \quad 1-23$$

The conductivity spectrum is obtained by plotting the values of the real part of the complex conductivity  $\sigma'$  vs the values of the frequency  $\nu$  in double-log-plot. It presents the conductivity of the sample at different frequencies (Figure 1-15). The spectrum can be divided into 3 regions. In the low frequency region, the conductivity increases rapidly with increasing frequency. In the intermediate frequency region, the conductivity shows a plateau, where the conductivity increases slowly with increasing frequency. In the high frequency region, the conductivity increases further with increasing frequency.

The electrical response of the ionic conductor in different frequency ranges can be explained with the Jump Relaxation Model: The ions migrate in the matrix by jumping from site to site. The jumping time is negligible. Consider one mobile ion in the matrix, which stays at first on a site with absolute minimum energy. When this ion jumps to another site with higher energy, there is a probability that this ion jumps back. It is called an unsuccessful jump when this ion jumps back to its original site. On the other hand, the ion can jump further to another site with absolute minimum energy. Alternatively, the neighboring ions at the new site can evade around the mobile ion, making the new site to an energetic absolute minimum. It is called a successful jump in these cases.

In a proper frequency range, the period of the measuring signal matches the interval of the “successful jump”. Only the successful jump is measured in these frequencies. The conductivity changes slowly with the frequency. The conductivity in this frequency range represents the DC ionic conductivity of the sample. The plateau is therefore called DC-plateau.

In lower frequency region, the period of the measuring signal is so large that electric charge has accumulated on the blocking electrodes and formed a polarization layer. The polarization effect reduces

## 1. Introduction

the current and the measured conductivity decreases with decreasing frequency. In higher frequency region, the unsuccessful jump is also counted to the conductivity. The higher the frequency, the more unsuccessful jumps would be counted. The measured conductivity increases with increasing frequency<sup>74</sup>. The conductivity shows dispersion effect.

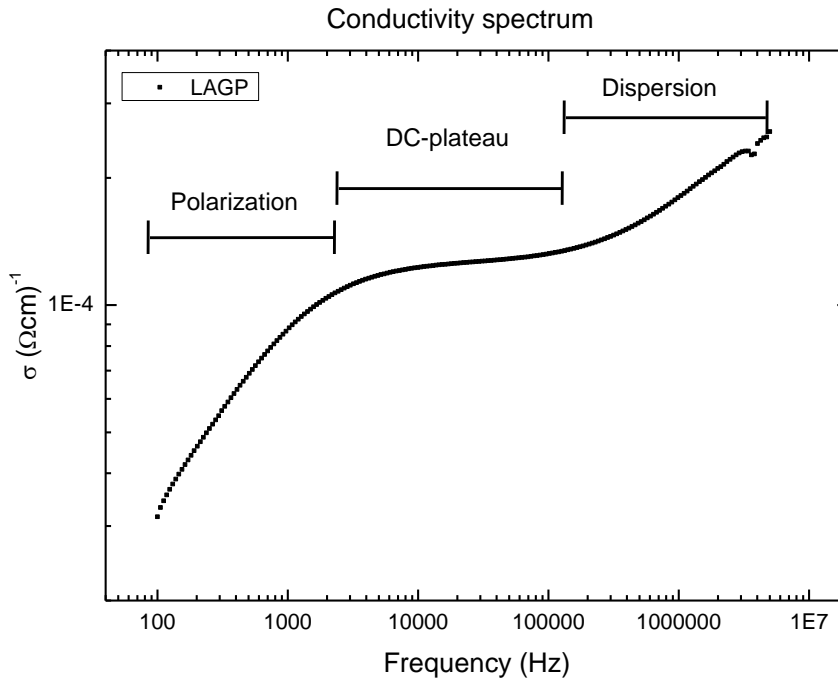


Figure 1-15 : The conductivity spectrum of a LAGP sample. The spectrum can be divided into 3 regions: the polarization effect in low frequency region, the DC-plateau in intermediate frequency region and the dispersion region in high frequency region.

### 1.7 Development of LAGP/LATP solid-state electrolytes

As the demand for lithium ion batteries increases, lithium ion conducting solid-state electrolytes draw more and more attention. Investigations have been carried out in the lithium aluminum titanium phosphate (LATP) and lithium aluminum germanium phosphate (LAGP) system with NaSICON structure.

Aono et. al investigated the lithium titanium phosphate(LTP) system doped with various metal ions in 1980s and 1990s<sup>76-78</sup>. It was reported that  $\text{LiTi}_2(\text{PO}_4)_3$  based materials with NaSICON-type structure had the most suitable tunnel size for Li-ion migration among the series of  $\text{LiM}_2(\text{PO}_4)_3$ , where  $M = \text{Ti, Ge, Hf, Sr, etc.}$  High ionic conductivity was obtained in the systems of  $\text{Li}_{1+x}\text{N}_x\text{Ti}_{2-x}(\text{PO}_4)_3$ , where  $N = \text{Al, Sc, Y, and La.}$  The conductivity and lattice parameters were measured for samples prepared via sintering route with different dopants and different x value. The lithium titanium phosphate doped with Al and Sc with  $x = 0.3$  showed the best conductivity of  $7 \cdot 10^{-4} \text{ S/cm}$  at 298 K.

Fu reported in 1997 the  $14\text{Li}_2\text{O}-9\text{Al}_2\text{O}_3-38\text{TiO}_2-39\text{P}_2\text{O}_5$  (which can be written as  $\text{Li}_{1.07}\text{Al}_{0.69}\text{Ti}_{1.46}(\text{PO}_4)_3$ ) compound with NaSICON structure with enhanced ionic conductivity<sup>79</sup>. The solid-state electrolyte samples were prepared using the heat-treating method. The optimized heat-treating process was found to be “950°C for 12 hours”. A maximum conductivity of  $1.3 \cdot 10^{-3}$  S/cm at room temperature was obtained. The glass transition and crystallization temperature was reported at 650°C and 690°C, respectively.

Beside the heat-treating route, wet chemical methods such as acetate precipitation, spray-dried precipitation and sol-gel synthesis were also reported for the preparation of LATP solid state electrolyte<sup>41, 51</sup>. However, the ionic conductivity achieved was significantly lower (in the order of  $10^{-8}$  S/cm at 293K).

It was reported in multiple studies that the  $\text{AlPO}_4$  minor phase is formed in LATP matrix<sup>43, 51, 61, 80</sup>.

The  $\text{Ti}^{4+}$  ions in LATP can be reduced to  $\text{Ti}^{3+}$ , which causes a stability problem of the LATP solid-state electrolyte. Due to the absence of Ti element, the lithium aluminum germanium phosphate (LAGP) is considered as stable by many authors<sup>62, 81-83</sup>.

LAGP was less investigated in the literature. Fu reported a high ionic conductivity of the LAGP solid-state electrolyte<sup>84</sup>. Samples were prepared by heat-treating of LAGP glasses with the composition of  $\text{Li}_{1+x}\text{Al}_x\text{Ge}_{2-x}(\text{PO}_4)_3$  with  $x = 0 - 0.8$ . The LAGP glass-ceramics exhibit a conductivity over  $10^{-4}$  S/cm<sup>-1</sup> in the composition range  $x = 0.3 - 0.7$ . The ionic conductivity reaches the maximum value of  $4.0 \cdot 10^{-4}$  S/cm<sup>-1</sup> at  $x = 0.5$ . The glass transition and crystallization of the LAGP glass was found at 597°C – 521°C and 651°C – 600°C for different  $x$  values, respectively. Both the glass transition and the crystallization temperature decrease with increasing  $x$  value.

Besides the heat-treating route, LAGP solid-state electrolytes were also prepared via powder sintering<sup>53</sup>, spark plasma sintering (SPS)<sup>82</sup> and sol-gel methods<sup>85, 86</sup>. LAGP synthesized via different routes shows the ionic conductivities values in the range of  $10^{-5} - 10^{-4}$  S/cm at room temperature. Some ionic conductivity values of LAGP solid-state electrolyte prepared via different methods are shown in Table 1-3. Several factors were found to have influence on the overall ionic transport process in LAGP such as chemical composition, secondary phases, microstructure, process route and process parameters<sup>53, 83, 87, 88</sup>.

A number of publications reported much higher ionic conductivity of LAGP ( $4 - 5 \cdot 10^{-3}$  S/cm)<sup>42, 89, 90</sup>. These conductivity values are one order of magnitude higher than the values reported in other sources. However, these high values are attributed to an incorrect interpretation of the impedance spectroscopy diagrams<sup>63</sup>: The grain boundary resistance was interpreted as the total resistance in these works and the grain resistance was interpreted as the “circuit resistance”.

## 1. Introduction

*Table 1-3: Different process routes, compositions and the obtained ionic conductivity values of LAGP solid-state electrolytes.*

Preparation route	Composition	Conductivity
heat-treating <sup>84</sup>	$\text{Li}_{1.5}\text{Al}_{0.5}\text{Ge}_{1.5}(\text{PO}_4)_3$	$4.0 \cdot 10^{-4}$ S/cm at 25°C
heat-treating <sup>62</sup>	$\text{Li}_{1.5}\text{Al}_{0.5}\text{Ge}_3(\text{PO}_4)_3 - 0.05\text{Li}_2\text{O}$	$7.25 \cdot 10^{-4}$ S/cm at room temperature
sol-gel method + sintering <sup>85</sup>	$\text{Li}_{1.5}\text{Al}_{0.5}\text{Ge}_{1.5}(\text{PO}_4)_3$	$1.8 \cdot 10^{-4}$ S/cm at 30°C
spark plasma sintering <sup>82</sup>	$\text{Li}_{1.5}\text{Al}_{0.5}\text{Ge}_{1.5}(\text{PO}_4)_3$	$3.3 \cdot 10^{-5}$ S/cm at 20°C
flame spray + sintering <sup>63</sup>	$\text{Li}_{1.5}\text{Al}_{0.5}\text{Ge}_{1.5}(\text{PO}_4)_3$	$2 \cdot 10^{-4}$ S/cm at room temperature

## 1.8 Objectives and experiments

One main objective of this study is to reveal the correlation between the process parameters, the microstructure and the ionic conductivity of the solid-state electrolyte and to optimize their fabrication process. A further objective is to prove the functionality of the LAGP and LATP solid-state electrolyte in lithium ion batteries.

For that purpose, lithium aluminum germanium phosphate (LAGP) and lithium aluminum titanium phosphate (LATP) solid-state electrolyte should be fabricated using melt quenching technique and characterized with various methods: Dilatometer measurements for the volume change studies during sintering/heat-treatment, impedance spectroscopy for the investigation of ionic conductivity and scanning electron microscope for the microstructure characterization of the samples.

To investigate the composition dependence of the ionic conductivity, multiple batches of LAGP with different compositions ( $\text{Li}_{1+x}\text{Al}_x\text{Ge}_{2-x}(\text{PO}_4)_3$  with  $x = 0.3 - 0.7$ ) are synthesized. LAGP solid-state electrolyte samples are prepared using sintering method and heat-treating method for the comparison of both methods. Different process parameters should be applied for developing the optimized ionic conductivity. The phase transitions during heat-treatment should be investigated using DSC and hot stage XRD.

Since the ionic conductivity of LAGP/LATP solid-state electrolyte increases strongly with increasing temperature, they are also supposed to operate at elevated temperature in high temperature cells. Therefore, thermophysical properties of the glass ceramic at higher temperature are of importance. The thermal conductivity of the LAGP glass ceramic, which was not measured in any other study up to now, should be derived using DSC and laser flash analysis for the first time. The combined determination of the ionic and the thermal conductivity can be used to proof the concept of a so-called "ionic" Wiedemann-Franz-law. I.e. the ionic transport is related to the thermal transport. This relation should be investigated in this study.

The test of the LAGP and LATP solid-state electrolytes in lithium ion battery is another important aspect of this study. For that purpose, lithium ion cells with different structure need to be built and tested with different electrode-electrolyte combinations (cells with hybrid (liquid/solid) electrolyte and cells with all-solid-state arrangement, cells with Li metal anode, with graphite anode and with  $\text{Li}_4\text{Ti}_5\text{O}_{12}$  anode).

## 2 Characterization of ceramic solid-state electrolytes

Multiple batches of lithium aluminum germanium phosphate (LAGP) glass were prepared using the melt-quench process. Samples were processed from LAGP glass using a powder-sintering method and a glass heat-treating method, respectively. The LAGP fabricated via the glass heat-treating route was reported to have a good ionic conductivity (Table 1-3). It requires also less steps to prepare the LAGP glass ceramic samples using heat-treating method. On the other hand, the powder-sintering method allows the fabrication of LAGP solid-state electrolyte with more complicated form and is better suited for production in large scale. Additives can be easily mixed into the powder for improved properties. The powder-sintering route and glass heat-treating route are compared in this study (Figure 2-1).

Lithium aluminum titanium phosphate (LATP) solid-state electrolyte was also prepared and investigated. One batch of LATP was prepared via sintering route. The sintering properties, microstructure and ionic conductivity were investigated.

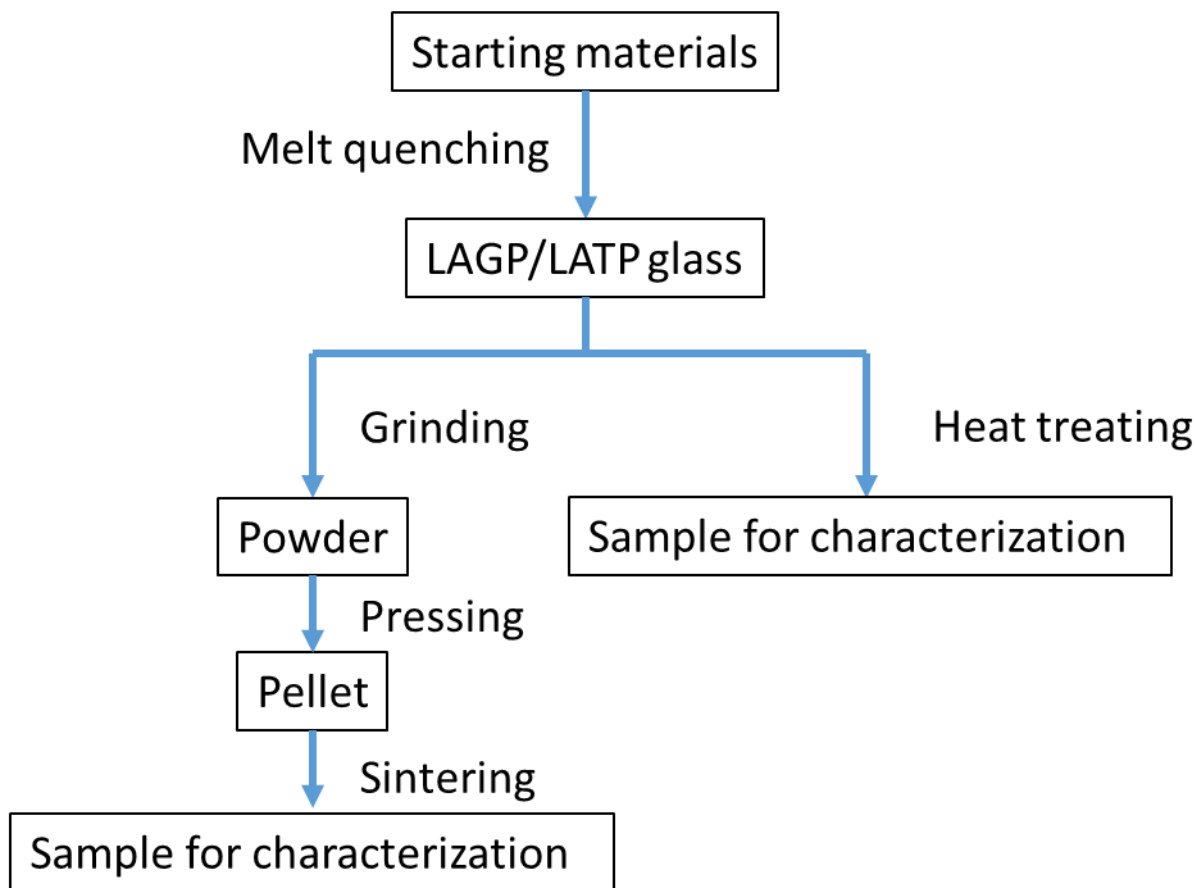


Figure 2-1: Flowchart diagram of the sample preparation via sintering route (left) and heat-treating route (right).

## 2. Characterization of ceramic solid-state electrolytes

### 2.1 Experimental methods

#### 2.1.1 Glass fabrication and sample preparation

The LATP and LAGP glasses were prepared using the melt quenching method. For LAGP glass,  $\text{Li}_2\text{CO}_3$  (Fluka, 99.0%),  $\text{Al}_2\text{O}_3$  (Sigma-Aldrich, 98.5%),  $\text{P}_2\text{O}_5$  (Analar Normapur, 99.1%) and  $\text{GeO}_2$  (Alfa Aesar, 99.98%) were used as starting materials. For LATP glass,  $\text{Li}_2\text{CO}_3$  (Fluka, 99.0%),  $\text{Al}_2\text{O}_3$  (Sigma-Aldrich, 98.5%),  $\text{P}_2\text{O}_5$  (Analar Normapur, 99.1%) and  $\text{TiO}_2$  (Alfa Aesar, 99.5%) were used as starting materials.

The reagents were weighted using an electronic balance and filled in an alumina crucible. The amounts of the starting materials are shown in Table 2-1. The reagents were mixed using a stir rod. The  $\text{P}_2\text{O}_5$  is highly hygroscopic and to minimize the moisture absorption, the mixed starting material was directly transferred into a chamber furnace where the mixture was melted.

*Table 2-1: The mass of starting materials used for each batch of LAGP and LATP glass.*

	$\text{Li}_2\text{CO}_3$ /g	$\text{Al}_2\text{O}_3$ /g	$\text{GeO}_2$ /g	$\text{P}_2\text{O}_5$ /g	Sum /g	Aimed composition
LAGP batch 1	2.16	0.84	5.20	7.60	14.51	$\text{Li}_{1.7}\text{Al}_{0.7}\text{Ge}_{1.3}\text{P}_3\text{O}_{12}$
LAGP batch 2	3.73	1.02	13.35	17.42	33.30	$\text{Li}_{1.3}\text{Al}_{0.3}\text{Ge}_{1.7}\text{P}_3\text{O}_{12}$
LAGP batch 3	4.82	2.00	12.54	18.14	34.63	$\text{Li}_{1.5}\text{Al}_{0.5}\text{Ge}_{1.5}\text{P}_3\text{O}_{12}$
LAGP batch 4	6.35	2.40	15.00	21.87	41.83	$\text{Li}_{1.7}\text{Al}_{0.6}\text{Ge}_{1.38}\text{P}_3\text{O}_{12}$
	$\text{Li}_2\text{CO}_3$ /g	$\text{Al}_2\text{O}_3$ /g	$\text{TiO}_2$ /g	$\text{P}_2\text{O}_5$ /g	Sum /g	
LATP batch 1	2.16	0.84	5.20	7.60	14.51	$\text{Li}_{1.1}\text{Al}_{0.7}\text{Ti}_{1.45}(\text{PO}_4)_3$

The temperature program of the furnace is shown in Figure 2-2. The material was heated up to 900°C with 10K/min and the  $\text{Li}_2\text{CO}_3$  decomposed. The material was further heated up to 1450°C with 15K/min and held at that temperature for 0.2 h. A viscous melt was formed. The melt was transferred out of the furnace and casted on a steel plate. Another steel plate was pressed on the melt immediately to shape the melt into a thin disk. The melt solidified after a few seconds and formed a glass disk with a thickness of 1 - 2 mm. The glass disk broke into pieces due to the thermal stress after the rapid cooling process. The glass pieces were transparent and did not show porosity.

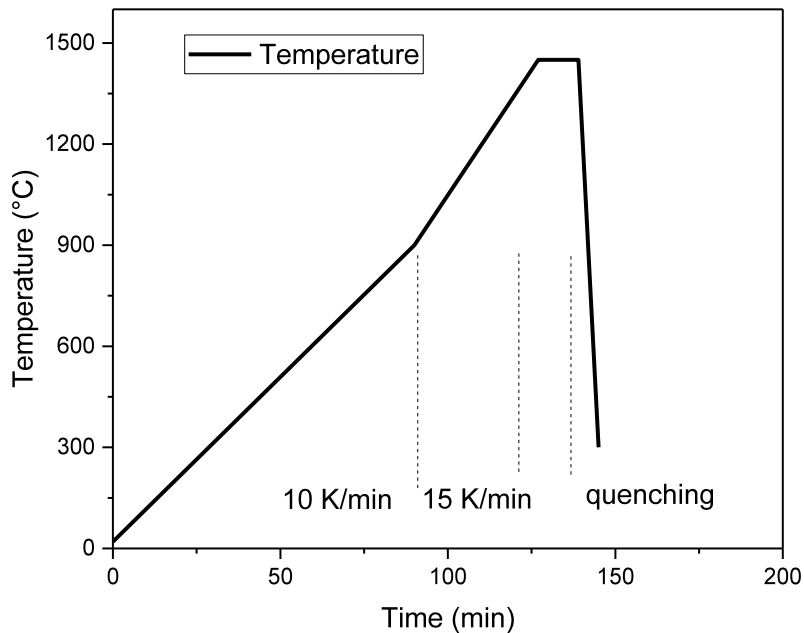


*Figure 2-2: Temperature program of the melt quenching method.*

Samples were prepared via heat-treating route and powder-sintering route.

Heat-treating route:

For the heat-treating route, the glass pieces obtained by casting were heated up in a furnace up to the preset heat-treatment temperature. The heating rate was 5K/min (300 K/hour) and the heat-treatment temperature varied from 600°C to 1100°C. The temperature was held for the preset length of time. The samples were then cooled down to room temperature with the cooling rate of 5K/min (300 K/hour) for further characterization.

Powder-sintering route:

For the powder-sintering route, the glass pieces obtained by melt quenching were first milled into a powder. The glass pieces were filled into a grinding crucible made of alumina together with seven alumina mill balls and isopropanol and were ground in a planetary mill for 2.5 hours. The obtained powder was transferred into a glass cup and dried in a temperature chamber at 100°C for 10 hours.

Cylindrical samples were pressed using uniaxial pressing. The press matrices have cylindrical inner volume with a diameter of 5 mm, 10 mm and 14 mm, respectively. The matrix filled with powder was placed in a uniaxial press machine and pressed for 5 min with a pressure of 130 MPa.

The pellet was further densified using cold isostatic pressing. The cold isostatic pressing applies hydraulic pressure from all directions onto the pellet to achieve a better uniformity of the compaction. The pellet was sealed in a plastic bag and placed in the oil vessel of the cold isostatic press. The press generated a

## 2. Characterization of ceramic solid-state electrolytes

pressure of 398 MPa in the vessel. After 3 min press time, the sample was taken out from the oil vessel and unsealed from the plastic bag.

The pressed pellets were then sintered in a chamber furnace or in a sinter dilatometer. The samples were heated up to the sintering temperature, held at that temperature for a preset time and cooled down to room temperature with a heating/cooling rate of 5K/min (300 K/hour).

### 2.1.2 Thermal analysis

#### 2.1.2.1 Dilatometry

In order to investigate the dimension change of the LAGP and LATP samples during heat-treatment and sintering, dilatometer (DIL) measurements were carried out on a Netzsch DIL 402E dilatometer.

The sample is fixed in a ceramic carrier with one face attached to a pushrod. The pushrod transmits the length change of the sample mechanically to the linear variable differential transformer (LVDT). The LVDT transforms the length change into an electrical signal, which is recorded by the controller, which is connected with a computer. The resolution of this sensor is 0.01  $\mu\text{m}$ , which is around 0.001% of the samples length.

The starting length of the sample was measured with a micrometer screw before each DIL measurement. The sample was mounted on the sample carrier and heated according to a preset temperature program. The length change of the sample and the temperature was recorded vs time.

#### 2.1.2.2 Differential scanning calorimetry (DSC)

Differential scanning calorimetry (DSC) was carried out to analyze possible phase changes during the heating process and to measure the heat capacity of the samples. For the measurements from room temperature up to 1100°C, a Netzsch DSC 404C device was applied. A Netzsch DSC 204 device was used as complement for the measurements between -25°C and 150°C. The uncertainties of the temperature values measured in these devices are  $\pm 1$  K. The temperature measurement was calibrated using a series of standard materials with defined melting points.

Before each measurement, the sample and the crucibles were weighted using an electronic balance. The DSC was operated at a heating rate of 15K/min with a constant Ar-gas flow of 100 ml/min.

For the heat capacity measurements, a base line measurement, a reference measurement and a sample measurement were carried out. The base line measurement was made without sample. The reference measurement was made with a sapphire standard reference material with known heat capacity. The base line was subtracted from the sample measurement and the reference measurement. The analyzing software "Netzsch Proteus" calculated the heat capacity by comparing the base line subtracted reference measurement and sample measurement. The uncertainties of the heat capacity were estimated by measuring the standard materials and comparing them with the literature values. The uncertainties of the results are estimated to be less than 1%.

### *2.1.2.3 Thermal gravimetric Analysis*

With the thermal gravimetric Analysis (TGA), the mass change of sample during the heating process can be analyzed. The TGA measurements were carried out using a “SETSYS Evolution” simultaneous thermal analysis system (SETARAM), which is a combination of differential thermal analysis (DTA) and thermal gravimetric analysis (TGA).

In this device, a sample carrier is configured hanging at the balance beam. The thermocouples on the sample carrier measure the temperature difference between the sample and the reference and deliver the differential thermal analysis results. The balance measures the mass change of the sample simultaneously and provides thermal gravimetric analysis results.

The furnace runs using a preset temperature program. The TGA and DTA data are recorded vs temperature. The measurements were carried out by Alexandra Reif and Dr. Damian Cupid at the IAM-AWP.

### *2.1.2.4 Laser flash analysis*

Laser flash analysis (LFA) was carried out to investigate the thermal diffusivity and thermal conductivity of the LAGP samples. A Netzsch LFA 427 device was used in this work. The device has a sample holder in a furnace, where a cylindrical sample is placed. A Nd:YAG (neodymium-doped yttrium aluminum garnet) laser generates a single laser pulse, which is absorbed by the sample. The lower surface of the sample is heated by the laser pulse. The resulting temperature change on the upper surface of the sample is measured with an infrared detector. Figure 2-3 shows the temperature change of the upper surface of a sample vs time. A steeper temperature curve represents a higher thermal diffusivity. The thermal diffusivity can be calculated using the half time (time value at half signal height) and sample thickness. The thermal conductivity can be calculated from the product of the thermal diffusivity, the heat capacity and the density<sup>91</sup>.

The thickness of the sample was measured before the measurement. The sample was coated with graphite in order to absorb laser energy. The sample was placed on the sample holder in the furnace, which was sealed and evacuated, and measured at different temperatures.

## 2. Characterization of ceramic solid-state electrolytes

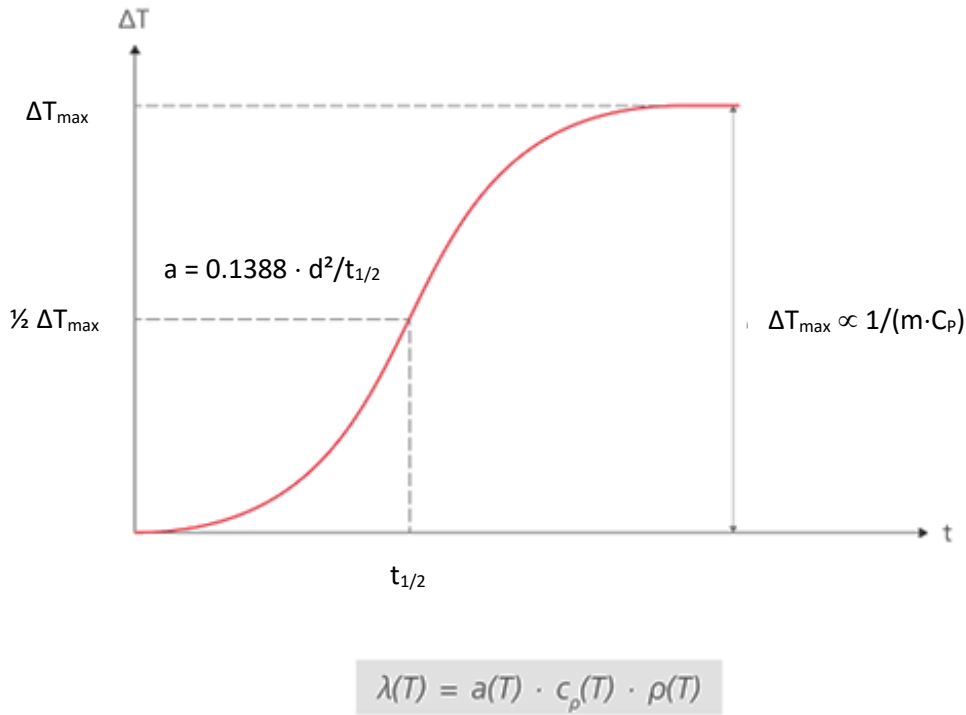


Figure 2-3 : Signal and calculation formula of the Laser flash measurement<sup>92</sup>.  $\lambda(T)$ : thermal conductivity at temperature  $T$ ,  $a(T)$ : thermal diffusivity at  $T$ ,  $C_p(T)$ : heat capacity at  $T$ ,  $\rho(T)$ : density at  $T$ ,  $m$ : mass of the sample.

### 2.1.3 Ionic conductivity measurement using electrical impedance spectroscopy

A Sourcetric 2826 LCR meter was used to measure the impedance spectrum of the solid-state electrolytes in this work. Samples were polished on both sides and gold electrodes were sputtered on the parallel surfaces. The electrodes are opposite to each other and have the same area. Conductive silver paint was dripped on each electrode to protect the thin gold layer and form a connecting point with wires of the measuring circuit.

The setup for the impedance measurement is shown in Figure 2-4. The sample is placed on a heating plate. A thermocouple is mounted in the heating plate for the temperature measurement. The heating plate serves also as current conductor for the measuring signal. The two electrodes on the sample are connected to the measuring circuit via the heating plate on the bottom and the point contact at the top, respectively. The setup is enclosed in a steel case with heat insulating material to hold the temperature stable. The heating plate can heat the sample up to 300°C.

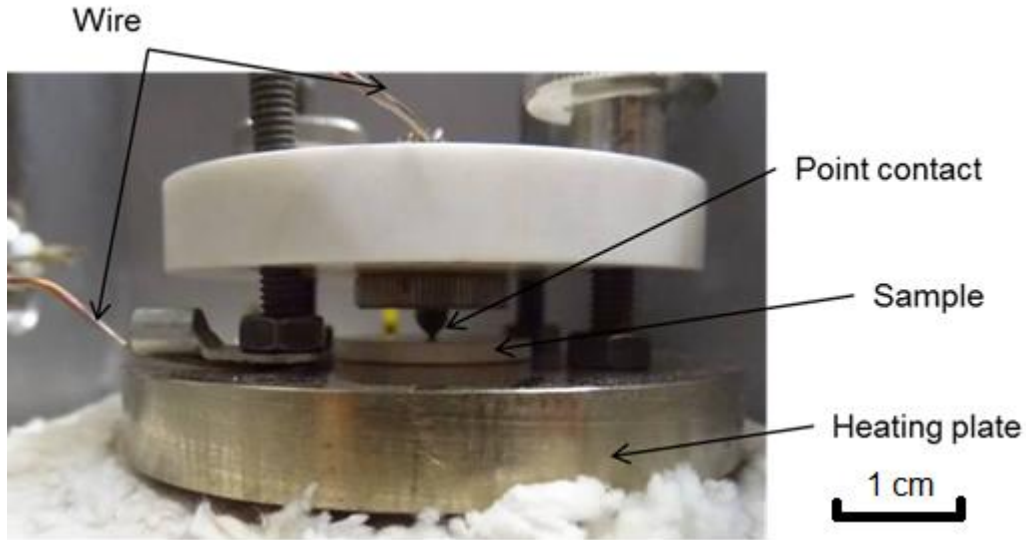


Figure 2-4: Setup for the complex impedance measurement.

The LCR meter presents the result in the absolute value of the impedance  $Z_0$ , the phase shift  $\phi$  and the corresponding frequency  $\nu$ . The complex impedance can be expressed as:

$$\begin{aligned} Z(\nu) &= Z' + iZ'' & 2-1 \\ &= Z_0(\nu) \cdot \cos(\phi(\nu)) + iZ_0(\nu) \cdot \sin(\phi(\nu)) \end{aligned}$$

with  $Z$ : complex impedance,  $Z'$ : real part of the complex impedance,  $Z''$ : imaginary part of the complex impedance.  $Z_0(\nu)$ : the absolute value of the impedance at the frequency  $\nu$  and  $\phi(\nu)$ : the phase shift at the frequency  $\nu$ .

The obtained data set can be plotted in Nyquist-diagram (see 1.6). A software "EIS Spectrum Analyzer EISSA" was used to fit the equivalent circuit model to the measured data. The equivalent circuit model for the fitting is shown on the inset of Figure 1-12. The software fits the parameter of the electrical elements of the equivalent circuit model so that the electrical response of the equivalent circuit matches with the real sample.

The ionic conductivity can be also evaluated via the conductivity spectrum (see 1.6). The conductivity on the DC plateau with the smallest slope was taken as the ionic conductivity of the sample. The uncertainty (error bar) of the ionic conductivity was taken from the maximum and minimum of the DC-plateau.

#### 2.1.4 Scanning electron microscopy and energy-dispersive X-ray spectroscopy

Scanning electron microscopes (SEM) were applied for the microstructure observation. A JEOL JSM-840 scanning electron microscope and a Philips XL30S FEG scanning electron microscope were used.

The JEOL JSM-840 scanning electron microscope has a tungsten cathode, which emits electrons. The electron beam scans the surface of the sample. The microscope has detectors for secondary electrons and back scattered electrons. Additionally, an energy-dispersive X-ray (EDX) detector is built in the microscope, which analyzes the elemental composition of a scanned area.

## 2. Characterization of ceramic solid-state electrolytes

The Philips XL30S FEG scanning electron microscope is a modern model with computer control. The device has a field emission cathode, secondary electron detector, back scattered electron detector and EDX detector.

For the surface observation, the samples were ground with sand paper (mesh 4000), polished with 3- $\mu$ m diamond particle suspension, cleaned with isopropanol in ultrasound bath and dried in warm air. The sample surface was sputtered with gold in order to avoid the electron accumulation on the sample. For the cross sectional observation, the sample was broken apart and the cross section was sputtered with a gold layer. After the preparation, the sample was carefully transferred into the vacuum chamber of the microscope for the SEM observation and EDX analysis.

### 2.1.5 Density measurement

The density of the samples was measured using the Archimedes method:

The sample is weighted in air and immersed in liquid. The density of the sample can be calculated with the known density of the liquid:

$$\rho_{sample} = \rho_{liquid} \cdot \frac{m_a}{m_a - m_l} \quad 2-2$$

with  $\rho_{sample}$ : density of the sample,  $\rho_{liquid}$ : density of the liquid,  $m_a$ : weight of the sample in air,  $m_l$ : weight of the sample in the liquid.

The density of the liquid can be measured with a calibration body with known volume. The calibration body is weighted in air and in the liquid. The density of the liquid  $\rho_{liquid}$ :

$$\rho_{liquid} = \frac{m_a - m_l}{V_a} \quad 2-3$$

with  $m_a$ : weight of the calibration body in air,  $m_l$ : weight of the calibration body in liquid,  $V_a$ : the volume of the calibration body.

The electronic balance used for the density measurement has the accuracy of 0.01 mg. The samples measured in this work have usually the weight of around 200 mg. However, the ceramic samples have always porosity. The pores on the sample surface can be filled with the liquid when the sample is weighted in liquid, which leads to an underestimation of the sample volume and hence an overestimation of the density. The uncertainty of the sample weight in liquid was estimated to be 0.2 mg, which leads to an uncertainty of around 0.4% of the sample density.

For samples with larger open porosity however, the above-mentioned error becomes too large. Therefore, the sample is coated with a lacquer layer. The sample is weighted first and then coated with a layer of Zapon lacquer. The coated sample is weighted again in air and in the liquid. The density of the porous sample can be calculated:

$$\rho_{sample} = \frac{m_1}{\frac{m_2 - m_3}{\rho_{liquid}} - \frac{m_2 - m_1}{\rho_{Zapon}}} \quad 2-4$$

with  $m_1$ : the mass of the sample in air,  $m_2$ : the mass of coated sample in air,  $m_3$ : the mass of coated sample in liquid,  $\rho_{Zapon}$ : the density of the Zapon lacquer and  $\rho_{liquid}$ : the density of the liquid.

The density of the Zapon lacquer ( $\rho_{Zapon}$ ) was measured also using the Archimedes method. Several droplets of the Zapon lacquer was dropped on a watch glass. The dried lacquer layer was separated from the watch glass and its density could be measured. However, the measured  $\rho_{Zapon}$  showed deviation from the value from literature. The uncertainty of the sample density measured using this method was estimated to be 1%.

### 2.1.6 X-ray diffraction (XRD)

X-ray diffraction (XRD) was applied for phase analysis. XRD uses an X-ray source, which radiates with an incident angle  $\theta$  onto the sample and a detector, which measures the diffracted X-ray at the angle  $180 - \theta$ . It undergoes constructive interference when conditions satisfy the Bragg's Law:

$$n\lambda = 2d \sin \theta \quad 2-5$$

with  $\lambda$ : the wave length of incident X-ray,  $d$ : the interplanar distance and  $\theta$ : the incident angle.

A Seifert XRD system was used in this study. The device has an X-ray tube of copper  $K_\alpha$  radiation. A nickel filter was used to filter the  $K_\beta$  radiation. The wavelength of the X-ray is 1.54056 Å. A Meteor 1D X-ray linear detector is integrated in this system, which has a capture angle of up to 20° in one sight. The detector can measure the X-ray intensity with different angle in the range of 20° simultaneously, which enhances the measuring speed.

The X-ray diffractogram presents the measured intensity vs the incident angle times 2 ( $2\theta$ ). The diffraction peaks can be converted to lattice plane spacing. By comparing the measured diffractogram with the database (Powder Diffraction Files (PDF) provided by Joint Committee on Powder Diffraction Standards (JCPDS), ICSD – the Inorganic Crystal Structure Database provided by FIZ Karlsruhe), the different phases in the specimen can be identified and the lattice parameters can be calculated.

A hot stage XRD measurement was also carried out to follow the phase transition in-situ at elevated temperatures. The measurement system consists of a Bruker D8 Diffractometer with Copper  $K_\alpha$  radiation, a Bruker Lynxeye Detector and an Anton Paar heating chamber. The measurement was carried out by Dr. Morsi Mahmoud and Dr. Holger Gesswein at the Institut für Angewandte Materialien, Keramische Werkstoffe und Technologien (IAM-KWT) of KIT.

## 2. Characterization of ceramic solid-state electrolytes

### 2.1.7 Spectroscopic analysis

#### 2.1.7.1 *Laser-induced breakdown spectroscopy (LIBS)*

Laser-Induced Breakdown Spectroscopy (LIBS) is a type of atomic emission spectroscopy for the qualitative and quantitative chemical analysis of elements. The measuring principle of LIBS is based on the spectral analysis of characteristic emission lines of atoms and ions. A short pulse laser beam is focused onto the sample surface and induces a local heating of more than 10000 °C. A light emitting plasma is generated (ignition), which consists of ablated atoms and ions of the sample material. Shortly after the ignition, the expanding plasma emits unspecific “Bremsstrahlung” and recombination radiation (continuous spectrum). After several 100 ns, the atoms and ions recombine and emit a characteristic emission spectrum for the elements in the plasma. A spectral analysis by means of a high-resolution spectrometer allows the determination of the atomic composition of the sample.

By continuous ablation at one point of the sample, the surface can be etched layer by layer. The material under the surface is exposed and further analyzed. A composition-depth profile can be measured in that way.

A SECOPTA fiber LIBS device was employed for the measurements in this work. The measurements were carried out by Dr. Wilhelm Pflöging from the Laser group of IAM-AWP.

#### 2.1.7.2 *ICP-OES*

The inductively coupled plasma optical emission spectrometry (ICP-OES) was applied for quantitative analysis of the chemical composition. The principle of this measurement is based on the characteristic optical emission of atoms of a specific element. The atoms of the specimen are excited and ionized in the inductively coupled plasma. The ions emit electromagnetic radiation at wavelengths characteristic of the particular element.

The solid specimen is dissolved in 6 ml hydrochloric acid, 2 ml nitric acid and 1 ml hydrofluoric acid in order to be fed into the ICP-OES device for the chemical analysis. The solution is nebulized and introduced to the plasma. The molecules and ions in the solution dissociate and recombine in the plasma, emitting characteristic radiation. The elements in the solution are identified by their characteristic spectrum and their fraction is determined through the intensity of their characteristic spectral lines.

The measurements were carried out by the group of Chemical Analytics of IAM-AWP. A PerkinElmer Optima 4300 DV ICP-OES device was used for the measurements. The content of the elements lithium, aluminum, germanium, titanium and phosphorus in LAGP and LATP was measured using ICP-OES.

#### 2.1.7.3 *Carrier Gas Hot Extraction*

Carrier Gas Hot Extraction (CGHE) method was used for quantitative analysis of the oxygen and nitrogen content. A TC 600 device (Leco Co.) was employed for the measurement. The weighted specimen is placed in a high-purity graphite crucible and fused under a flowing helium gas stream at temperatures (~2500K) sufficient to release oxygen, nitrogen and hydrogen. The oxygen in the sample combines with the carbon from the crucible forming primarily carbon monoxide (CO). In some instances, depending upon sample

type and furnace temperature, some oxygen can be released directly as carbon dioxide (CO<sub>2</sub>). The nitrogen present in the sample releases as molecular nitrogen. The hydrogen is released as hydrogen gas. The oxygen content is measured quantitatively by infrared absorption. The nitrogen content is determined quantitatively by a thermal conductivity detector.

The carbon content is analyzed with the CS600 (LECO) device. The sample with the mass of 100 – 200 mg (weighting accuracy  $\pm 0.1$  mg) is weighted in a ceramic crucible. About 1 g of accelerator material (W with Sn) is added. The sample is purged with oxygen to drive off residual atmosphere gas after loading into the furnace. The materials combust in oxygen at about 2200 K and are completely oxidized. The carbon is converted with the oxygen into CO or CO<sub>2</sub> and finally converted to CO<sub>2</sub>. The CO<sub>2</sub> gas is measured quantitatively with infrared absorption same as in the TC 600 device.

## 2. Characterization of ceramic solid-state electrolytes

### 2.2 LAGP solid-state electrolyte via sintering route

LAGP solid-state electrolyte was first prepared via sintering route. Since the LAGP with excess  $\text{Li}_2\text{O}$  showed high ionic conductivity<sup>62</sup>, the LAGP batch 1 was prepared with a higher lithium content. The obtained LAGP glass has an overall chemical formula of  $\text{Li}_{1.68}\text{Al}_{0.61}\text{Ge}_{1.32}\text{P}_3\text{O}_{11.90}$ , which corresponds approximately to  $x = 0.7$  in the general formula of  $\text{Li}_{1+x}\text{Al}_x\text{Ge}_{2-x}\text{P}_3\text{O}_{12}$ .

The starting material used for each batch is shown in Table 2-1. The chemical compositions of the fabricated glasses powder were analyzed (CGHE for oxygen and ICP-OES for other elements) and shown in Table 2-2. The uncertainties shown in this table were evaluated from the deviation of three measurements. The atom percent of each element was calculated from the weight percent. The overall chemical formula was calculated from the atom percent and fitted to the general formula of  $\text{Li}_{1+x}\text{Al}_x\text{Ge}_{2-x}\text{P}_3\text{O}_{12}$ <sup>84, 2</sup>. The number of phosphorous element in the chemical formula was set to 3. The numbers of other elements are calculated via the element ratios between phosphorous and the specific element. This LAGP batch has a higher Li and Al content and is designated as high lithium LAGP.

*Table 2-2: Composition of the LAGP powder batch 1 in weight percent, atom percent and the overall chemical formula.*

		Li	Al	P	Ge	O
High Li LAGP- batch-1	wt. %	2.82±0.02	3.98±0.03	22.5±0.25	23.3±0.1	46.3±0.46
	at. %	9.04±0.06	3.28±0.03	16.2±0.18	7.13±0.03	64.4±0.64
	overall chemical formula	$\text{Li}_{1.68}\text{Al}_{0.61}\text{Ge}_{1.32}\text{P}_3\text{O}_{11.90}$				

Since the Carrier Gas Hot Extraction (CGHE) method is less accurate, the oxygen content of the sample has a higher uncertainty. The sum of the weight percent of all the elements has therefore deviation from one. The overall chemical formula, which corresponds to the composition of the starting material, is  $\text{Li}_{1.64}\text{Al}_{0.46}\text{Ge}_{1.39}\text{P}_3\text{O}_{11.79}$  (calculated from data of Table 2-1). The composition of the LAGP glass ( $\text{Li}_{1.68}\text{Al}_{0.61}\text{Ge}_{1.32}\text{P}_3\text{O}_{11.90}$ ) shows higher Al content as the composition of the starting material. That can be attributed to the  $\text{Al}_2\text{O}_3$ , which diffused from the alumina crucible into the LAGP melt during the melting-process and which was rubbed off from the alumina grinding crucible and grinding balls during the powder preparation.

## 2.2.1 Sample characterization

Samples of high Li LAGP batch 1 prepared with different process parameters are listed in Table 2-3 along with the characterization methods.

*Table 2-3: List of the samples of high Li LAGP batch fabricated with different process parameters and characterized with DSC, Dilatometry (DIL), Thermal gravimetric analysis (TGA), XRD, scanning electron microscopy (SEM) and impedance spectroscopy (IS).*

Sample No.	Fabrication process parameters	Characterization methods
#1	Pellet pressed from glass powder	DSC
#2	Sintered at 900°C for 6h using not calcined powder	DIL, XRD, SEM, IS
#3	Sintered at 700°C for 6h using calcined powder*	DIL, SEM
#4	Sintered at 750°C for 6h using calcined powder*	DIL, IS
#5	Sintered at 800°C for 6h using calcined powder*	DIL, IS, SEM, XRD
#6	Sintered at 900°C for 6h using calcined powder*	DIL, IS, SEM
#7	Sintered at 850°C for 6h using calcined powder*	IS
#8	Sintered at 800°C for 3h using calcined powder*	IS
#9	Sintered at 800°C for 9h using calcined powder*	IS
#10	Pellet pressed from glass powder	TGA

\*700°C 3h calcined

### 2.2.1.1 DSC measurement

The heating and cooling curves of the first DSC measurement of the pellet sample #1 pressed from the high Li LAGP ( $\text{Li}_{1.68}\text{Al}_{0.61}\text{Ge}_{1.32}\text{P}_3\text{O}_{11.90}$ ) glass powder are shown Figure 2-5. The glass sample was heated up with a heating rate of 15K/min. The glass transition took place at 504°C – 532°C. The crystallization onset temperature lies at 596°C. No other peak was observed while the sample was further heated up to 900°C. On the cooling curve, two exothermal peaks are observed at 703°C and 632°C, which are significantly smaller than the crystallization peak.

The crystallized sample was measurement again in the DSC to determine the heat capacity (Figure 2-6). The uncertainty of the heat capacity was estimated to be 1%. An endothermal peak is shown at 647°C on the heating curve. Two much smaller peaks are shown at 622°C and 592°C. These peaks appeared repetitively in the repeated measurements, showing that they represent reversible phase transitions.

## 2. Characterization of ceramic solid-state electrolytes

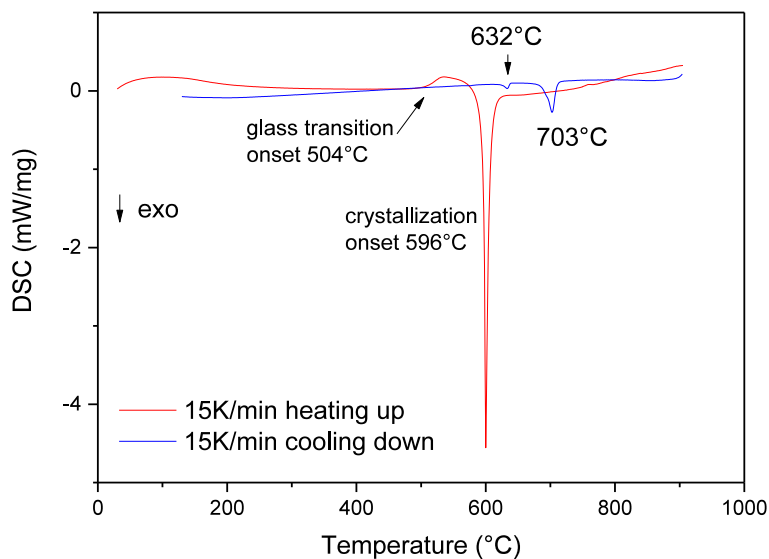


Figure 2-5: DSC curve of the sample #1 of high Li LAGP with  $x = 0.7$  in  $\text{Li}_{1+x}\text{Al}_x\text{Ge}_{2-x}\text{P}_3\text{O}_{12}$ . The sample was heated up to 900 °C and cooled down with the rate of 15 K/min.

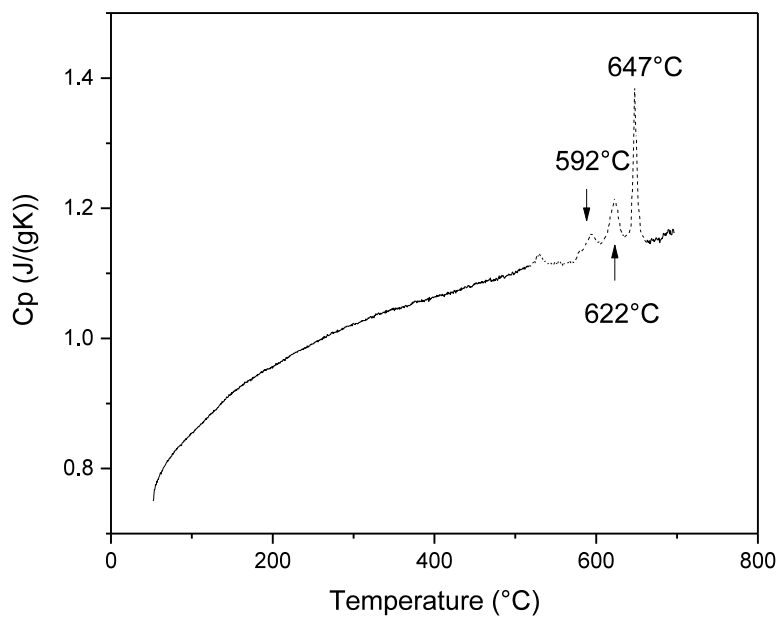


Figure 2-6: Heat capacity curve of the high Li LAGP #1 with  $x = 0.7$ . The peaks represent the heat of reversible phase transitions.

### 2.2.1.2 Dilatometry

The dilatometer curves of the sample #2 pressed from the as prepared glass powder (not calcined) of high Li LAGP with  $x = 0.7$  are shown in Figure 2-7. The sample showed an expansion during the sintering process. The samples began to shrink rapidly at 500°C. The sample showed a shrinkage of about 20% up to 590°C. The length of the sample stayed unchanged between 590°C and 670°C. However, the sample showed an expansions starting at 670°C. At 750°C – 770°C, the sample showed a drastic expansion of more than 10%. The expansion of the sample continued until the temperature stopped to increase at 900°C. The sample shrank gradually at 900°C and achieved a net expansion of 15% at the end of the sintering process.

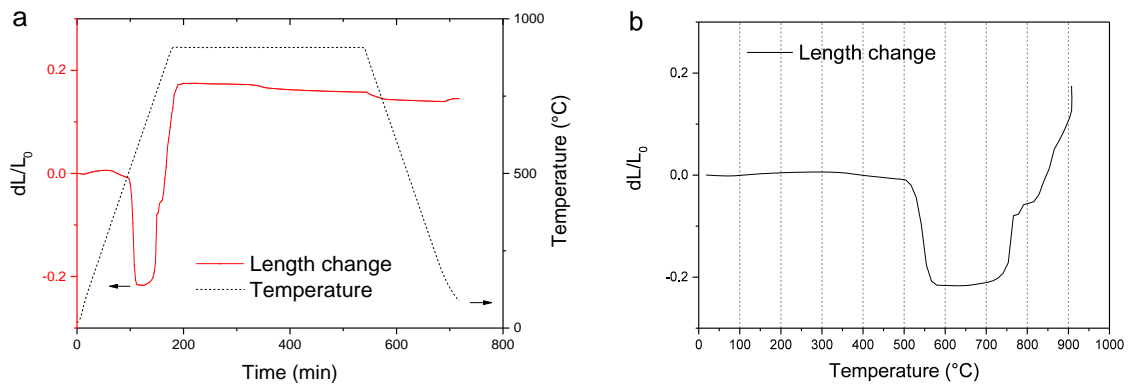


Figure 2-7: Dilatometer measurements of sample #2 from not calcined powder of the high Li LAGP. a: The solid line shows the length changes vs. time. The axis on the left presents the relative length changes of the sample. The dashed line shows the temperature vs. time. The right axis presents the temperature in the dilatometer. b: Relative length changes of the same sample vs. temperature.

In order to avoid the unwanted expansion, samples were prepared using calcined powder. The glass powder of high Li LAGP batch was heated up to 700°C with a heating rate of 5K/min in a furnace, held for 3 hours and cooled down with the same rate. The calcined powder was ground again and pressed into pellets.

Figure 2-8 shows the length change of the samples #3 – #6 vs. sintering time, which were pressed from calcined powder and sintered at different temperatures. Since the powder was already calcined and crystallized, the samples did not show the shrinkage at 500°C. The samples #3 and #4 sintered for 6 hours at 700°C and 750°C showed only limited densification (2.5% and 6.8% length shrinkage, respectively). The sample #5 sintered at 800°C for 6 hours showed the highest shrinkage (18.1% length shrinkage at the end of the sintering). The fastest shrinkage took place when the temperature reached 800°C.

However, as shown in Figure 2-8, the sample #6 showed expansion again at 900°C. The expansion lasted more than 5 hours before the sample began to shrink slowly. The sample showed a net expansion of 1.4% of its original length at the end of the sintering.

## 2. Characterization of ceramic solid-state electrolytes

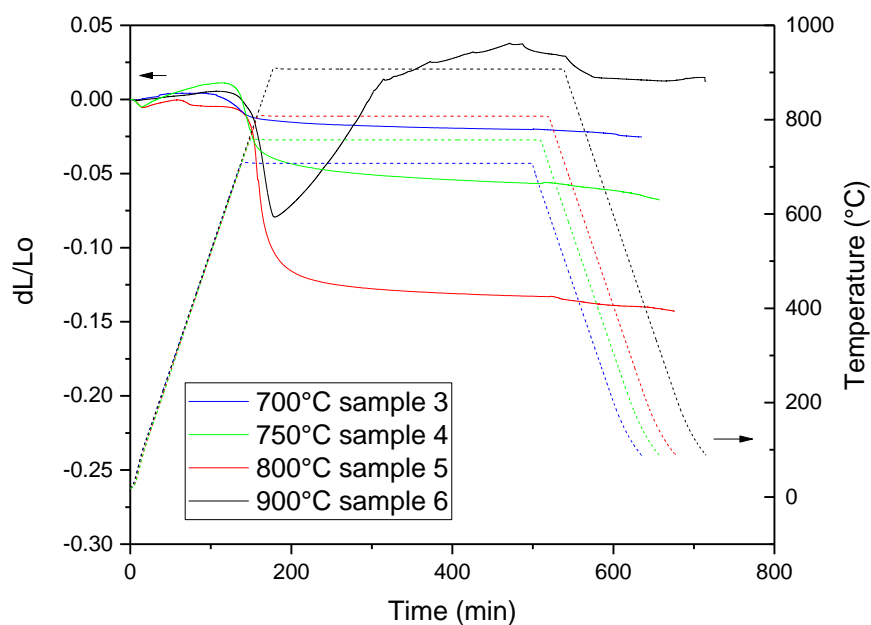


Figure 2-8: Dilatometer measurements of samples made of calcined powders of the high Li LAGP with  $x = 0.7$  in  $\text{Li}_{1+x}\text{Al}_x\text{Ge}_{2-x}\text{P}_3\text{O}_{12}$ . The axis on the left presents the relative length changes of the sample. The solid lines show the length changes vs. time. The right axis presents the temperature in the dilatometer. The dashed lines show the temperature vs. time.

### 2.2.1.3 Thermal gravimetric analysis (TGA)

Thermal gravimetric analysis (TGA) was carried out on the sample #10 pressed from the not calcined powder of high Li LAGP batch ( $x = 0.7$ ) to follow the mass change during the sintering process. The sample had an initial mass of 12.92 mg. The sample was heated up to 900°C with a rate of 5K/min, held at the temperature for 1 hour, cooled down to 200°C, heated up to 900°C again, held at the temperature for 1 hour and cooled down to room temperature.

The TGA result of the first heating and isotherm segment is shown in Figure 2-9-a. There was a relatively fast mass loss at about 100°C, which can be attributed to the elimination of moisture in the LAGP powder. The mass loss became slower at 150°C and stopped at 500°C. The sample exhibited another mass loss at temperatures higher than 670°C. The sample mass had some fluctuation between 740°C and 840°C and decreased continually at over 860°C and during the isotherm segment at 900°C. The sample had a total mass loss of 0.293 mg/2.27% in the first heating and isotherm segment. The mass loss at the temperature higher than 860°C was 0.066 mg/0.51%. The sample did not show mass loss under 800°C in the second heating segment (Figure 2-9-b). Above 800°C however, there was again a gradually mass loss of 0.043 mg/0.33%.

The mass loss of the sample at the temperature higher than 700°C indicates that a reaction took place in the LAGP, which reduced the weight of the solid sample. This will be discussed in section 2.2.2.

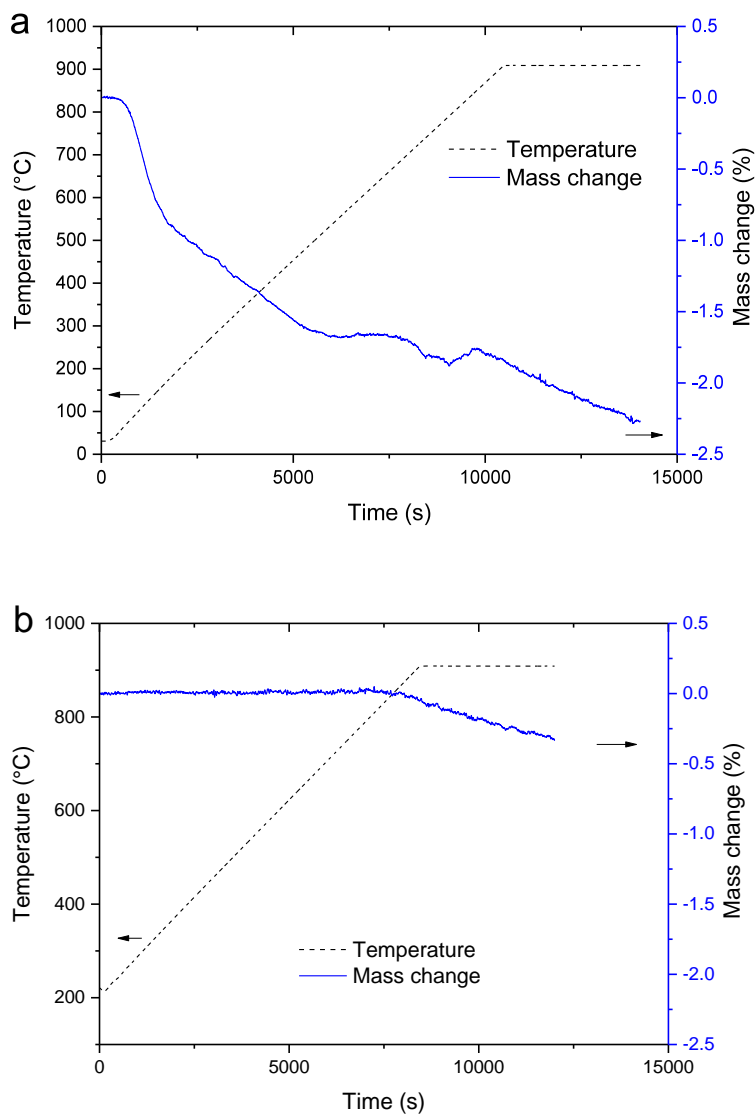


Figure 2-9: TGA result of the sample #10 pressed from the not calcined powder of high Li LAGP. a: first heating and isotherm segment: mass change vs. time and temperature vs. time. The sample has a mass loss of 2.27%; b: second heating and isotherm segment: mass change vs. time and temperature vs. time. The sample has a mass loss of 0.33%.

## 2. Characterization of ceramic solid-state electrolytes

### 2.2.1.4 XRD

The X-ray diffractograms of the sample #2 sintered at 900°C and #5 sintered at 800°C of high Li LAGP ( $x=0.7$ ) are shown in Figure 2-10. Most of the diffraction peaks can be attributed to the LGP phase (PDF 41-0034/01-080-1922,  $\text{LiGe}_2(\text{PO}_4)_3$ ), which has a hexagonal crystal structure and  $R\bar{3}c$  space group (space group number 167). The lattice parameters are calculated from the sample sintered at 800°C and shown in Table 2-4. The diffraction peaks of the  $\text{GeO}_2$  phase (PDF 36-1463) are also observed on the diffractogram. The  $\text{GeO}_2$  has hexagonal crystal structure and the  $P3_21$  space group (space group number 154). The diffraction peaks of LAGP and  $\text{GeO}_2$  phase are the same on both samples, which were sintered at 800°C and 900°C.

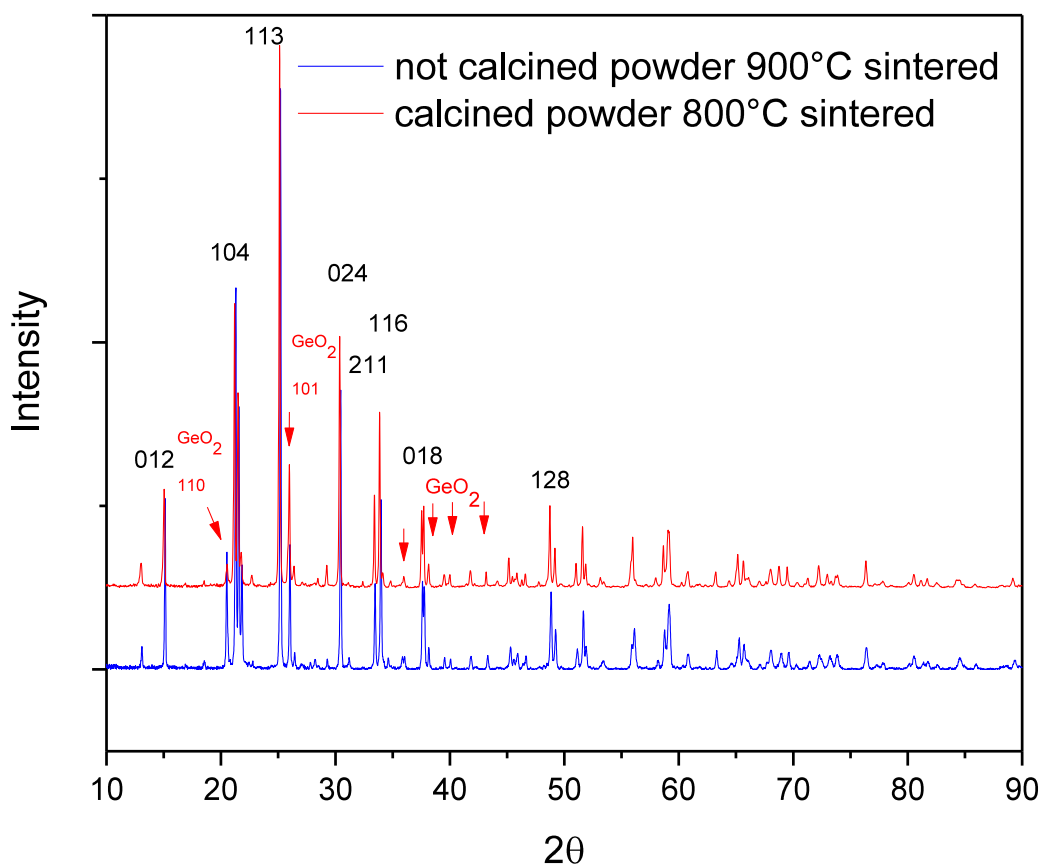


Figure 2-10: X-ray diffractogram of the samples of high Li LAGP with  $x = 0.7$ . Blue line: the sample #2 from not calcined powder sintered at 900°C for 6h. Red line: the sample #5 from calcined powder sintered at 800°C for 6h. The diffraction peaks of  $\text{LiGe}_2(\text{PO}_4)_3$  phase (PDF 41-0034) are indexed with black number. The diffraction peaks of  $\text{GeO}_2$  phase are pointed with red arrows.

Table 2-4: Lattice parameters of the LAGP sample.

	High Li LAGP (x =0.7)
a	8.241 ± 0.001 Å
b	8.241 ± 0.001 Å
c	20.524 ± 0.004 Å
α	90°
β	90°
γ	120°
volume	1207.1 ± 0.6 Å <sup>3</sup>

#### 2.2.1.5 Scanning electron microscopy and energy-dispersive X-ray spectroscopy

SEM (scanning electron microscopy) was applied for the microstructure observation. EDX (energy-dispersive X-ray spectroscopy) was carried out to measure the elemental composition at certain positions on the sample. Figure 2-11 - Figure 2-15 show the SEM images of samples of the high lithium LAGP (x = 0.7).

The SEM images of the sample #2 from the not calcined powder sintered at 900°C are shown in Figure 2-11. Large pores can be observed. The largest pores have the diameter of 1 mm. Cubic grains are visible on the inner wall of the pores. The grains have the dimension of 1 – 2 μm. The large size of the pores indicates that the pores were inflated by gas.

The Figure 2-12 – Figure 2-15 show the samples from calcined LAGP powder. The sample #3 sintered at 700°C shows open porosity (Figure 2-12). The large amount of pores shows that the sample was insufficiently sintered at 700°C. On the other hand, only one single phase was observed in this sample.

The sample #5 sintered at 800°C for 6 hours has much less porosity (Figure 2-13). Two new minor phases appear in the matrix: one bright phase and one dark phase. EDX measurement was carried out on these phases. The compositions of the matrix, the bright phase and the dark phase, respectively, are shown in Table 2-5. The quantitative EDX analysis has relatively large uncertainty since no reference sample was used. Furthermore, the X-ray can excite larger area than the diameter of the X-ray beam. The different phases are close to each other. It is difficult to limit the scan area to one single phase and the signals from multiple phase can be counted in one measurement. Considering the uncertainty of the EDX measurement, the EDX result of the matrix is close to the result of the chemical analysis, which confirmed that the matrix is the LAGP phase.

The main elements in the bright phase, Ge and O, have the ratio of nearly 1 : 2, showing that the bright phase is GeO<sub>2</sub>. The GeO<sub>2</sub> grains have a nearly spherical form. The main elements in the dark phase are Al, P and O. The Al : P : O ratio is about 1 : 1 : 3. Considering the uncertainty of EDX measurements, the dark phase is AlPO<sub>4</sub>. There are larger AlPO<sub>4</sub> grains with a size of 1 – 5 μm and small AlPO<sub>4</sub> areas between the LAGP grains (Figure 2-13-b). Grains with different size could be observed on the fracture surface (Figure 2-14). There are small grains with the size of around 1 μm located around the large grains with the size of 3 μm or more. Pores with the size of 3 – 5 μm are visible in the sample.

## 2. Characterization of ceramic solid-state electrolytes

The SEM images of the sample #6 sintered at 900°C for 6 hours are shown Figure 2-15. Large pores are visible on the fracture surface of the sample, which are similar to the sample sintered from not calcined powder. The pores have a size of about 50 μm. The GeO<sub>2</sub> and AlPO<sub>4</sub> minor phase are visible on the polished surface. The fraction of AlPO<sub>4</sub> phase at the grain boundary has increased significantly in comparison with the sample sintered at 800°C.

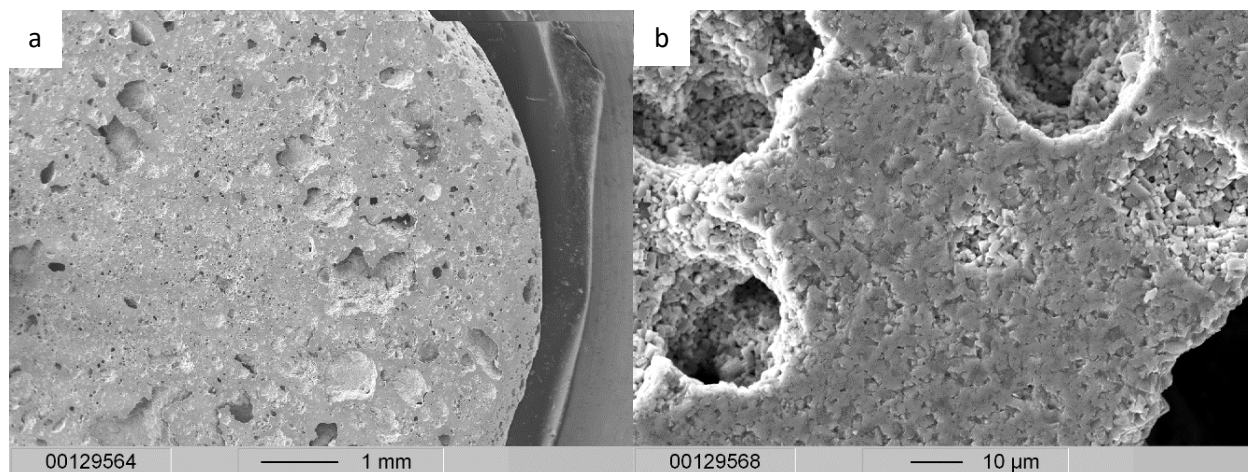


Figure 2-11: SEM images of the sample #2 from not calcined high lithium LAGP powder, which was sintered at 900°C for 6 hours. a: 15x magnification; b 1000x magnification.

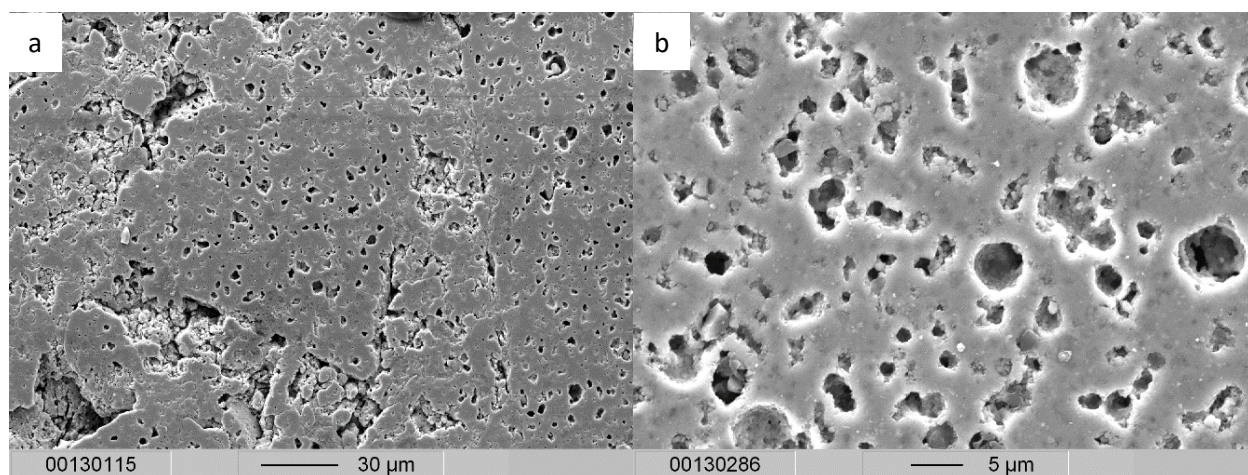


Figure 2-12: SEM images of the sample #3 from calcined high lithium LAGP powder, which was sintered at 700°C for 6 hours. a: 500x magnification; b 2000x magnification.

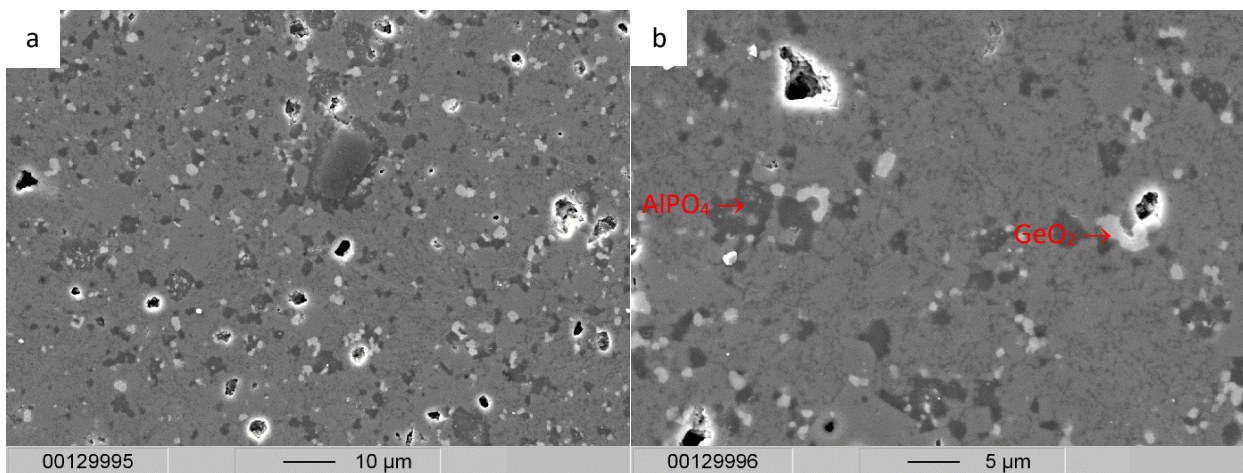


Figure 2-13: Polished surface of the sample #5 from calcined high lithium LAGP powder, which was sintered at 800°C for 6 hours. a: 1000x magnification; b 2000x magnification.

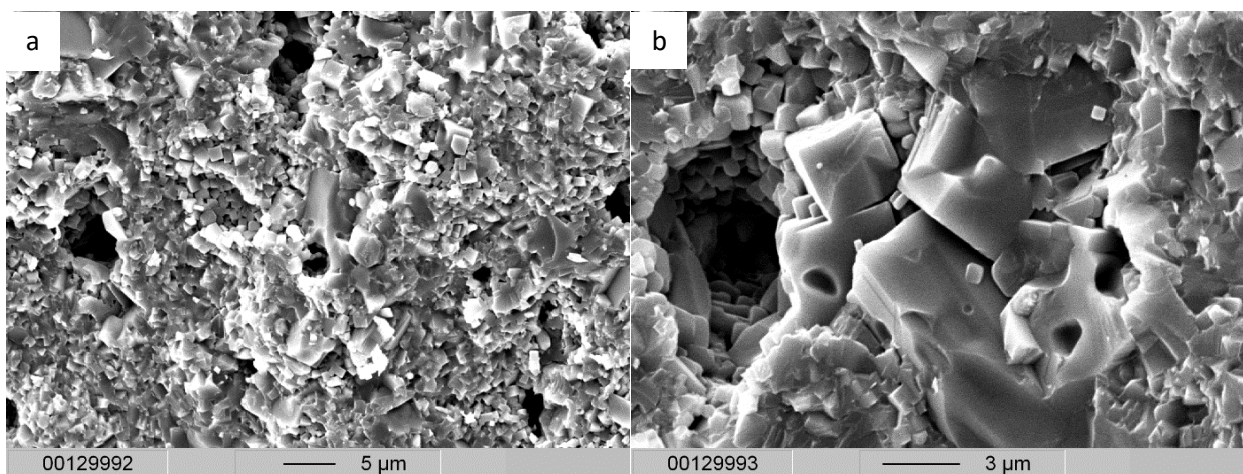


Figure 2-14: Fracture surface of the sample #5 from calcined high lithium LAGP powder, which was sintered at 800°C for 6 hours. a: 2000x magnification; b 5000x magnification.

Table 2-5: EDX results of the composition of different phases in the LAGP sample, which was sintered at 800°C (Figure 2-13). The elements Al, O, P and Ge are taken into account for the calculation of the atom fraction, since the EDX device employed here is not able to detect lithium element.

Atom % of the element	Matrix (LAGP)	Bright phase (GeO <sub>2</sub> )	Dark phase (AlPO <sub>4</sub> )
O	64.0%	55.1%	53.3%
Al	6.2%	2.3%	23.2%
P	17.0%	5.0%	19.5%
Ge	11.1%	35.7%	2.4%

## 2. Characterization of ceramic solid-state electrolytes

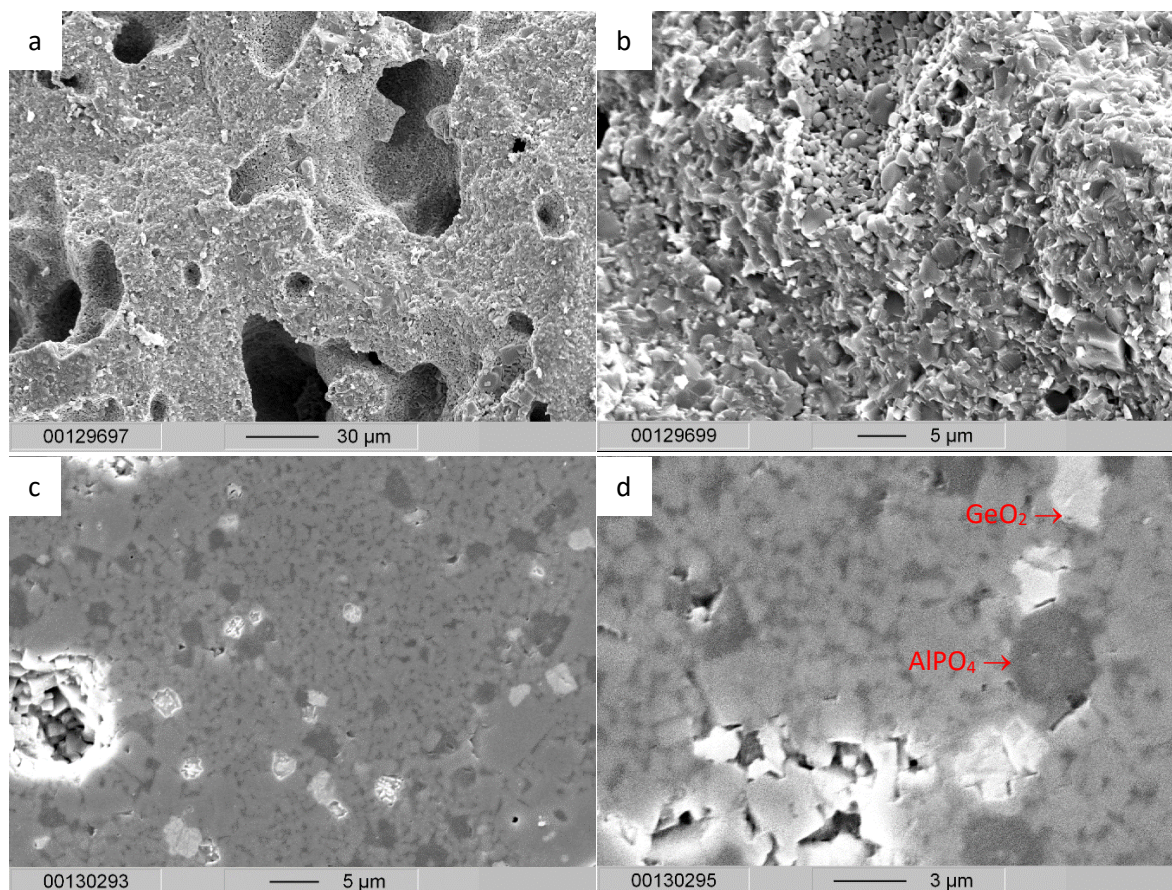


Figure 2-15: SEM images of the sample #6 from calcined high lithium LAGP powder, which was sintered at 900°C for 6 hours. a, b: the fracture surface with 500x and 2000x magnification, respectively; c, d: the polished surface with 2000x and 5000x magnification, respectively..

Comparing the SEM images of the samples of high lithium LAGP sintered at 700°C, 800°C and 900°C, the sample, which was sintered at 800°C, shows the lowest porosity. The fraction of the minor phases increases with increasing sintering temperature. In the 900°C sample, the amount of the  $\text{AlPO}_4$  phase had significantly increased. The minor phases tend to precipitate from the LAGP phase and accumulate at the boundary between the LAGP grains.

### 2.2.1.6 Ionic conductivity

The conductivity can be evaluated by fitting on the Nyquist-diagram and by reading the conductivity spectrum. Figure 2-16 shows the Nyquist-Diagram of the sample #2 measured at -28°C, 25°C and 50°C, respectively, which was sintered at 900°C for 6h using not calcined LAGP powder. The conductivity spectrums of the same measurements are shown Figure 2-18. Both diagrams show that the scale of the impedance decreased drastically with increasing temperature.

Figure 2-17-a shows the Nyquist-Diagram of the sample measured at -28°C and the fitted curve (red). Two semicircles can be recognized on the diagram. The equivalent circuit model is fitted with the measured data. The  $R_1$  and  $R_2$  represents the resistance of the grain and grain boundary (see 1.5). The  $R_1$  has a smaller

value and lies at higher frequency. The  $R_2$  has a larger value and lies at lower frequency. In the LAGP super ionic conductor, the grain resistance is lower than the grain boundary resistance<sup>93,94</sup>. Simulation shows that the high-frequency semicircle on the Nyquist-Diagram can be attributed to the grain and the low-frequency semicircle to the grain boundary<sup>95</sup>. Therefore, the  $R_1$  is attributed to the resistance of the grain and the  $R_2$  to the grain boundary.

The conductivity value can be calculated from resistance value and the sample geometry factor. The total conductivity of the sample is:

$$\sigma_{total} = \frac{1}{(R_1 + R_2)} \cdot \frac{d}{A} \quad 2-6$$

It is assumed that the volume of the grain boundary is negligible compared to the volume of the grains. The grain conductivity can be therefore calculated:

$$\sigma_{grain} = \frac{1}{R_1} \cdot \frac{d}{A} \quad 2-7$$

where the  $d$  is thickness and the  $A$  is the top/bottom surface area of the cylindrical sample.

The cylindrical sample has a thickness  $d = 0.369$  cm and a top surface area  $A = 0.648$  cm<sup>2</sup>. The grain conductivity at  $-28^\circ\text{C}$  is  $4.2 \cdot 10^{-6}$  S/cm and the total conductivity is  $4.5 \cdot 10^{-7}$  S/cm. On the conductivity spectrum, DC plateaus with smaller slope are visible (Figure 2-18). On the curve of the measurement at that temperature ( $-28^\circ\text{C}$ ), the higher plateau corresponds to the grain conductivity and the lower plateau corresponds to the total conductivity.

At higher temperature however, the small semicircle on the Nyquist-Diagram begins to merge in the larger one (Figure 2-17-b and -c). The  $R_1$  and  $R_2$  have then large uncertainty by fitting. However, the sum of  $R_1$  and  $R_2$  has smaller uncertainty. On the conductivity spectrum, only one plateau is visible (Figure 2-18 the top two lines), which represents the total conductivity of the sample calculated using equation

2-6. At the temperature higher than  $50^\circ\text{C}$ , only one semicircle can be recognized on the Nyquist-Diagram and only one plateau on the conductivity spectrum. The grain and grain boundary contribution cannot be separated.

As shown on Figure 2-17, it is difficult to fit the equivalent circuit model perfectly with the measured data. The real material is much more complicated than the equivalent circuit model with limited elements.

Since the conductivity values evaluated by the Nyquist-diagram and by reading the conductivity spectrum are the same, the ionic conductivity of the samples are evaluated by reading the conductivity spectrum throughout this work. The conductivity values are taken from the position with the smallest slope on the conductivity spectrum curve (where the first derivative of the conductivity curve has minimum). The uncertainty (error bar) of the ionic conductivity of the sample is taken from the width of the plateau in Y-direction, which is determined by the intersection points of the extrapolated lines of different sections of the conductivity curve. (Figure 2-18).

## 2. Characterization of ceramic solid-state electrolytes

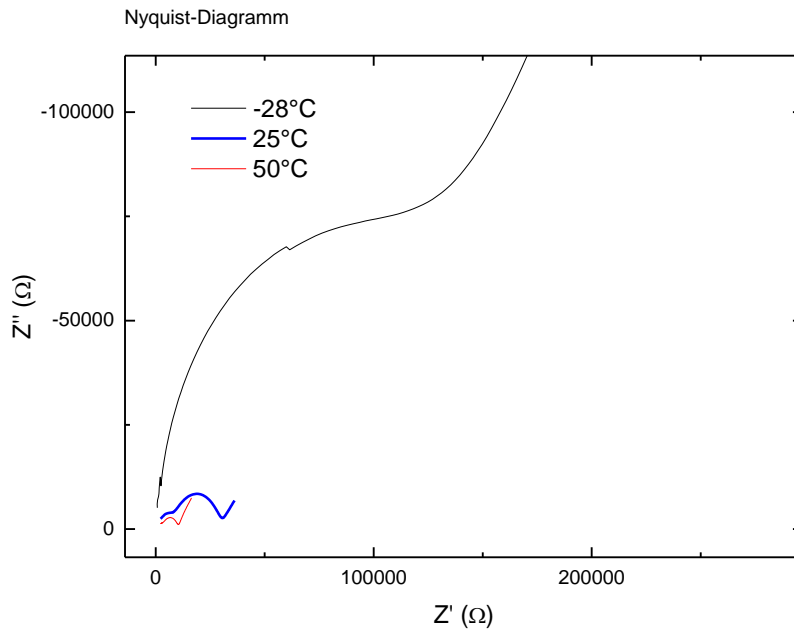
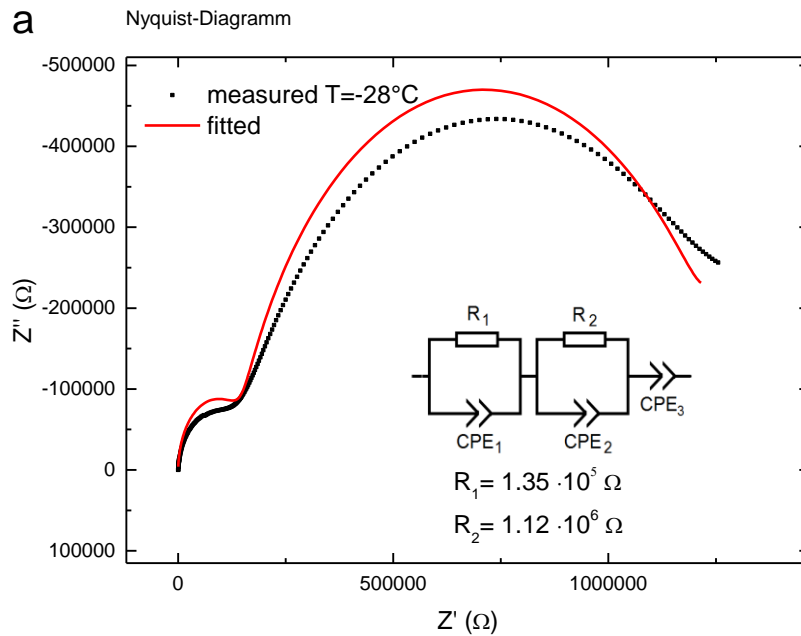


Figure 2-16: The Nyquist-Diagrams of the sample #2 of high Li LAGP with  $x = 0.7$  in  $Li_{1+x}Al_xGe_{2-x}P_3O_{12}$  measured at -28°C, 25°C and 50°C.



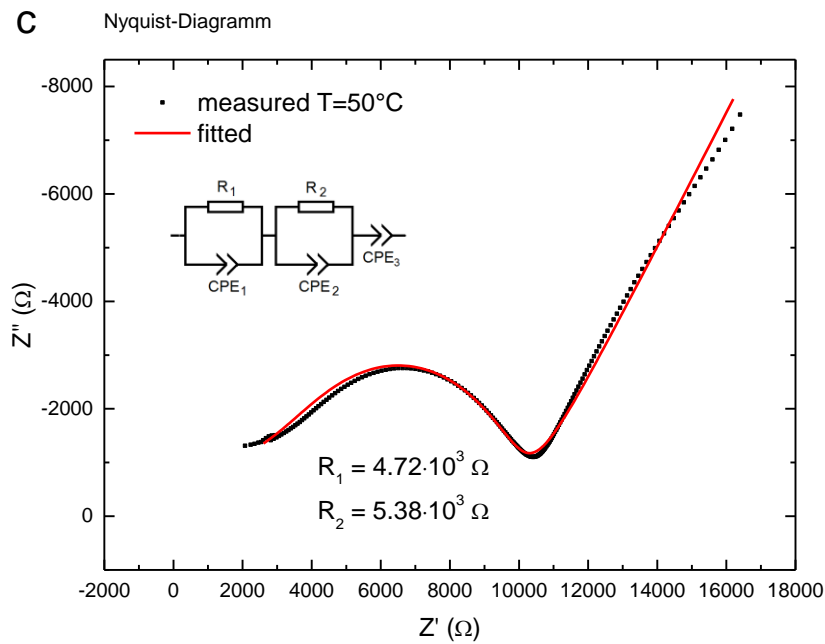
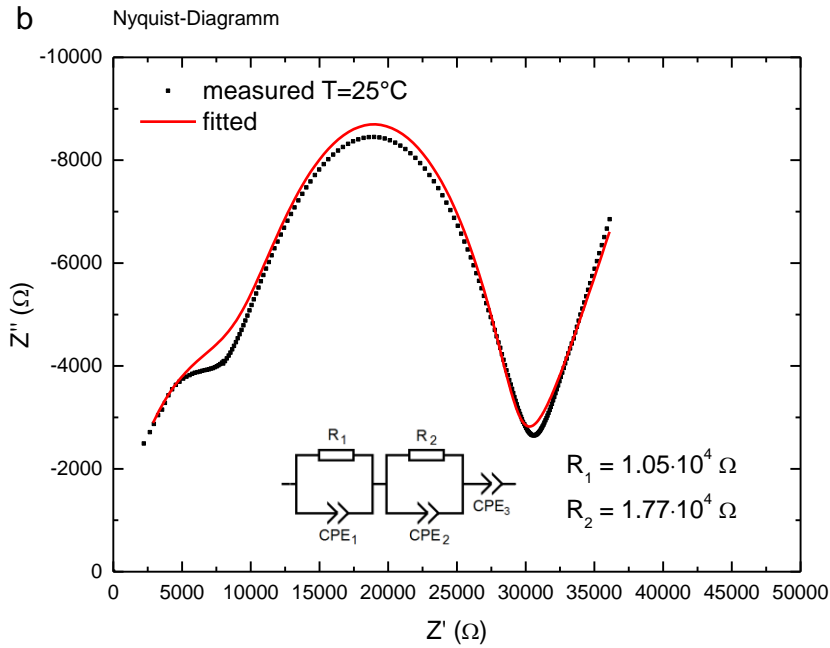


Figure 2-17: The Nyquist-Diagrams of the sample #2 of the high lithium LAGP measured at a:  $-28^{\circ}\text{C}$ , b:  $25^{\circ}\text{C}$  and c:  $50^{\circ}\text{C}$ . The equivalent circuit model and the fitted resistance value are shown on the diagrams. The cylindrical sample has a thickness  $d = 0.369 \text{ cm}$  and a top surface area  $A = 0.648 \text{ cm}^2$ .

## 2. Characterization of ceramic solid-state electrolytes

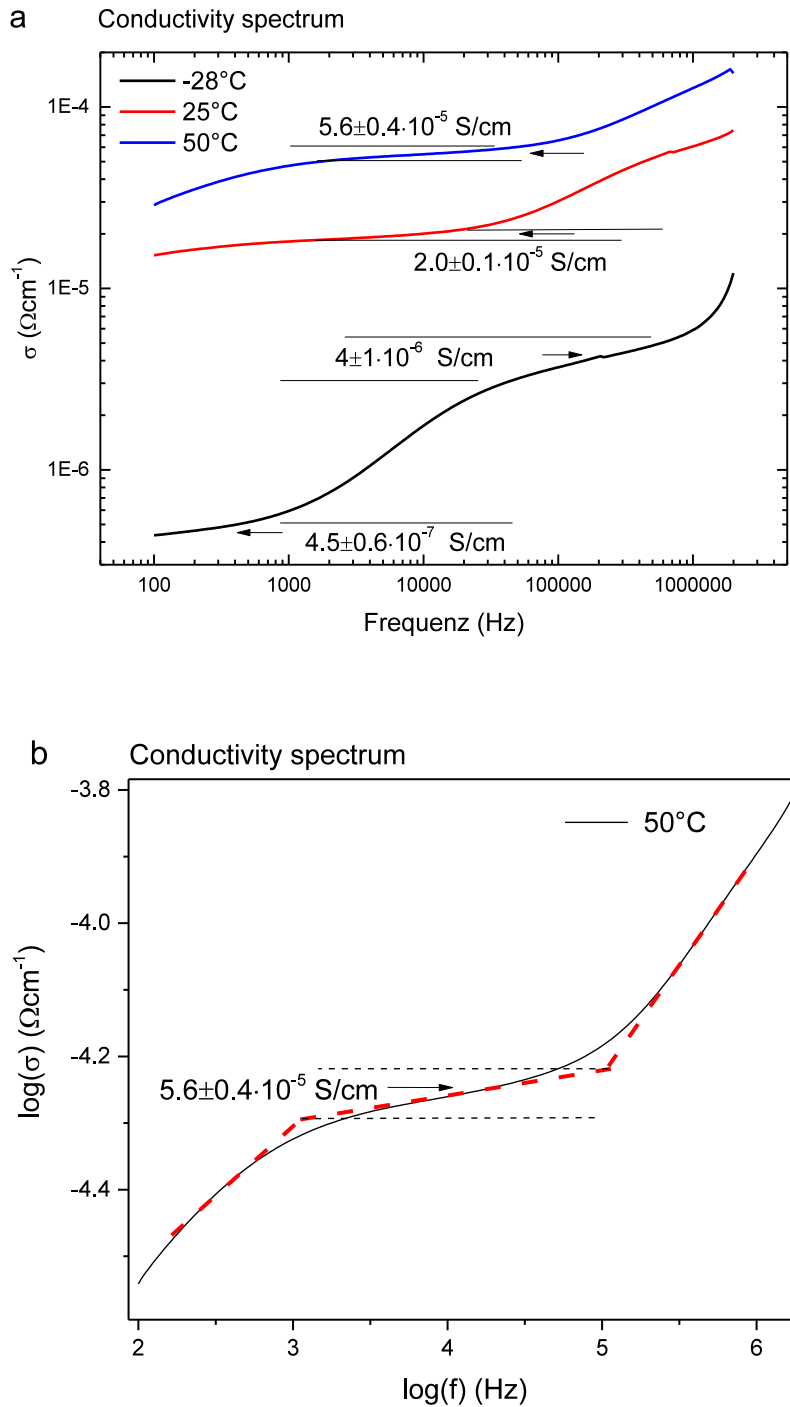


Figure 2-18: The conductivity spectrums of the sample #2 of high Li LAGP. *a*: The conductivity spectrums measured at  $-28^{\circ}\text{C}$ ,  $25^{\circ}\text{C}$  and  $50^{\circ}\text{C}$  corresponding to Figure 2-17, respectively; *b*: The conductivity spectrum measured at  $50^{\circ}\text{C}$ . The uncertainty (error bar) of the ionic conductivity is taken from the width of the plateau in vertical direction, which is determined by the intersection points of the extrapolated lines of different sections of the conductivity curve.

The ionic conductivities of the samples of high Li LAGP ( $x = 0.7$ ) are shown in Figure 2-19 and Figure 2-20. The measured ionic conductivity is plotted in a semi-log plot over  $1000/T$ . The numerical values of the ionic conductivity are shown in the appendix.

As shown in Figure 2-19, the sample #5, which was sintered at  $800^{\circ}\text{C}$  for 6 hours using the calcined LAGP powder, has the highest ionic conductivity ( $1.5 \cdot 10^{-4} \text{ S/cm}$  at room temperature,  $3.0 \cdot 10^{-3} \text{ S/cm}$  at  $100^{\circ}\text{C}$  and  $2.2 \cdot 10^{-2} \text{ S/cm}$  at  $200^{\circ}\text{C}$ ). The samples #7 and #6, which were sintered at  $850^{\circ}\text{C}$  and  $900^{\circ}\text{C}$ , respectively, have a lower conductivity. The ionic conductivity of sample #4 sintered at  $750^{\circ}\text{C}$  is lower as the other samples.

As shown in Figure 2-20, the conductivity of the sample #8 sintered 3 hours at  $800^{\circ}\text{C}$  is slightly lower than the sample #5 sintered for 6 hours. The conductivity decreases again as the sintering time increases to 9 hours (sample #9).

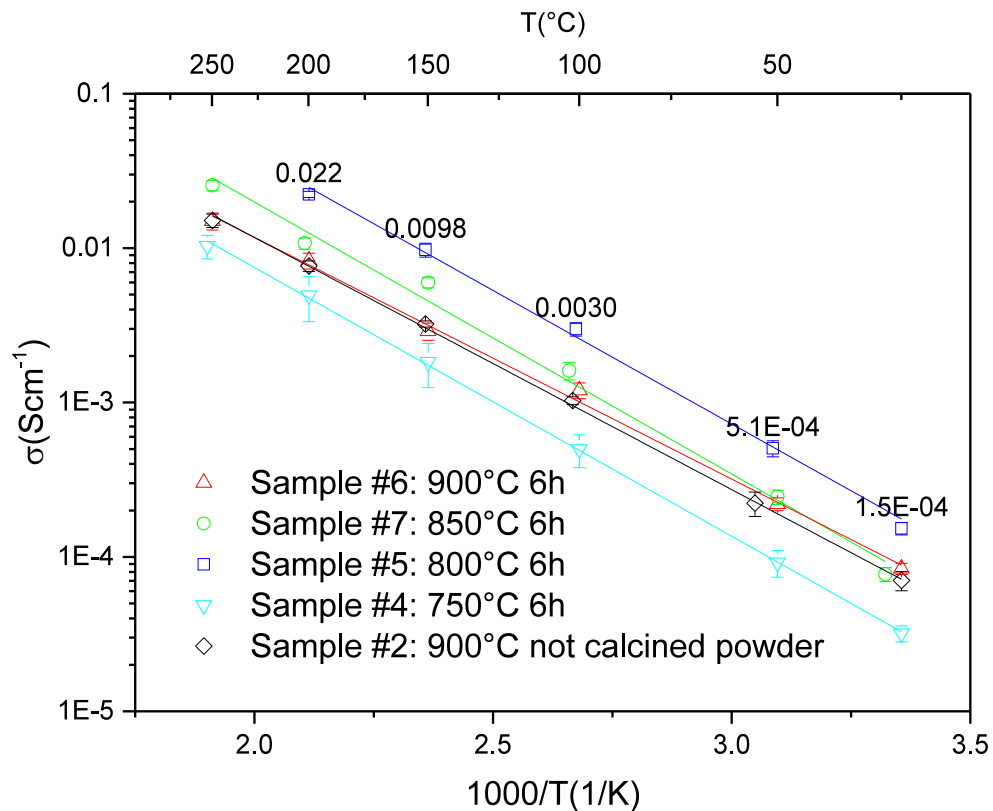


Figure 2-19: Ionic conductivity of the samples made of the calcined and not calcined powder of the high Li LAGP with  $x = 0.7$  in  $\text{Li}_{1+x}\text{Al}_x\text{Ge}_{2-x}\text{P}_3\text{O}_{12}$ . The samples were sintered for 6 hours at  $750^{\circ}\text{C} - 900^{\circ}\text{C}$ . The numerical values of the ionic conductivity are shown in the appendix Table A- 1 – Table A- 5

## 2. Characterization of ceramic solid-state electrolytes

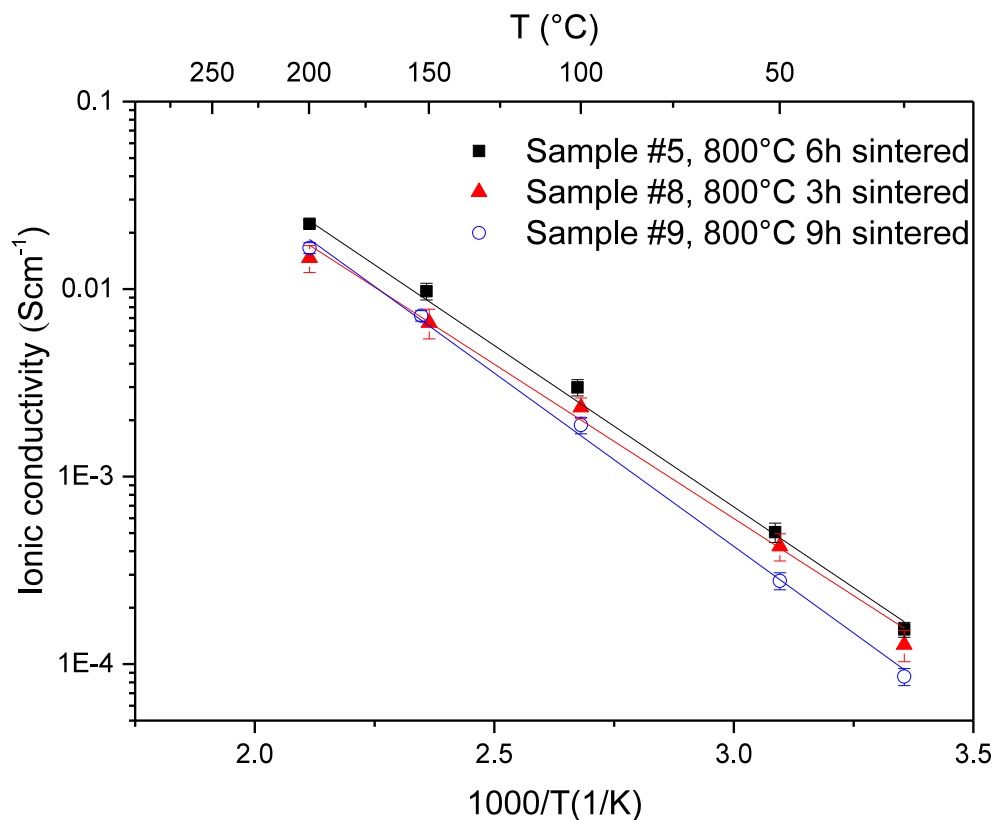


Figure 2-20: Ionic conductivity of the samples made of the calcined high Li LAGP powder sintered at 800°C for 3 – 9 h. The numerical values of the ionic conductivity are shown in the appendix Table A- 3, Table A- 6 and Table A- 7.

### 2.2.1.7 Density

The densities of the samples were measured with the Archimedes method (see 2.1.5). The sample #3 and #4 were measured with help of Zapon lacquer and other samples were measured without Zapon lacquer. The theoretical density of the LAGP crystal is calculated from the lattice parameters measured by the XRD and the formula molecular weight of LAGP. LAGP of batch 1 ( $x \approx 0.7$  in the general formula of  $\text{Li}_{1+x}\text{Al}_x\text{Ge}_{2-x}\text{P}_3\text{O}_{12}$ ) has the theoretical density of  $3.40 \text{ g/cm}^3$ . Table 2-6 shows the density and the relative density of the samples of the high Li LAGP. The uncertainty of the density was estimated to be less than 1%.

Table 2-6: Density and relative density of samples of LAGP batch 1.

Sample	Density $\rho$ (g/cm <sup>3</sup> )	Relative density( $\rho/\rho_{\text{theo}}$ )
#2. not calcined powder 900°C sintered for 6 h	1.79	52.6%
#3. calcined powder 700°C sintered for 6 h	2.82	82.9%
#4. calcined powder 750°C sintered for 6 h	2.88	84.7%
#5. calcined powder 800°C sintered for 6 h	3.10	91.2%
#6. calcined powder 900°C sintered for 6 h	2.47	72.6%
#7. calcined powder 850°C sintered for 6 h	2.87	84.4%

## 2.2.2 Discussion

The characterization results of the LAGP samples are discussed in this section for the optimized sintering procedure.

The first batch of LAGP has the composition of  $\text{Li}_{1.68}\text{Al}_{0.61}\text{Ge}_{1.32}\text{P}_3\text{O}_{11.90}$ . The glass transition temperature and crystallization temperature of the LAGP glass is shown in Table 2-7.

Table 2-7: Glass transition temperature and crystallization temperature of the LAGP glass batch 1.

LAGP	Glass transition onset	Crystallization onset
Batch 1: high Li, $x \approx 0.7$ $\text{Li}_{1.68}\text{Al}_{0.61}\text{Ge}_{1.32}\text{P}_3\text{O}_{11.90}$	504°C	596°C

During the sinter process, the sample #2 from the not calcined powder showed a rapid shrinkage starting at 510°C (Figure 2-7), which matches the glass transition temperature of the LAGP glass measured by DSC. An amorphous material transforms from a hard and brittle glassy state into a viscous state when the temperature exceeds the glass transition temperature. The samples is therefore compacted via viscous flow of the glass particles and achieved high shrinking rate.

However, the sample #2 pressed from the not calcined LAGP powder showed unusual behavior at higher temperature: As shown in Figure 2-7, the sample exhibited an expansion starting at 670°C. The large expansion (40% in total) indicates that the expansion is not caused by a phase transition in the solid phase, because no phase transition was reported in these materials with such large dimensional change. SEM images show large pores in this sample (Figure 2-11). The pores have the size of up to 1000  $\mu\text{m}$ , which are hardly formed except inflated by gas.

## 2. Characterization of ceramic solid-state electrolytes

Thermal gravimetric analysis (TGA) was carried out on a sample of the high Li LAGP ( $x = 0.7$ ) to investigate the mass change during sintering (Figure 2-9). The TGA results showed a mass loss of the sample at the temperature higher than 670°C, which took place simultaneously with the sample expansion measured by dilatometer, showing that the mass loss and the expansion of the sample are in one single process. It confirms that there is a gas release of the LAGP sample during sintering, which inflates the pores in the sample and results in an expansion of up to 40%.

$\text{Li}_2\text{CO}_3$  is one of the starting materials for the preparation of the LAGP glass. It was assumed at first that  $\text{CO}_2$  gas was formed from the carbonate left in the LAGP glass during the sintering. However, the chemical analysis showed no carbon (C) element in the LAGP powder. It is therefore not possible for the LAGP samples to release  $\text{CO}_2$  gas.

Another possible gaseous substance in this Li-Al-Ge-P-O-system is the  $\text{P}_2\text{O}_5$ . It has the sublimation point at 362°C. Since gaseous substance has much larger volume than in solid state (3 orders of magnitude higher), small amount of gaseous  $\text{P}_2\text{O}_5$  is enough to cause a significant expansion of the sample by sintering.

It has been mentioned that the  $\text{Al}(\text{PO}_3)_3$  decomposes at 800°C – 1200°C and releases  $\text{P}_2\text{O}_5$ <sup>96, 97</sup>:



The  $\text{Al}(\text{PO}_3)_3$  can be prepared in glassy state by melting the  $\text{Al}_2\text{O}_3$  and  $\text{HPO}_3$ <sup>98, 99</sup>.  $\text{Al}_2\text{O}_3$  was used as one of the starting materials for LAGP glass. The mole ratio between the element Al and P in the starting material is around 1 : 5. Therefore, there might be  $\text{Al}(\text{PO}_3)_3$  formed in the LAGP glass during the melt quenching process. As the LAGP glass was later sintered,  $\text{P}_2\text{O}_5$  was released from  $\text{Al}(\text{PO}_3)_3$  and resulted in the expansion of the sample.

The rest of the LAGP powder was calcined at 700°C for 3 hours. Samples pressed from the calcined powder were sintered at 700°C – 900°C (sample #3 – #9). Unlike the samples of not calcined glass powder, which has a rapid shrinkage at the glass transition temperature (around 500°C), the shrinkage of the samples of calcined powder took place at much higher temperatures (750°C – 800°C). The samples were not sufficiently densified at lower temperature (700°C – 750°C). The sample sintered at 800°C for 6 hours showed the highest density and the highest ionic conductivity (Figure 2-8, Figure 2-21, Figure 2-19, Figure 2-20). At higher temperature (900°C), the decomposition reaction of the  $\text{Al}(\text{PO}_3)_3$  minor phase took place again, which resulted in a gas release and an increase of porosity.

The amount of the  $\text{AlPO}_4$  minor phase increased as the sintering temperature increased. On the other hand, the ionic conductivity increased as the sintering temperature increased to 800°C but decreased as it increased to 900°C. The minor phase in the LAGP matrix has both positive and negative effect on the ionic conductivity of LAGP ceramic. An appropriate amount of  $\text{AlPO}_4$  minor phase can fill the porosity and mediate the ion transport, as it showed on the sample #5 sintered at 800°C. However, the  $\text{AlPO}_4$  is not a lithium ion conductor. The lithium ion transport is hindered when larger amount of  $\text{AlPO}_4$  phase is formed at the grain boundary. As shown in Figure 2-13 and Figure 2-15, the amount of  $\text{AlPO}_4$  increased at the boundary between LAGP grains at 900°C and hence the ionic conductivity decreased in comparison with the sample sintered at 800°C.

J. Thokchom et. al proposed a theory about the enhancing and blocking effect of  $\text{AlPO}_4$  minor phase on the ionic transport in LAGP<sup>100</sup>: The minor phase can induce space charge effect when it is in contact with LAGP. Charged complexes might be formed by  $\text{AlPO}_4$  and  $\text{Li}^+$  ions at the  $\text{AlPO}_4$ -LAGP interface. The  $\text{AlPO}_4$  minor phase affects the lithium conduction path depending on its size: while larger  $\text{AlPO}_4$  blocks the ion transport, smaller  $\text{AlPO}_4$ : $\text{Li}^+$  complex might mediate the lithium ion transport between LAGP grains. Grains of the minor phase with a proper size can therefore enhance the ionic conductivity, although they have poor conductivity themselves.

The sample #2 sintered at 900°C had higher ionic conductivity as the sample #4 sintered at 750°C, although the sample #2 was less compacted (Figure 2-19, Figure 2-21). That is due to the better contact between the grains in the sample #2.

Resulting from the combined effect of the sintering property and the formation of minor phases, the optimized sintering procedure for the LAGP ( $\text{Li}_{1.68}\text{Al}_{0.61}\text{Ge}_{1.32}\text{P}_3\text{O}_{11.90}$ ) is using a sintering temperature of 800°C and a holding period of 6 hours.

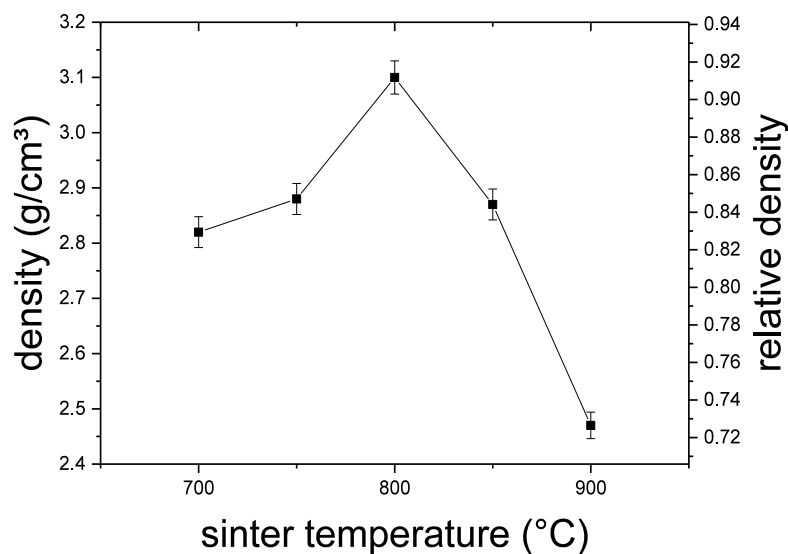


Figure 2-21: The density of the LAGP samples of high lithium LAGP ( $x = 0.7$ ) sintered at different temperatures for 6 hours.

The ionic conductivity obtained on the sintered LAGP samples ( $1.5 \cdot 10^{-4}$  S/cm at 25°C by  $x = 0.7$ ) agrees with the value reported in literature using sintering method. In the work of Kichambare et. al, an optimized ionic conductivity of  $1.03 \cdot 10^{-4}$  S/cm at room temperature was achieved by sintering  $\text{Li}_{1.5}\text{Al}_{0.5}\text{Ge}_{1.5}\text{P}_3\text{O}_{12}$  powder prepared by sol-gel process<sup>101</sup>. Kotobuki et. al reported a highest ionic conductivity of  $1.8 \cdot 10^{-4}$  S/cm at 30°C also using sol-gel powder synthesis and sintering route<sup>85</sup>. They found an optimized sintering procedure at a temperature of 850°C held for 12 hours, which is higher and longer as found in this work. The difference could be due to the composition and morphology of LAGP powder. Similar results were also reported by Mariappan et. al<sup>63</sup> and Leo et. al<sup>102</sup>.

## 2. Characterization of ceramic solid-state electrolytes

### 2.3 LAGP solid-state electrolyte via heat-treating route

An alternative preparation route is the heat-treating of quenched LAGP glass (see 2.1.1). Three different compositions of LAGP were fabricated via the heat-treating route. The compositions are shown in Table 2-8.

The overall chemical formula is calculated from the atomic fraction. The number of phosphorous element in the chemical formula is set to 3 according to the formula of  $\text{Li}_{1+x}\text{Al}_x\text{Ge}_{2-x}\text{P}_3\text{O}_{12}^{2-,84}$ . The numbers of the elements Li, Al and Ge are calculated via the ratios between the specific element and the phosphorous and the numbers of oxygen are calculated according the charge neutrality. The x value for the LAGP solid-state electrolyte in this work are approximately 0.3 (LAGP batch 2), 0.5 (LAGP batch 3) and 0.7 (LAGP batch 4), respectively.

*Table 2-8: Chemical composition of the LAGP batch 2 – 4.*

LAGP		Li	Al	P	Ge	O
Batch 2 low Li	wt. %	2.18±0.02	2.70±0.02	22.90±0.04	26.5±0.4	43.7±0.3
	at. %	7.39±0.07	2.35±0.02	17.40±0.03	8.58±0.12	64.3±0.5
	Overall chemical formula	$\text{Li}_{1.27}\text{Al}_{0.41}\text{Ge}_{1.48}\text{P}_3\text{O}_{11.70}$				
Batch 3 Medium Li	wt. %	2.57±0.02	3.39±0.07	22.60±0.03	24.10±0.02	46.2±0.2
	at. %	8.33±0.07	2.83±0.06	16.42±0.02	7.46±0.01	65.0±0.3
	Overall chemical formula	$\text{Li}_{1.52}\text{Al}_{0.52}\text{Ge}_{1.36}\text{P}_3\text{O}_{11.76}$				
Batch 4 High Li	wt. %	2.85±0.02	3.45±0.04	22.2±0.1	23.7±0.2	44.4±0.6
	at. %	9.43±0.07	2.94±0.02	16.45±0.07	7.49±0.06	63.7±0.8
	Overall chemical formula	$\text{Li}_{1.72}\text{Al}_{0.54}\text{Ge}_{1.37}\text{P}_3\text{O}_{11.89}$				

Since the Carrier Gas Hot Extraction (CGHE) method is less accurate, the oxygen content of the sample has a higher uncertainty. The sum of the weight percent of all the elements has therefore deviation from 100%. The composition of the starting material (calculated using data in Table 2-1) and the composition of the glass after the melt quenching process are compared in Table 2-9. The compositions of the LAGP glasses show higher Al content as the composition of the starting material. That can be attributed to the  $\text{Al}_2\text{O}_3$ , which diffused from the alumina crucible into the LAGP melt during the melting-process.

Table 2-9: Comparison of the composition of the starting material with the composition of the glass after the melt quenching process.

	Batch 2, low Li	Batch 3, medium Li	Batch 4, high Li
Composition of the starting material	$\text{Li}_{1.23}\text{Al}_{0.24}\text{Ge}_{1.56}\text{P}_3\text{O}_{11.60}$	$\text{Li}_{1.53}\text{Al}_{0.46}\text{Ge}_{1.40}\text{P}_3\text{O}_{11.77}$	$\text{Li}_{1.67}\text{Al}_{0.46}\text{Ge}_{1.40}\text{P}_3\text{O}_{11.81}$
Composition of the glass	$\text{Li}_{1.27}\text{Al}_{0.41}\text{Ge}_{1.48}\text{P}_3\text{O}_{11.70}$	$\text{Li}_{1.52}\text{Al}_{0.52}\text{Ge}_{1.36}\text{P}_3\text{O}_{11.76}$	$\text{Li}_{1.72}\text{Al}_{0.54}\text{Ge}_{1.37}\text{P}_3\text{O}_{11.89}$

### 2.3.1 Sample characterization

LAGP glass samples with low lithium content ( $\text{Li}_{1.27}\text{Al}_{0.41}\text{Ge}_{1.48}\text{P}_3\text{O}_{11.70}$ , batch 2), medium lithium content ( $\text{Li}_{1.52}\text{Al}_{0.52}\text{Ge}_{1.36}\text{P}_3\text{O}_{11.76}$ , batch 3) and high lithium content ( $\text{Li}_{1.72}\text{Al}_{0.54}\text{Ge}_{1.37}\text{P}_3\text{O}_{11.89}$ , batch 4) were heat-treated using different process parameters and characterized as listed in Table 2-10, Table 2-11 and Table 2-12.

Table 2-10: List of the samples of low lithium LAGP batch 2 fabricated with different process parameters and characterized with Dilatometry (DIL), XRD, scanning electron microscopy (SEM), impedance spectroscopy (IS) and laser flash analysis (LFA).

Sample No.	Fabrication process parameters	Characterization methods
#1	Heat treated at 800°C for 6h in dilatometer	DIL, XRD
#2	Heat treated at 660°C for 3h	IS, SEM, LFA
#3	Heat treated at 800°C for 3h and then 6h	IS, SEM, LFA
#4	Heat treated at 800°C for 6h	IS, SEM, LFA
#5	Glass	IS, LFA
#6	Heat treated in hot stage XRD device	Hot stage XRD
#7	Glass	DSC

Table 2-11: List of the samples of medium lithium LAGP batch 3 fabricated with different process parameters and characterized with XRD, scanning electron microscopy (SEM), impedance spectroscopy (IS) and laser flash analysis (LFA).

Sample No.	Fabrication process parameters	Characterization methods
#1	Heat treated at 800°C for 6h	SEM, IS, XRD, LFA
#2	Heat treated at 550°C for 10 min + 650°C for 2h	SEM, IS
#3	Sintered from powder at 800°C for 6h	SEM, IS
#4	Heat treated in hot stage XRD device	Hot stage XRD
#5	Glass	DSC

## 2. Characterization of ceramic solid-state electrolytes

*Table 2-12: List of the samples of high lithium LAGP batch 4 fabricated with different process parameters and characterized with dilatometer(DIL), XRD, scanning electron microscopy (SEM), impedance spectroscopy (IS), DSC and laser flash analysis (LFA).*

Sample No.	Fabrication process parameters	Characterization methods
#1	Heat treated at 800°C for 6h in dilatometer	DIL, SEM, IS, DSC up to 900°C
#2	Heat treated at 550°C for 1h + 630°C for 1h + 800°C for 1h in dilatometer	DIL, SEM, IS
#3	Heat treated at 600°C for 2h + 800°C for 6h	IS, XRD
#4	Heat treated at 900°C for 6h	IS
#5	Heat treated at 800°C for 12h	IS
#6	Heat treated in hot stage XRD device	Hot stage XRD
#7	Heat treated at 800°C for 6h	LFA
#8	Glass	DSC

### 2.3.1.1 DSC measurements

Samples of LAGP were measured in the DSC device to analyze the phase transitions during heat-treatment. Phase transitions taking place in the LAGP samples are discussed together with results of other investigation methods in section 2.3.3.

Figure 2-22 shows the first heating and cooling curves of the low lithium LAGP glass sample #7 (batch 2,  $x = 0.3$ ). The glass transition took place between 535°C (onset) and 564°C (end). The crystallization onset temperature was at 649°C. No other peak is observed during the further heating and cooling. The crystallized sample was measured in the DSC for three times to determine the heat capacity. The median value of the three measurements was taken as the result. The difference between the different measurements were smaller than 1%. Figure 2-23 shows the heat capacity curve of the crystallized LAGP sample between -20°C and 900°C. The heat capacity increased throughout the whole temperature range. The slope became smaller as the temperature reached 800°C and became larger above that temperature.

Figure 2-24 shows the first heating and cooling curve of the medium lithium LAGP glass sample #5 (batch 3,  $x = 0.5$ ). The sample had the glass transition between 530°C (onset) – 558°C (end) and the crystallization onset temperature at 640°C. On the cooling curve, a small peak was visible at 700°C. The heat capacity of the sample of medium lithium LAGP is shown in Figure 2-25. Five peaks appeared at 562°C, 644°C, 696°C, 731°C and 750°C on the heat capacity curve. These peaks appeared repetitively on the further measurement cycles, showing that they are presenting reversible transitions.

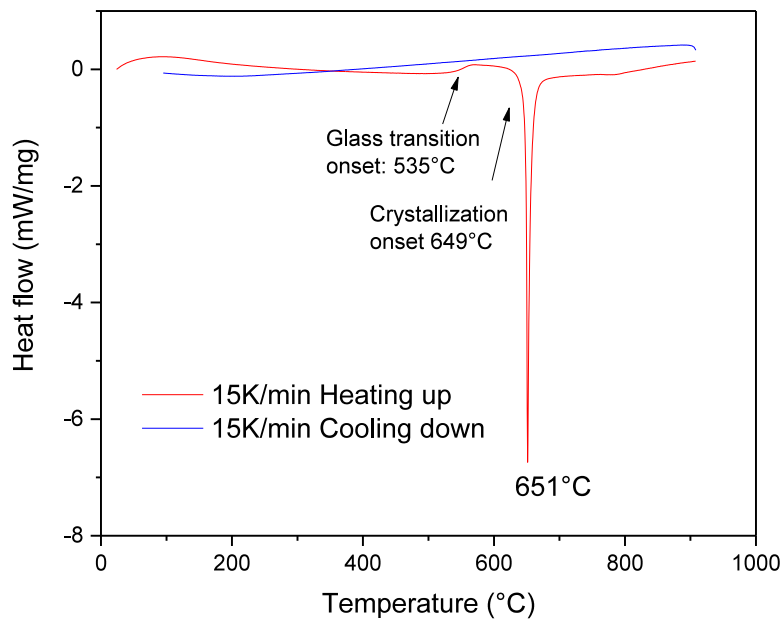


Figure 2-22: DSC curve of the low lithium LAGP sample #7 (with  $x = 0.3$  in  $\text{Li}_{1+x}\text{Al}_x\text{Ge}_{2-x}\text{P}_3\text{O}_{12}$ ). The sample was heated up to 900°C with a heating rate of 15K/min and cooled down to room temperature.

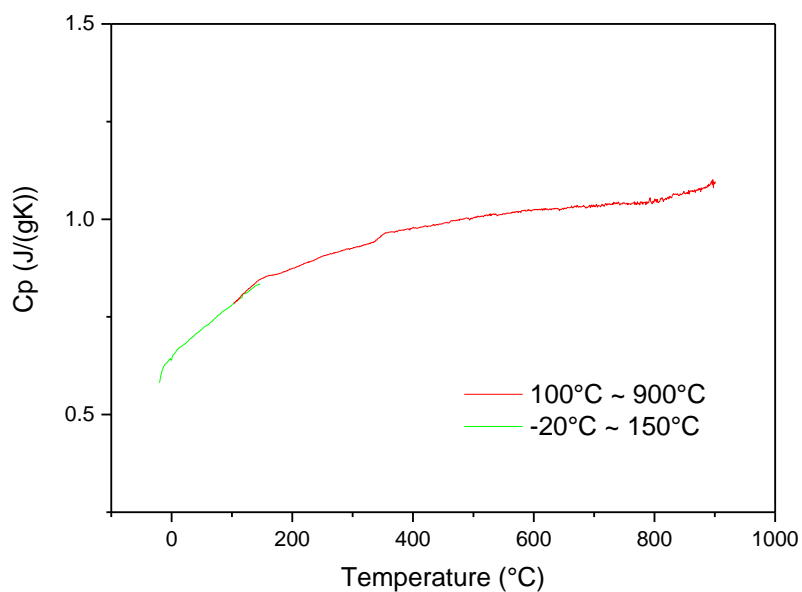


Figure 2-23: Heat capacity of the crystallized sample #7 of the low lithium LAGP.

## 2. Characterization of ceramic solid-state electrolytes

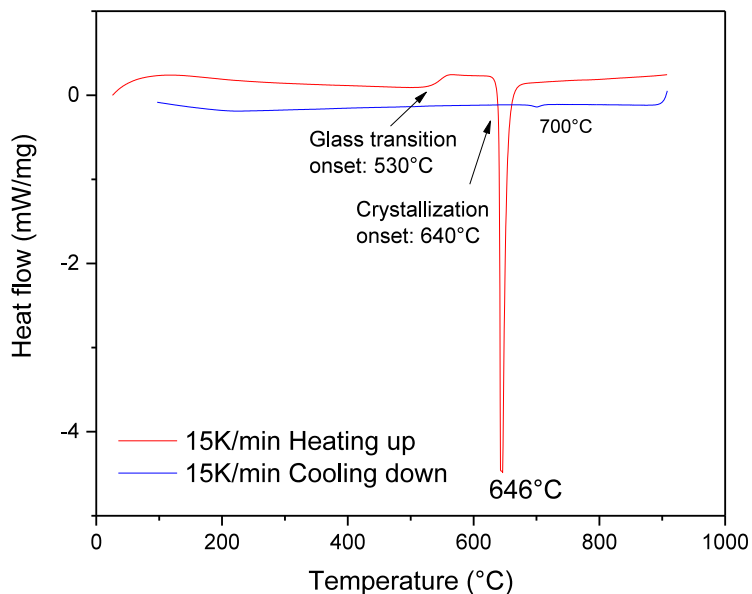


Figure 2-24: DSC curve of the medium lithium LAGP sample #5 ( $x = 0.5$ ). The sample was heated up to 900°C with a heating rate of 15K/min and cooled down to room temperature.

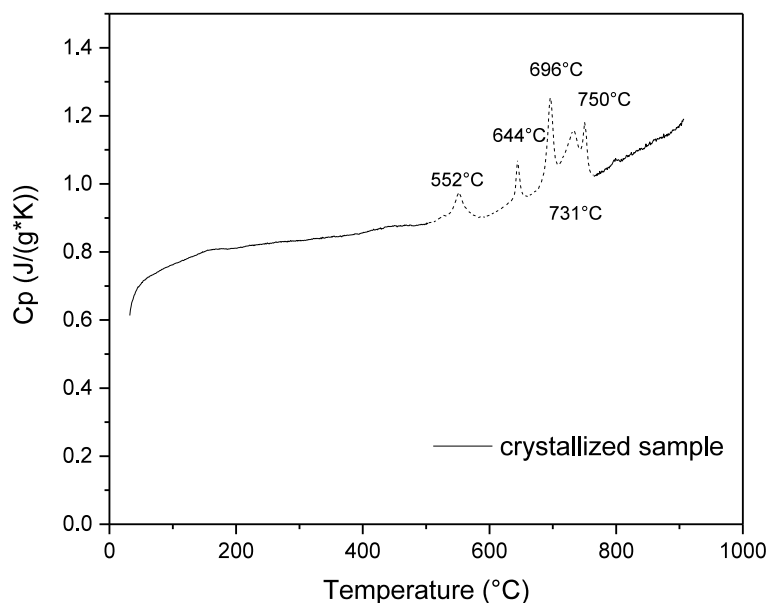


Figure 2-25: Heat capacity of the sample of medium lithium LAGP sample #5 (with  $x = 0.5$  in the general formula of  $\text{Li}_{1+x}\text{Al}_x\text{Ge}_{2-x}\text{P}_3\text{O}_{12}$ ), which was crystallized during the previous DSC measurements. The peaks on the curve represent the heat of reversible phase transitions. The temperatures shown on the curve are the positions of the peaks.

Figure 2-26 shows the DSC curves of the high lithium LAGP sample #8 (batch 4,  $x = 0.7$ ) measured for three times with a heating and cooling rate of 15K/min. The glass transition took place at 510°C – 534°C. The crystallization onset temperature was at 625°C. An exothermal peak appeared at 693°C on the first cooling curve.

No glass transition and crystallization peak was observed on the second and the third measurement. Endothermal peaks were observed on the heating curves at 648°C, 746°C and 792°C. Exothermal peaks were observed on the cooling curves at around 707°C. These peaks are significantly smaller compared to the crystallization peak.

Heat capacity of the high lithium LAGP was measured on the sample #1 batch 4, which was previously heat-treated at 800°C for 6 hours. The crystallized sample was measured in the DSC for 8 times. The median value of the last three measurements was taken as the result. Two peaks were visible at 644°C and 757°C. These peaks appeared repetitively in each measurement. The heat capacity of the sample increased with increasing temperature. At the temperature higher than 757°C, the heat capacity had a higher increasing rate.

The peaks on the heat capacity curves and on the DSC curve are at different temperatures (Figure 2-26 vs. Figure 2-27), which is because the heat capacity was measured on the sample which was heat-treated at 800°C for 6 hours. Due to the formation of the minor phase during heat-treatment, the composition of the LAGP main phase changed over time. The position of the peak changed therefore when the samples was heat-treated for a relatively long period (e.g. 6 hours).

## 2. Characterization of ceramic solid-state electrolytes

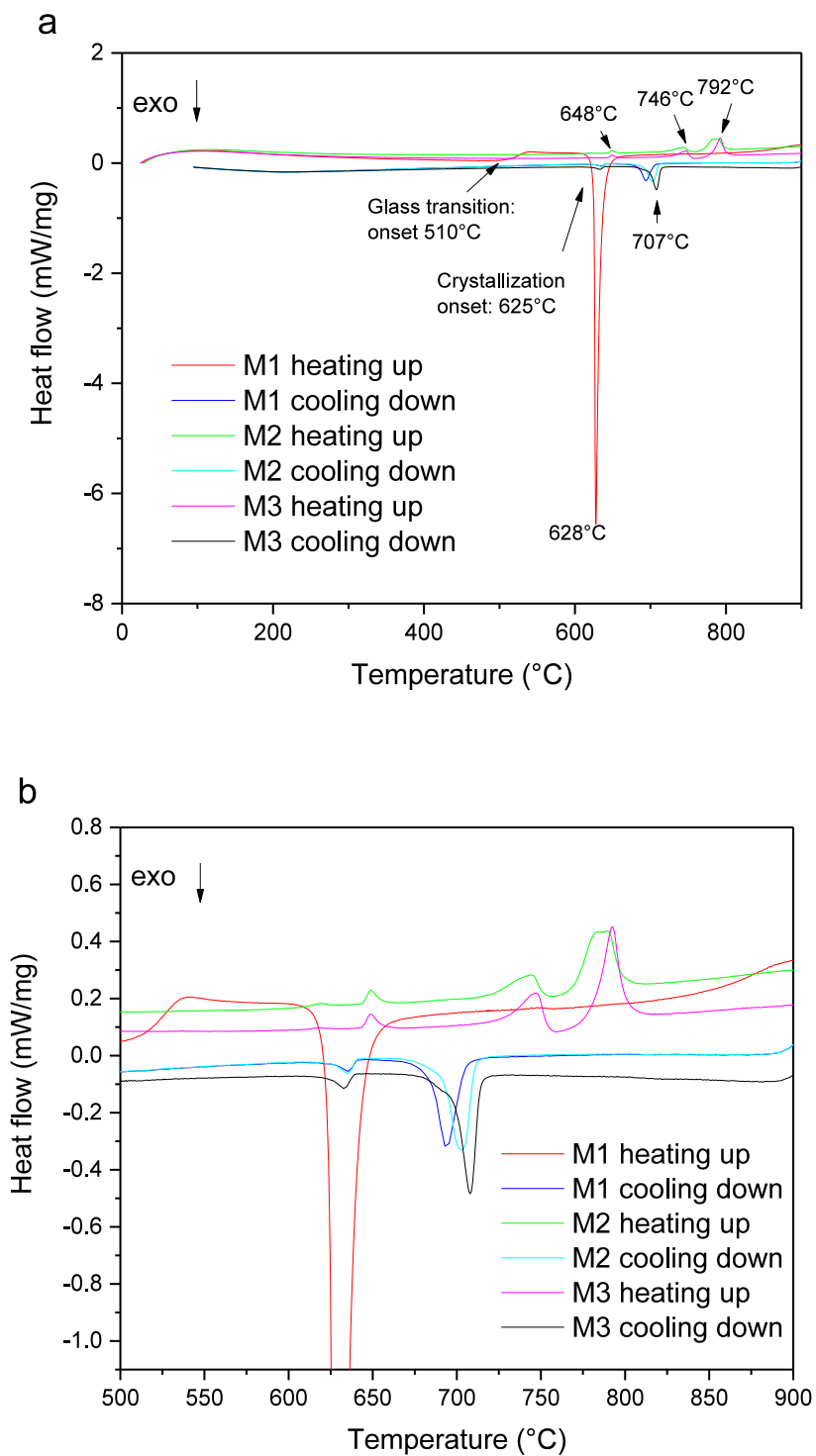


Figure 2-26: DSC curves of the high lithium LAGP sample #8 with  $x = 0.7$ . The sample was heated up to 900°C with the heating rate of 15K/min and cooled down back to room temperature for 3 times. M1, M2, M3: the first, second and third measurement, respectively. a: the full temperature range. B: the curves between 500°C and 900°C.

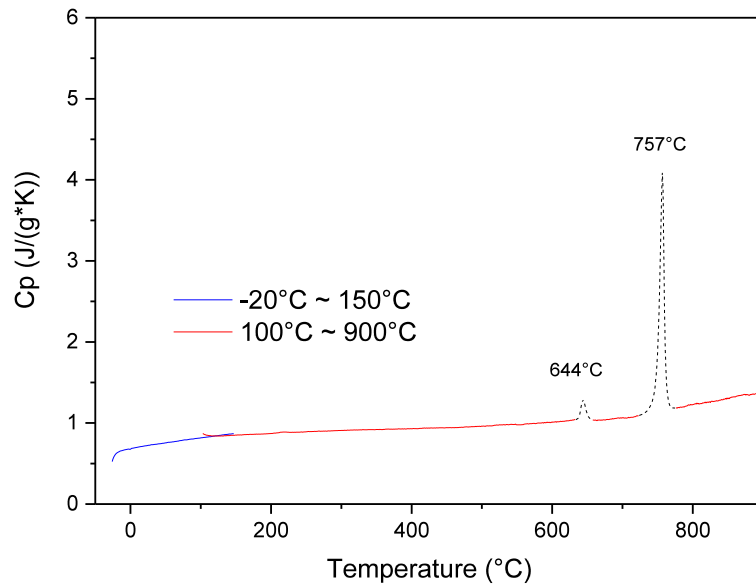


Figure 2-27: Heat capacity of the sample #1 of high lithium LAGP with  $x = 0.7$  which was heat-treated at  $800^{\circ}\text{C}$  for 6h. The peaks represent the heat of reversible phase transitions. The temperatures shown on the curve are the positions of the peaks.

### 2.3.1.2 Dilatometry

The relative length change of a low lithium LAGP sample #1 (batch 2,  $x = 0.3$ ) and the temperature vs. heat-treating time are shown in Figure 2-28. The heating and cooling rate is 5 K/min. The sample showed a thermal expansion up to  $480^{\circ}\text{C}$ . A rapid shrinkage occurred at  $520^{\circ}\text{C} - 616^{\circ}\text{C}$ . The sample had a shrinkage of 16.1% in 26 min. The shrinkage inverted at  $616^{\circ}\text{C}$  and the sample had a short expansion for 26 min from  $616^{\circ}\text{C}$  to  $753^{\circ}\text{C}$ , with a length change of 0.9%. The sample length reached a local maximum and decreased then slowly. At the end of the heat-treatment, the sample had an overall shrinkage of 19.8%.

The temperature range, at which the rapid shrinkage took place ( $520^{\circ}\text{C} - 616^{\circ}\text{C}$ ), is approximately the temperature range between the glass transition and the crystallization temperature ( $535^{\circ}\text{C} - 649^{\circ}\text{C}$ ). The bulk glass sample began to shrink at the glass transition temperature and stopped to shrink when the glass began to crystallize.

## 2. Characterization of ceramic solid-state electrolytes

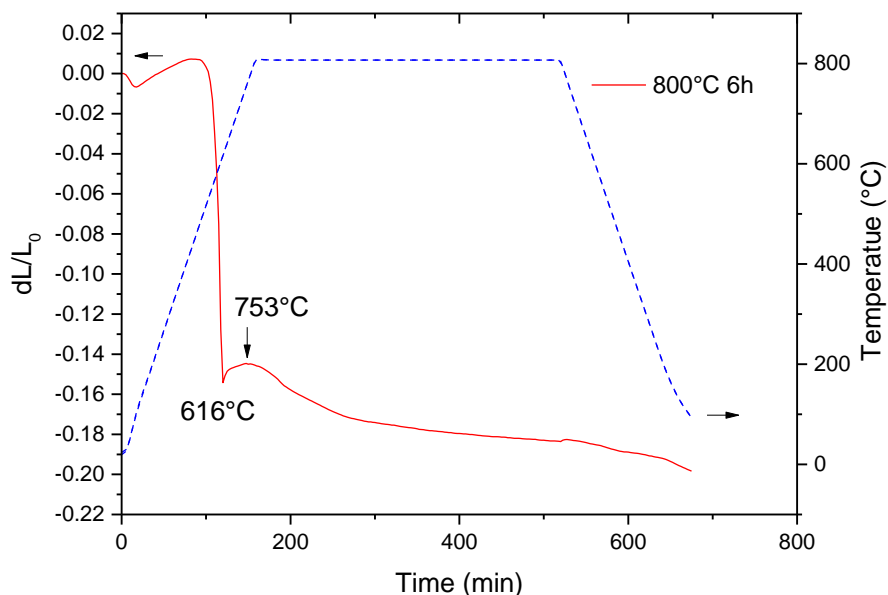


Figure 2-28: Dilatometer measurements of the sample #1 of low lithium LAGP (batch 2,  $x = 0.3$ ). The axis on the left presents the relative length changes of the sample. The solid lines show the length changes vs. time. The right axis presents the temperature in the dilatometer. The dashed lines show the temperature vs. time.

Figure 2-29 shows the dilatometry measurement of samples of high lithium LAGP (batch 4,  $x = 0.7$ ). The sample #1 was heat-treated at 800°C for 6 hours and the sample #2 was heat-treated in succession at 550°C, 630°C and 800°C for each 1 hour in dilatometer. The samples showed thermal expansion at the beginning of the measurement (below 430°C) and rapidly shrinkage at 520°C. The sample #1 had a shrinkage of 12% in 16 min. The shrinkage stopped at 599°C and the sample had then an expansion of 0.5% for 5 min before it shrank slowly further. The sample had a total shrinkage of 12.8% at the end of the dilatometry measurement.

The sample #2 was heated up to 550°C and held at that temperature for 1h. The shrinking rate became smaller when the temperature stopped to increase. The sample had another faster shrinkage when the temperature further rose. Similar to sample #1, the sample #2 had also short expansion for 2 min at 589°C.

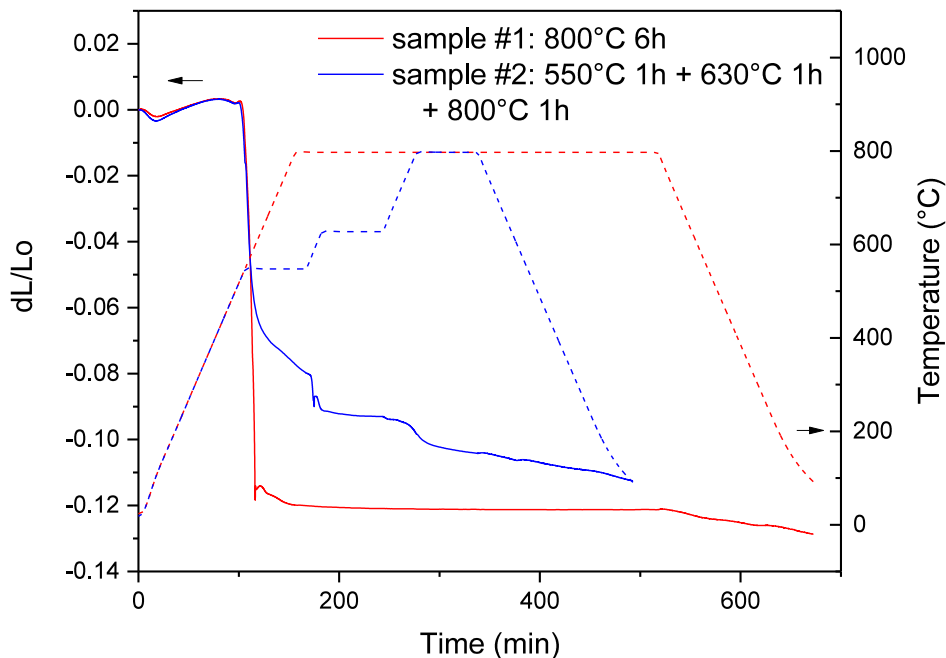


Figure 2-29: Dilatometer measurements of samples of high lithium LAGP batch 4 with  $x = 0.7$ . The axis on the left presents the relative length changes of the sample. The solid lines show the length changes vs. time. The right axis presents the temperature in the dilatometer. The dashed lines show the temperature vs. time.

### 2.3.1.3 XRD

The X-ray diffractograms of samples of different LAGP compositions (batch 2 sample #1, batch 3 sample #1 and batch 4 sample #3 with  $x = 0.3 - 0.7$ ) are shown in Figure 2-30. The most intensive peaks are attributed to the  $\text{LiGe}_2(\text{PO}_4)_3$  phase (PDF 01-080-1924). The peaks at  $20.8^\circ$  and  $26.1^\circ$  are from the  $\text{AlPO}_4$  phase (PDF 01-077-5502). Peaks of  $\text{GeO}_2$  phase are not observed.

The lattice parameters are calculated from the X-ray diffractogram using a least squares refinement and shown in Table 2-13. As the  $x$  value increases from 0.3 to 0.5, the lattice parameters and the cell volume decrease slightly. As the  $x$  increases from 0.5 to 0.7 however, the lattice parameters and the cell volume increase again. It shows that the lattice parameter of LAGP has a minimum when  $x = 0.5$ .

Different composition dependences of the lattice parameters have been reported in literature. It has been reported by Safanama et al. that the parameter  $c$  of LAGP lattice increases monotonously with increasing  $x$  value in  $\text{Li}_{1+x}\text{Al}_x\text{Ge}_{2-x}\text{P}_3\text{O}_{12}$  ( $0 < x < 0.5$ )<sup>103</sup>. Arbi et al. has reported that the parameter  $c$  of LAGP lattice increases monotonously with increasing  $x$  while the parameter  $a$  &  $b$  increases when  $x$  increases from 0 to 0.2 and decreases when  $x$  increases from 0.2 to 0.5<sup>83</sup>. Liu et al. has reported that the parameter  $a$  &  $b$  stay almost constant by varying  $x$  and parameter  $c$  increases with increasing  $x$  with the exception of  $x = 0.7$ <sup>104</sup>. The deviation between the reported values and the values in this work can be attributed to the strain of

## 2. Characterization of ceramic solid-state electrolytes

the lattice due to stress in the matrix, the difference of the sample composition and errors during the XRD measurements.

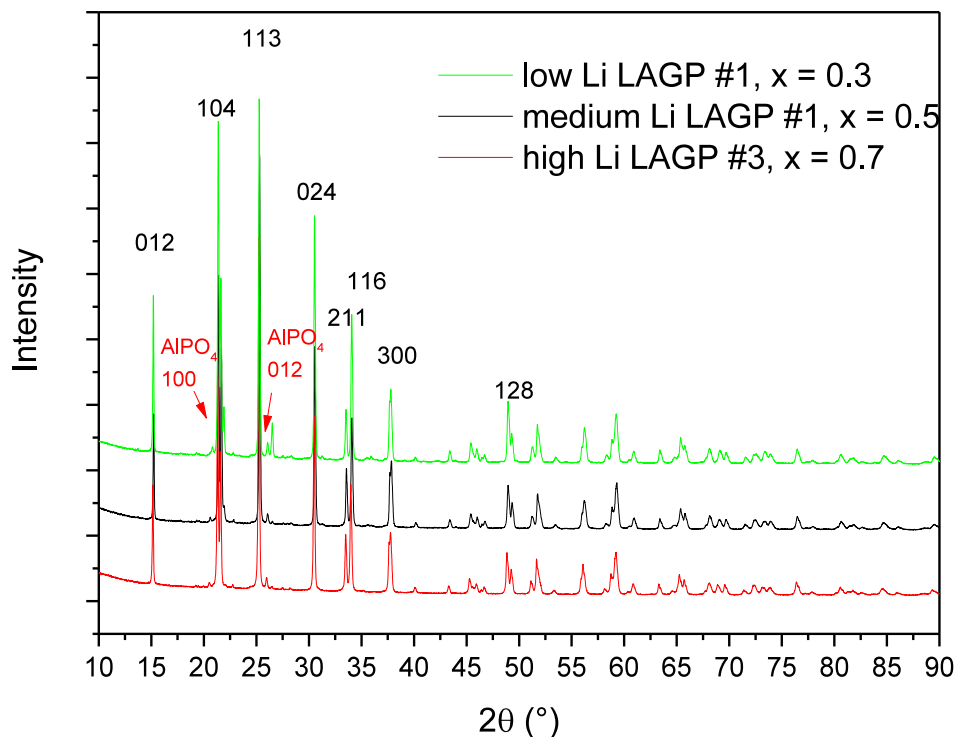
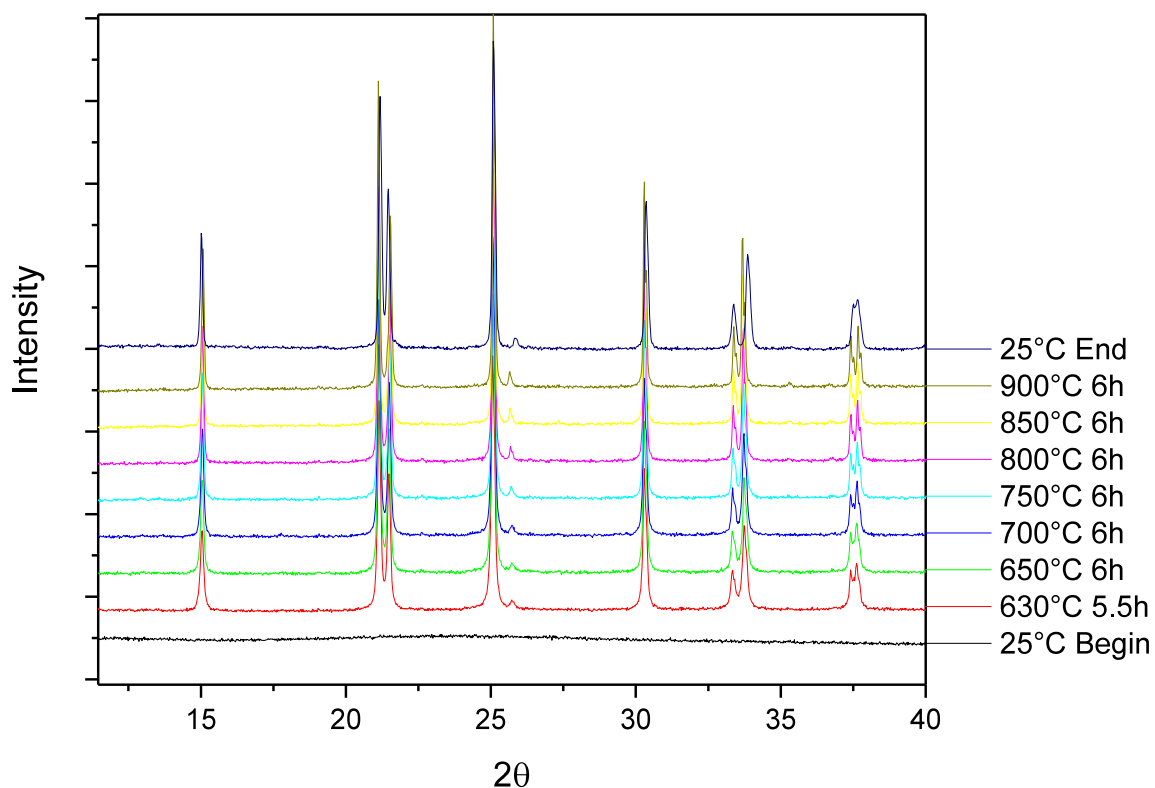


Figure 2-30: X-ray diffractogram of samples of LAGP with  $x = 0.3$  (batch 2, sample #1),  $x = 0.5$  (batch 3, sample #1) and  $x = 0.7$  (batch 4, sample #3), respectively. The black numbers index the diffractions of  $\text{LiGe}_2(\text{PO}_4)_3$  phase (PDF reference 01-080-1924). The reds arrows indicate the diffraction lines of  $\text{AlPO}_4$  phase (PDF 01-077-5502).

Table 2-13: Lattice parameters of the LAGP phases with different compositions.

	Low Li LAGP ( $x=0.3$ )	Medium Li LAGP ( $x=0.5$ )	High Li LAGP ( $x=0.7$ )
a	$8.230 \pm 0.001 \text{ \AA}$	$8.223 \pm 0.001 \text{ \AA}$	$8.240 \pm 0.001 \text{ \AA}$
b	$8.230 \pm 0.001 \text{ \AA}$	$8.223 \pm 0.001 \text{ \AA}$	$8.240 \pm 0.001 \text{ \AA}$
c	$20.497 \pm 0.004 \text{ \AA}$	$20.484 \pm 0.004 \text{ \AA}$	$20.570 \pm 0.004 \text{ \AA}$
$\alpha$	$90^\circ$	$90^\circ$	$90^\circ$
$\beta$	$90^\circ$	$90^\circ$	$90^\circ$
$\gamma$	$120^\circ$	$120^\circ$	$120^\circ$
volume	$1202.3 \pm 0.6 \text{ \AA}^3$	$1199.5 \pm 0.6 \text{ \AA}^3$	$1209.5 \pm 0.6 \text{ \AA}^3$

Hot stage XRD was applied to obtain the diffractograms at higher temperature up to 900°C. The results of the low Li LAGP sample #6 ( $x = 0.3$ ) are shown in Figure 2-31. The first diffractogram at 25°C showed no peak since the sample was in glassy state. The sample was then heated up to 630°C. Eleven diffractograms were taken at that temperature and each measurement took 30 min. The last diffractogram, which was taken after 5.5 hours at 630°C, is shown on Figure 2-31. Diffraction peaks appeared in the diagram, showing that the glass was crystallized. The diffraction peaks are attributed to  $\text{LiGe}_2(\text{PO}_4)_3$ . The sample was heated up further and held at 650°C, 700°C, 750°C, 800°C, 850°C and 900°C for each 6h. The diffractograms, which were taken after 6 hours at each temperature, are shown in Figure 2-31. At higher temperature, the diffraction peaks became sharper and higher. The position of the diffraction peaks shifted slightly due to thermal expansion.



*Figure 2-31: Hot stage X-ray diffractograms of the sample #6 of low lithium LAGP ( $x = 0.3$ , batch2) heat-treated at different temperatures.*

The lattice parameters of the LAGP were calculated from the hot stage XRD data obtained at different temperatures using a least squares refinement (Software name: UnitCell). Figure 2-32 shows the lattice parameters of the low Li LAGP at different temperatures. The parameter  $c$  increased with increasing temperature. The parameter  $a$  &  $b$  decreased with increasing temperature, showing that the  $a$  and  $b$  axis

## 2. Characterization of ceramic solid-state electrolytes

have a negative coefficient of thermal expansion. It was shown in the work of Alami et al. that the parameter  $a$  &  $b$  of the  $\text{LiGe}_2(\text{PO}_4)_3$  phase have a negative thermal expansion coefficient<sup>56</sup>, which matches the results of this work.

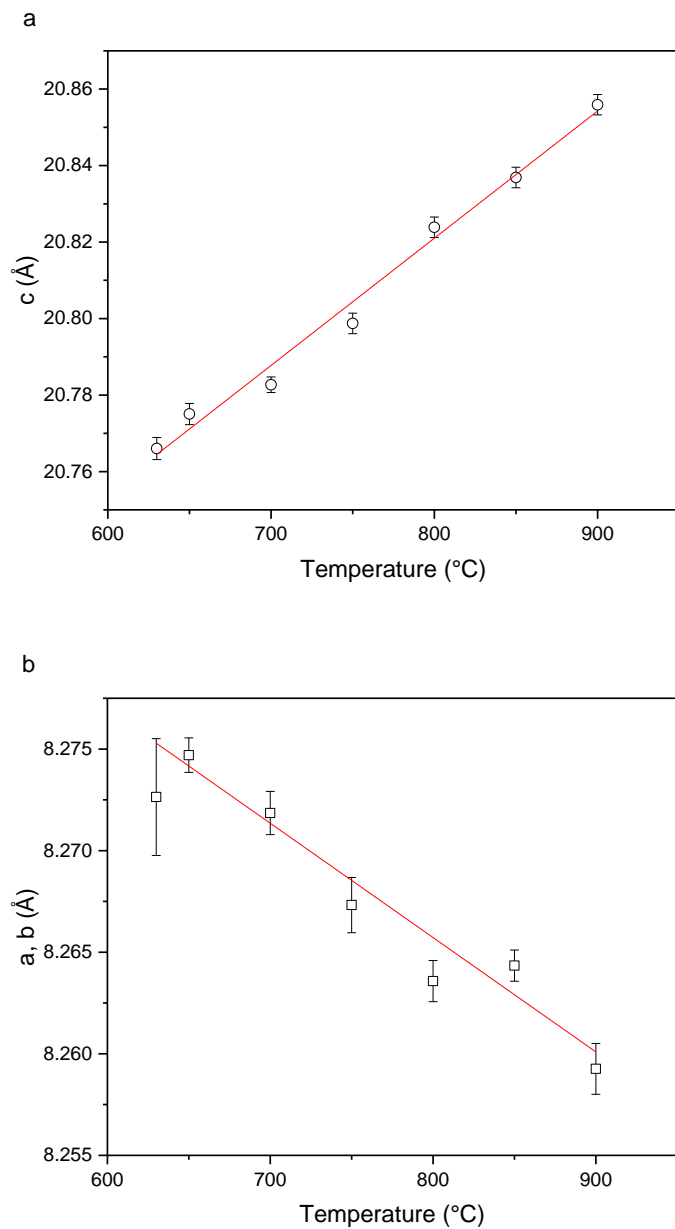


Figure 2-32: Lattice parameters of the low Li LAGP sample at different temperatures calculated from the hot stage XRD data. a: the parameter  $c$ , b: the parameter  $a$  &  $b$ .

Figure 2-33 shows the diffractograms obtained using hot stage XRD on the sample # 4 of medium lithium LAGP with  $x = 0.5$ . The sample was in glassy state at the beginning 25°C and crystallized at 630°C. The diffraction peaks matched that of the  $\text{LiGe}_2(\text{PO}_4)_3$  phase. In addition at 650°C, 700°C and 750°C, new peaks appeared at 13.2°, 18.0°, 22.8° and 29.4°. When the temperature further increased to 800°C, these peaks

of minor phase disappeared again, showing that a new phase appeared at 650°C and disappeared at 800°C. The peaks of LAGP main phase shifted due to thermal expansion/shrinkage. After the sample was cooled down from 900°C to 25°C, new peaks appeared at 20.7° and 21.9° belonging to the hexagonal  $\text{AlPO}_4$  phase (PDF 00-046-0253).

The lattice parameters of this LAGP sample was calculated from the hot stage XRD data obtained at different temperatures with help of the Rietveld refinement. The refinements were carried out on a single  $\text{LiGe}_2(\text{PO}_4)_3$  phase. Refined parameters are lattice parameters with a sample displacement error (because of the thermal displacement of the sample stage) and microstructure parameters (crystallite size, microstrain). The lattice parameter values are the average value of the multiple measurements at the same temperature. The uncertainty of the parameters are calculated from the deviation of the measurements. Figure 2-34 shows the lattice parameters of the medium Li LAGP at different temperatures. Same as the low Li LAGP sample, the parameter  $c$  increased with increasing temperature and the parameter  $a$  &  $b$  decreased with increasing temperature.

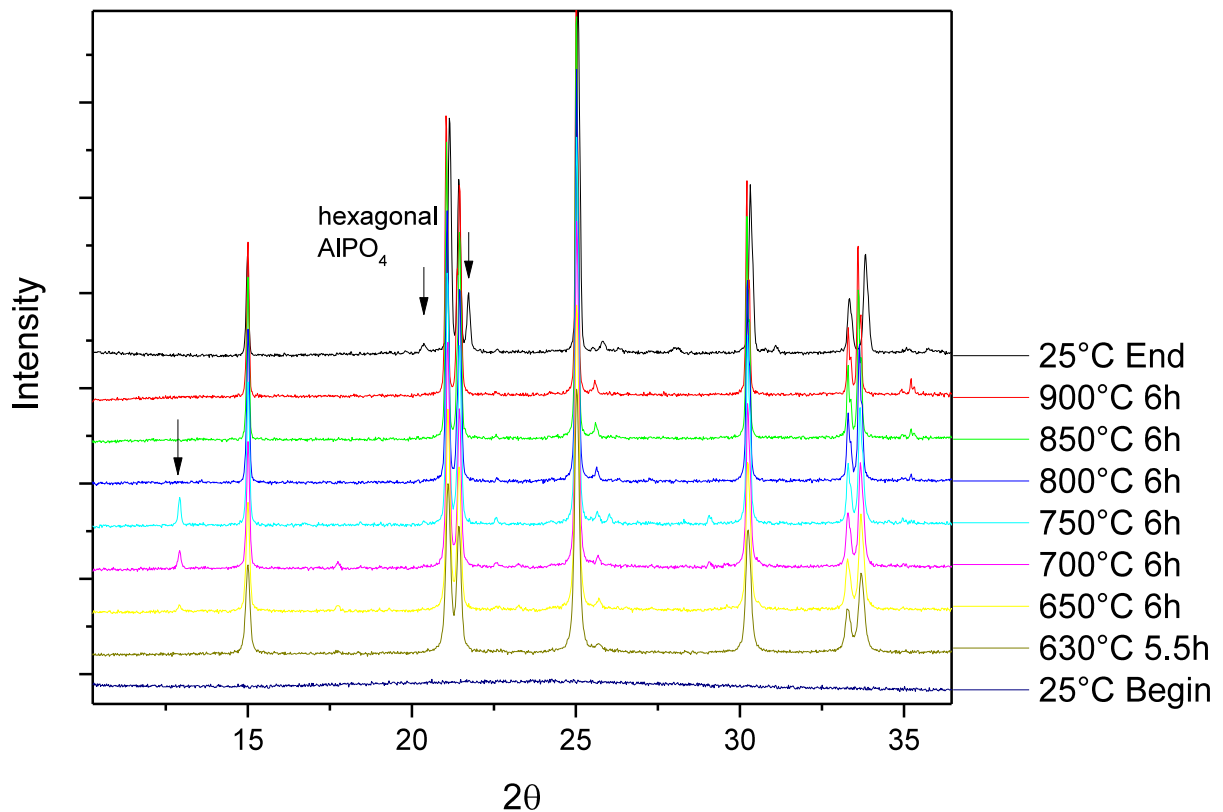


Figure 2-33: Hot stage X-ray diffractograms of the sample #4 of medium lithium LAGP (batch 3,  $x = 0.5$ ) heat-treated at different temperatures.

## 2. Characterization of ceramic solid-state electrolytes

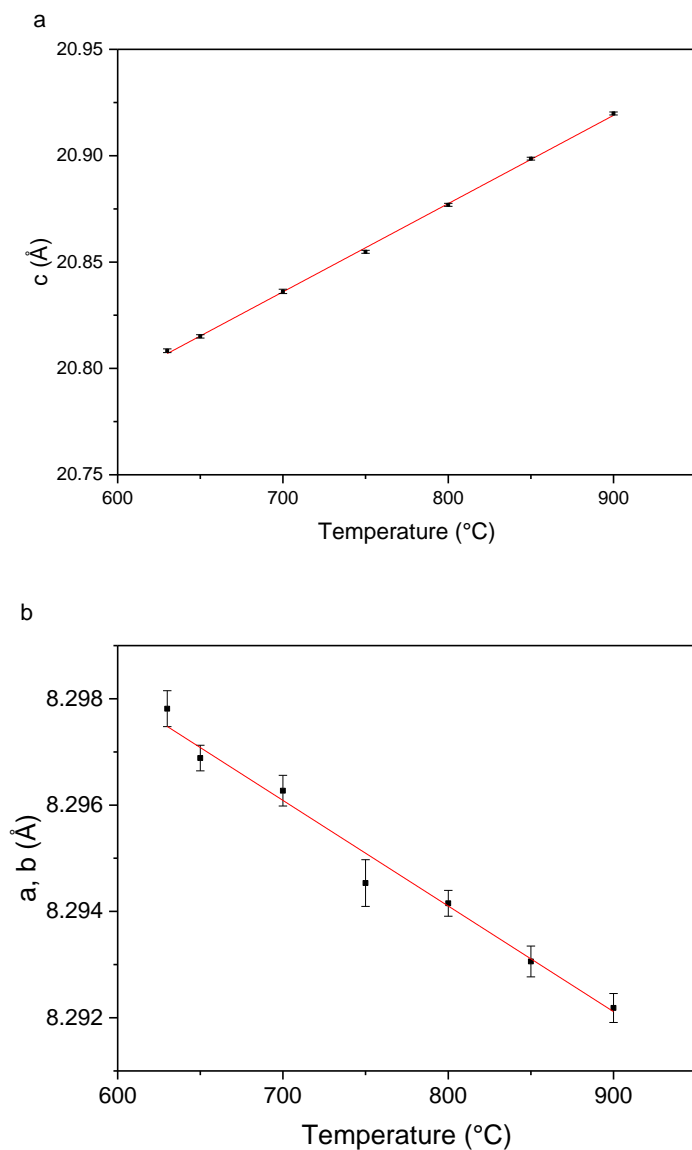


Figure 2-34: Lattice parameters of the medium Li LAGP at different temperatures calculated from the hot stage XRD data. a: the parameter c, b: the parameter a & b.

The diffractograms of the sample #6 of high lithium LAGP batch 4 with  $x = 0.7$  obtained at different temperatures are shown in Figure 2-35. The position of the diffraction peaks also matched the  $\text{LiGe}_2(\text{PO}_4)_3$  phase. Same as the medium lithium LAGP ( $x = 0.5$ ), new diffraction peaks appeared at  $13.1^\circ$ ,  $22.6^\circ$  and  $29.4^\circ$  at  $650^\circ\text{C}$ ,  $700^\circ\text{C}$  and  $750^\circ\text{C}$ . These peaks disappeared as the temperature further increased to  $800^\circ\text{C}$ . As the sample was cooled back to  $25^\circ\text{C}$ , new peaks appeared at  $20.6^\circ$  and  $21.8^\circ$ , which belong to the hexagonal  $\text{AlPO}_4$  phase (PDF 00-046-0253).

The lattice parameters of this LAGP sample was calculated from the hot stage XRD data obtained at different temperatures with help of the Rietveld refinement. Figure 2-36 shows the lattice parameters at different temperatures. The parameter c increased with increasing temperature in the whole temperature

range. Different as the samples of low Li and medium Li LAGP, the parameter a & b of the high Li LAGP samples showed an abrupt increase and deviation from the linearity as the temperature increased to 800°C. The lattice parameter decreased again at 850°C.

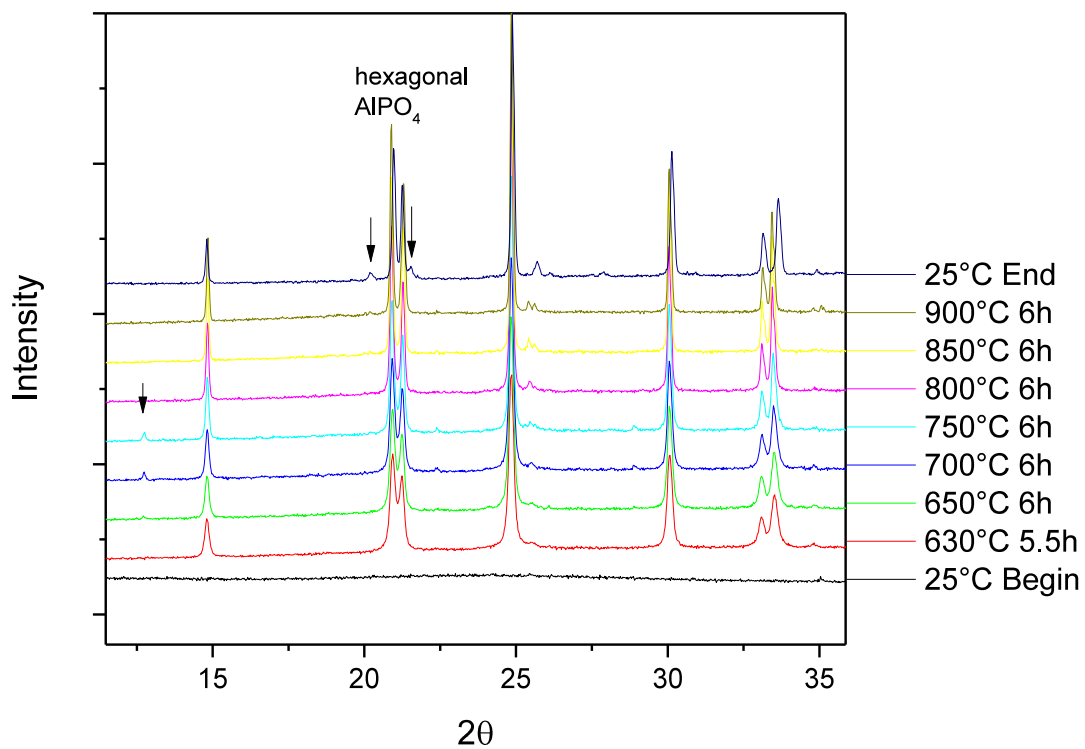


Figure 2-35: Hot stage X-ray diffractograms of the sample #6 of the high Li LAGP (batch 4, x = 0.7) heat-treated at different temperatures.

## 2. Characterization of ceramic solid-state electrolytes

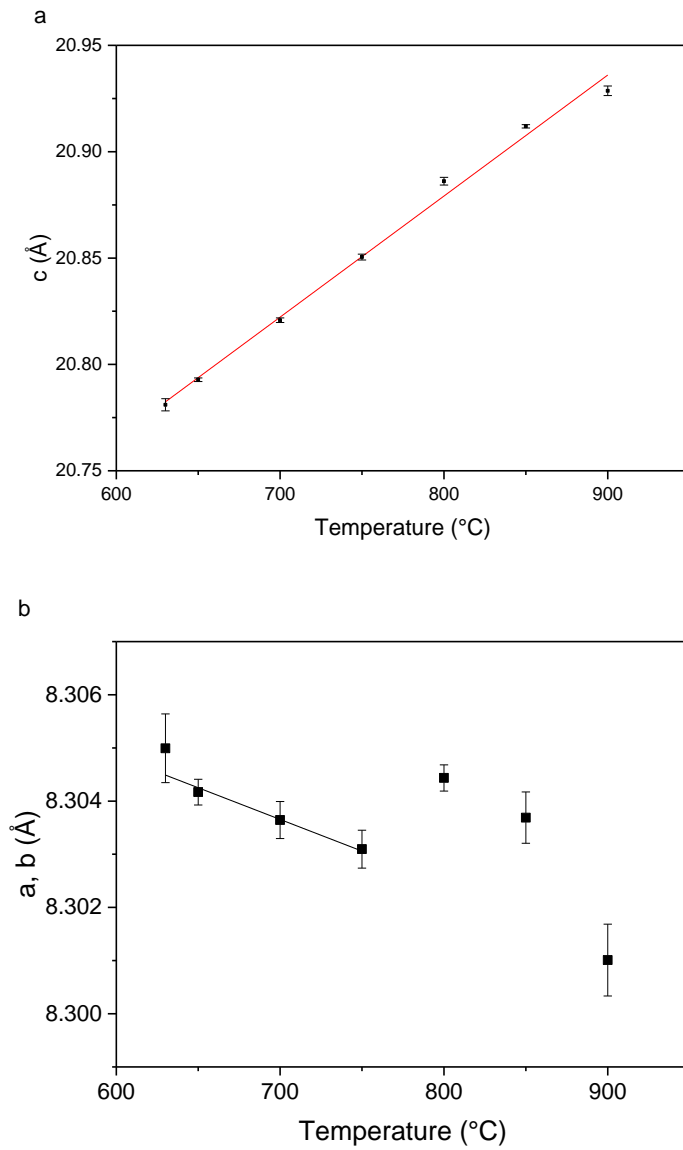


Figure 2-36: Lattice parameters at different temperatures calculated from the hot stage XRD data. a: the parameter  $c$ , b: the parameter  $a$  &  $b$ .

### 2.3.1.4 Ionic conductivity

The ionic conductivity of the samples of the low lithium LAGP (batch2,  $x = 0.3$ ) are shown in Figure 2-37. The ionic conductivity of the glass sample #5 was far below the value of the heat-treated samples. The ionic conductivity of the glass was not measurable for the temperature below 150°C. The sample #2, which was heat-treated at 660°C for 3 hours, has at room temperature the ionic conductivity of  $4.8 \cdot 10^{-6}$  S/cm, which is higher than the conductivity of the glass sample at 250°C.

The samples, which were heat-treated at 800°C, had significant higher ionic conductivity than the sample, which was heat-treated at 660°C, although all of them were crystallized. The conductivity increased gradually as the length of heat-treatment increased at 800°C. The sample, which was heat-treated at 800°C for 3+6 hours, has reached  $1.2 \cdot 10^{-4}$  S/cm at 27°C,  $4.8 \cdot 10^{-3}$  S/cm at 150°C and  $1.1 \cdot 10^{-2}$  S/cm at 202°C. The best conductivity value of the low lithium LAGP was in the same order of magnitude as the sintered LAGP samples.

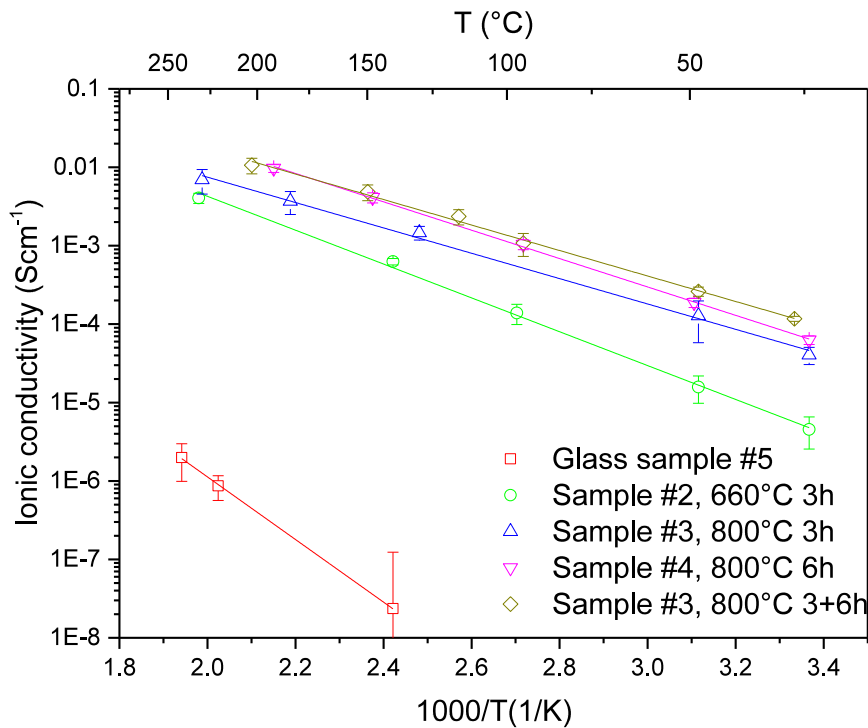


Figure 2-37: Ionic conductivity of the samples of the low lithium LAGP (batch 2,  $x = 0.3$  in  $Li_{1-x}Al_xGe_{2-x}P_3O_{12}$ ). The heat-treating temperature and time are labeled by each sample. The numerical values of the ionic conductivity are shown in the appendix Table A-8 – Table A-11.

Samples of the medium lithium LAGP (batch 3,  $x = 0.5$ ) were fabricated via the heat-treating route and the sintering route. Their ionic conductivities are shown in Figure 2-38. The sample #1, which was heat-treated at 800°C for 6 hours, had an ionic conductivity of  $1.7 \cdot 10^{-4}$  S/cm at room temperature and  $7.4 \cdot 10^{-3}$  S/cm at 150°C, which is significantly higher than the sample #2, which was heat-treated at 550°C for 10 min and then at 650°C for 2 hours. The sample #3, which was prepared via the sintering route (sintered at 800°C for 6 hours), showed also lower conductivity.

## 2. Characterization of ceramic solid-state electrolytes

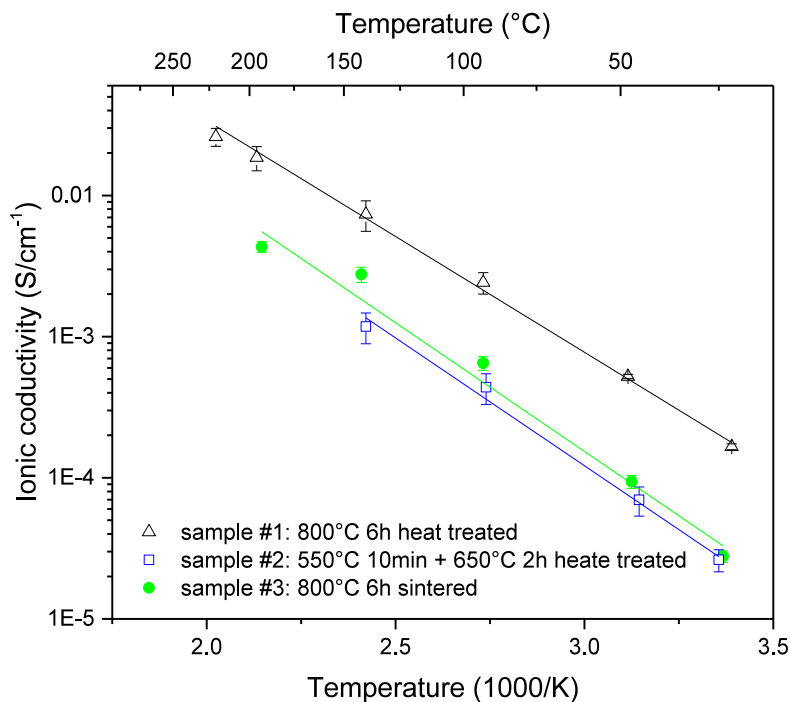


Figure 2-38: Ionic conductivity of the samples of the medium lithium LAGP batch 3 with  $x = 0.5$ . The numerical values of the ionic conductivity are shown in the appendix Table A- 12 – Table A- 14.

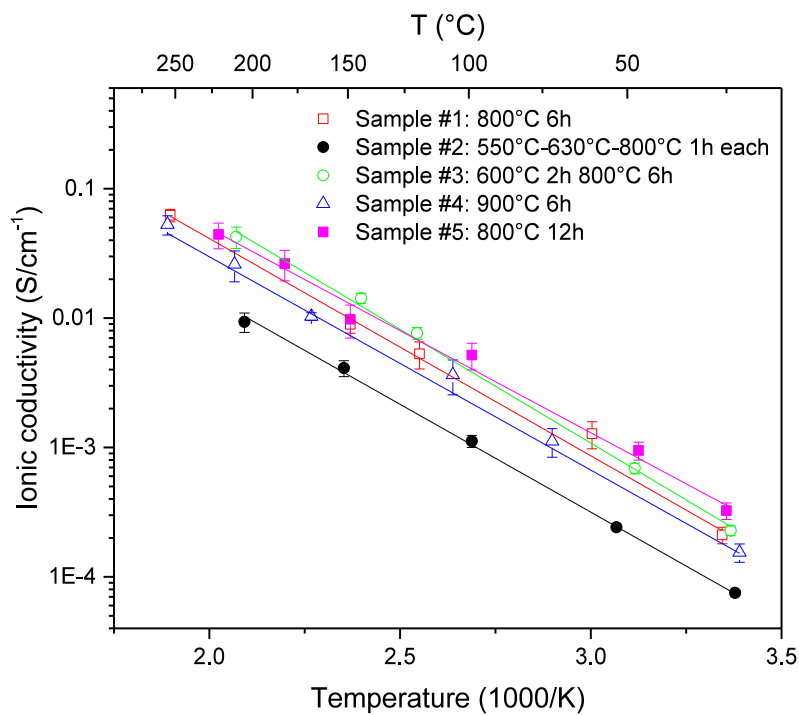


Figure 2-39: Ionic conductivity of the samples of the high lithium LAGP batch 4 with  $x = 0.7$ . The numerical values of the ionic conductivity are shown in the appendix Table A- 15 – Table A- 19.

The ionic conductivities of the samples of the high lithium LAGP (batch 4,  $x = 0.7$ ) are shown in Figure 2-39. The sample #2, which was heat-treated in succession at 550°C, 630°C and 800°C for each 1h showed lower ionic conductivity. The conductivity increased significantly as the sample was heat-treated at 800°C for 6 hours (sample #1,  $2.1 \cdot 10^{-4}$  S/cm at room temperature and  $9.0 \cdot 10^{-3}$  S/cm at 150°C). The sample #3, which was heat-treated in two steps (600°C for 2h and 800°C for 6h) has a slightly higher conductivity as the sample #1. The conductivity increased further when the heat-treating time at 800°C increased to 12 h (sample #5). However, the ionic conductivity decreased as the heat-treating temperature increased to 900°C (sample #4).

#### 2.3.1.5 Scanning electron microscopy

The SEM images of the low lithium LAGP samples (batch 2,  $x = 0.3$ ) heat-treated with different process parameters are shown in Figure 2-40 - Figure 2-42.

The polished surface of the sample #2, which was heat-treated at 660°C for 3 hours, showed bright areas formed by small pores (Figure 2-40-a). The fracture surface of this sample is shown in Figure 2-40-b. The grains had an average size of 0.3  $\mu\text{m}$  (estimated using the intercept method). The pores in the matrix were also visible on the fracture surface. Since there were no pores initially in the glass, the pores were formed during the heat-treatment. Due to the amorphous atom arrangement, the glass had a lower density compared with crystallized material. The volume of the LAGP shrank by crystallization and pores were formed therefore in the samples. At the temperature lower than 800°C, the porosity was not eliminated in the heat-treating process. The samples heat-treated at lower temperature had therefore less good contact between grains and lower ionic conductivity.

The polished surface of the sample, which was heat-treated at 800°C for 3 hours, is shown in Figure 2-41. Small pores were visible with a size of 2 – 5  $\mu\text{m}$ . The bright areas formed by small pores became smaller, indicating that the amount of pores was much smaller than in the sample #2 (Figure 2-41-a vs Figure 2-40-a). The pores are inhomogeneously distributed (Figure 2-41-b). An  $\text{AlPO}_4$  minor phase was visible in the LAGP matrix (Figure 2-41-c and -d).

Figure 2-42 shows the fracture surface of the sample #4 of low lithium LAGP, which was heat-treated at 800°C for 6 hours. The grains had the similar size as in the sample #2, which was heat-treated at 660°C. On the other hand, significantly less pores could be seen on the sample which was heat-treated at 800°C. The grains had better contact with each other, which resulted in a higher ionic conductivity.

## 2. Characterization of ceramic solid-state electrolytes

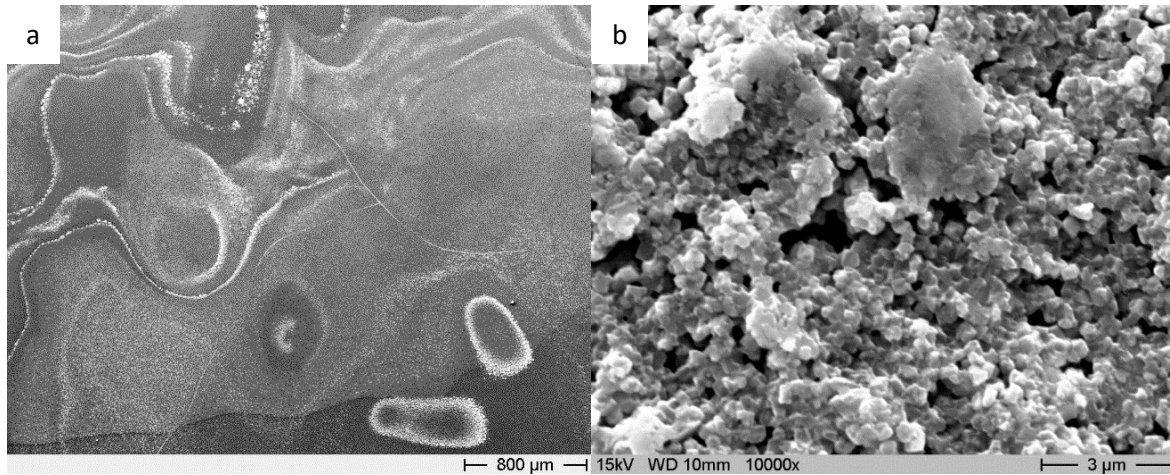


Figure 2-40: SEM images of the sample #2 of low lithium LAGP, which was heat-treated at 660°C for 3 hours. a: the polished surface of the sample(35x magnification); The bright textures are formed by small pores. b: the fracture surface of the sample (10000x magnification).

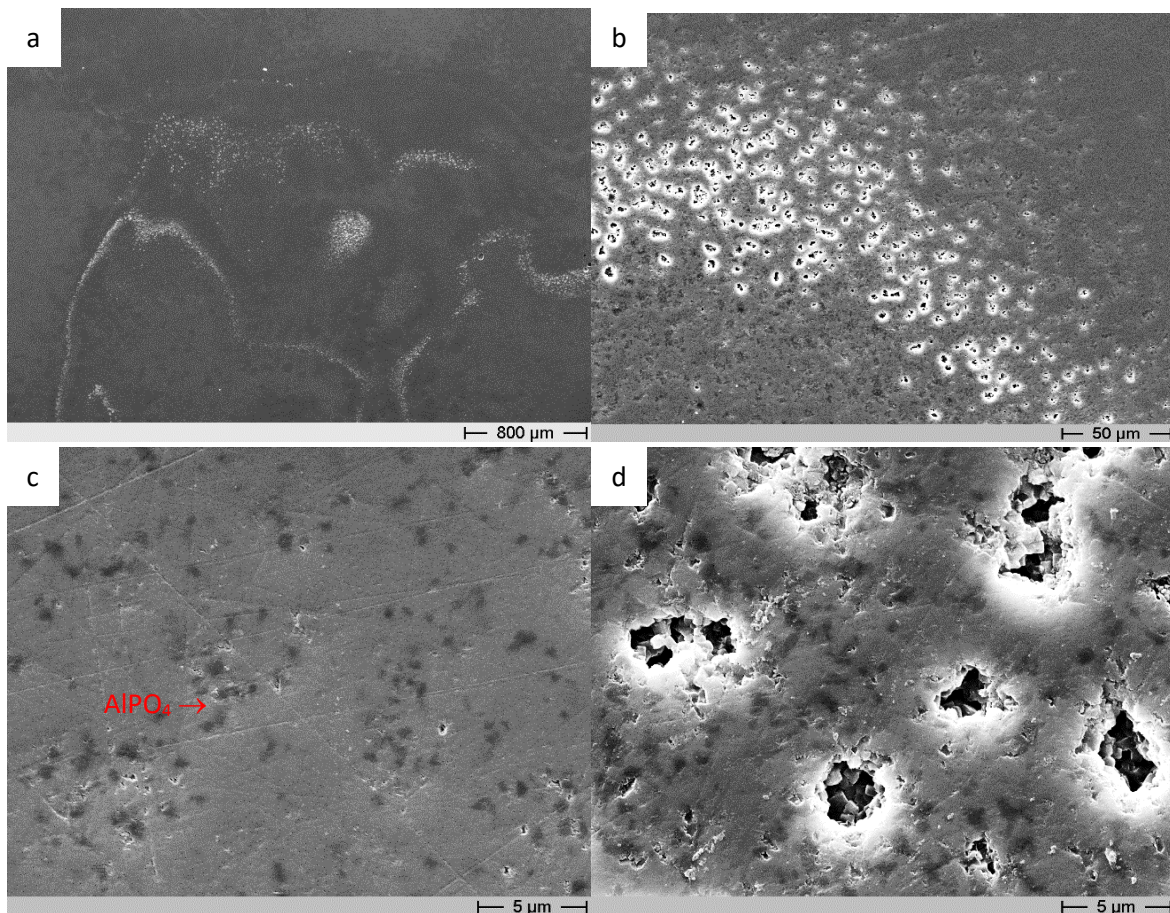
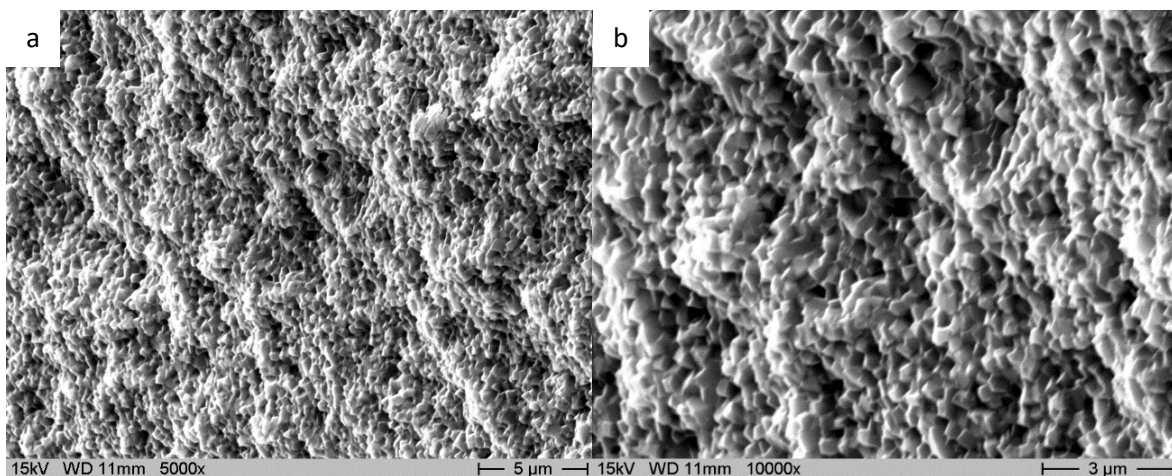


Figure 2-41: SEM images of the polished surface of the sample #3 of low lithium LAGP, which was heat-treated at 800°C for 3 hours. a: 35x magnification; b: 500x magnification. The bright area is formed by higher density of small pores; c: area without pores, 5000x magnification; d: area with pores, 5000x magnification.



*Figure 2-42: SEM images of the fracture surface of the sample #4 of low lithium LAGP, which was heat-treated at 800°C for 6 hours. a: 5000x magnification; b: 10000x magnification.*

The polished surface and the fracture surface of samples of medium lithium LAGP (batch 3,  $x = 0.5$ ) are shown on Figure 2-43 - Figure 2-45.

The sample #1 prepared by heat-treating at 800°C for 6 hours showed stripe-like areas of pores on its surface (Figure 2-43-a). The pores had a size of 2 - 10  $\mu\text{m}$ . There were areas with almost no porosity between the stripes. The  $\text{AlPO}_4$  minor phase could be seen in the matrix (Figure 2-43-b). Figure 2-44-d shows the fracture surface, where the pores are also visible.

The polished surface and fracture surface of the sample #2, which was heat-treated at 550°C for 10 min and 650°C for 2 hours, are shown in Figure 2-44. Gaps between grains were visible on the sample surface. The contact between the LAGP grains were weak compared to the sample heat-treated at 800°C, which resulted in the lower ionic conductivity of this sample.

The sample #3 was prepared via sintering route using the powder of the medium Li LAGP (batch 3). The fracture surface of this sample is shown in Figure 2-45. The fracture surface was full of pores. Unlike the irregular pores in the heat-treated samples, the pores here were spherical with a size of 5 - 10  $\mu\text{m}$ , indicating that the pores were inflated by a gas.

Among the samples of the medium lithium LAGP, the sample heat-treated at 800°C showed higher conductivity (Figure 2-38), which is attributed to the lower porosity and better contact between grains. The  $\text{AlPO}_4$  phase filled the porosity between the LAGP grains and hence improved the ionic conductivity. The  $\text{AlPO}_4$  minor phase is therefore not always a negative factor in terms of ionic conductivity of the ceramic LAGP samples, although it is not a good ionic conductor.

## 2. Characterization of ceramic solid-state electrolytes

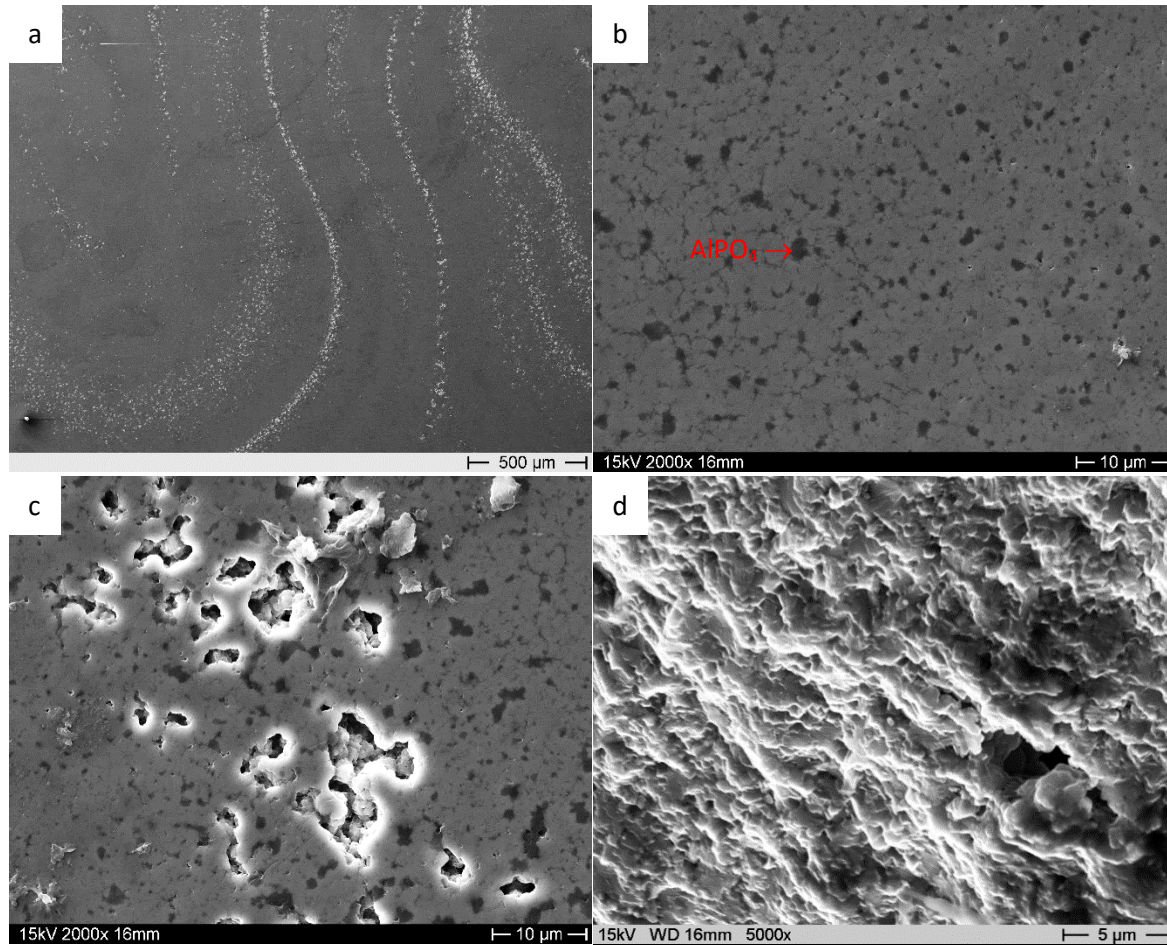


Figure 2-43: SEM images of the sample #1 of medium lithium LAGP (batch3,  $x = 0.5$ ), which was heat-treated at 800°C for 6 hours. a, b and c: the polished surface with 50x, 2000x and 2000x magnification, respectively; d: the fracture surface with 5000x magnification.

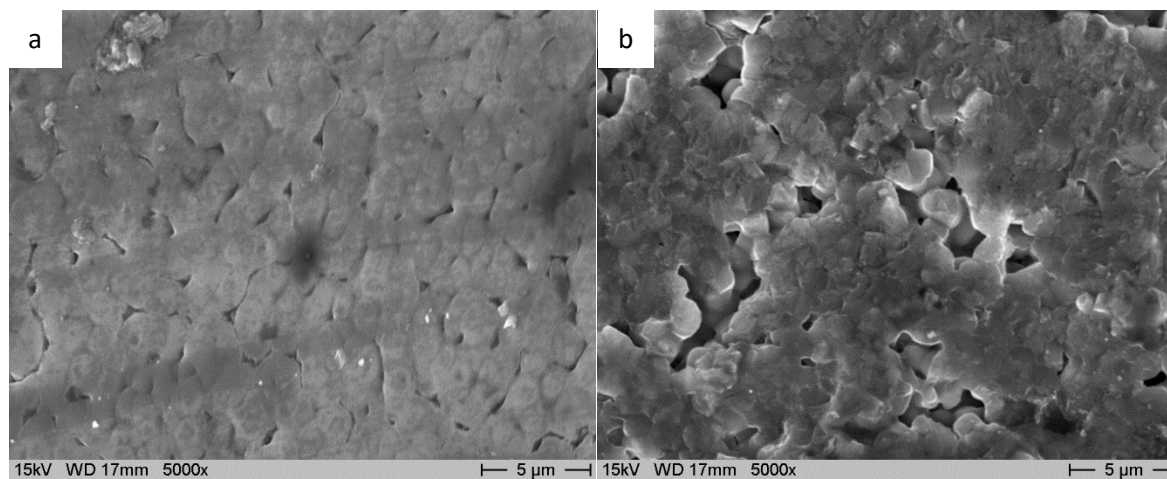
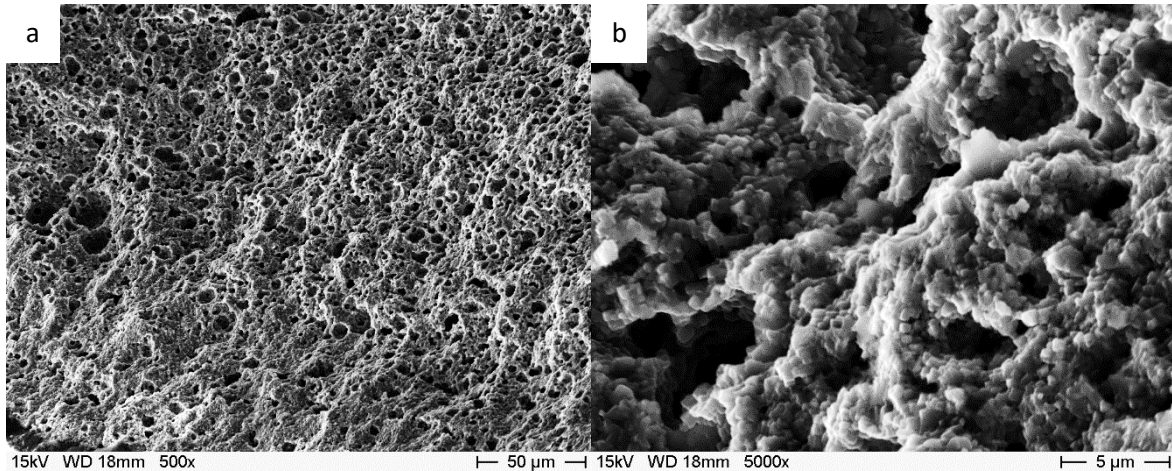


Figure 2-44: SEM images of the sample #2 of medium lithium LAGP (batch 3,  $x = 0.5$ ), which was heat-treated at 550°C for 10 min and 650°C for 2 hours. a: the polished surface (2000x); b: the fracture surface (2000x).



*Figure 2-45: SEM images of the sample #3 of medium lithium LAGP ( $x = 0.5$ ), which was sintered from powder at 800°C for 6 hours. a: 500x magnification; b: 5000x magnification.*

The SEM images of the heat-treated samples of the high lithium LAGP (batch 4,  $x = 0.7$ ) are shown in Figure 2-46 - Figure 2-48.

Figure 2-46 shows the sample #1 heat-treated at 800°C for 6h. Large grains in the matrix with a size of 4 – 10  $\mu\text{m}$  and smaller grains with a size of 0.3  $\mu\text{m}$  were visible. Small amount of  $\text{AlPO}_4$  phase was observed on the polished surface. Pores with a size of 5 – 10  $\mu\text{m}$  were observed, which were inhomogeneously distributed.

SEM images of the sample #1, which was heat-treated at 800°C for 6h and then heated up to 900°C for 8 times in DSC device, are shown in Figure 2-47. Larger pores with a size of 15 – 25  $\mu\text{m}$  are visible on this sample, which are 2 – 3 times larger than in the sample heat-treated at 800°C. Larger amount of  $\text{AlPO}_4$  phase was formed in the matrix with larger size (up to 4  $\mu\text{m}$ ). Table 2-14 shows the elemental composition of the matrix and the minor phase measured by EDX. The minor phase was richer on Al and its composition (Al : P : O  $\approx$  1 : 1 : 5) matched approximately the  $\text{AlPO}_4$ .

Figure 2-48 shows the polished surface of the sample #2, which was heat-treated in succession at 550°C, 630°C and 800°C for each 1h. This sample had also larger porosity compared to the sample, which was heat-treated at 800°C for 6 h.

## 2. Characterization of ceramic solid-state electrolytes

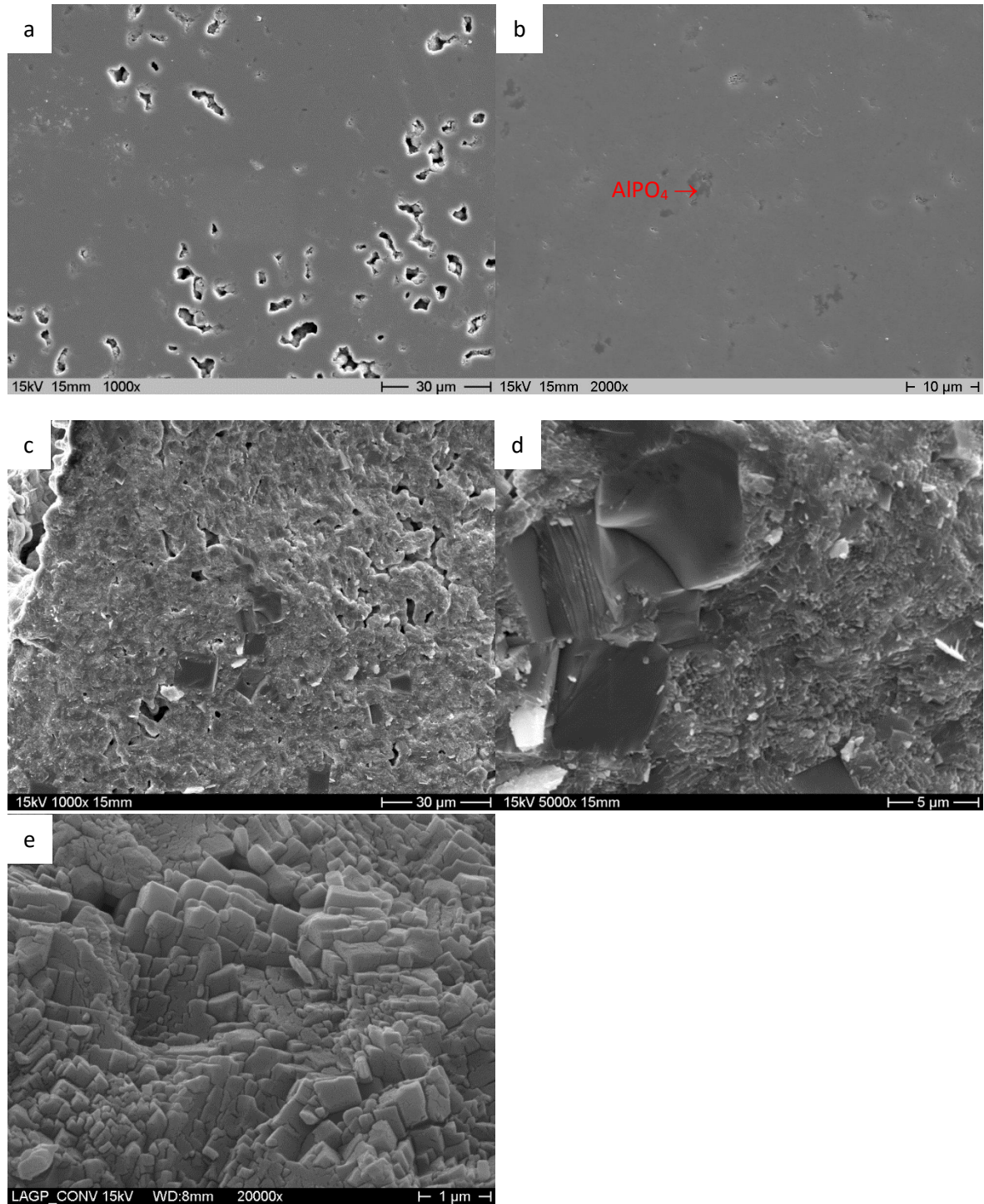


Figure 2-46: Polished surface (a: 1000x magnification and b: 2000x magnification) and fracture surface (c: 1000x magnification, d: 5000x magnification and e: 20000x magnification) of the sample #1 of high lithium LAGP (batch 4,  $x = 0.7$ ), which was heat-treated at 800°C for 6h.

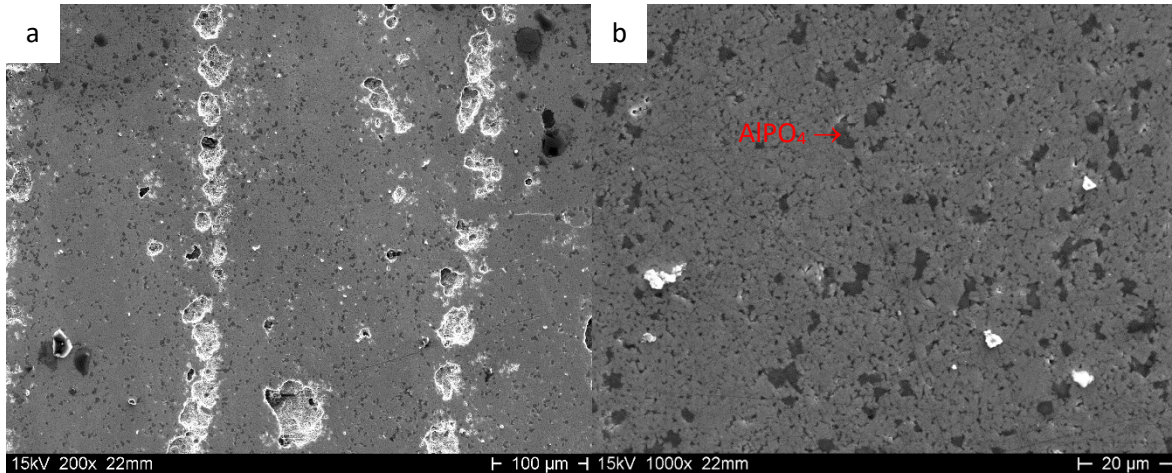


Figure 2-47: Polished surface of the sample #1 of high Li LAGP batch 4, which was heat-treated at 800°C in succession for 6h (Figure 2-46) and then heated up to 900°C for 8 times in DSC device. a: 200x magnification; b: 1000x magnification.

Table 2-14: The composition of the matrix and the dark minor phase of the sample shown in Figure 2-47-b measured with EDX.

Atom % of the element	Matrix	Dark phase
O	74.5%	72.0%
Al	1.4%	12.4%
P	15.4%	15.0%
Ge	8.6%	0.6%

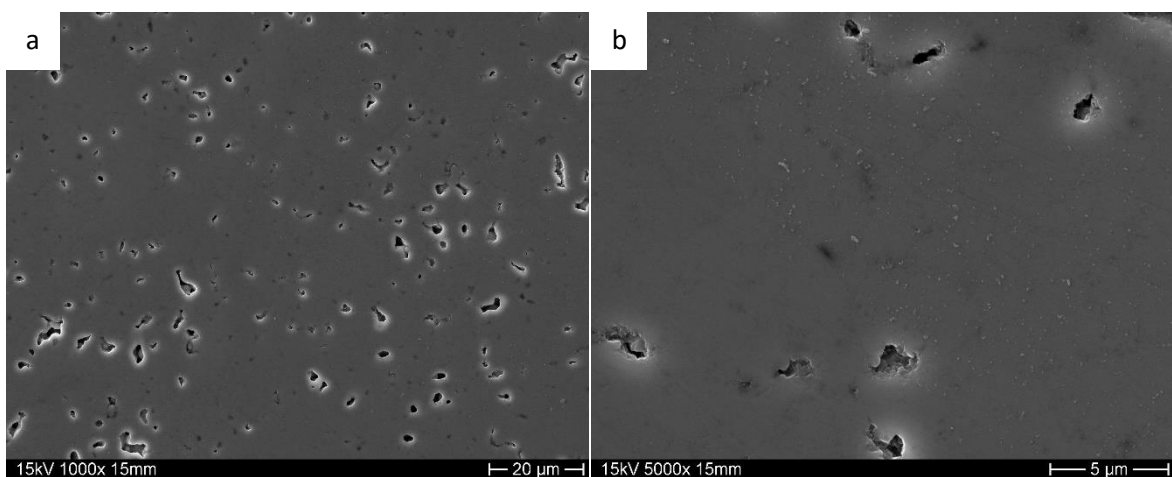


Figure 2-48: Polished surface of the sample #2 of high Li LAGP batch 4, which was heat-treated at 550°C, 630°C and 800°C in succession for each 1h. a: 1000x magnification; b: 5000x magnification.

## 2. Characterization of ceramic solid-state electrolytes

As shown on the SEM images of the high lithium LAGP samples #1 and #2, as the heat-treating temperature and heat-treating time increased, the number of the pores decreased but the size of the pores increased. Considering the ionic conductivity of these samples, it is shown that the decreased number of pores had a positive effect on the ionic conductivity. On the other hand, a larger amount of minor phases was observed in the sample heat-treated up to 900°C, which reduced the conductivity.

As shown on the SEM images, the  $\text{AlPO}_4$  minor phase was formed when the samples were heat-treated at over 800°C (Figure 2-41, Figure 2-43 and Figure 2-47). Unlike the samples of high lithium LAGP batch 1 prepared via sintering route, the  $\text{GeO}_2$  phase was not observed in the samples prepared via heat-treating route. The amount of the  $\text{AlPO}_4$  in the heat-treated samples was smaller at the same time. It indicates that the minor phase formation is enhanced in the sintering route: By grinding the LAGP bulk glass into powder, a larger surface area is created, which is favorable for precipitation of minor phases.

### 2.3.1.6 Density

The densities of the samples were measured with the Archimedes method without Zapon lacquer (see 2.1.5). The theoretical density of the LAGP crystal is calculated from lattice parameters measured by XRD (Table 2-15). The density and the relative density (density/theoretical density) of the samples are shown in Table 2-16. The uncertainty of the density was estimated to be around 0.4%.

The LAGP glass samples had a relative density of around 88%. After crystallization, the density reached more than 90%. The density increased further as the heat-treatment temperature was increased to 800°C and as the heat-treating time increased. However, when the heat-treating temperature was increased to 900°C, the density of the sample decreased again. That was due to the formation of larger pores in the LAGP samples (Figure 2-47-a), which might be related to the decomposition of minor phases and the gas release inside the samples (see 2.2.2 and).

Compared to the sample fabricated through the sintering route, the samples prepared through heat-treatment are significantly denser.

*Table 2-15: Theoretical density of the LAGP crystal of different composition calculated from lattice parameters measured by the XRD.*

	Low Li LAGP batch 2 ( $x = 0.3$ )	Medium Li LAGP batch 3 ( $x = 0.5$ )	High Li LAGP batch 4 ( $x = 0.7$ )
theoretical density	3.472 g/cm <sup>3</sup>	3.470 g/cm <sup>3</sup>	3.360 g/cm <sup>3</sup>

Table 2-16: Density and relative density of the LAGP samples from different batches of LAGP with  $x = 0.3$ ,  $0.5$  and  $0.7$  in the general formula of  $\text{Li}_{1+x}\text{Al}_x\text{Ge}_{2-x}\text{P}_3\text{O}_{12}$ .

Sample	Density $\rho$ (g/cm <sup>3</sup> )	Relative density $\rho/\rho_{\text{theo}}$
Low lithium LAGP $x = 0.3$		
#5. Glass	3.09	88.8%
#2. 660°C 3h heat-treated	3.14	90.5%
#3. 800°C 3h heat-treated	3.32	95.6%
#3. 800°C 3h+6h heat-treated	3.36	96.7%
#4. 800°C 6h heat-treated	3.31	95.3%
Medium lithium LAGP $x = 0.5$		
#1. 800°C 6h heat-treated	3.23	93.0%
High lithium LAGP $x = 0.7$		
Glass	2.96	88.1%
#1. 800°C 6h heat-treated	3.15	93.7%
#2. 550°C-630°C-800°C 1h each heat-treated	3.14	93.4%
#4. 900°C 6h heat-treated	3.14	93.4%
#5. 800°C 12h heat-treated	3.16	94.2%

## 2. Characterization of ceramic solid-state electrolytes

### 2.3.2 Optimized ionic conductivity

In the work of Fu, the ionic conductivity of the  $\text{Li}_{1+x}\text{Al}_x\text{Ge}_{2-x}(\text{PO}_4)_3$  glass-ceramics was obtained as a function of  $x$ <sup>84</sup>. The ionic conductivity had a jump from  $x = 0.2 - 0.3$ . At  $x = 0.3 - 0.7$ , the conductivity stayed on a plateau at a high level. Therefore, the composition of the LAGP were chosen to be within this range in this work.

The overall chemical formula of all the LAGP batches are shown in Table 2-17 (with batch 2 – 4 for heat-treating route and also batch 1 for sintering route). The most significant difference between the different batches is the lithium content ( $x = 0.3, 0.5$  and  $0.7$  in  $\text{Li}_{1+x}\text{Al}_x\text{Ge}_{2-x}\text{P}_3\text{O}_{12}$ ).

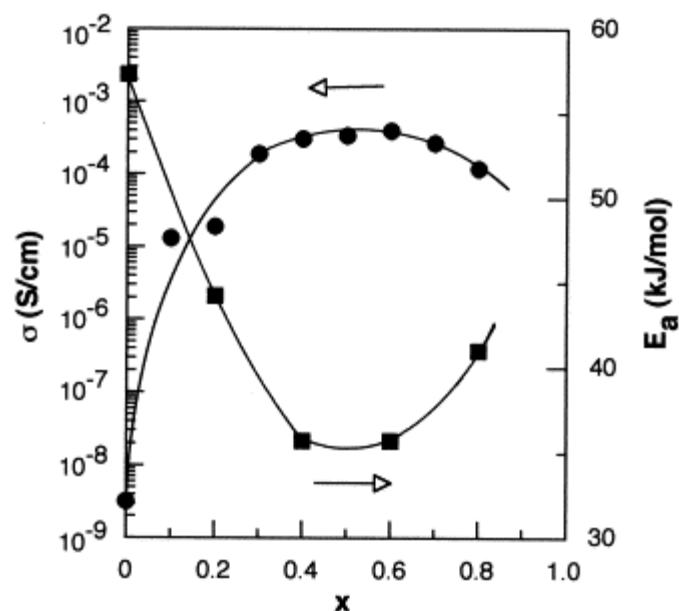


Figure 2-49: Ionic conductivity and activation energy vs  $x$  in the  $\text{Li}_{1+x}\text{Al}_x\text{Ge}_{2-x}(\text{PO}_4)_3$  (the work of Fu<sup>84</sup>).

Table 2-17: The overall chemical formula of LAGP batch 1 – 4.

batch	overall chemical formula	
1 sintering	$\text{Li}_{1.68}\text{Al}_{0.61}\text{Ge}_{1.32}\text{P}_3\text{O}_{11.90}$	High lithium, $x \approx 0.7$
2 heat-treating	$\text{Li}_{1.27}\text{Al}_{0.41}\text{Ge}_{1.48}\text{P}_3\text{O}_{11.70}$	Low lithium, $x \approx 0.3$
3 heat-treating	$\text{Li}_{1.52}\text{Al}_{0.52}\text{Ge}_{1.36}\text{P}_3\text{O}_{11.76}$	Medium lithium, $x \approx 0.5$
4 heat-treating	$\text{Li}_{1.72}\text{Al}_{0.54}\text{Ge}_{1.37}\text{P}_3\text{O}_{11.89}$	High lithium, $x \approx 0.7$

The ionic conductivities of the samples of LAGP with different compositions ( $x = 0.3 - 0.7$ ) prepared via heat-treating route with different process parameters are shown in Figure 2-50 (at room temperature) and Figure 2-51 (at 150°C). The experimental results can be summarized as follows:

By each composition, the sample, which was heat-treated at 800°C, showed higher ionic conductivity. The ionic conductivity increased as the heat-treatment duration at 800°C increased. However, as the heat-treating temperature increased to 900°C, the ionic conductivity decreased again, which is attributed to the

growth of minor phases in the sample (Figure 2-47). The samples heat-treated at lower temperature showed significant lower ionic conductivity, which is due to the porosity between the LAGP grains.

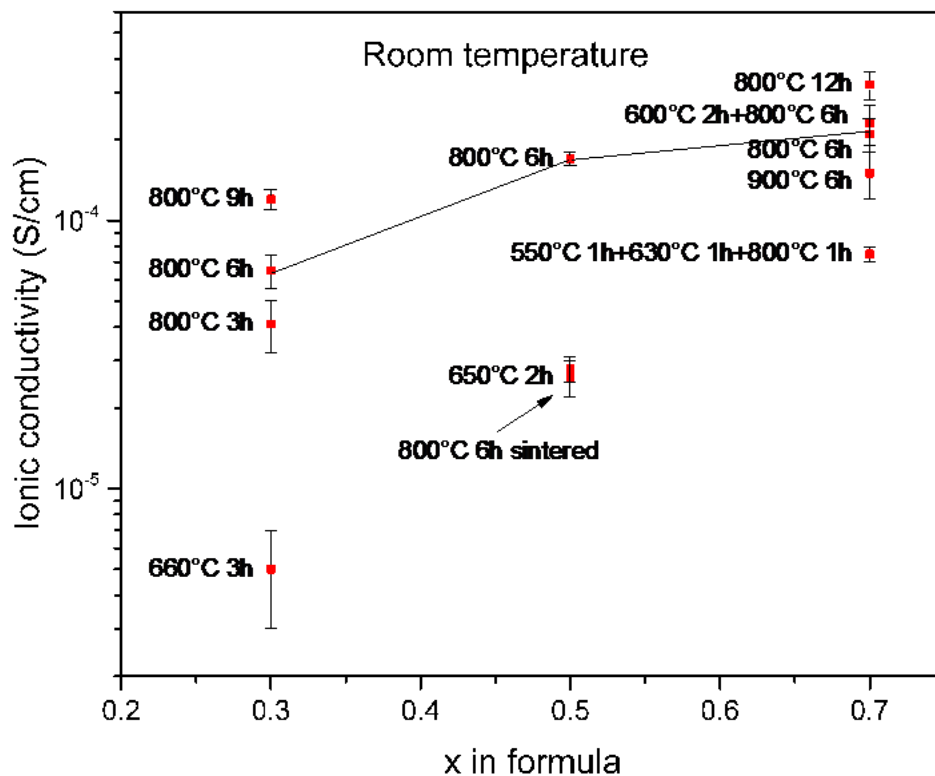


Figure 2-50: Ionic conductivity of the samples of low Li, medium Li and high Li LAGP ( $x = 0.3 - 0.7$ ) at room temperature prepared via heat-treating route with different process parameters (with one exception of the sample with  $x = 0.5$ , which was sintered at 800°C). The conductivity is plotted vs the  $x$  value in the general formula  $\text{Li}_{1+x}\text{Al}_x\text{Ge}_{2-x}(\text{PO}_4)_3$ . The heat-treating temperature and time period is labeled left of each data point.

## 2. Characterization of ceramic solid-state electrolytes

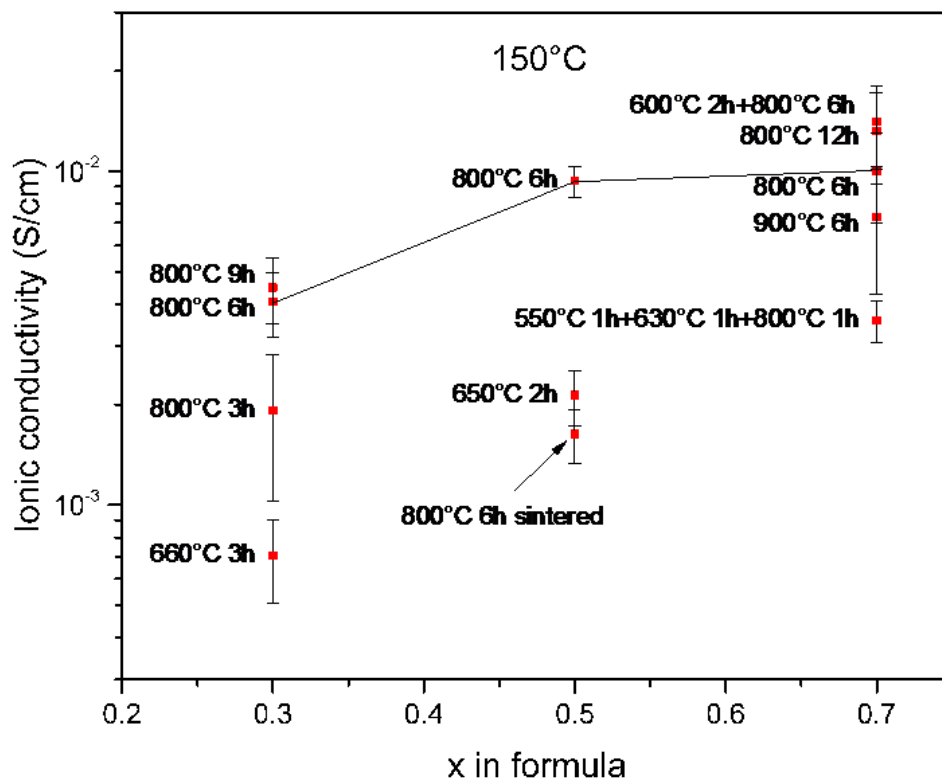


Figure 2-51: Ionic conductivity of the samples of low Li, medium Li and high Li LAGP ( $x = 0.3 - 0.7$ ) at 150°C temperature prepared via heat-treating route with different process parameters (with one exception of the sample with  $x = 0.5$ , sintered at 800°C).

Among the samples with different composition, the samples of high lithium LAGP ( $x = 0.7$ ) showed higher ionic conductivity. Figure 2-52 shows the ionic conductivity of the samples of low lithium, medium lithium and high lithium LAGP, which were heat-treated at the same condition (800°C for 6 hours).

The conductivity difference can be attributed to the different lithium content. In the LAGP crystal, the charge carriers are the mobile  $\text{Li}^+$  ions in the A2 position. The concentration of the charge carriers increases as the  $x$  value in the general formula increases (see 1.4). The low lithium LAGP has lower charge carrier concentration and hence lower ionic conductivity. On the other hand, the medium lithium and the high lithium LAGP have smaller difference in ionic conductivity, which might be due to that part of the  $\text{Li}^+$  ions in the high lithium LAGP are located on the immobile position (the position of  $\text{Ge}^{4+}$ ) instead of the mobile position A2. The immobile  $\text{Li}^+$  ions do not contribute to the ionic conductivity and the higher Li content has limited effect enhancing the ionic conductivity. In addition, the minor phases in the matrix can accommodate the extra  $\text{Li}^+$  ions and hence increase the overall Li content.

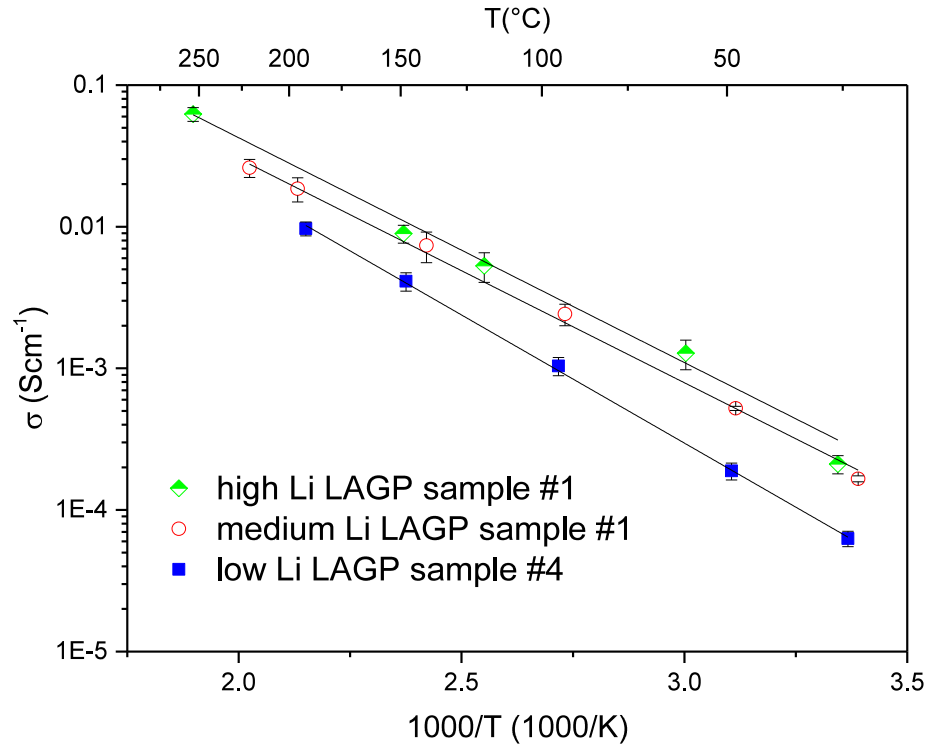


Figure 2-52: Ionic conductivity of the samples of low Li, medium Li and high Li LAGP ( $x = 0.3 - 0.7$ ), which were heat-treated at 800°C for 6 hours.

The samples of the high lithium LAGP (batch 4,  $x = 0.7$ ) prepared through heat-treating route showed higher ionic conductivity (sample #1, 800°C 6h heat-treated,  $2.1 \cdot 10^{-4}$  S/cm at room temperature) than the high lithium samples (batch 1,  $x = 0.7$ ) prepared through sintering route (sample #5, 800°C 6h sintered,  $1.5 \cdot 10^{-4}$  S/cm at room temperature). The density of these samples has less than 2% difference. However, the heat-treated samples had increasing ionic conductivity with increasing heat-treating time at 800°C, while the conductivity of sintered samples decreased by longer sintering time (> 6h). That can be attributed to the formation of minor phases: the  $\text{AlPO}_4$  are formed more easily in the sample pressed from powder than in the bulk sample. Larger amount of  $\text{AlPO}_4$  was formed rather via sintering route than via heat-treating route (both at the same sintering/heat-treating temperature).

Most of the ionic conductivity values measured in the literature are around  $10^{-4}$  S/cm. Xu et. al has investigated the  $\text{Li}_{1.5}\text{Al}_{0.5}\text{Ge}_3(\text{PO}_4)_3 - x\text{Li}_2\text{O}$  with  $x = 0 - 0.2$ . A highest conductivity value was found to be  $7.25 \cdot 10^{-4}$  S/cm at  $x = 0.05$ <sup>62</sup>. The optimum ionic conductivity of  $4 \cdot 10^{-4}$  S/cm has been reported by Fu, which is similar to the results in this work ( $3.2 \cdot 10^{-4}$  S/cm)<sup>84</sup>. Lower ionic conductivities were reported by Leo et. al<sup>53</sup>, Katoh et al.<sup>81</sup> and Kubanska et al. ( $\sigma < 10^{-4}$  S/cm)<sup>82</sup>. The ionic conductivity achieved in this work is not the highest value among the literature data. However, this work provides a systematic investigation of the influence of different factors on the ionic conductivity (such as the composition, heat-treating temperature and time-period and the formation of minor phases), which were not fully (i.e. adequate) revealed in previous investigations.

## 2. Characterization of ceramic solid-state electrolytes

### 2.3.3 Phase transitions in LAGP

Figure 2-53 shows the DSC curves of the low Li, medium Li and high Li LAGP ( $x = 0.3 - 0.7$  in the general formula  $\text{Li}_{1+x}\text{Al}_x\text{Ge}_{2-x}(\text{PO}_4)_3$ ). The glass transition onset and the crystallization onset temperature are listed in Table 2-18. Both decreased as the lithium content increased. The same trend was also reported by He et al.<sup>105</sup> and Fu<sup>84</sup>. However, the exact temperature reported in literature varies from the values measured in this work. The differences are due to minor differences in the composition and the different heating rate.

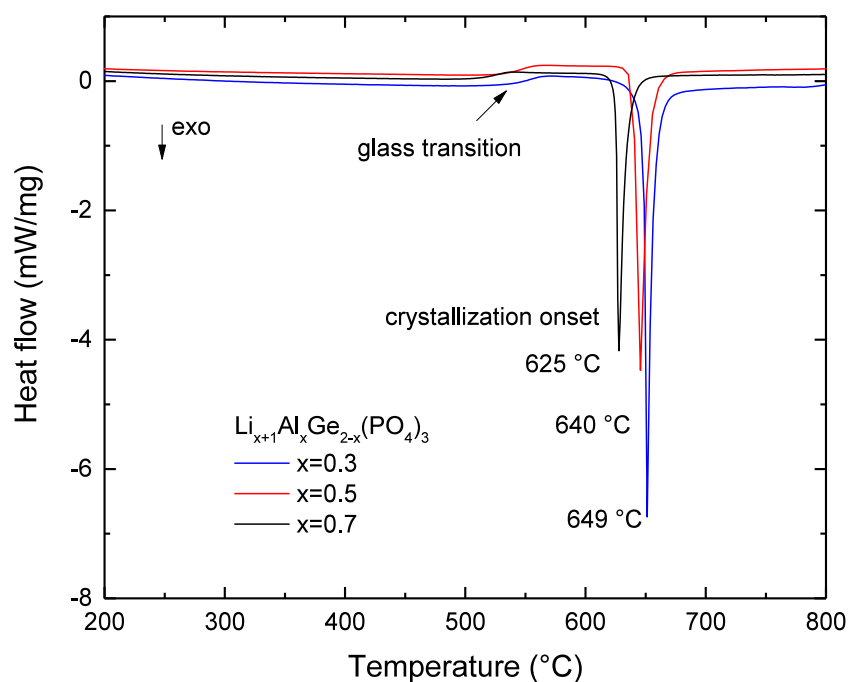


Figure 2-53: DSC curves of the glass samples with different composition.

Additional peaks were observed on the DSC curves when the crystallized samples of the medium Li LAGP (batch 3) and high Li LAGP (batch 4) were further analyzed. On the DSC curves of the high lithium LAGP sample #8 ( $x=0.7$ , Figure 2-26), small peaks appeared at 600°C – 800°C on the first cooling curve and the repeated heating and cooling cycles. These peaks indicate phase transitions in the crystallized LAGP samples. The peaks appeared repeatedly in each DSC measurement, showing that these phase transitions are reversible processes. The medium lithium LAGP ( $x = 0.5$ ) showed no significant peak on the first cooling curve (Figure 2-24) and small peaks appeared on the following measurements (Figure 2-25). Unlike samples from the high lithium and medium lithium LAGP, no peak was observed on the DSC curve of the low lithium LAGP ( $x = 0.3$ ) except the crystallization peak (Figure 2-22 and Figure 2-23).

*Table 2-18: Glass transition and crystallization temperatures of LAGP with different compositions measured with a 15K/min heating rate.*

LAGP	Glass transition onset	Crystallization onset
Batch 1: high lithium, x=0.7	504°C	596°C
Batch 2: low lithium, x=0.3	535°C	649°C
Batch 3: medium lithium, x=0.5	530°C	640°C
Batch 4: high lithium, x=0.7	510°C	625°C

The heat capacity ( $C_p$ ) curves of the crystallized samples of LAGP ( $x = 0.3 - 0.7$ ) are shown in Figure 2-54. For all the samples, the heat capacity increased with increasing temperature. Different peaks were observed on the different curves. While the sample of the low lithium LAGP showed no peak on the heat capacity curve, a series of minor peaks appeared at 552°C – 750°C on the curve of the medium lithium LAGP. On the curve of the high lithium LAGP, two peaks were observed at 644°C and 757°C. The peak at 757°C was significantly higher than other peaks. These peaks appeared in repeated measurements, showing that these are reversible phase transitions.

The peak at 644°C might be attributed to the phase transition of  $\text{Li}_4\text{P}_2\text{O}_7$ <sup>106</sup>. It has been reported in the work of Tien et al. that the  $\text{Li}_4\text{P}_2\text{O}_7$  has a reversible polymorphic inversion at 630°C and the melting point at 885°C<sup>107</sup>.  $\text{Li}_4\text{P}_2\text{O}_7$  phase might be formed in the high lithium ( $x = 0.7$ ) and medium lithium ( $x = 0.5$ ) LAGP because of the higher lithium content. However, the  $\text{Li}_4\text{P}_2\text{O}_7$  phase was not identified by XRD, which could be due to that the volume fraction of the  $\text{Li}_4\text{P}_2\text{O}_7$  is too small for the XRD detection. On the other hand, the minor phases observed in LAGP samples are rich in aluminum, which did not confirm the existence of the  $\text{Li}_4\text{P}_2\text{O}_7$  phase.

It was also reported that the compound  $\text{LiPO}_3$  shows a melting temperature of around 688°C – 665°C<sup>107</sup>. The small peaks at 600°C – 750°C on the medium lithium LAGP sample can be attributed to different kinds of phosphate compounds.

## 2. Characterization of ceramic solid-state electrolytes

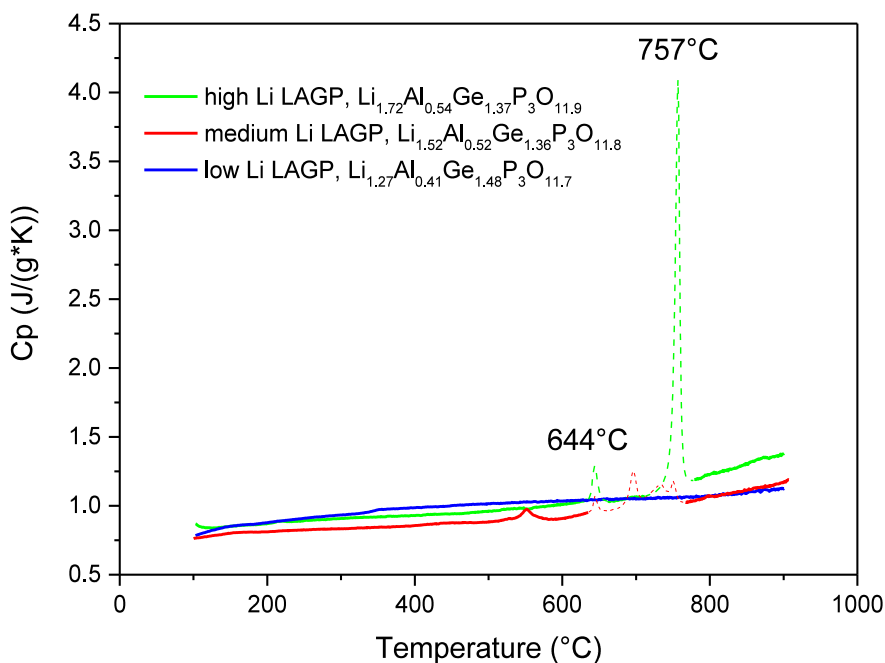
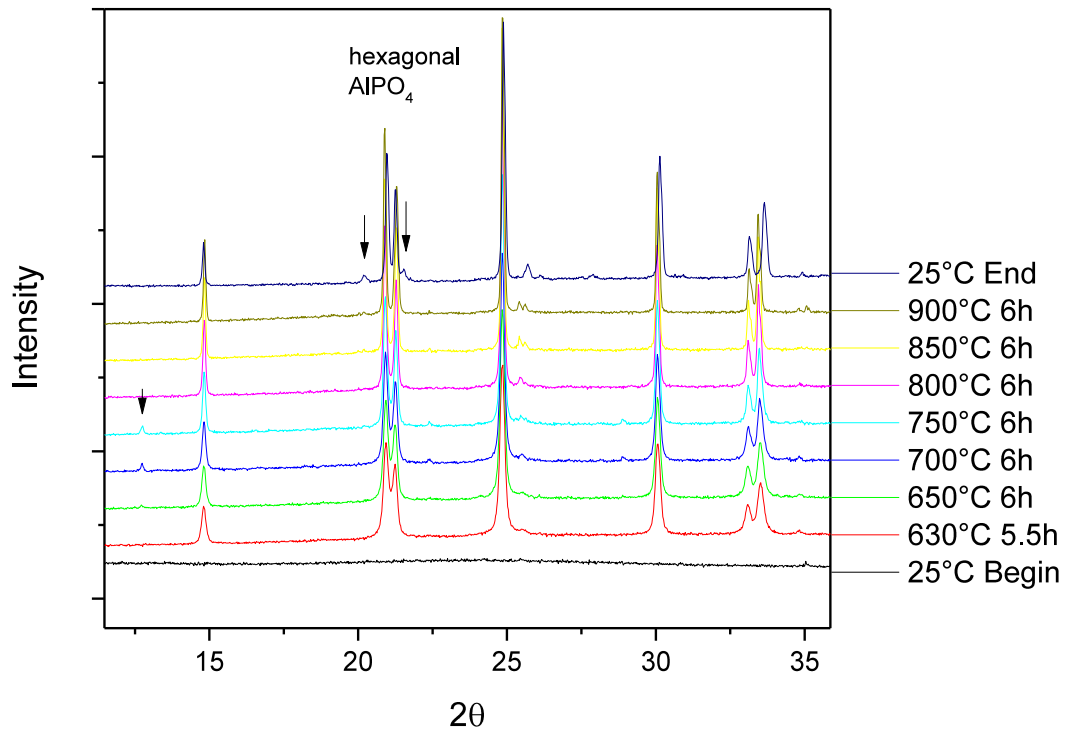


Figure 2-54: Heat capacity curves of samples of LAGP with different composition between 100°C and 900°C.

The high lithium sample ( $x = 0.7$ ) showed a much larger peak at 757°C. This peak was much higher than other peaks, which indicates that it was related with a phase transition of the main LAGP phase instead of other minor phases. The slope of the heat capacity curve of the high lithium LAGP had an increase at the temperature higher than 757°C.

There is a smaller peak at the same temperature on the medium lithium sample ( $x = 0.5$ ), showing that the same phase transition took place also in the medium lithium LAGP sample. The slope of the heat capacity curve above 757°C is also higher than that of the low lithium LAGP (Figure 2-54).

The phase transitions in LAGP samples were also observed on the hot stage XRD-diagrams measured between 25°C and 900°C. On the XRD-diagrams of the low lithium LAGP sample ( $x = 0.3$ ), only the diffraction of LAGP phase could be identified (Figure 2-31). The diffractogram had no remarkable change except the peak shift due to thermal expansion. The samples of medium lithium LAGP ( $x = 0.5$ ) and the high lithium LAGP ( $x = 0.7$ ) showed new diffraction peaks between 650°C and 750°C (Figure 2-55, Figure 2-33, Figure 2-35). The DSC measurements showed also a minor phase transition at 644°C, which could be related to the new diffraction peaks (Figure 2-54). At higher temperatures, the new diffraction peaks disappeared again in the hot stage XRD-diagrams.



*Figure 2-55: Hot stage X-ray diffractogram of the sample of high lithium LAGP ( $x = 0.7$ ) at different temperatures.*

The lattice parameters calculated from hot stage XRD data showed clues of phase transitions in the high lithium LAGP sample. A comparison of the lattice parameters  $a$ ,  $b$  of the medium and high lithium LAGP is shown in Figure 2-56. While the  $a$ ,  $b$  parameters of the medium Li LAGP were linearly decreasing between 600°C – 900°C, the  $a$ ,  $b$  parameters of the high Li LAGP sample showed a deviation from linearity between 750°C and 900°C. The abrupt change of the lattice parameter  $a$  &  $b$  between 750°C and 800°C shows that the high Li LAGP exhibited a phase transition in the main phase, which was also shown by the DSC measurements.

## 2. Characterization of ceramic solid-state electrolytes

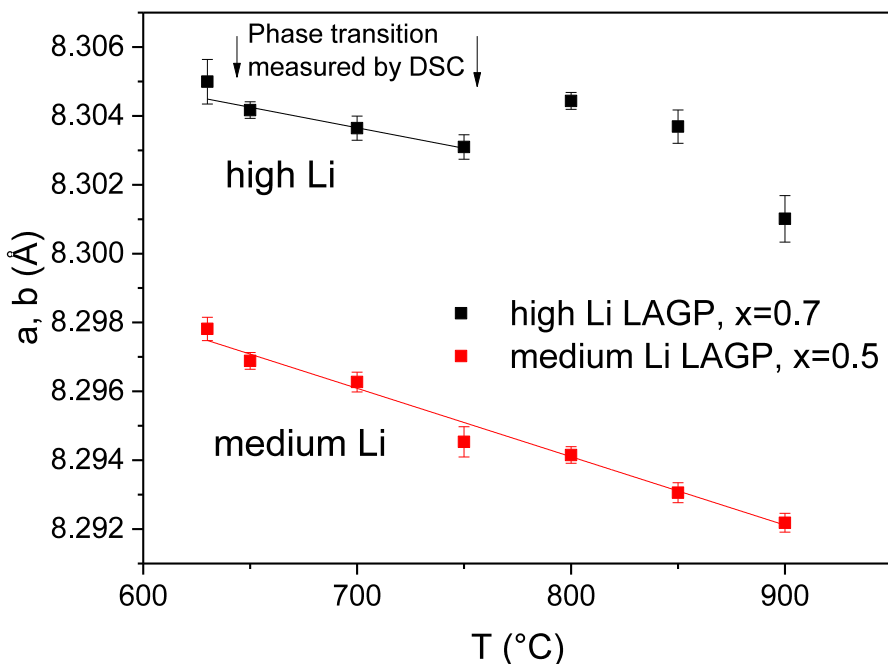


Figure 2-56: Lattice parameters  $a$  &  $b$  of the samples of high and medium lithium LAGP measured by hot stage XRD.

The thermal analysis and hot stage XRD measurements showed agreement with regard to phase transition in the high Li LAGP ceramic. The DSC measurements showed the same phase transition also in the medium Li LAGP ( $x = 0.5$ ). However, the effect was much weaker. In the low Li LAGP, no phase transition was observed via thermal analysis and hot stage XRD.

This phase transition in the high lithium LAGP was not reported in other publications before. However, similar phase transitions were reported in analogous NaSICON materials. In the Zirconium based NaSICON ( $\text{LiZr}_2(\text{PO}_4)_3$ ) materials, a monoclinic-rhombohedral phase transition takes place at around  $40^\circ\text{C}$ <sup>108, 109</sup>. However, this did not explain the composition dependence of the phase transition.

In the work of Pet'kov et. al, the phosphates  $\text{NaMe}_2(\text{PO}_4)_3$  and  $\text{Na}_5\text{Me}(\text{PO}_4)_3$  ( $\text{Me}=\text{Ti}, \text{Zr}, \text{Hf}$ ) were investigated<sup>110, 111</sup>. These compounds have the NaSICON structure. For the Na-rich  $\text{Na}_5\text{Zr}(\text{PO}_4)_3$  and  $\text{Na}_5\text{Hf}(\text{PO}_4)_3$ , endothermic reversible phase transitions take place at 389 K – 424 K and 476 K – 572 K, respectively. While Na-poor  $\text{NaMe}_2(\text{PO}_4)_3$  ( $\text{Me}=\text{Ti}, \text{Zr}, \text{Hf}$ ) does not show such phase transition. The phase transition of  $\text{Na}_5\text{Zr}(\text{PO}_4)_3$  corresponds to a centering of off-centered zirconium atoms in octahedral sites and  $\text{Na}^+$  occupation transfer between sodium sites.

The  $\text{Na}_5\text{Zr}(\text{PO}_4)_3$  was also investigated by Boilot et. al<sup>112</sup> and the  $\text{Na}_5\text{Ti}(\text{PO}_4)_3$  was investigated by Krimi et. al<sup>50</sup>. These compounds have the NaSICON-structure. In these compounds, the excess  $\text{Na}^+$  ions take their place on interstitial sites and on half of the Zr-site (or Ti respectively). These compounds have a different lattice symmetry and belong to the space group R32 (instead of R-3c for  $\text{NaZr}_2(\text{PO}_4)_3$ ).

In another work of Boilot<sup>113, 114</sup>, both the structure and the phase transition of  $\text{Na}_{5.5}\text{ZrSi}_{0.5}\text{P}_{2.5}\text{O}_{12}$  were investigated. The occupation factors of different sites were calculated. The  $\text{Na}_{5.5}\text{ZrSi}_{0.5}\text{P}_{2.5}\text{O}_{12}$  exhibits two phase transitions: The first phase transition is at 120°C and is related to the off-centering of Zr atoms from the theoretical position. The second is at 200°C and involves the centering of Zr atoms and a Na occupation transfer.

The information from the literature mentioned above indicates that there exists a Li-rich  $\text{Li}_5\text{Ge}(\text{PO}_4)_3$  phase in the samples of high lithium LAGP ( $x = 0.7$ ). Analog to the compound with analogous structure mentioned above, the  $\text{Li}_5\text{Ge}(\text{PO}_4)_3$  phase has a similar phase transition at 750°C – 800°C, which was detected by DSC and XRD measurements. The medium lithium LAGP ( $x = 0.5$ ) might have a small amount of the Li-rich  $\text{Li}_5\text{Ge}(\text{PO}_4)_3$  phase in its matrix, which results in a smaller peak detected by DSC measurement. In the low Li LAGP ( $x = 0.3$ ), there is no Li-rich  $\text{Li}_5\text{Ge}(\text{PO}_4)_3$  phase and no phase transition, too.

## 2. Characterization of ceramic solid-state electrolytes

### 2.3.4 Thermal conductivity

For the solid-state electrolytes, which are supposed to be used at elevated temperature, the thermal conductivity needs to be known. Moreover, both thermal conductivity and ionic conductivity can reflect other material properties such as lattice defects and imperfections. Revealing of the correlation between the thermal and ionic conductivity would give deeper understanding about the material.

In the metallic materials with free electrons, the thermal and electronic conductivity are related. The investigation of Gustav Wiedemann and Rudolph Franz in 1853 has shown that the ratio of the thermal conductivity and the electrical conductivity has approximately the same value for different metals at the same temperature, because the heat is transported by the free electrons in the metallic materials<sup>115</sup>. The heat and electrical transport both involve the free electrons in the metal.

The Wiedemann–Franz law describes this correlation:

$$\frac{\lambda}{\sigma} = L \cdot T \quad 2-9$$

with  $\lambda$ : the thermal conductivity,  $\sigma$ : the electrical conductivity,  $L$ : the Lorentz number. The Lorentz number is not a constant but varies with the temperature<sup>116</sup>.

In the non-electrical conducting material such as the solid electrolyte, there are no free electrons in the lattice. Thermal energy is mainly conducted via the lattice vibration (lattice wave). The lattice vibration in crystalline material can be characterized by the standing waves. The quanta of the standing wave is referred as “phonons”. The thermal conductivity equals<sup>117</sup>:

$$\lambda = \frac{1}{3} C v l \quad 2-10$$

where  $C$  is the heat capacity,  $v$  is the average velocity of the phonons and  $l$  is the mean free path of the phonons before they are scattered.

The scattering of phonons has great influence on the thermal conductivity, which is largely influenced by the grain boundaries and the impurities in the grain<sup>117</sup>.

In the ionic conductor material, the mobile ions provide the ionic conductivity. It is therefore interesting to investigate, whether the mobile ions can also carry thermal energy and if there exists a correlation between the thermal conductivity and the ionic conductivity in the LAGP material. In that case, the total thermal conductivity  $\lambda_{total}$  would consist of the contribution of phonons  $\lambda_{phonon}$  and the contribution of ions  $\lambda_{ion}$ :

$$\lambda_{total} = \lambda_{phonon} + \lambda_{ion} \quad 2-11$$

The thermal conductivity is related to the thermal diffusivity via the equation:

$$\lambda = C_p(T) \cdot \alpha(T) \cdot \rho(T)$$

2-12

with  $\alpha(T)$ : the thermal diffusivity,  $C_p(T)$ : the heat capacity at constant pressure and  $\rho(T)$ : the density of the material, which are changing at different temperatures.

The thermal diffusivity of LAGP samples with different compositions, which were prepared via heat-treating route, was measured with a laser flash device. Five measurements were carried out for each temperature. The average values were taken as the thermal diffusivity results. The uncertainties were calculated from the deviation of the measured values. The thermal conductivity was calculated from the thermal diffusivity, the heat capacity and the density of the LAGP. The uncertainty of the thermal conductivity was calculated from the uncertainties of the thermal diffusivity, the heat capacity and the density.

The thermal diffusivity of the samples of low lithium LAGP (batch 2,  $x = 0.3$ ) is shown in Figure 2-57. The thermal diffusivity increased as the heat-treating temperature and time increased. The sample #3, which was heat-treated at 800°C for 3+6h, exhibited the highest thermal diffusivity. The same sample had exhibited also higher density and ionic conductivity than other samples (Figure 2-37 and Table 2-16). The glass sample #5 had lowest thermal diffusivity.

It could be noticed that the thermal diffusivity of the crystallized samples decreased with increasing temperature. That is expected since the thermal energy is mainly conducted via phonons in the crystallized samples. The phonons are more strongly scattered at higher temperature, which reduces the mean free path of the phonons and the thermal diffusivity. On the other hand, the thermal diffusivity of the glass sample increased with increasing temperature. The difference might be attributed to the contribution of radiative heat flux in the glass sample<sup>118, 119</sup>. The radiative heat flux increases with increasing temperature and changes the temperature dependence of the thermal diffusivity.

The thermal conductivity is calculated using equation 2-12 and shown in Figure 2-58. The heat conductivity of all the samples increase with increasing temperature, which is because the heat capacity increase with increasing temperature (2.3.1.1, Figure 2-23) and this increase overwhelmed the change of the thermal diffusivity (Figure 2-57) and the density. The sample #3 heat-treated at 800°C for 3+6 hours showed the highest thermal conductivity (Figure 2-42, Figure 2-41 and Table 2-16).

The sample #4, which was initially heat-treated at 800°C for 6h, was measured for 3 times in laser flash device (Figure 2-59 and Figure 2-60). The thermal diffusivity and thermal conductivity showed small changes in the second and third measurements.

## 2. Characterization of ceramic solid-state electrolytes

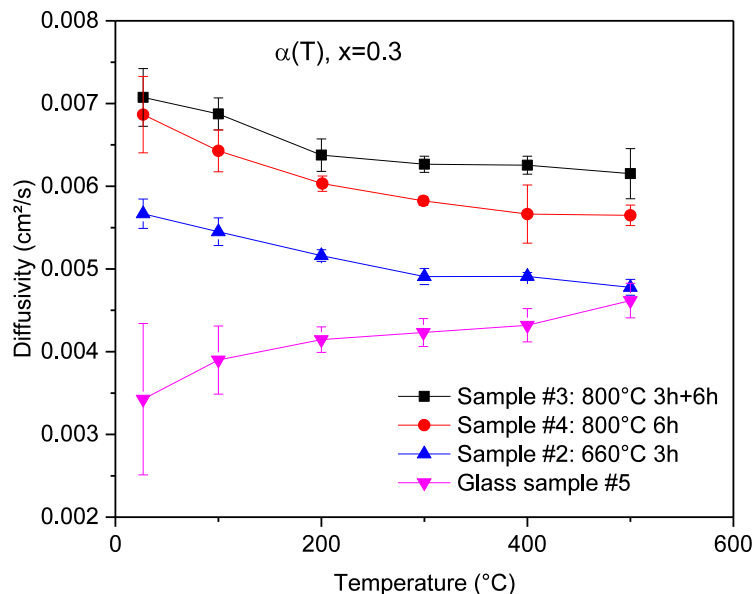


Figure 2-57: Thermal diffusivity of the glass sample of low lithium LAGP (batch 2 with  $x = 0.3$  in  $Li_{1+x}Al_xGe_{2-x}P_3O_{12}$ ) and crystalline samples, which were heat-treated at  $660^\circ\text{C} - 800^\circ\text{C}$ . The numerical values of the thermal diffusivity are listed in the appendix Table A- 28 – Table A- 31.

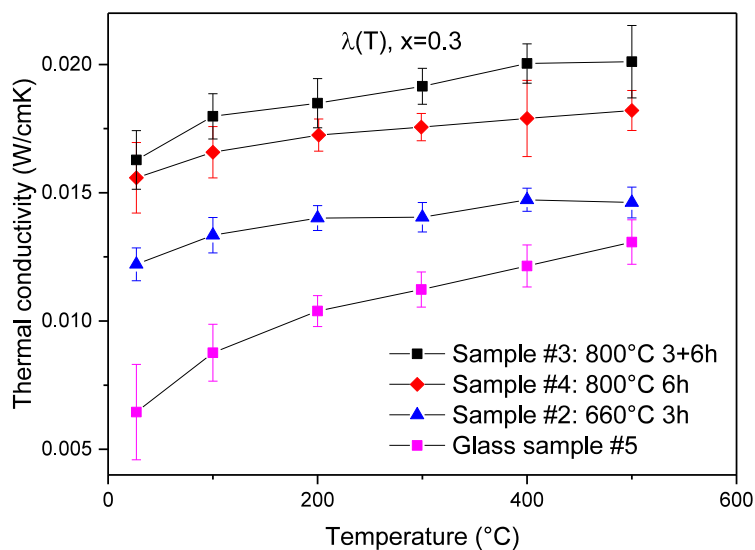


Figure 2-58: Thermal conductivity of the glass sample of low lithium LAGP (batch2,  $x = 0.3$ ) and different crystalline samples heat-treated at  $660^\circ\text{C} - 800^\circ\text{C}$ . The numerical values of the thermal conductivity are listed in the appendix Table A- 28 – Table A- 31.

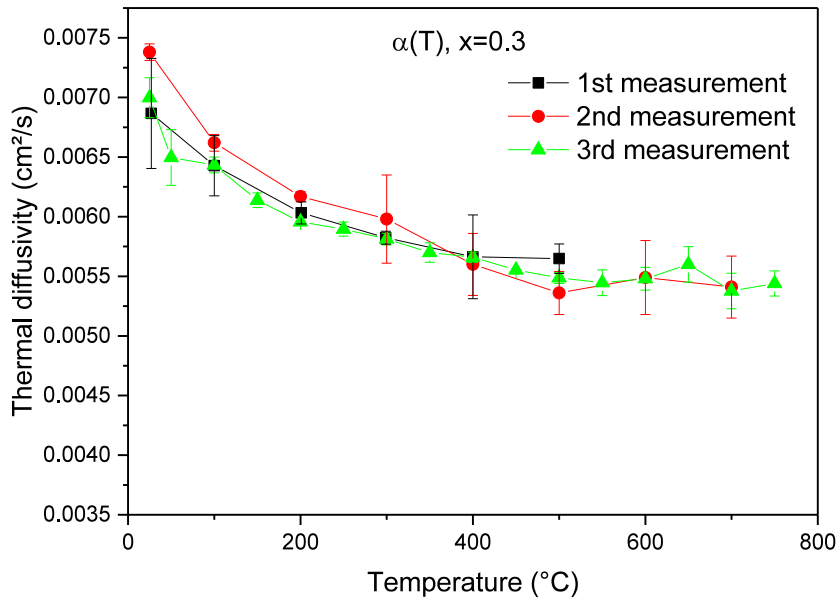


Figure 2-59: Thermal diffusivity of the sample #4 of low lithium LAGP (batch 2,  $x = 0.3$ ), which was initially heat-treated at 800°C for 6h, in three measurements. The numerical values are listed in the appendix Table A- 30.

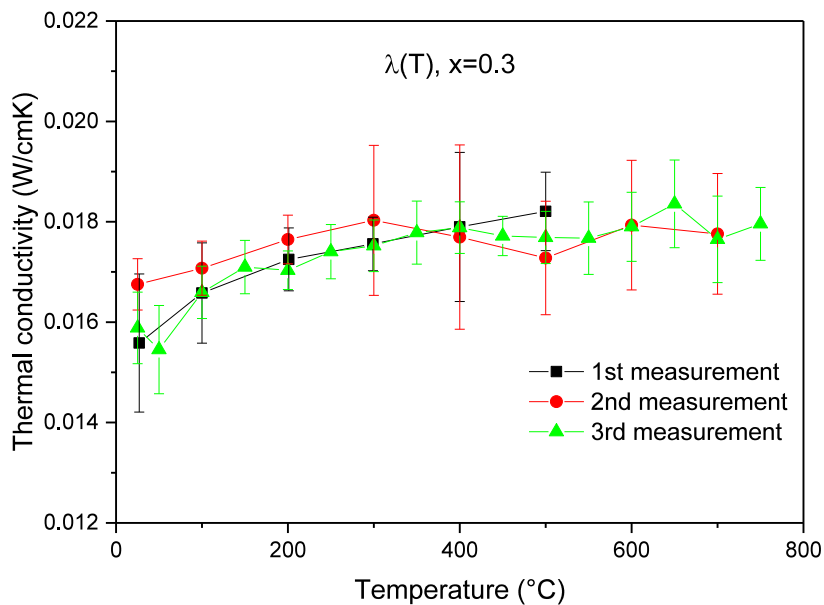


Figure 2-60: Thermal conductivity of three measurements of the sample #4 of low lithium LAGP ( $x = 0.3$ ), which was initially heat-treated at 800°C for 6h. The numerical values are listed in the appendix Table A-30.

## 2. Characterization of ceramic solid-state electrolytes

The thermal diffusivity and thermal conductivity of the medium lithium LAGP (batch 3,  $x = 0.5$ ) are shown in Figure 2-61 and Figure 2-62, respectively. The sample #1 was heat-treated at 800°C for 6h before its thermal diffusivity was measured three times in the laser flash device. Same as for the low lithium LAGP samples, the thermal diffusivity of the medium lithium LAGP decreased with increasing temperature. The thermal conductivity showed a weak dependence on the temperature.

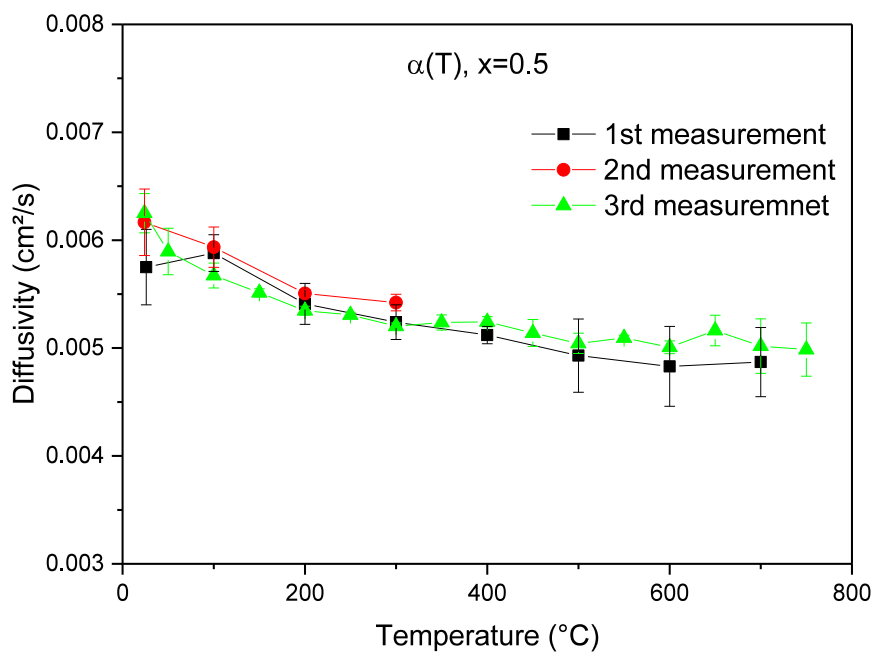


Figure 2-61: Thermal diffusivity of the sample #1 of medium lithium LAGP (batch 3,  $x = 0.5$ ), which was initially heat-treated at 800°C for 6h. The numerical values are shown in the appendix Table A- 32.

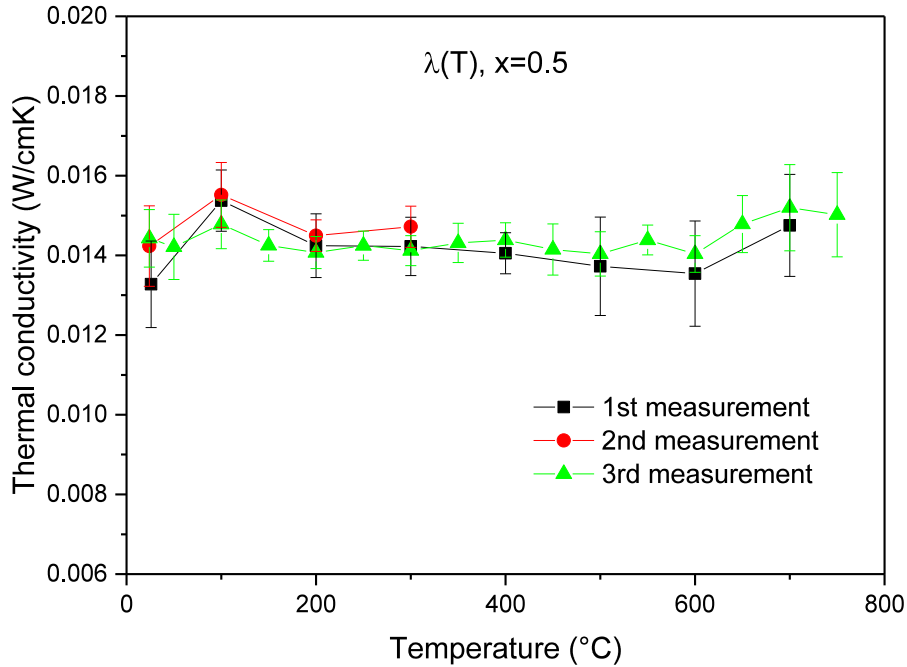


Figure 2-62: Thermal conductivity of the sample #1 of medium lithium LAGP ( $x = 0.5$ ) which was initially heat-treated at 800°C for 6h. The numerical values are shown in the appendix Table A- 32.

Figure 2-63 and Figure 2-64 show the thermal diffusivity and the thermal conductivity of the sample of the high lithium LAGP (batch 4,  $x = 0.7$ ) measured with laser flash for three times. In contrast to the samples of the low lithium and medium lithium LAGP, the thermal diffusivity and thermal conductivity of the high lithium sample decreased with each measurement. Since the measuring temperature was up to 750°C and the measurements at each temperature took around 1.5 hour, there was a heat-treating effect during the laser flash measurement at over 700°C. The heat-treating induced change (formation of minor phases) in the sample and reduced the thermal conductivity.

## 2. Characterization of ceramic solid-state electrolytes

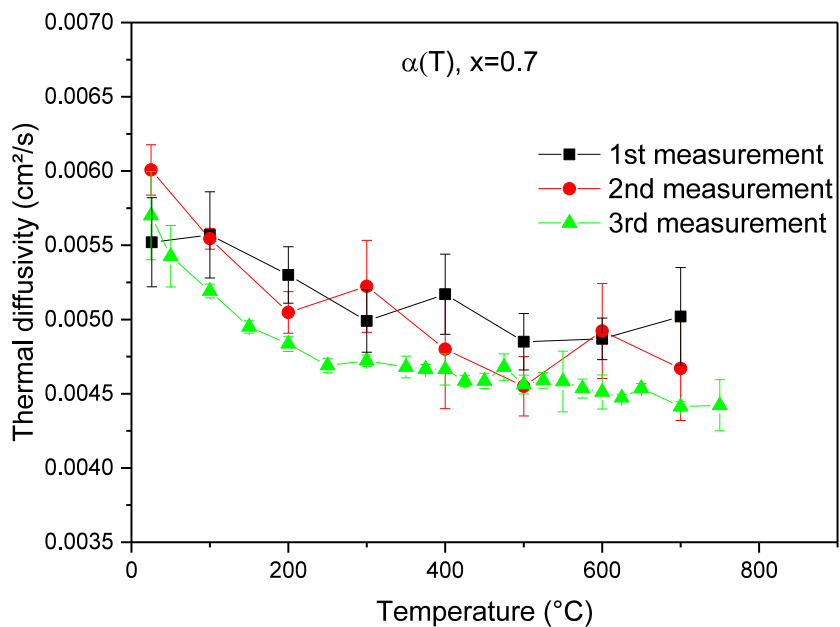


Figure 2-63: Thermal diffusivity of the sample #7 of the high lithium LAGP (batch 4,  $x = 0.7$ ) which was heat-treated at 800°C for 6h. The numerical values are shown in the appendix Table A- 33.

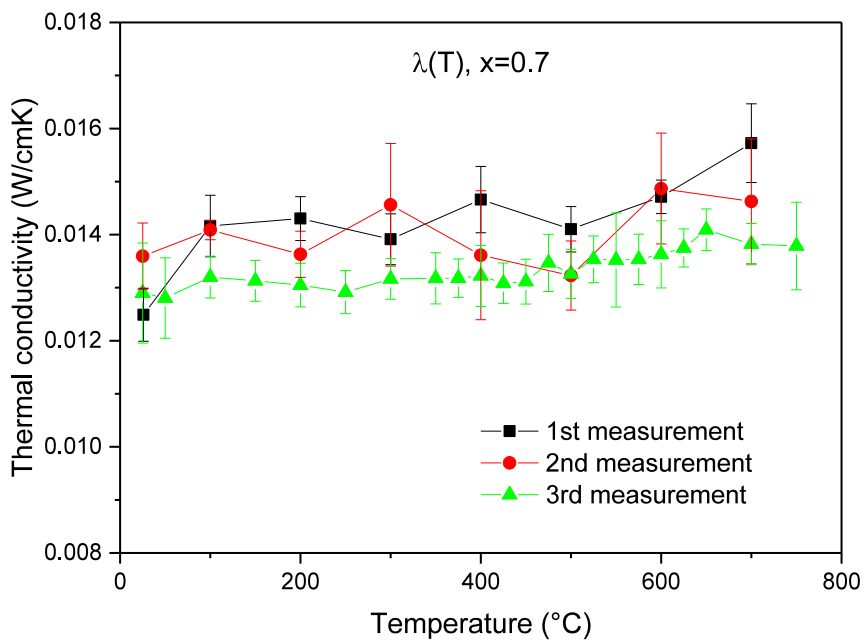


Figure 2-64: Thermal conductivity of the sample #7 of the high lithium LAGP batch 4 which was heat-treated at 800°C for 6h. The numerical values are shown in the appendix Table A- 33.

Ionic conductivity of the samples of the low lithium LAGP batch 2 is plotted against their thermal conductivity at different temperatures and shown in Figure 2-65. Among the samples of the low Li LAGP ( $x = 0.3$ ), the one with higher ionic conductivity shows higher thermal conductivity. It indicates that there might be a positive correlation between the ionic conductivity and thermal conductivity.

However, the ratio between the thermal conductivity and the ionic conductivity varies much by different samples. A correlation analog to the Wiedemann–Franz law (Equation 2-9) could not be established.

The positive correlation was not valid among samples of different LAGP batches. As the dashed lines on Figure 2-66 show, the high lithium LAGP sample had higher ionic conductivity as the medium lithium LAGP but had a lower thermal conductivity as the medium lithium LAGP. The medium LAGP sample had again higher ionic conductivity as the low lithium LAGP but had a lower thermal conductivity as the low lithium LAGP.

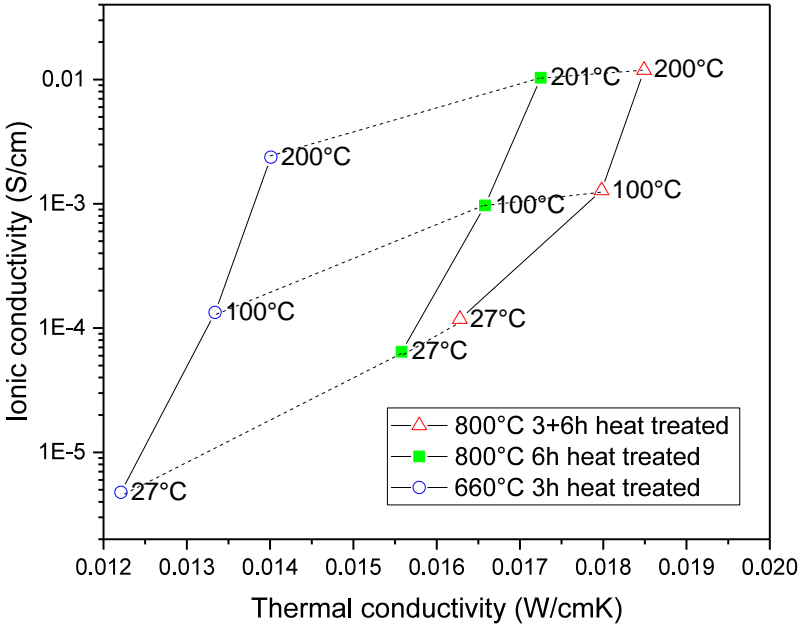


Figure 2-65: Ionic conductivity of samples #2, #3 and #4 of the low Li LAGP (batch 2,  $x = 0.3$ ) plotted vs their thermal conductivity at different temperatures (labeled right of the data points). The samples were heat-treated at 660°C – 800°C.

## 2. Characterization of ceramic solid-state electrolytes

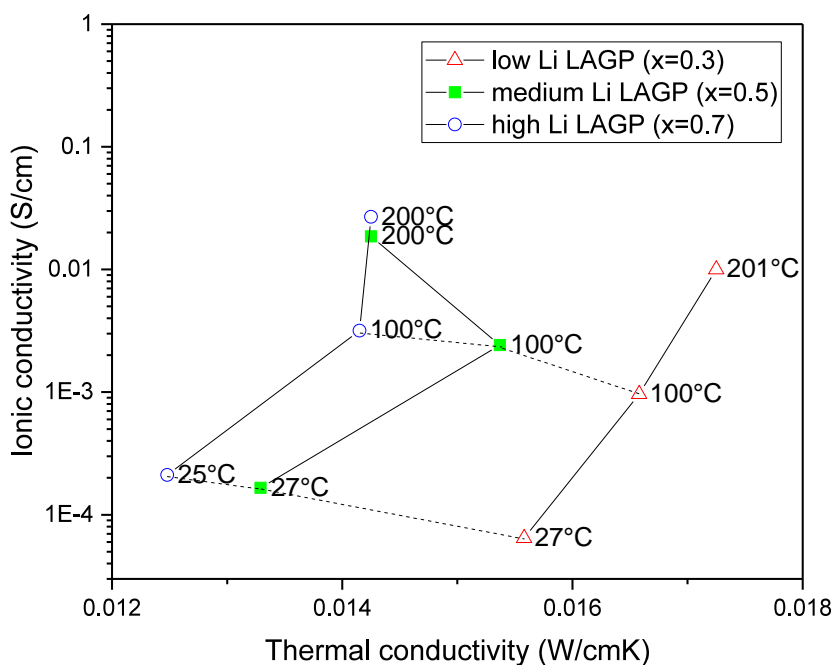


Figure 2-66: Ionic conductivity of samples of LAGP with different composition (batch 2 sample #4, batch 3 sample #1 and batch 4 sample #1 and #7) plotted vs their thermal conductivity at different temperatures (labeled right of the data points). The samples were heat-treated at 800°C for 6 hours.

As shown on Figure 2-67 and Table 2-19, as the  $x$  value in  $\text{Li}_{1+x}\text{Al}_x\text{Ge}_{2-x}\text{P}_3\text{O}_{12}$  increased, the ionic conductivity increased and the thermal conductivity decreased. The increase of ionic conductivity by increasing  $x$  could be attributed to the increase of mobile  $\text{Li}^+$  ions, which is the charge carrier in the LAGP lattice (see 2.3.2). The decrease of thermal conductivity with increasing  $x$  value is attributed to the decrease of the mean free path of the phonons in the LAGP matrix. The  $x$  value in the general formula  $\text{Li}_{1+x}\text{Al}_x\text{Ge}_{2-x}\text{P}_3\text{O}_{12}$  increases when more aluminum and lithium are doped in LAGP. The doping introduces more defects into the LAGP lattice, which scatter the phonons stronger and hence reduce the mean free path. Furthermore, minor phases are formed with higher doping level, which also scatter the phonon and reduce the thermal conductivity.

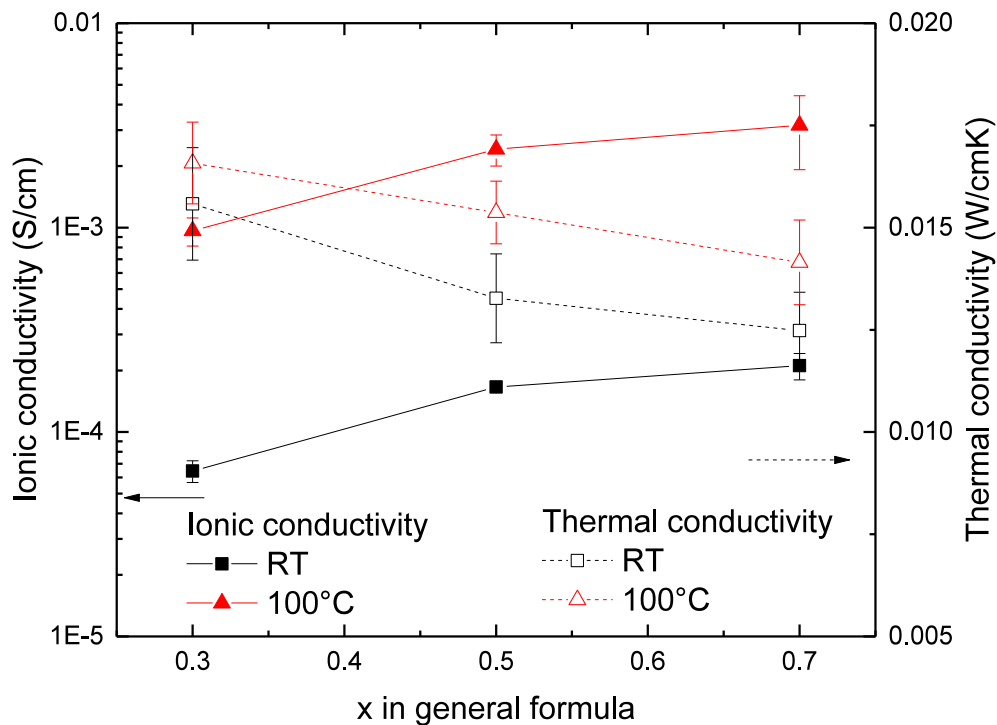


Figure 2-67: Ionic conductivity and thermal conductivity of LAGP samples with different compositions (batch 2 sample #4, batch 3 sample #1 and batch 4 sample #1 and #7) at room temperature and 100°C plotted vs x value in the general formula of  $Li_{1+x}Al_xGe_{2-x}P_3O_{12}$ .

Table 2-19: Ionic conductivity and thermal conductivity of LAGP samples with different compositions ( $x = 0.3 - 0.7$  in  $Li_{1+x}Al_xGe_{2-x}P_3O_{12}$ ) at room temperature and 100°C shown on Figure 2-67.

x	Ionic conductivity (S/cm)		Thermal conductivity (W/cmK)	
	Room temperature	100°C	Room temperature	100°C
0.3	$6.3 \pm 0.8 \cdot 10^{-5}$	$10 \pm 1.5 \cdot 10^{-4}$	$0.016 \pm 0.0014$	$0.0165 \pm 0.0009$
0.5	$1.7 \pm 0.1 \cdot 10^{-4}$	$2.4 \pm 0.4 \cdot 10^{-3}$	$0.013 \pm 0.0011$	$0.0154 \pm 0.0009$
0.7	$2.1 \pm 0.3 \cdot 10^{-4}$	$3 \pm 1.3 \cdot 10^{-3}$	$0.012 \pm 0.0009$	$0.014 \pm 0.0010$

The sample #4 of low Li LAGP has a higher relative density than the sample #1 of medium Li LAGP and the sample #1 of high Li LAGP (Table 2-16). The larger porosity has negative influence on the thermal conductivity. The difference of the thermal conductivity between LAGP samples from different batches can be also attributed to the porosity of the samples.

## 2. Characterization of ceramic solid-state electrolytes

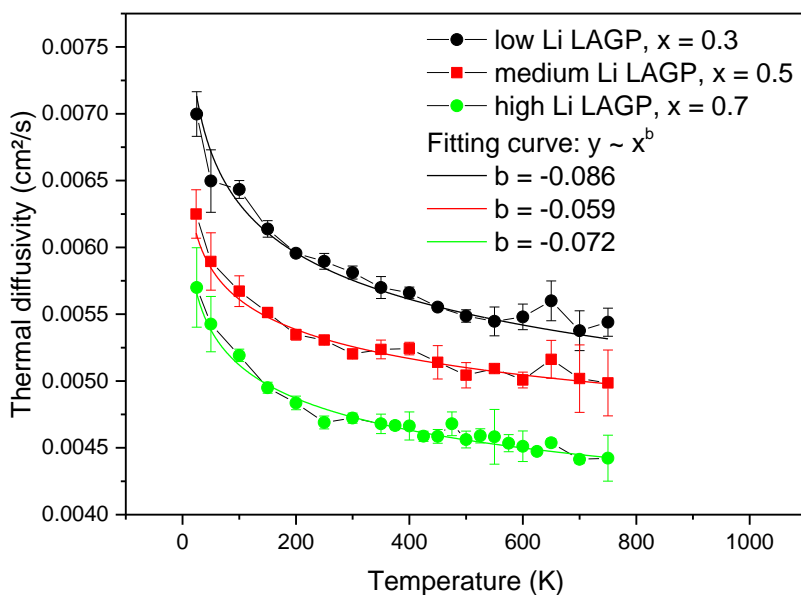


Figure 2-68: Thermal diffusivity of the samples (batch 2 sample #4, batch 3 sample #1 and batch 4 sample #7) by the 3rd measurement. The temperature dependence of the thermal diffusivity is fitted with the  $y \propto x^b$ , where  $y$  represents the thermal diffusivity and  $x$  represents the temperature.

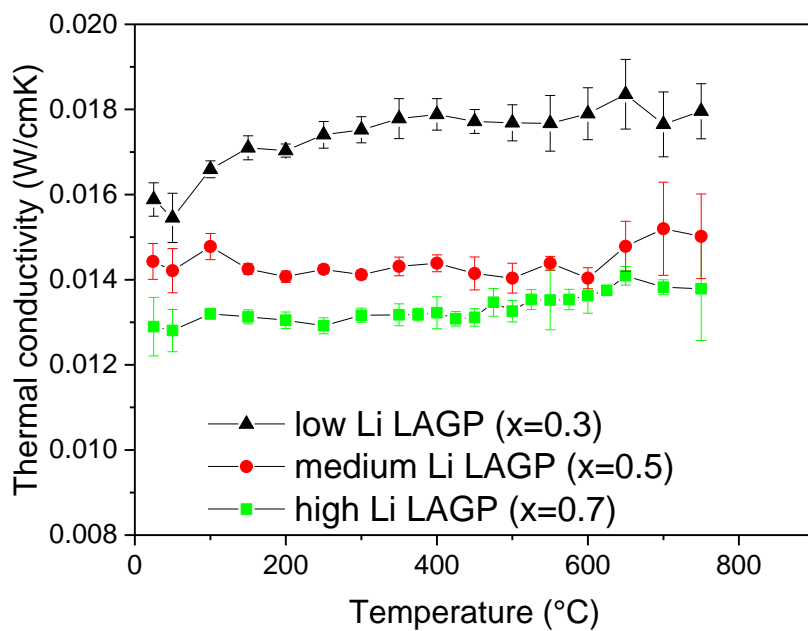


Figure 2-69: Thermal conductivity of the samples of low Li, medium Li and high Li LAGP (batch 2 sample #4, batch 3 sample #1 and batch 4 sample #7) by the 3rd measurement.

Figure 2-68 shows the temperature dependence of the thermal diffusivity of the LAGP samples with different composition. The thermal diffusivities scales approximately with  $\alpha \propto T^{-x}$  where  $0.086 < x < 0.059$ . On the other hand, the thermal conductivity of those samples had not shown clear dependence on temperature (Figure 2-69).

According to the theory of thermal conductivity via phonons, at not too low temperatures, the thermal conductivity is proportional to the inverse of temperature ( $\lambda \propto T^{-1}$ )<sup>117, 120</sup>. In the material with strong phonon-defect interaction, the dependence can change to  $\lambda \propto T^{-0.5}$ <sup>121, 122</sup>. The thermal conductivity decreases with increasing temperature because atoms have a stronger vibration at higher temperature, the phonons would be stronger scattered, the mean free path of the phonons becomes smaller. In the material with strong phonon-defect interaction, the phonons are already strongly scattered and the decrease of the mean free path is not such significant as in the material with less defects. The temperature dependence is therefore less strong.

In conclusion, the thermal conductivity measurements on the different LAGP batch showed that the lattice vibration (lattice wave) was the dominating conducting mechanism. On the other hand, there was not enough evidence to prove that the mobile ions have a contribution to the total thermal conductivity.

## 2. Characterization of ceramic solid-state electrolytes

### 2.4 LATP solid-state electrolyte through sintering route

The  $\text{Li}_2\text{CO}_3$  (Fluka, 99.0%),  $\text{Al}_2\text{O}_3$  (Sigma-Aldrich, 98.5%),  $\text{P}_2\text{O}_5$  (Analar Normapur, 99.1%) and  $\text{TiO}_2$  (Alfa Aesar, 99.5%) was used as starting material for the lithium aluminum titanium phosphate (LATP) solid-state electrolyte. The samples were fabricated through the sintering route described in 2.1.1.

#### 2.4.1 Sample characterization

The composition of the LATP glass was measured using ICP-OES and Carrier Gas Hot Extraction (for oxygen) (see Table 2-20). The overall chemical formula of the LATP powder is  $\text{Li}_{1.20}\text{Al}_{0.67}\text{Ti}_{1.44}\text{P}_3\text{O}_{12.40}$ . The composition was similar to that reported in the work of Fu<sup>79</sup>.

Table 2-20: The chemical composition of the LATP glass powder batch 1.

LATP	Li	O	Al	P	Ti
weight-%	2.18%	51.90%	4.73%	24.30%	18.00%
atom-%	6.41%	66.29%	3.58%	16.03%	7.68%
Overall chemical formula	$\text{Li}_{1.20}\text{Al}_{0.67}\text{Ti}_{1.44}\text{P}_3\text{O}_{12.40}$				

Table 2-21: List of the samples of LATP batch 1 fabricated with different process parameters and characterized with Dilatometry (DIL), XRD, scanning electron microscopy (SEM) and impedance spectroscopy (IS).

Sample No	Fabrication process parameters	Characterization methods
#1	Sintered at 1200°C for 6h	DIL, IS
#2	Sintered at 1100°C for 6h	DIL, IS, SEM
#3	Sintered at 1000°C for 6h	DIL, SEM, XRD
#4	Sintered at 900°C for 6h	DIL, IS
#5	Sintered at 950°C for 6h	DIL, IS
#6	Sintered at 1000°C for 3h	IS, SEM
#7	Sintered at 1000°C for 6h + 900°C 6h	IS
#8	Sintered at 900°C for 12h	IS, SEM
#9	Glass	DSC

### 2.4.1.1 DSC measurements

A sample pressed from the LATP powder was heated in a differential scanning calorimeter from 25°C up to 1200°C (sample #9, Figure 2-70). The glass transition onset temperature  $T_g$  of this sample was 588°C. The sample crystallized at 657°C. Another endothermic peak appeared at 1091°C. Two small peaks appeared at 842°C and 891°C on the cooling curve.

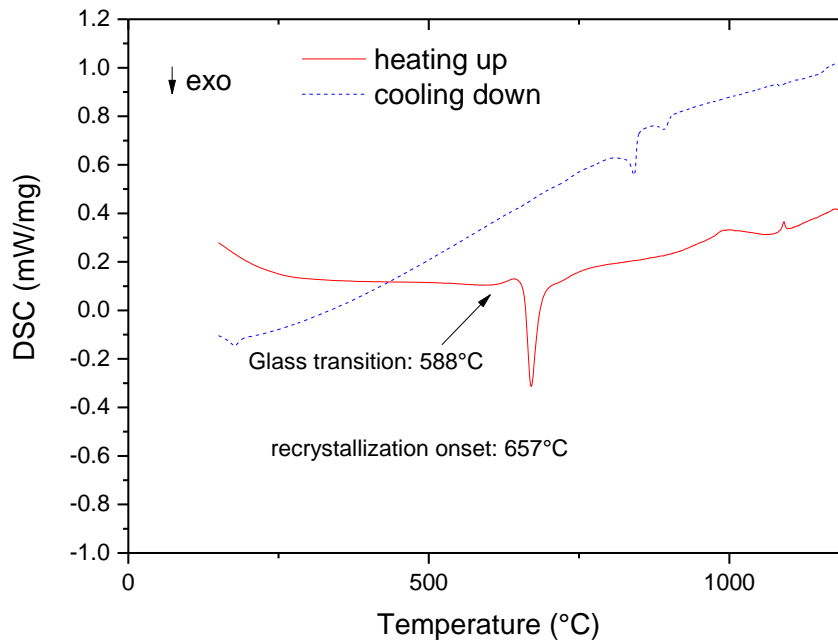


Figure 2-70: DSC curves of the LATP sample #9 pressed from the glass powder.

### 2.4.1.2 Dilatometry

Figure 2-71 shows the dilatometer curves of the samples, which were sintered between 900°C and 1200°C for 6 hours. The samples had the largest shrinking rate at the temperature 850° – 1000°C. The sample #4 sintered at 900°C had a shrinkage of 4% at the end of the sintering process. The shrinkage increased with increasing sintering temperature until 1000°C and decreased as the sintering temperature increased further to 1100°C and 1200°C. The sample #3 sintered at 1000°C showed the largest shrinkage of 20%.

## 2. Characterization of ceramic solid-state electrolytes

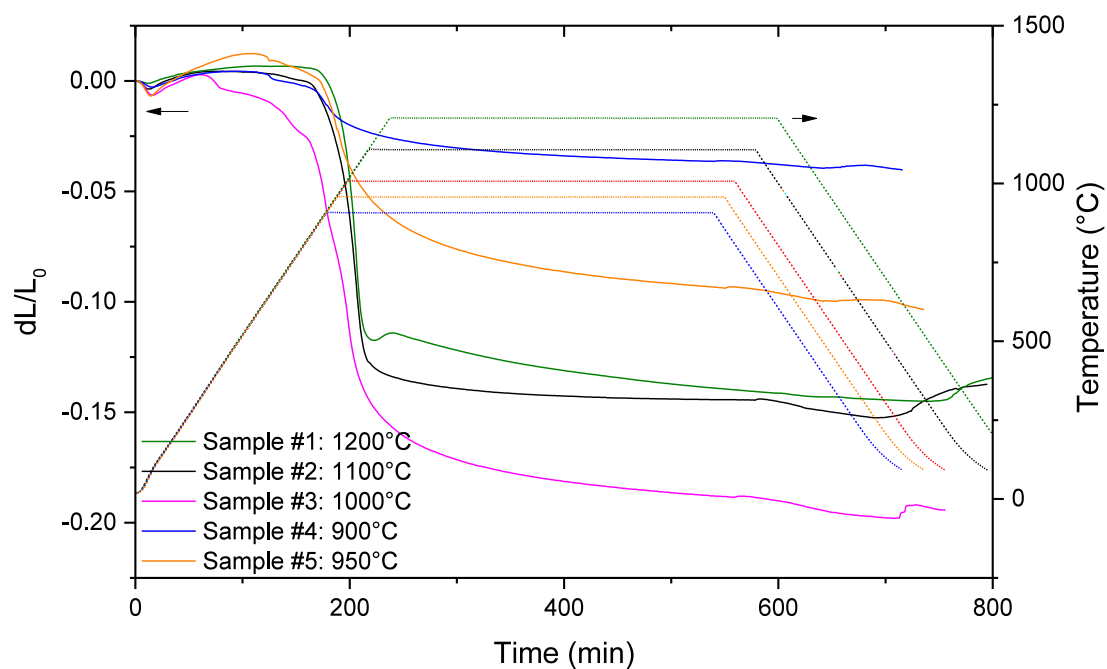


Figure 2-71: Dilatometer curves of LAMP samples #1–#5 during sinter process. The solid lines and the axis on the left show the shrinkage. The dash lines and the axis on the right show the temperature.

### 2.4.1.3 XRD measurement

XRD measurement was carried out on the sample #3, which was sintered at 1000°C for 6 hours. The diffractogram shows that the main phase has a structure of  $\text{LiTi}_2(\text{PO}_4)_3$  (PDF 35-754). The diffraction peaks of  $\text{AlPO}_4$  phase are also observed (PDF 45-478).

The LAMP phase has a hexagonal crystal system and the space group  $R\bar{3}c$  (space group number 167). The lattice parameters were calculated using a least squares refinement and are shown in Table 2-22.

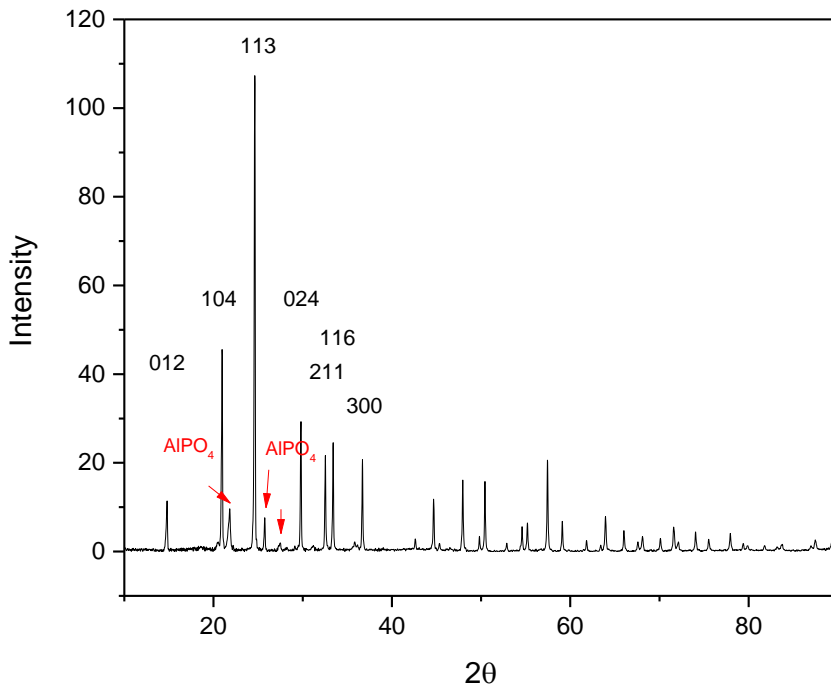


Figure 2-72: XRD diagram of the LATP sample #3 sintered at 1000°C for 6 hours. The lattice planes of  $\text{LiTi}_2(\text{PO}_4)_3$  are indicated on the corresponding peaks. The arrows indicate the diffractions of  $\text{AlPO}_4$ .

Table 2-22: Lattice parameters of the LATP phase.

a	$8.477 \pm 0.003 \text{ \AA}$
b	$8.477 \pm 0.003 \text{ \AA}$
c	$20.789 \pm 0.004 \text{ \AA}$
$\alpha$	$90^\circ$
$\beta$	$90^\circ$
$\gamma$	$120^\circ$
Volume	$1293.6 \text{ \AA}^3$

#### 2.4.1.4 Ionic conductivity

The ionic conductivities of the samples #1–#5, which were sintered for 6 hours at different temperatures, are shown in Figure 2-73. The numerical values of the ionic conductivity are shown in the appendix. The sample, which was sintered at 1000°C, showed the highest ionic conductivity ( $6.2 \cdot 10^{-4} \text{ S/cm}$  at room temperature and  $1.2 \cdot 10^{-2} \text{ S/cm}$  at 150°C). The ionic conductivity increased with increasing sintering temperature until 1000°C. However, the samples sintered at 1100°C and 1200°C had lower conductivity than the samples, which were sintered at 900°C and 950°C.

## 2. Characterization of ceramic solid-state electrolytes

Figure 2-74 shows the conductivity of the samples #3 and #6–#8. The sample #3 that was sintered at 1000°C for 6 hours showed a higher conductivity than the samples which were sintered for shorter and longer time.

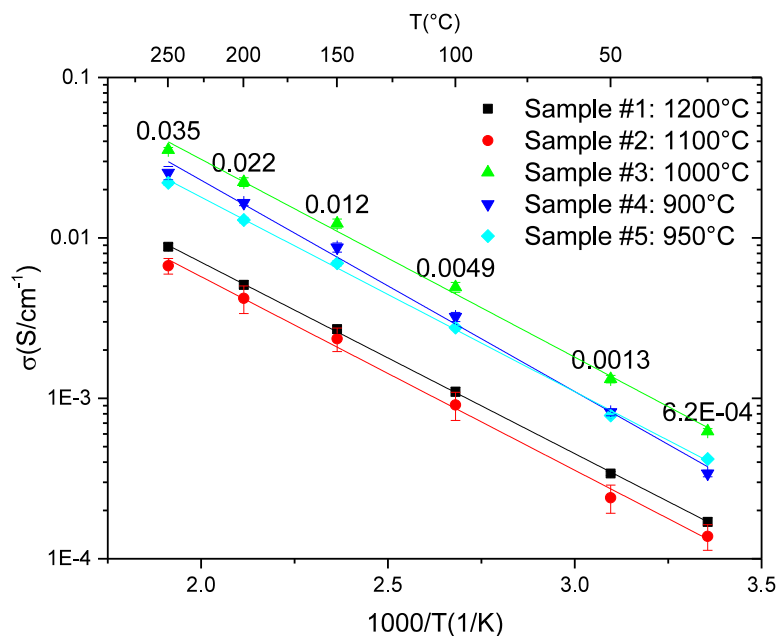


Figure 2-73: Ionic conductivity of LTP samples, which were sintered for 6 hours at different temperatures. The numerical values of the ionic conductivity are shown in the appendix Table A- 20 – Table A- 24.

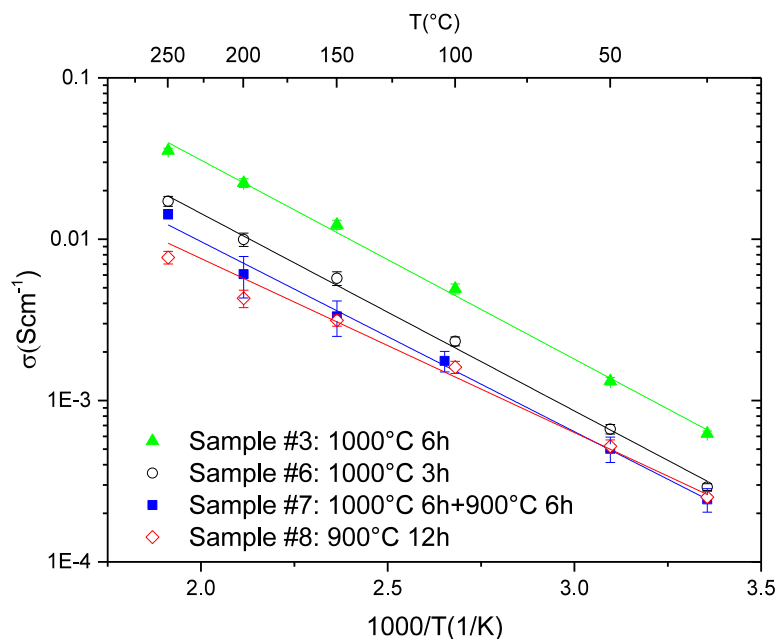


Figure 2-74: Ionic conductivity of LTP samples which were sintered for 3 – 12 h at 900°C and 1000°C. The numerical values of the ionic conductivity are shown in the appendix Table A- 22, Table A- 25 – Table A- 27.

#### 2.4.1.5 Scanning electron microscopy

Samples sintered at different temperatures were observed in SEM. The sample #8 sintered at 900°C for 12h showed large porosity (Figure 2-75-a). The pores are not isolated from each other. Porosity was also observed in the other samples. However, here these pores are not connected to each other (Figure 2-76-a, Figure 2-77 and Figure 2-78-a).

The size of ten well visible and randomly selected grains was measured on the SEM images of the fracture surfaces (Figure 2-75-b and Figure 2-76-b). The grains had the size of 0.6 – 1.1  $\mu\text{m}$  in the sample #8, which was sintered at 900°C for 12h (Figure 2-75-b), and increased to 1.1 – 2.1  $\mu\text{m}$  in the sample #6, which was sintered at 1000°C for 3h (Figure 2-76-b). The grain size enlarged further to over 5  $\mu\text{m}$  in the sample #2, which was sintered at 1100°C (Figure 2-78-b).

The secondary phase  $\text{AlPO}_4$  is visible in the matrix in the samples, which were sintered at 1000°C (#3 and #6) and 1100°C (#2). The secondary phase accumulated at the grain boundaries. The size of secondary phase is significantly larger in the sample #2, which was sintered at 1100°C. (Figure 2-76-a, Figure 2-77 and Figure 2-78-a).

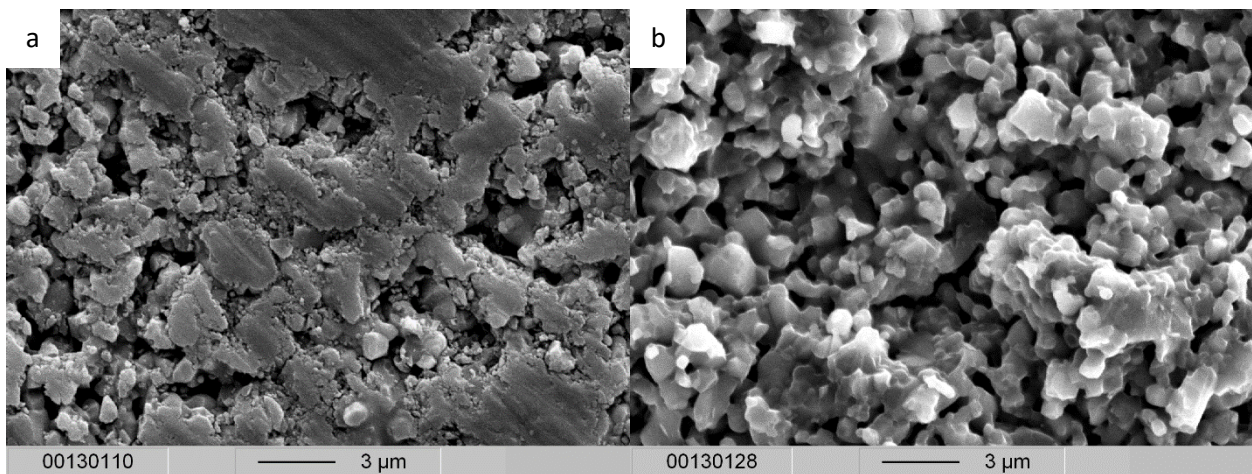


Figure 2-75: Sample #8, which was sintered at 900°C for 12 hours. a: Polished surface with 5000x magnification; b: Fracture surface with 5000x magnification.

## 2. Characterization of ceramic solid-state electrolytes

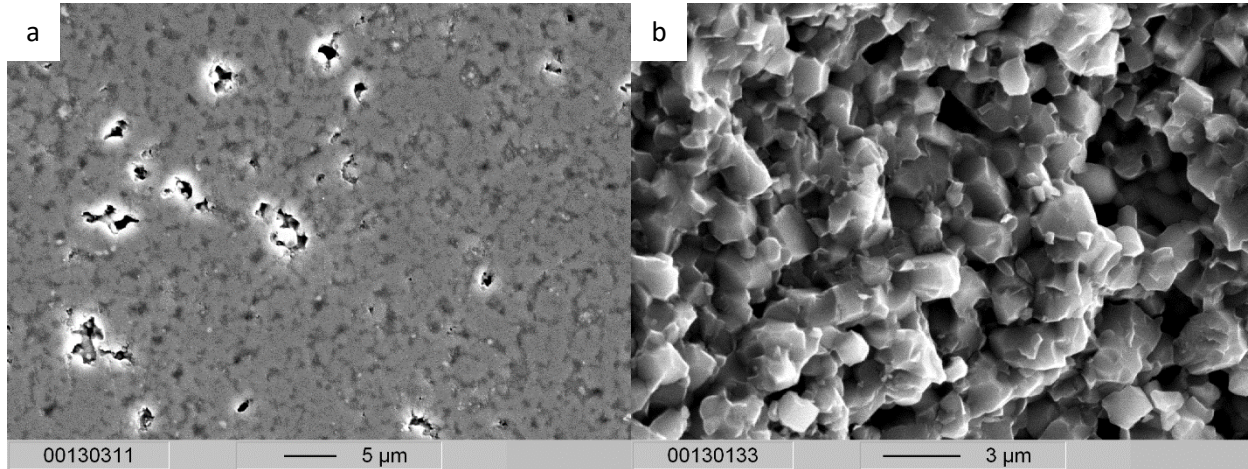


Figure 2-76: Sample #6, which was sintered at 1000°C for 3 hours. a: Polished surface with 2000x magnification; b: Fracture surface with 5000x magnification.

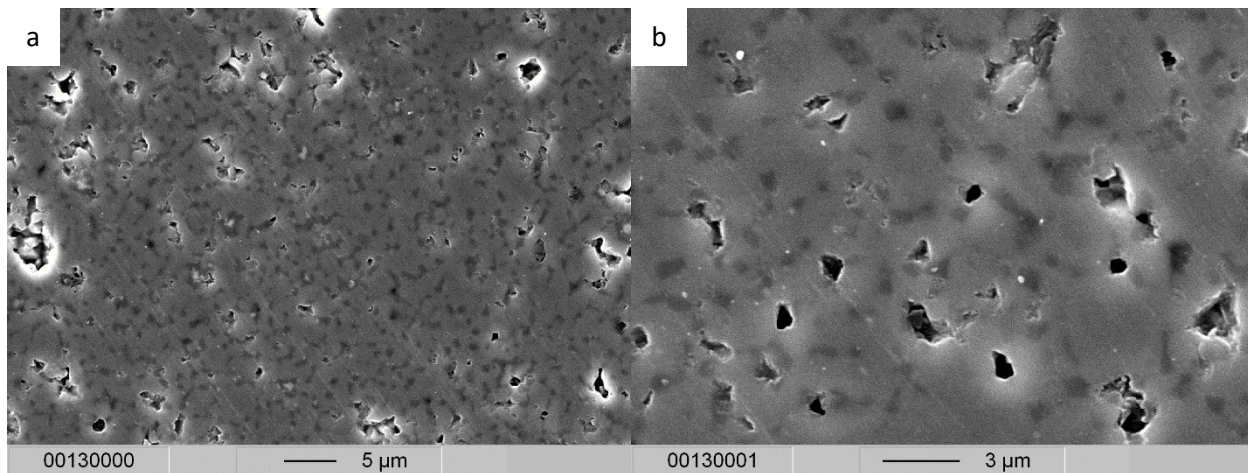


Figure 2-77: Polished surface of the sample #3, which was sintered at 1000°C for 6 hours. a: 2000x magnification; b: 5000x magnification.

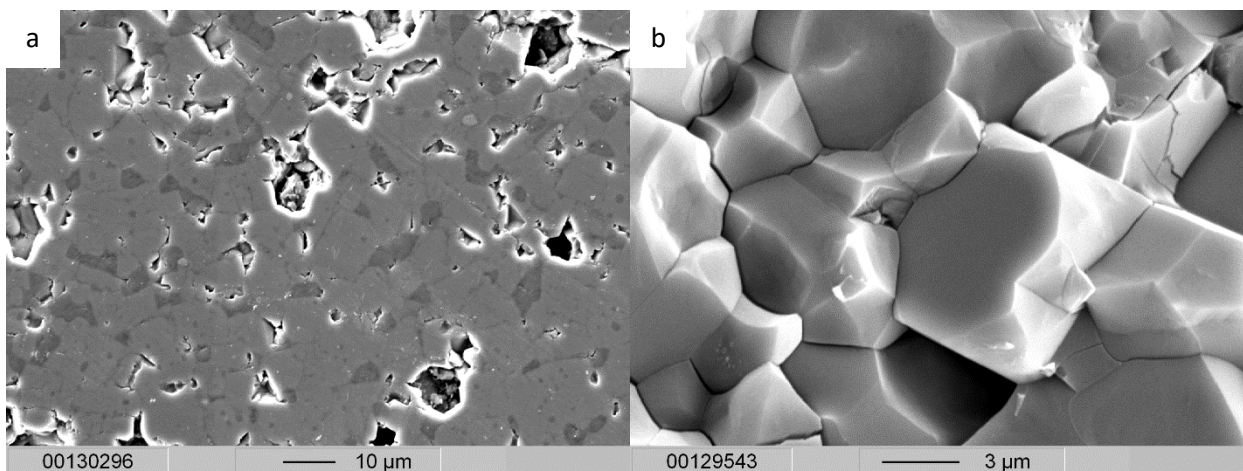


Figure 2-78: Sample #2, which was sintered at 1100°C for 6 hours. a: Polished surface with 1000x magnification; b: Fracture surface with 5000x magnification.

#### 2.4.1.6 Density

The theoretical density of the LATP crystal was calculated from the lattice parameters measured by the XRD. The theoretical density of the LATP crystal is 2.977 g/cm<sup>3</sup>. The densities of the samples were measured with the Archimedes method without Zapon lacquer (see 2.1.5). Table 2-23 shows the density and the relative density of these samples. The uncertainty of the density was estimated to be around 0.4%.

Table 2-23: Density and relative density of the LATP samples.

Sample	Density (g/cm <sup>3</sup> )	Relative density
1. 1200°C 6h sintered	2.66	89.3%
2. 1100°C 6h sintered	2.75	92.5%
3. 1000°C 6h sintered	2.82	94.7%
4. 950°C 6h sintered	2.79	94.0%
5. 900°C 6h sintered	2.76	92.7%

## 2.4.2 Discussion

Summarizing the experimental results: The sample, which was sintered at 1000°C for 6 hours, had the highest ionic conductivity among all the samples (Figure 2-73, Figure 2-74). This sample showed also the largest shrinkage in dilatometer measurement (Figure 2-71) and the highest density (Table 2-23).

On the X-ray diffractograms, the diffractions of the main phase LiTi<sub>2</sub>(PO<sub>4</sub>)<sub>3</sub> (PDF 35-754) and the minor phase AlPO<sub>4</sub> (PDF 45-478) could be identified. The LATP phase has the same crystal structure as the LiTi<sub>2</sub>(PO<sub>4</sub>)<sub>3</sub> phase.

## 2. Characterization of ceramic solid-state electrolytes

As shown on the SEM images (Figure 2-75 - Figure 2-78), the sample sintered at 900°C showed large porosity, which had negative effect on the ionic conductivity. The samples sintered at 1000°C had lower porosity and the contact between the grains was largely improved. In the sample sintered at 1100°C, the size of the grains increased by several times. The larger grain size is beneficial for the ionic conductivity, since the grains have better ionic conductivity as the grain boundary. However, the ionic conductivity of the sample, which was sintered at 1100°C, was lower than the sample sintered at 1000°C and 900°C. On the other hand, the  $\text{AlPO}_4$  secondary phase was observed in the matrix. The size of the secondary phase increased significantly as the sample was sintered at 1100°C. The decreased ionic conductivity of the sample sintered at 1100°C could be attributed to the increased size of the  $\text{AlPO}_4$  secondary phase. The larger  $\text{AlPO}_4$  phase at the grain boundaries blocked the ion transport and the sample had therefore a lower ionic conductivity despite the larger grains.

In the work of Fu, a highest conductivity value of  $1.3 \times 10^{-3} \text{ Scm}^{-1}$  at room temperature was reported on the LATP sample, which was heat-treated at 950°C for 12 hours. This conductivity value is higher as the conductivity obtained in this work ( $6.2 \times 10^{-4} \text{ Scm}^{-1}$ ). The conductivity values reported in other literature are mostly significantly lower than reported by Fu and comparable with the value measured in this work ( $1.5 \times 10^{-4} \text{ S/cm}^{123}$ ,  $6.5 \times 10^{-4} \text{ S/cm}^{124}$ ,  $7 \times 10^{-4} \text{ S/cm}^{125}$ ). However, the influence of the minor phase was not revealed in the work of Fu and in the other works.

### 3 Test of lithium ion cells with solid-state electrolyte

The LAGP and LATP solid-state electrolytes have an ionic conductivity in the order of  $10^{-4}$  S/cm at room temperature and  $10^{-2}$  S/cm at 150°C. The ionic conductivity of the LAGP/LATP solid-state electrolyte at elevated temperature is comparable with that of liquid electrolyte ( $\approx 10^{-2}$  S/cm) and higher than polymer electrolytes (lower than  $10^{-3}$  S/cm) and ionic liquids (lower than  $10^{-2}$  S/cm) at room temperature<sup>30, 126–128</sup>. It is therefore possible to apply the LAGP/LATP as solid-state electrolyte and test the electrochemical behavior in lithium ion cells, which is also one of the objectives of this work.

Lithium ion cells were assembled to test the functionality of LAGP and LATP as solid-state electrolyte. LiCoO<sub>2</sub> (LCO) and Li<sub>4</sub>Ti<sub>5</sub>O<sub>12</sub> (LTO) were used as cathode materials in different cells. Li metal, graphite and Li<sub>4</sub>Ti<sub>5</sub>O<sub>12</sub> (LTO) were used as anode materials (Table 3-1). Liquid electrolyte was used in some cells to assist the ion transport at the interface between the electrodes and the solid-state electrolyte.

*Table 3-1: Test cells with different configurations and electrode materials.*

name	anode	electrolyte	cathode
Li-LAGP+LP30-LCO	Li metal	LAGP pellet wetted with LP30 liquid electrolyte (1M LiPF <sub>6</sub> in 1:1 EC/DMC solvent)	LiCoO <sub>2</sub>
Li-LAGP+LP30+sep-LCO	Li metal	LAGP pellet and glass fiber separator soaked with LP30 liquid electrolyte	LiCoO <sub>2</sub>
C-LAGP+LP30-LCO	graphite	LAGP pellet wetted with LP30 liquid electrolyte	LiCoO <sub>2</sub>
LTO-LAGP+LP30-LCO	Li <sub>4</sub> Ti <sub>5</sub> O <sub>12</sub>	LAGP pellet wetted with LP30 liquid electrolyte	LiCoO <sub>2</sub>
LTO-LATP+LP30-LCO	Li <sub>4</sub> Ti <sub>5</sub> O <sub>12</sub>	LATP pellet wetted with LP30 liquid electrolyte	LiCoO <sub>2</sub>
Li-LAGP-LTO	Li metal	LAGP pellet (all solid state)	Li <sub>4</sub> Ti <sub>5</sub> O <sub>12</sub>
Li-LAGP-LCO	Li metal	LAGP pellet (all solid state)	LiCoO <sub>2</sub> thin layer

### 3. Test of lithium ion cells with solid-state electrolyte

#### 3.1 Lithium ion battery cell assembly and test

The lithium ion test cells are integrated in a tube connector produced by the Swagelok® Company. Cells with this construction are usually called “Swagelok cell” in the literature. The tube connector is designed to connect two tubes watertight together. For the application as cell package, the tubes are replaced with two electrode bolts made of steel. The connector and the bolts enclose a space where the electrochemical active materials can be placed. The structure of the Swagelok cell is shown in Figure 3-1. Anode, electrode, cathode, current collector and a spring are all mounted in the cell. One of the electrode bolts and the inner surface is isolated with a PTFE (Teflon) foil to avoid short circuits. The assembling work was carried out in a glove box filled with argon.

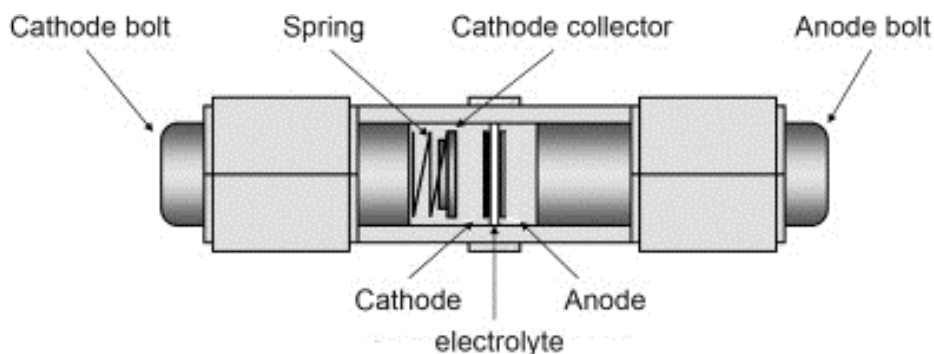


Figure 3-1: Schematic presentation of a Swagelok lithium ion cell.

##### 3.1.1 Hybrid cell with liquid and solid-state electrolyte

Since the LAGP and LATP samples are rigid pellets and the cathode materials are also solid, it is difficult to get sufficient contact at the interface for the ion migration. One solution is to use a liquid electrolyte at the interface between the electrolyte and electrodes. A commercial liquid electrolyte LP-30 electrolyte (1M LiPF<sub>6</sub> in 1:1 EC/DMC solvent) was used.

The LAGP and LATP solid-state electrolyte was fabricated using the optimized sintering or heat-treating procedure found in this work (800°C 6h for LAGP and 1000°C 6h for LATP). The pellet samples had a diameter of about 9 mm and were ground as thin as 0.3 mm – 0.4 mm.

The cathode material is a mixture of LiCoO<sub>2</sub> (LCO, active material), carbon black (electrical conducting agent) and polyvinylidene difluoride (PVDF, binder). The LCO (90 wt.%), carbon black (5 wt.%) and PVDF (5 wt.%) was weighted, mixed and suspended in isopropanol (2-Propanol) by stirring with a magnetic stirrer. The suspension was heated to 80°C and the suspension became increasingly viscous as the isopropanol evaporated. The mixture was further dried at 100°C in a drying chamber and the cathode mixture was obtained as powder. Pellets with the thickness of 0.4 mm and the diameter of 10 mm were pressed. The cathode pellets were weighted and their theoretical capacity was calculated from the weight of the LCO

and the specific capacity of LCO (140mAh/g). A gold current collector was sputtered on one side of the pressed pellets.

The lithium anode was prepared in the glovebox before the cell assembly. The anode was cut out of a lithium metal foil with a 9 mm diameter punching tool. A round Li foil with 1 mm thickness and 9 mm diameter was obtained. The lithium metal was brushed to remove the oxide and nitride from the surface and assembled in the cell.

Alternatively to the Li metal anode,  $\text{Li}_4\text{Ti}_5\text{O}_{12}$  (LTO) was used in several cells. It has a potential of 1.5 V vs.  $\text{Li}^+/\text{Li}$  and can serve as anode vs.  $\text{LiCoO}_2$  cathode. LTO pellets were prepared using the same procedure as the LCO pellets mentioned above.

The Swagelok cell was assembled in the glovebox. The anode bolt was isolated with a PTFE (Teflon) foil and mounted on the Swagelok connector. The lithium anode was pressed on the solid-state electrolyte pellet. One droplet of liquid electrolyte was dropped on the solid-state electrolyte pellet. The cathode pellet was then placed on the wetted solid-state electrolyte pellet. The anode-electrolyte-cathode pellet was mounted with an aluminum spacer/current collector, a spring and the cathode bolt in the Swagelok connector. The screws of the Swagelok connector were tightened to ensure the gas-tightness of the cell. The voltage of the cell was checked with a portable multimeter to make sure that the cell is properly assembled. In some cells, the lithium metal anode and the solid-state electrolyte were separated with a glass fiber separator. The separator was soaked with liquid electrolyte LP30 in order to keep the ionic conductivity.

### 3.1.2 All solid state cell with LAGP solid-state electrolyte

Three different methods were used to fabricate all solid-state test cells:

The slurry deposition method was carried out first to produce the cathode-electrolyte pellet. The cathode mixture suspension was prepared with the same procedure as mentioned in 3.1.1. A slurry was made from the suspension by controlled evaporation of the isopropanol solvent. Several droplets of the suspension slurry were dripped on the top side of a solid-state electrolyte pellet. The pellet was then dried on a heating plate and a cathode layer was formed. This cathode-electrolyte pellet was assembled with the lithium metal anode in a Swagelok cell.

The sintering method was applied to produce the cathode-electrolyte pellet.  $\text{Li}_4\text{Ti}_5\text{O}_{12}$  (LTO) (47 wt.%) was mixed with carbon black (3 wt.%) and LAGP glass powder (50 wt.%) and thoroughly mixed. A cathode-electrolyte 2-layer pellet was pressed using the LTO-LAGP powder and LAGP powder. The pellet was then sintered in vacuum. However, this method does not work with  $\text{LiCoO}_2$  (LCO). The LCO+LAGP+carbon black mixture has a different shrinkage as the LAGP during sintering. The pellet delaminates during sintering and breaks. After sintering, the cathode layer and the electrolyte layer of the tablet were ground to 0.5 mm each. A gold current collector was sputtered on the cathode. The pellet was dried in a temperature chamber at 100°C to expel the moisture and assembled in Swagelok cells with the lithium metal anode.

Radio frequency (RF) magnetron sputtering was also used to fabricate the cathode-electrolyte two-layer pellet. LAGP pellets were coated with a  $\text{LiCoO}_2$  layer on the top side: The pellets were ground to a thickness

### 3. Test of lithium ion cells with solid-state electrolyte

of about 4 mm, polished and positioned in the RF-magnetron sputtering chamber. A cover with an 8 mm diameter hole over the pellet ensured that only the top side of the pellet was coated. The LiCoO<sub>2</sub> (LCO) target was positioned on the opposite side of the chamber. A pre-sputtering treatment was performed to clean the target surface for 12 min using argon plasma (0.5 Pa). After that, the argon atmosphere in the chamber was set to 10 Pa. The LCO target was sputtered and a LCO-film was deposited on the LAGP pellet with a deposition rate of 20nm/min and a deposition time of 230 min. The cathode-electrolyte pellets with lithium metal anode were assembled in Swagelok cells as mentioned before. The RF-magnetron sputtering were carried out by Dr. Julian Fischer at the “Abteilung Stoffverbunde und Dünnschichten” of the IAM-AWP.

#### 3.1.3 Galvanostatic cycling with potential limitation

The assembled cells were tested using galvanostatic cycling, i.e. the cells are charged and discharged with constant current (CC). The battery tester regulates the charge voltage to keep the preset current constant. The voltage is recorded vs time. After the voltage reaches the preset high potential limit, the current is cut off and switched to discharging mode. The discharge current is held constant while the discharge voltage is recorded. When the discharge voltage drops below the lower preset limit, the current is cut off and switched back to charging mode.

In this study, an Arbin BT2000 battery tester and a BioLogic BCS-815 battery cycling system were used for the galvanostatic cycling test. Cycling parameters can be set in the controlling program, including the charge and discharge current, the high and low voltage limit and the cycle number. In addition, the measurement range and data recording frequency could be set.

All solid state cells were tested at elevated temperatures up to 150°C. The tests were carried out in a temperature chamber with an air fan for homogenous temperature distribution. A heatproof cell holder was placed in the furnace and connected with the cell tester outside with heatproof cables.

#### 3.1.4 Cyclic voltammetry

The cyclic voltammetry (CV) measurement was carried out to investigate the stability of the LAGP solid-state electrolyte. The cyclic voltammetry (CV) is a potentiodynamic electrochemical measurement. A sweeping potential is applied to the material to be tested (working electrode, LAGP) vs the reference electrode. The potential is scanned with a constant rate. After the preset maximum or minimum potential is reached, the potential ramps in the inverse direction to the other potential limit.

The cyclic voltammogram presents the current through the working electrode plotted vs the voltage applied between the working and the reference electrode. The voltammogram contains information of the chemical reaction, which takes place during the cyclic voltammetry. It can be used to study the redox processes, the electron transfer kinetics, the reversibility of a reaction and the reduction potential<sup>129, 130</sup>.

In this work, test cells for cyclic voltammetry were built in form of a Swagelok cell. Due to the geometry of the Swagelok cells, a two-electrode electrolysis system was applied for the cyclic voltammetry (working electrode + reference/counter electrode). A LAGP pellet was connected with the positive pole as working

electrode. Li metal was connected to the negative pole and worked both as a reference and a counter electrode. In hybrid cells, the LP30 was used as electrolyte. In all solid-state cells, the LAGP itself worked as the electrolyte.

The CV measurements were carried out using the cyclic voltammetry function of the BioLogic BCS-815 battery cycling system. The scanning rate, the scanning potential window and the cycle number were set in the control program for the CV measurement.

### 3.1.5 Impedance spectroscopy on cell

In order to evaluate the internal resistance, the impedance spectroscopy was carried out on the assembled test cells. The resistance of the cell can be evaluated with help of the Nyquist-diagram.

The measurements were carried out using the impedance spectroscopy function of the BioLogic BCS-815 battery cycling system. The cells were connected with the tester in the same way as for the cycling test. The measurements were carried out at room temperature as well as at elevated temperatures up to 150°C.

### 3. Test of lithium ion cells with solid-state electrolyte

## 3.2 Cell tests and post mortem investigation

### 3.2.1 Cells with hybrid solid + liquid electrolyte

In a conventional lithium ion battery, graphite is used as anode material.  $\text{LiCoO}_2$ ,  $\text{LiNi}_x\text{Mn}_y\text{Co}_z\text{O}_2$  or  $\text{LiFePO}_4$ , etc. are used as cathode material. These anode and cathode materials have the form of small particles, which are deposited on the current collector together with binder and electron conducting agent (as shown in Figure 3-2-a). The liquid electrolyte is filled between anode and cathode. A separator prevents the direct electron-conducting path between the anode and cathode. Since the electrolyte is liquid, it could wet the entire electrode surface regardless of its roughness. The electrodes have therefore perfect contact with the electrolyte.

If the liquid electrolyte and the separator are replaced with solid-state electrolyte without any adaption, the cell structure would be like Figure 3-2-a. The particles cannot form a perfect surface. In addition, the LAGP/LATP solid-state electrolyte cannot deform to match the rough surface of the electrodes. Only a small part of the electrode surface gets into contact with the solid-state electrolyte, which would result in a high resistance at the interface. Therefore, the first test cells were assembled using LAGP solid-state electrolyte + liquid electrolyte (LAGP + LP30). The liquid electrolyte can wet the interface and assist the ion transport at the interface between the electrodes and the solid-state electrolyte (Figure 3-2-b).

The LAGP samples sintered from the high Li LAGP (batch 1, 800°C 6h sintered) and LATP samples sintered from the LATP powder (batch 1, 1000°C 6h sintered) were applied as solid electrolyte.

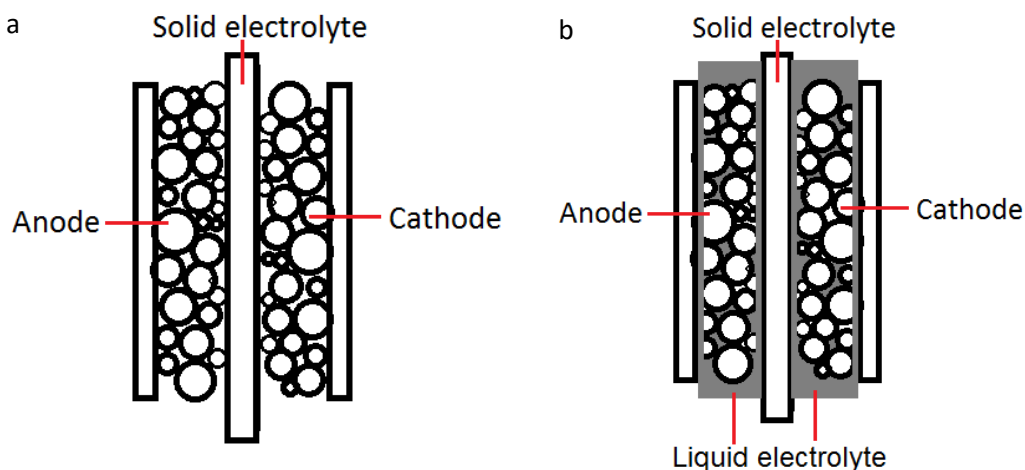


Figure 3-2: Schematic presentation of lithium ion cells with rigid solid-state electrolyte. a: without adaption of liquid electrolyte; b: with liquid electrolyte at the electrode-electrolyte interface.

### 3.2.1.1 Li-LAGP+LP30-LCO cells

The LAGP solid electrolyte pellets have a diameter of 9 mm. They were ground to a thickness of 0.4 mm and polished to get a mirror surface. After the preparation, the LAGP pellets were assembled with other components ( $\text{LiCoO}_2$  (LCO) cathode, lithium (Li) metal anode, LP30 liquid electrolyte and current collector) in Swagelok cells. The structure of the cells is shown in Figure 3-3. The interface between the cathode, the LAGP solid-state electrolyte and the Li metal anode was wetted with LP30 liquid electrolyte. The cells are designated as the Li-LAGP+LP30-LCO cells.

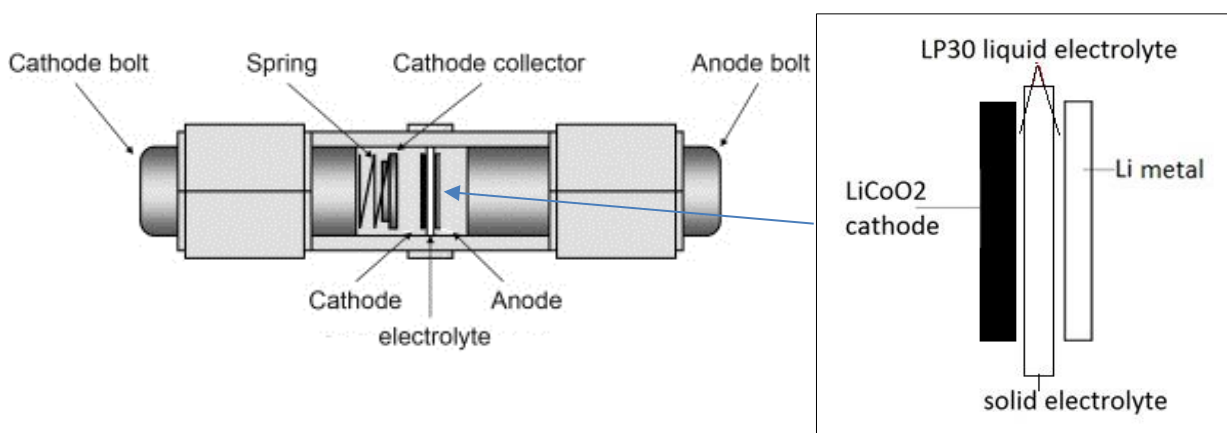


Figure 3-3: Schematic presentation of a Li-LAGP+LP30-LCO cell.

The assembled cells were tested with an Arbin BT2000 tester at room temperature. The cells were charged with a current of 0.4 mA. The current of 0.4 mA corresponds to a charging rate of 0.1 C, since the  $\text{LiCoO}_2$  cathodes have a theoretical capacity of 4 mAh.

The test result of the Li-LAGP+LP30-LCO cell-1 is shown in Figure 3-4. The voltage and current are plotted vs the test time. The  $\text{LiCoO}_2$  cathode (LCO) was initially in the lithium rich state, i.e. the cells were in discharged state as assembled. The cell had a voltage of 3.2 V at the beginning of the test, which matched the voltage of the  $\text{LiCoO}_2$  vs Li in discharged state<sup>131, 132</sup>. It shows that the cell was properly assembled and the electrical circuit was closed.

The voltage of the cell increases as the Li ions are extracted from the  $\text{LiCoO}_2$ . The voltage of the cell Li-LAGP+LP30-LCO cell-1 increased to a plateau at 3.97 V – 3.98 V in short time (13 min). The voltage of the plateau is higher than that of a lithium ion cell using liquid electrolyte<sup>133, 134</sup>. The difference can be attributed of the higher resistance of the LAGP solid-state electrolyte; the cell using LAGP solid-state electrolyte has a high internal resistance. A higher charging voltage is therefore required to overcome this resistance and achieve the required charging current.

After 40 min at the voltage plateau of 3.97 V – 3.98 V, The voltage had an unexpected drop from 3.98 V to 3.93 V. The cell voltage became unstable and did not increase further as in normal Li ion cells for the next 23 hours. The 23 hours of charging at 0.4 mA exceeded twice the cathode capacity (The  $\text{LiCoO}_2$  cathode had a theoretical capacity of 4 mAh). The cell voltage should increase when  $\text{Li}^+$  ions are extracted from the

### 3. Test of lithium ion cells with solid-state electrolyte

LiCoO<sub>2</sub> cathode, which did not occur in this cell. It shows that the cell was not properly charged since the initial electrochemical reaction was interrupted.

After the tester was manually switched to discharge mode, the voltage had a drop from 3.93 V to 3.81 V. The cell had discharged for only 2 hours before the voltage dropped to 3.0 V. In the second cycle, the cell showed the same behavior as in the first cycle.

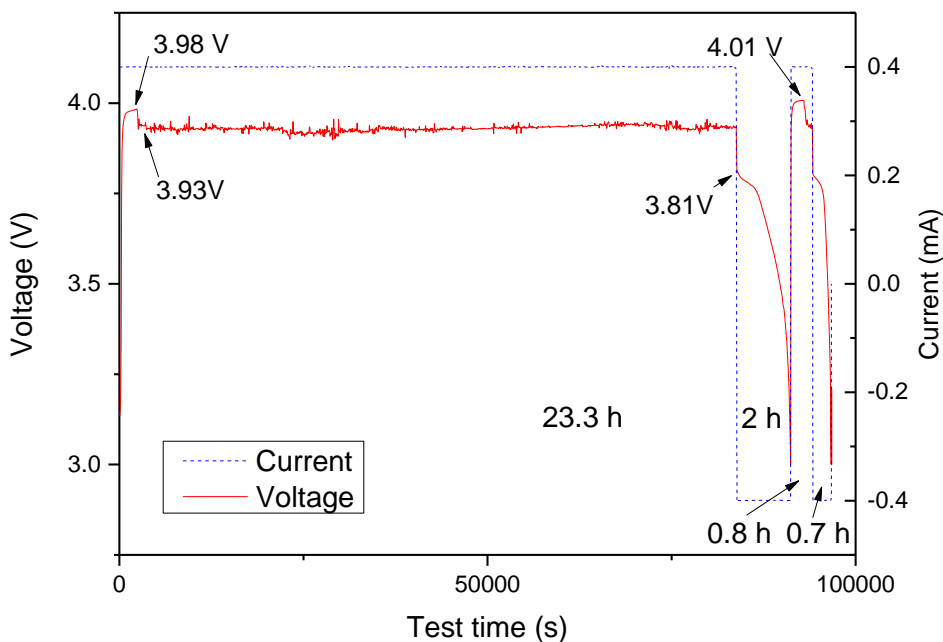


Figure 3-4: Charge and discharge test of the Li-LAGP+LP30-LCO cell-1.

An internal short circuit could explain the abnormal behavior by charging of the Li-LAGP+LP30-LCO cell: The cell showed a normal behavior when Li<sup>+</sup> ions were extracted from the LCO cathode and transported to Li anode at the beginning of the test. As the cell was further charged, an electron-conducting route was formed in the cell between the cathode and anode (a bypass for electric current). As the result, the electrochemical cell became an ohmic resistor. As the bypass was formed, the current flowed through it and the cell voltage had a drop. Assuming that all the current (0.4 mA) flowed through the bypass and the full voltage (3.93 V) was applied on the bypass, the resistance of the bypass can be estimated to 9.8 kΩ. The unstable voltage indicates that the electronic conducting bypass was unstable.

The cell could provide current in the discharging periods, showing that the electronic conducting bypass was broken in the discharging period. The cell had a voltage of 3.81 V at the beginning of discharge. The lower voltage shows that the cell was not fully charged, which also confirms that charging current had flown through the bypass. The cell was discharged for 121 min until the voltage decreased to 3.0 V, which is much shorter than the charging time. Different as by charging, the voltage had no fluctuation, showing that the electronic circuit was stable.

A second cell was assembled with the same material. The test result of the Li-LAGP+LP30-LCO cell-2 is shown in Figure 3-5. The cell showed the same behavior as the first cell. The voltage had a sudden drop after the cell was charged for 1 hour and became unstable. After the test was switched to discharge mode, the cell could be discharged normally but for a shorter time.

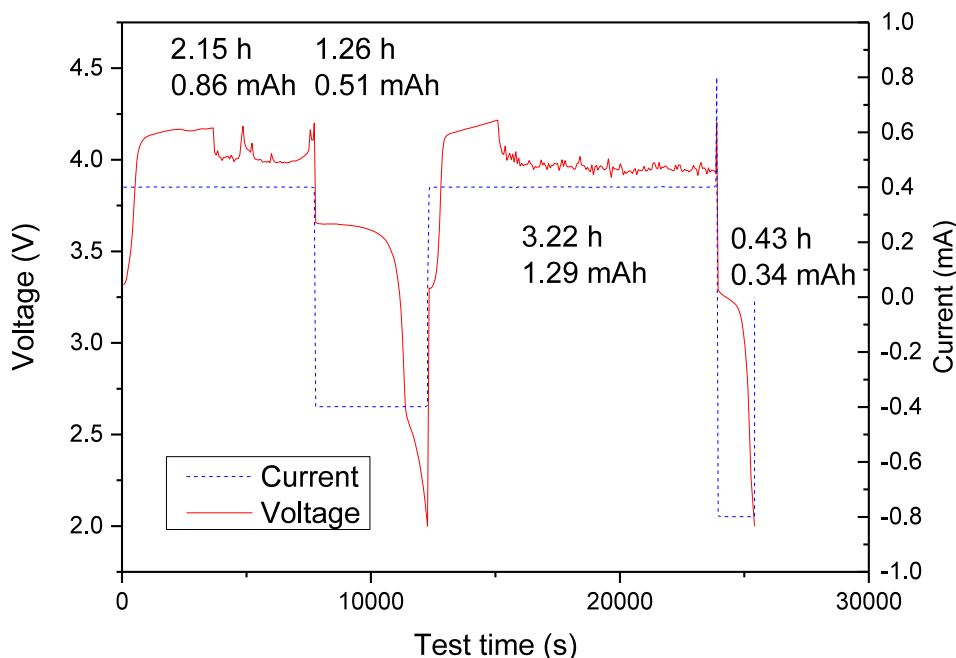


Figure 3-5: Charge and discharge test of the Li-LAGP+LP30-LCO cell-2.

The electronic conducting bypass could be formed by lithium dendrites. It is well known that lithium dendrites are formed on the Li anode while the lithium ion cell is charged<sup>135</sup>. It is likely that cracks were formed on the LAGP electrolyte and Li dendrites grew into the cracks. Since the interface was wetted with liquid electrolyte, the liquid electrolyte could fill the cracks. Since the cracked area had the smaller thickness of the solid-state electrolyte pellet, current concentrated on the cracked area. The Li dendrites grew faster in that area and penetrated the solid electrolyte.

After the cycling tests, the cells were disassembled and checked in a glove box with Argon protecting atmosphere. On the cathode side of the LAGP solid-state electrolyte, which was in contact with the LiCoO<sub>2</sub> cathode in the test cell, no remarkable change was observed. Cracks were observed on the solid-state electrolyte pellet and the pellet was broken in several pieces. On the other side of the pellet, a black substance was formed at the interface between the Li anode and LAGP solid-state electrolyte.

The disassembled LAGP solid-state electrolyte and the Li anode was further inspected in the SEM. Figure 3-6 shows the SEM images of the anode side of the LAGP solid-state electrolyte, which was in contact with the Li anode during the test. The surface was initially polished. After the test, it became uneven in certain areas. An unidentified substance was formed at the interface between the Li anode and the LAGP solid-

### 3. Test of lithium ion cells with solid-state electrolyte

state electrolyte. Figure 3-7 shows the SEM image of the Li anode after the test. Lithium dendrites were observed on the Li anode. An unidentified substance was also observed.

The substance formed at the LAGP-Lithium interface is different as the Li dendrites (see Figure 3-6 and Figure 3-7-a), showing that there was a reaction on the LAGP solid-state electrolyte. In addition, the LAGP sample with this substance was exposed in air after the SEM inspection. The black substance remained on the sample and did not change its color. On the other hand, when elemental lithium is exposed in air, it will react with the  $O_2$ ,  $H_2O$ ,  $N_2$  and  $CO_2$  and finally form the  $Li_2CO_3$ , which has a white color.

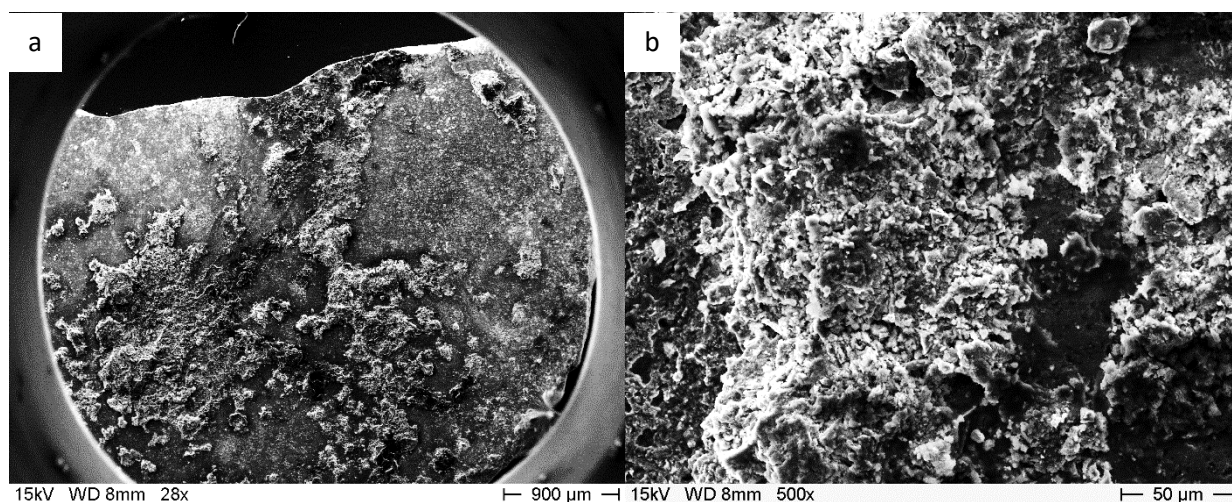


Figure 3-6: SEM images of the LAGP solid-state electrolyte after test. a: The LAGP solid-state electrolyte with the interface neighboring the Li anode in the test cell (28x magnification); b: the reaction area on the LAGP solid electrolyte (500x magnification).

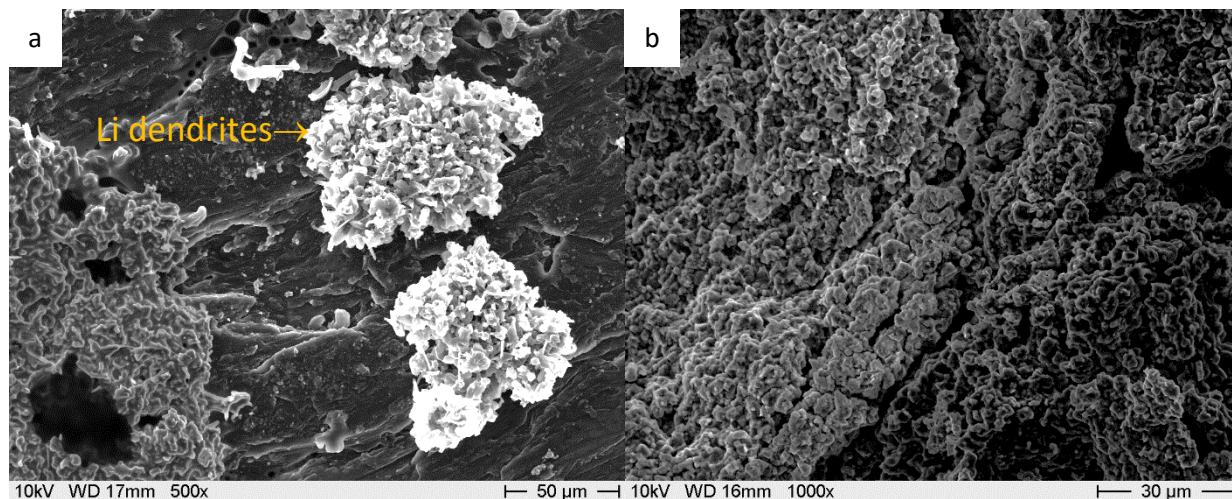


Figure 3-7: The Li metal anode after test. a: the lithium dendrites (bright on the right) and the unidentified reaction product (dark on the left) on the Li anode (back ground) (500x magnification); b: the reaction product in higher magnification.

### 3.2.1.2 Li-LAGP+LP30+sep-LCO cells

Due to the reaction at the interface between the Li anode and the LAGP, a glass fiber separator was applied at the interface between the LAGP solid-state electrolyte and the Li anode. The structure of the cell is presented in Figure 3-8. The glass fiber separator was soaked with the LP30 liquid electrolyte and placed between Li anode and LAGP solid-state electrolyte. Disregarding this exception, the cell structure was identical as the previous built cells. These cells are designated as Li-LAGP+LP30+sep-LCO cell.

The cells were tested in the same procedure as the previous cells. The test results of the Li-LAGP+LP30+sep-LCO cell-1 are shown in Figure 3-9. The cell was charged and discharged with 0.1 mA current in the first 2 cycles and with the current of 0.5 mA in the following cycles. Unlike the previous cells, this cell could be properly charged and discharged. The cell had a charge capacity of 3.88 mAh and a discharge capacity of 3.46 mAh at 0.1 mA charge/discharge current in the 2<sup>nd</sup> cycle. When the current increased to 0.5 mA, the charge capacity decreased to 1.72 mAh and the discharge capacity to 1.55 mAh in the 3<sup>rd</sup> cycle (see Figure 3-10).

After the test, this cell was also disassembled in argon atmosphere. The LAGP pellet was stable and not broken. Li dendrites had grown from the Li anode into the separator but not penetrated the separator. It shows that the cell could operate properly when the LAGP pellet was not in contact with lithium.

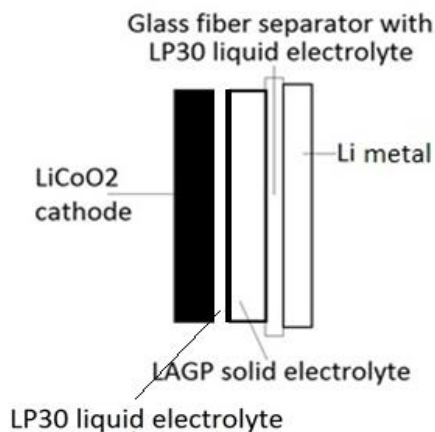


Figure 3-8: Schematic presentation of the Li-LAGP+LP30+sep-LCO cells with glass fiber separator between Li anode and LAGP solid-state electrolyte.

### 3. Test of lithium ion cells with solid-state electrolyte

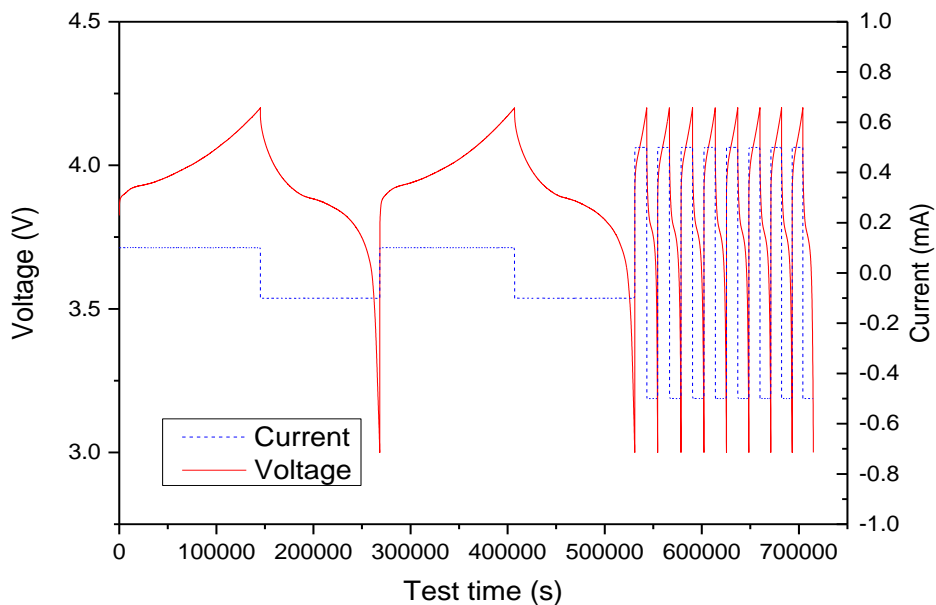


Figure 3-9: Charge and discharge test of the Li-LAGP+LP30+sep-LCO cell-1 with glass fiber separator between Li anode and LAGP solid-state electrolyte.

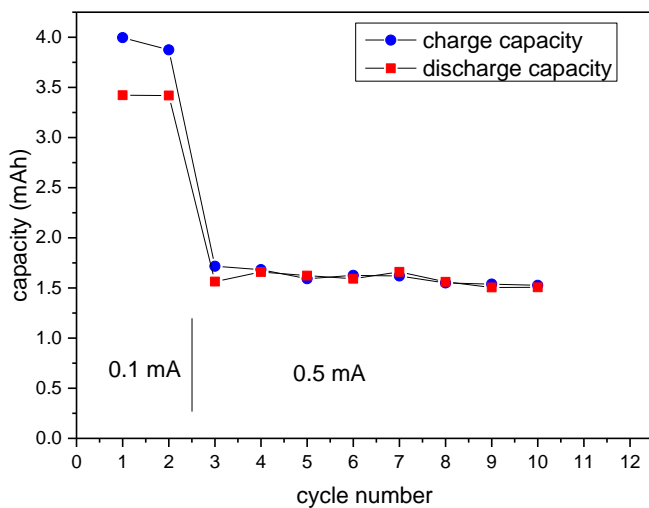


Figure 3-10: charge and discharge capacity of the Li-LAGP+LP30+sep-LCO cell-1.

Another cell (Li-LAGP+LP30+sep-LCO cell-2) with the same structure was tested and the result is shown in Figure 3-11. However, this cell showed different charge/discharge behavior as the first cell. The charge voltage had an abrupt drop and became extremely unstable.

Black spots could be observed on the LAGP pellet (Figure 3-12-a) after the cell was disassembled. As shown in Figure 3-12-b, large numbers of Li dendrites were formed in the separator on the side neighboring the Li anode. A part of the dendrites penetrated the separator and reached the LAGP solid-state electrolyte as shown in Figure 3-12-c. These Li dendrites reacted with the LAGP solid-state electrolyte and formed the black spots. The LAGP pellet was broken along those spots, showing that cracks were formed in the LAGP pellet.

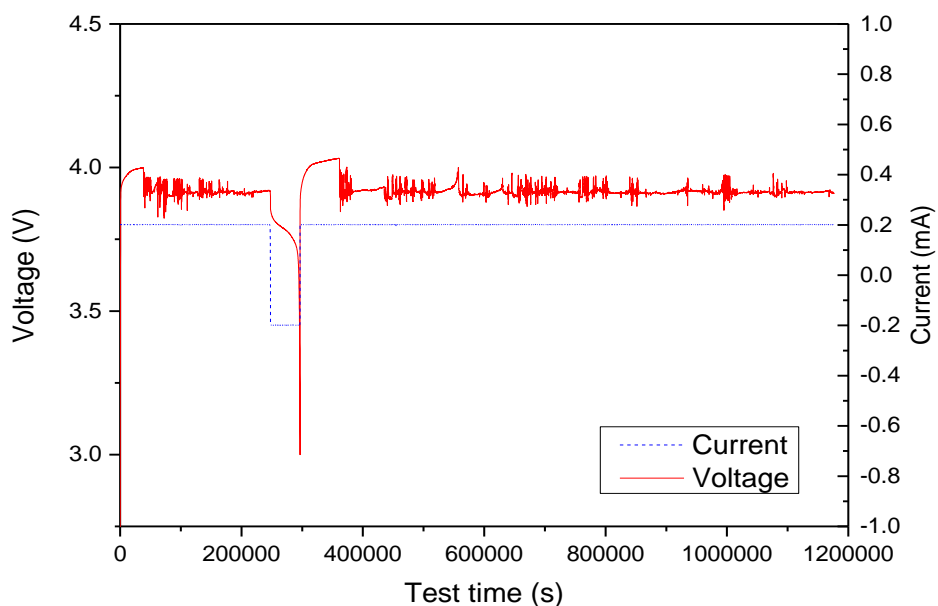


Figure 3-11: Charge and discharge test of the Li-LAGP+LP30+sep-LCO cell-2 with glass fiber separator between Li anode and LAGP solid-state electrolyte.

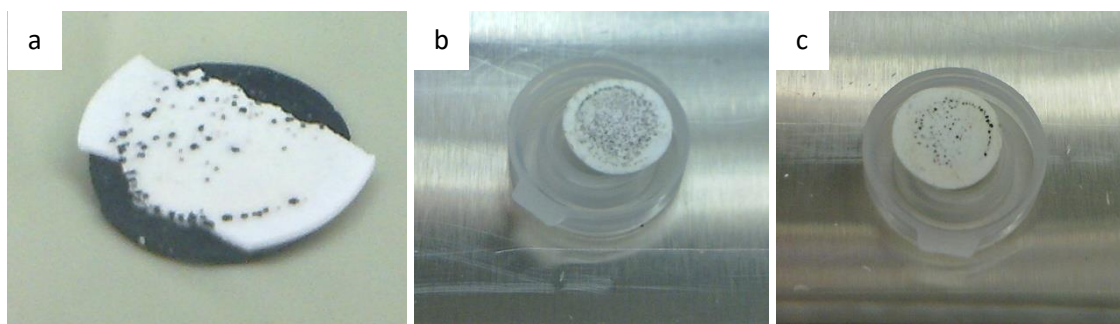


Figure 3-12: The  $\text{LiCoO}_2$  cathode, LAGP solid-state electrolyte and both sides of the separator after tested in the Li-LAGP+LP30+sep-LCO cell-2. a: The LCO cathode and the LAGP solid-state electrolyte, b: the separator with the side neighboring the Li metal, c: the separator with the side neighboring the LAGP pellet.

### 3. Test of lithium ion cells with solid-state electrolyte

#### 3.2.1.3 C-LAGP+LP30-LCO cell

Due to the stability problems observed in LAGP in contact with Li metal, a graphite anode was applied to replace the Li metal anode. Figure 3-13 shows the structure of the C-LAGP+LP30-LCO cell using a graphite anode, a  $\text{LiCoO}_2$  cathode and a hybrid solid + liquid electrolyte.

The test result of the C-LAGP+LP30-LCO cell is shown in Figure 3-14. The cell was charged with a current of 0.1 mA. The voltage increased to 2.73 V after 2 hours of charging and showed a long plateau. The voltage plateau is significantly lower as a cell using  $\text{LiCoO}_2$  cathode, liquid electrolyte and graphite anode (higher than 3.5 V) <sup>133, 134, 136</sup>. Unlike in the cells using lithium anode, the voltage rose up to 4.2 V without the abnormal behavior shown in the previous cells. The voltage increased continuously during charge, showing that the  $\text{Li}^+$  ions were extracted from the  $\text{LiCoO}_2$  cathode.

However, the cell could be discharged for a much shorter time before the voltage dropped to the low limit of 3.0 V. The cell could hardly be charged or discharged after the first cycle, indicating that the  $\text{Li}^+$  ions became immobile in the cell. The  $\text{Li}^+$  ions were trapped in the electrolyte. Otherwise, when the  $\text{Li}^+$  ions were inserted into the graphite anode, they should be able to be extracted from that as well.

The post-mortem investigation showed that a large area was black colored on the anode side of the LAGP pellet (Figure 3-15). As shown on the light microscope image of the cross section of the pellet (Figure 3-16-a), the black colored area reached the middle of the pellet. These coloring could therefore not be attributed to the graphite, since the graphite could not penetrate the LAGP pellet. This sample was exposed in air during the preparation and after the observation. The black coloring did not change, showing that it was not lithium dendrite.

On the SEM image however (Figure 3-16-b), the colored area is not visible.

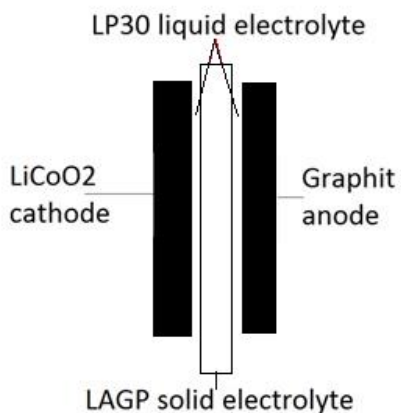


Figure 3-13: Schematic presentation of the C-LAGP+LP30-LCO cell.

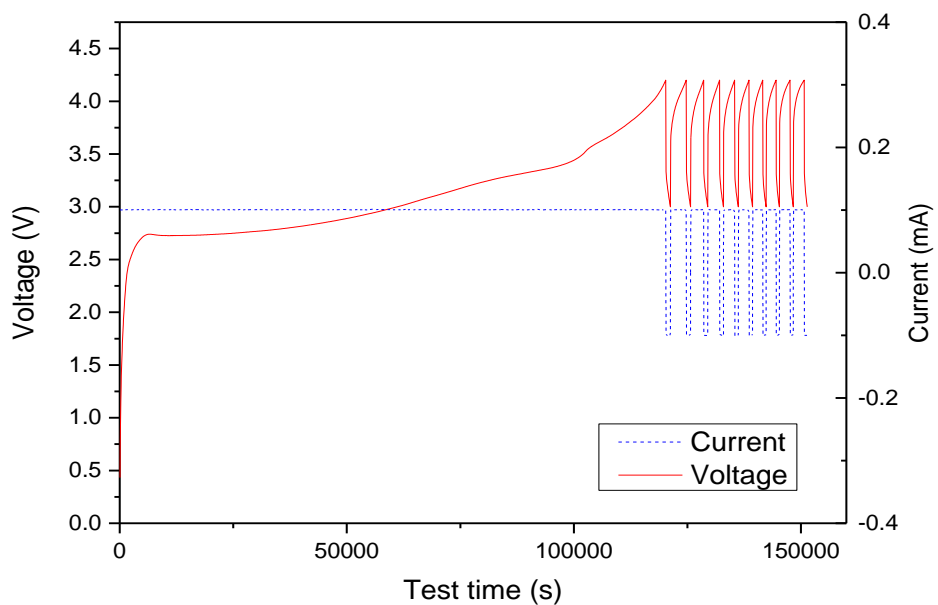


Figure 3-14: Charge and discharge test of the C-LAGP+LP30-LCO cell. The cell could not operate further after the first charging.

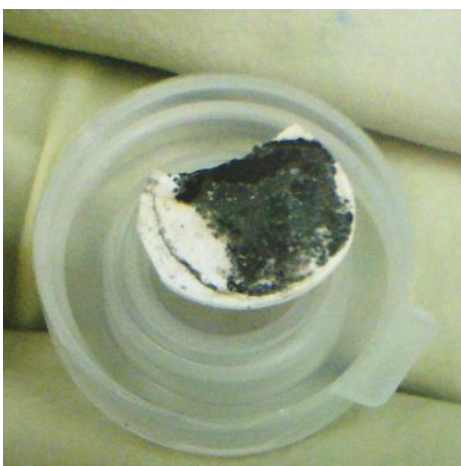


Figure 3-15: The anode side of the LAGP solid-state electrolyte pellet after the test in the C-LAGP+LP30-LCO cell. Large area on the anode side is black colored.

### 3. Test of lithium ion cells with solid-state electrolyte

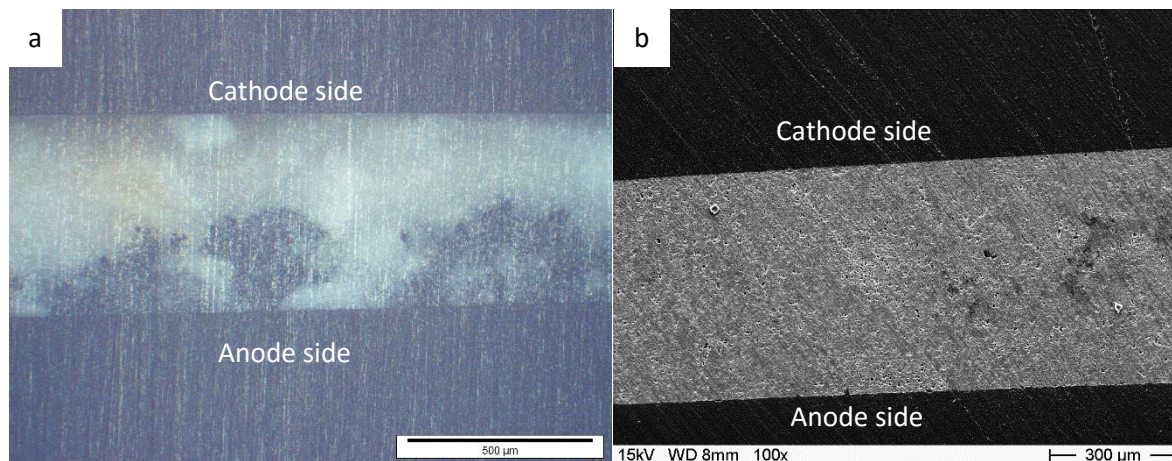
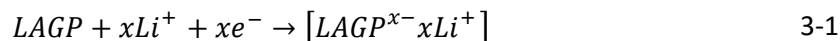


Figure 3-16: Cross section of the LAGP solid-state electrolyte after the test in the C-LAGP+LP30-LCO cell (100x magnification). a: the optical microscope photo, b: the Scanning electron microscope photo.

The behavior of the cell can be explained as follows: Since the anode of the lithium ion cell is a strong reducing agent, the  $\text{Ge}^{4+}$  ions in the LAGP lattice are reduced to an intermediate oxidation state (probably  $\text{Ge}^{2+}$ ). For the charge neutrality, extra  $\text{Li}^+$  ions are incorporated in the LAGP lattice:



This electrochemical reaction takes place when the cell is charged. The  $\text{Li}^+$  ions are from the  $\text{LiCoO}_2$  cathode and the electrons are from the anode. The  $\text{Li}^+$  ions from the anode are trapped in the LAGP solid-state electrolyte instead of being inserted in the graphite anode. The cell cannot further operate since there are no free  $\text{Li}^+$  ions in the cathode and anode.

In this case, the LAGP becomes the actual anode of the cell. This reaction on LAGP explains also, why the charging voltage plateau was lower as in normal cells with graphite anode (Figure 3-16): The voltage measured during the test was actually the voltage between  $\text{LiCoO}_2$  and LAGP. The electrical potential difference between  $\text{LiCoO}_2$  and LAGP solid-state electrolyte is smaller as that between  $\text{LiCoO}_2$  and the graphite anode.

Unlike the cells using Li metal anode, the cell using the graphite anode could hardly discharge. That is because the graphite anode had initially no lithium content and the  $\text{LiCoO}_2$  was the only lithium source. The cell could not operate when all the  $\text{Li}^+$  ions were bound with LAGP. In the cells using Li metal anode however, the Li metal had overcapacity of  $\text{Li}^+$  ions. It could always supply  $\text{Li}^+$  ions to compensate the loss of free  $\text{Li}^+$  ions and the cell could further discharge.

The voltage drop during charging had not appeared in the cell using graphite anode, showing that no electronic conducting bypass was built as in the cells using Li anode. That is because of the absent of Li dendrite. The graphite has a slightly higher potential as Li metal. The  $\text{Li}^+$  ion will be inserted into the graphite. The dendrite formation is only possible at high current or lower temperature. The Li dendrite

would not form in this cell. Therefore, even there was also crack on the LAGP pellet, the internal short circuit had not occurred in the cell using graphite anode.

#### 3.2.1.4 LTO-LAGP+LP30-LCO cell

Since the LAGP could be reduced by the Li anode, an anode material with higher redox potential was used. The lithium titanate  $\text{Li}_4\text{Ti}_5\text{O}_{12}$  (LTO) has a potential of 1.5 V vs  $\text{Li}/\text{Li}^+$ , which is significantly higher than other anode materials<sup>134</sup>. LTO can work as anode vs  $\text{LiCoO}_2$  (LCO) cathode. A LTO-LAGP+LP30-LCO cell was assembled with a LTO-anode, a LCO-cathode and a LAGP solid-state electrolyte between them. The interface between them was also wetted with the LP30 liquid electrolyte (Figure 3-17). The voltage of the LTO-LAGP+LP30-LCO cell is 1.5 V lower than the cell using Li anode and it was therefore cycled between 1.7 V and 2.7 V.

Figure 3-18 shows the result of the galvanostatic-cycling test. The current was set to 0.05 mA in the first 2 cycles and 0.1 mA for the 3<sup>rd</sup> - 6<sup>th</sup> cycle. The voltage showed a plateau at around 2.39 V and reached the high limit of 2.70 V after 130 hours of charging. The voltage jumped directly to 2.50 V when the cell began to discharge. The cell had discharged for 103 hours. In the 2<sup>nd</sup> cycle, the cell behaved almost the same. In the 3<sup>rd</sup> cycle, since the current was doubled (0.1 mA), the voltage plateau increased to around 2.59 V. The cell was charged for 32.3 hours. The voltage jumped directly to 2.22 V when the cell was switched to discharge mode. The cell could discharge for 29.9 hours before the voltage decreased to 1.70 V.

After 4 cycles with 0.1 mA current, the current was set to 0.2 mA. However, the cell could not be charged with this current. The voltage jumped directly to 2.7 V when it was charged and jumped back immediately to 1.7 V when it was switched to discharge.

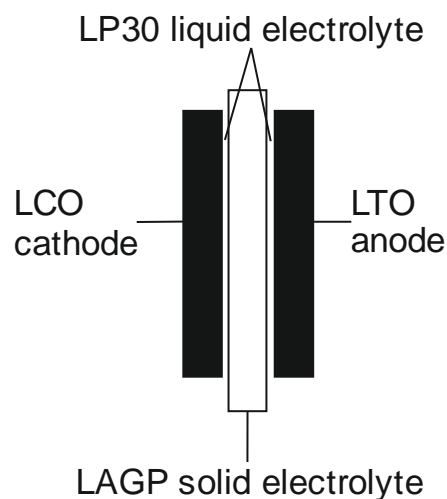


Figure 3-17: Schematic presentation of the LTO-LAGP+LP30-LCO cell.

### 3. Test of lithium ion cells with solid-state electrolyte

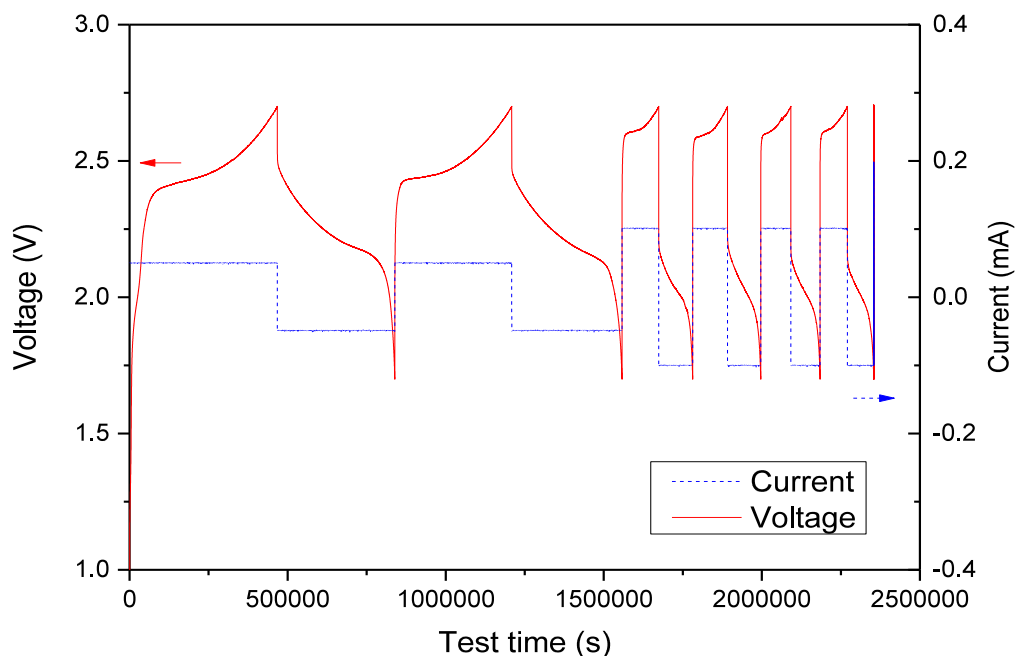


Figure 3-18: Charge and discharge test of the LTO-LAGP+LP30-LCO cell.

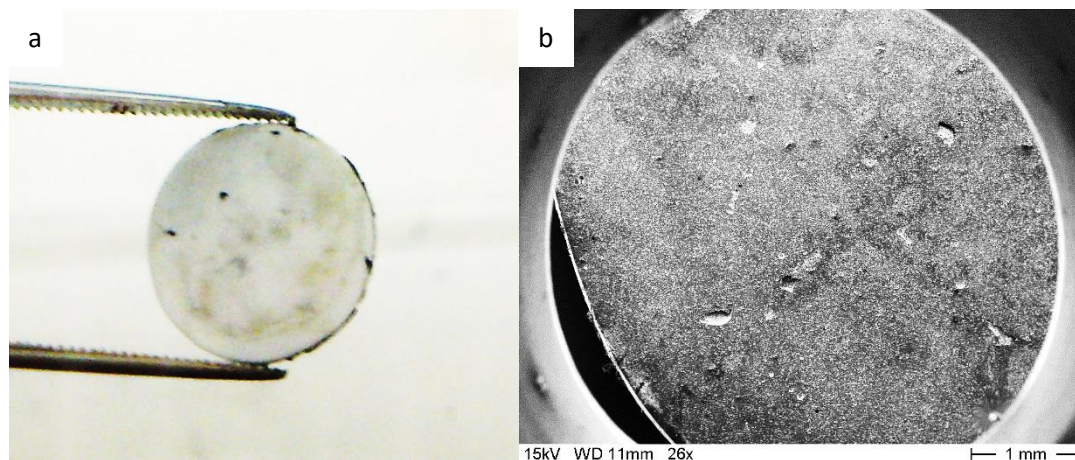


Figure 3-19: The LAGP solid-state electrolyte pellet, which was tested in the LTO-LAGP+LP30-LCO cell. a: the LAGP pellet with the side neighboring LTO anode; b: SEM image of the anode side of the LAGP pellet.

The images of the LAGP solid-state electrolyte after the cycling test are shown in Figure 3-19. Unlike the damaged electrolyte pellets in the previous cells, this LAGP pellet was still intact. No reaction products are formed on the LAGP pellet, showing that the LAGP is stable vs LTO and the LP30 liquid electrolyte.

The charge and discharge capacity are shown in Figure 3-20. The cell showed irreversible capacity in the first cycle. The cell capacity decreased as the charge and discharge current increased.

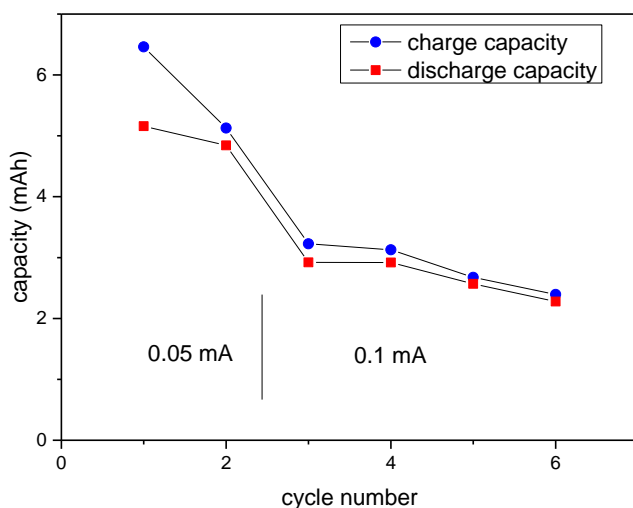


Figure 3-20: charge and discharge capacity of the LTO-LAGP+LP30-LCO cell.

### 3.2.1.5 Li-LATP+LP30-LCO cell

The lithium aluminum titanium phosphate (LATP) was also tested as solid-state electrolyte in lithium ion cells. The LATP pellets were prepared using the optimized sintering process (1000°C 6 hours). The LATP pellets were ground to 0.4 mm thickness and polished.

The test cell was assembled using a Li metal anode, a LiCoO<sub>2</sub> (LCO) cathode and a LATP + liquid hybrid electrolyte with the structure shown in Figure 3-3. The cell was designated as Li-LATP+LP30-LCO cell and tested at the same condition as the cells mentioned above. Figure 3-21 shows the Galvanostatic cycling test results. The cell showed a similar behavior as the cells using LAGP solid-state electrolyte (see 3.2.1.1). The charge voltage showed a sudden drop and became unstable. The discharge periods were much smaller as the charge periods.

Figure 3-22 shows the images of the LATP solid-state electrolyte and the Li metal anode after the test. The LATP pellet showed a blue coloring and was broken apart. The blue coloring on the LATP pellet is attributed to the Ti<sup>3+</sup> ions. The Ti<sup>4+</sup> can be reduced to Ti<sup>3+</sup>, which has a blue color<sup>137, 124</sup>. The reduction reaction:



takes place on LATP at a voltage of 2.4 V vs. Li/Li<sup>+</sup> <sup>138-140</sup>.

### 3. Test of lithium ion cells with solid-state electrolyte

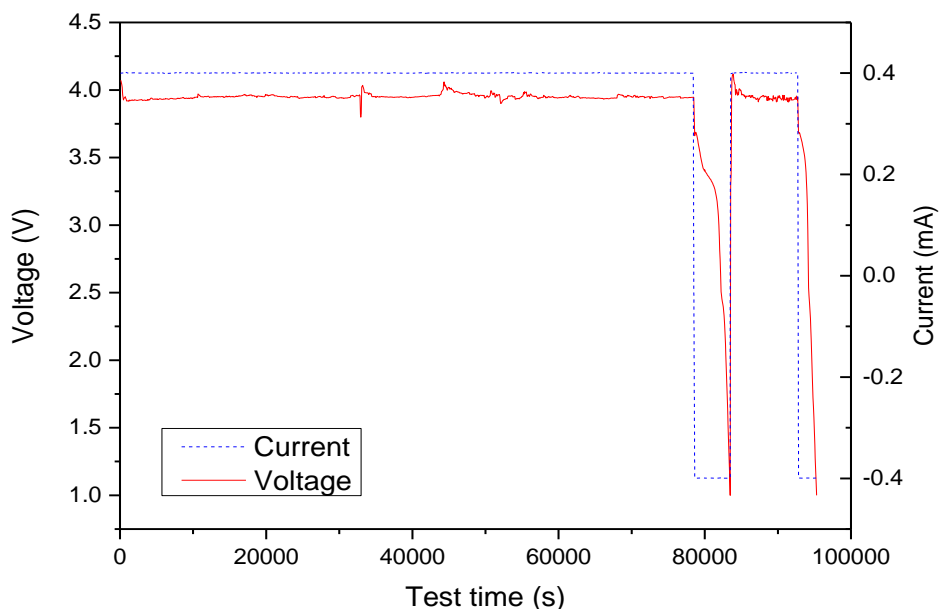


Figure 3-21: Voltage and current curves of the Li-LATP+LP30-LCO cell by charging and discharging.



Figure 3-22: The LATP solid-state electrolyte after the test. The LATP pellet was blue colored and broken apart.

#### 3.2.1.6 LTO-LATP+LP30-LCO cell

A cell using  $\text{Li}_4\text{Ti}_5\text{O}_{12}$  (LTO) as anode, LATP+LP30 as electrolyte and  $\text{LiCoO}_2$  (LCO) as cathode was also assembled and tested. The structure of the LTO-LATP+LP30-LCO cell is the same as shown in Figure 3-17 with LATP instead of LAGP. Figure 3-23 shows the results of the galvanostatic-cycling test of the LTO-LATP+LP30-LCO cell.

The cell can be cycled. However, the capacity decayed in each cycle (Figure 3-24). The capacity in the 9<sup>th</sup> cycle dropped to one third of the capacity of the 2<sup>nd</sup> cycle. The capacity loss is attributed to the loss of  $\text{Li}^+$

ions in the cell: The  $Ti^{4+}$  ions in LATP were reduced into  $Ti^{3+}$ . In order to keep the charge neutrality in LATP, extra  $Li^+$  ions were incorporated in the LATP lattice. The amount of mobile  $Li^+$  ions in the cell was reduced and hence the cell capacity decreased in each cycle.

Figure 3-25 shows the image of the LATP pellet with the side, which was neighboring the LTO anode. The blue coloring is visible on the pellet, which confirms that the  $Ti^{4+}$  was reduced to  $Ti^{3+}$ .

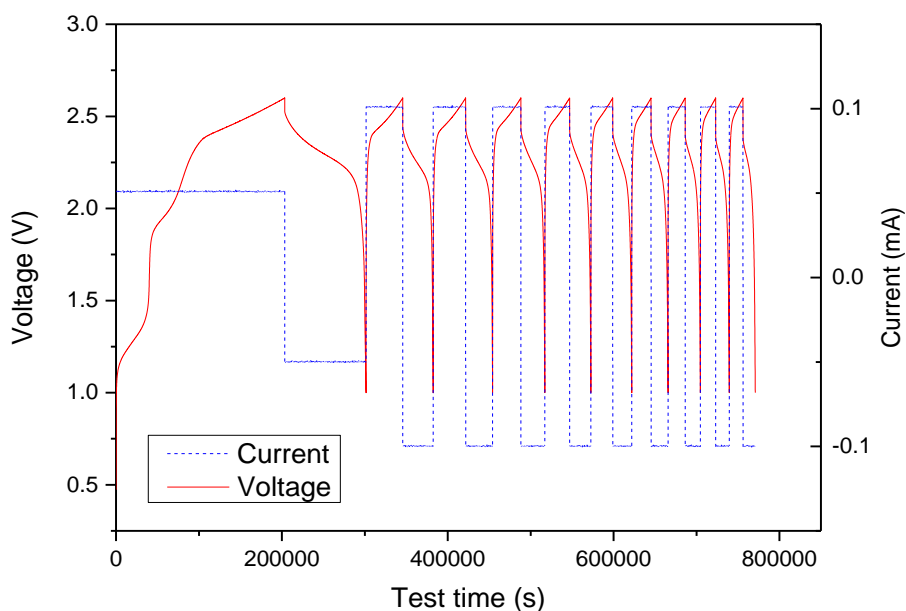


Figure 3-23: Voltage and current curves of the LTO-LATP+LP30-LCO cell during cycling.

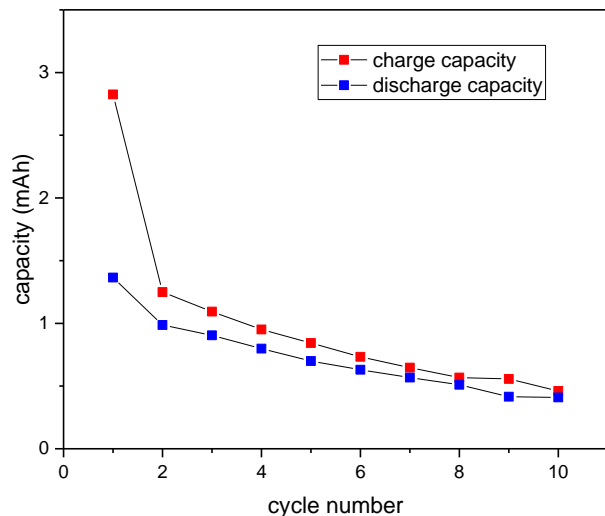


Figure 3-24: Charge and discharge capacity of the LTO-LATP+LP30-LCO cell.

### 3. Test of lithium ion cells with solid-state electrolyte



*Figure 3-25: The anode side of the LATP solid-state electrolyte pellet (the side, which was in contact with the LTO anode) after test.*

The test results of the Li-LATP+LP30-LCO and LTO-LATP+LP30-LCO cells show that the LATP solid-state electrolyte is not suitable for application in lithium ion batteries. The LATP is unstable vs Li metal and  $\text{Li}_4\text{Ti}_5\text{O}_{12}$  (LTO) as anode.

The reaction  $\text{Ti}^{4+} + e^- \leftrightarrow \text{Ti}^{3+}$  takes place at a potential of 2.4 V vs.  $\text{Li}/\text{Li}^+$  <sup>138-140</sup>, which means that the  $\text{Ti}^{4+}$  is reduced spontaneously when the LATP solid-state electrolyte is in contact with lithium metal.

The LTO has a redox potential of 1.5 V vs  $\text{Li}/\text{Li}^+$ , which is lower than that of  $\text{Ti}^{4+}/\text{Ti}^{3+}$ . The  $\text{Ti}^{4+}$  ions in LATP are easier to be reduced than the LTO anode. The  $\text{Li}^+$  ions are trapped in LATP and the cell capacity shows a significant decay. The LATP solid-state electrolyte is also not stable in the cell using  $\text{Li}_4\text{Ti}_5\text{O}_{12}$  (LTO) as anode.

#### 3.2.2 All-solid-state cells with LAGP solid-state electrolyte

In the previous investigation, the LAGP solid-state electrolyte showed instability vs the Li metal anode and the graphite anode in the presence of the liquid electrolyte. For the investigation of solid-state electrolyte however, the liquid electrolyte in the cell is always a disturbing factor. There was always the uncertainty, whether the liquid electrolyte took part in the reaction. Therefore, it is important to investigate the all-solid-state lithium ion cells without liquid electrolyte.

The contact between the electrolyte and electrodes needs to be improved for the all solid-state lithium ion cells. The Li metal is easy to deform and to get a good contact with LAGP solid-state electrolyte. On the cathode side however, it is more difficult to achieve sufficient contact between the solid cathode material and the LAGP solid-state electrolyte. Slurry deposition techniques (see 3.1.2), which are used in cells with liquid electrolyte, could not provide a sufficient contact.

On the other hand, since there was no liquid electrolyte in the cell, the cell can be tested at elevated temperatures (100°C – 150°C). The ionic conductivity of the LAGP solid-state electrolyte at this temperature is much higher than at room temperature and comparable with a conventional liquid

electrolyte. The electrode materials  $\text{LiCoO}_2$  and  $\text{Li}_4\text{Ti}_5\text{O}_{12}$  are also stable at this temperature<sup>141</sup>. Lithium metal has the melting point of  $180.5\text{ }^\circ\text{C}$ <sup>142</sup> and is in solid form at  $150^\circ\text{C}$ .

### 3.2.2.1 Li-LAGP-LTO cell

The attempt of using sintering method to fabricate cathode-electrolyte-anode multilayer pellet was not successful (see 2.8.2). The cathode mixture  $\text{LiCoO}_2 + \text{LAGP} + \text{carbon black}$  showed different sintering behavior as the LAGP powder. The multilayer pellet delaminated after sintering.

On the other hand, this procedure worked with the  $\text{Li}_4\text{Ti}_5\text{O}_{12} + \text{LAGP} + \text{carbon black}$  mixture. A LAGP-LTO two-layer pellet was successfully sintered.  $\text{Li}_4\text{Ti}_5\text{O}_{12}$  (LTO) has a potential of  $1.5\text{ V}$  vs  $\text{Li}/\text{Li}^+$ , which can be used as cathode material vs lithium metal anode.

The LAGP side of the LAGP-LTO pellet was polished and pressed together with a Li metal foil. The Li-LAGP-LTO three-layer pellet was mounted in a Swagelok cell and tested in the temperature chamber at  $150^\circ\text{C}$  in the voltage range of  $2.5\text{ V} - 1.0\text{ V}$ . The  $\text{Li}_4\text{Ti}_5\text{O}_{12}$  was initially in its Li poor state and the cell was therefore in a discharged state at the beginning of the cycling test.

The result of the galvanostatic-cycling test is shown in Figure 3-27. The first discharge took 8.7 hours. It could be noticed that the voltage decreased continuously with the same rate to  $1.0\text{ V}$ . No voltage plateau was observed in the first discharge period. However, the lithium titanate (LTO) has a very flat voltage plateau by charging and discharging<sup>143, 144</sup> and the cell voltage should have little change until the whole capacity is exhausted. However, the discharging voltage decreases continuously, indicating that the internal resistance of the cell was increasing. As shown on Figure 3-28, according the Voltage divider rule, the discharging voltage is a fraction of the cell potential, when the cell internal resistance is larger than zero. As the cell internal resistance increases, the discharging voltage decreases.

Figure 3-29 shows the charge and discharge capacity of the Li-LAGP-LTO cell. The cell had a discharge capacity of  $0.17\text{ mAh}$  in the first cycle, which was one order of magnitude smaller compared to the cells using liquid electrolyte. The capacity of the Li-LAGP-LTO cell has a 90% decay in the second cycle.

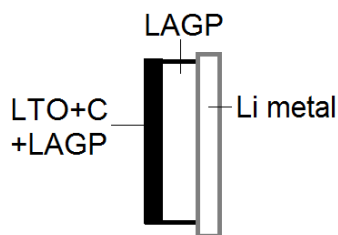


Figure 3-26: Schematic presentation of the Li-LAGP-LTO cell.

### 3. Test of lithium ion cells with solid-state electrolyte

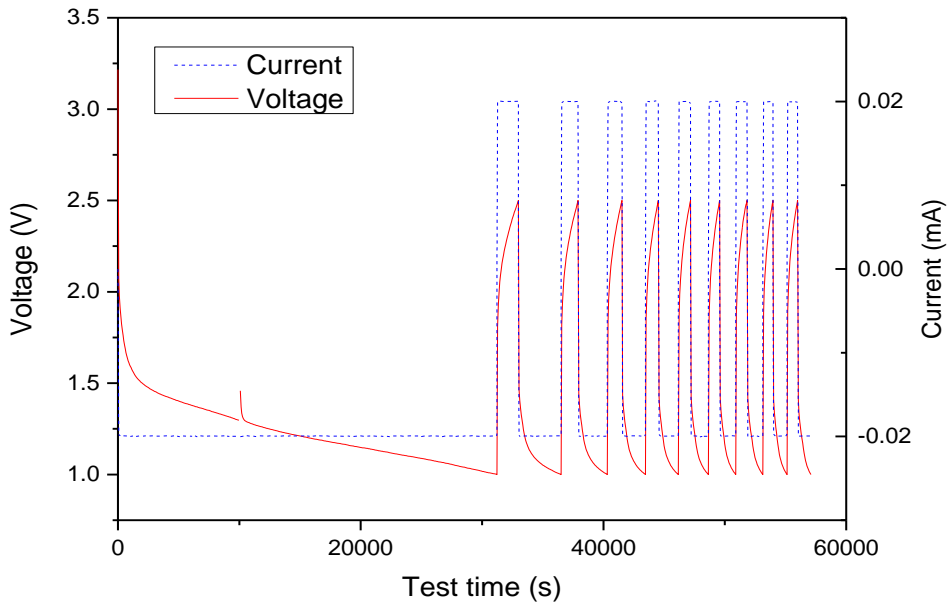


Figure 3-27: Voltage and current curves of the Li-LAGP-LTO cell during cycling.

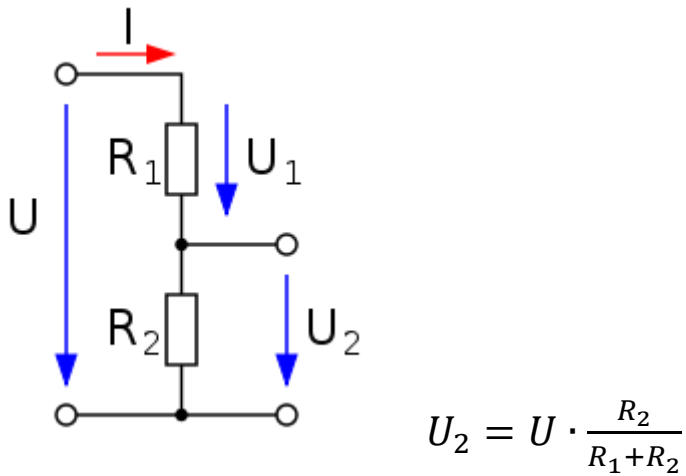
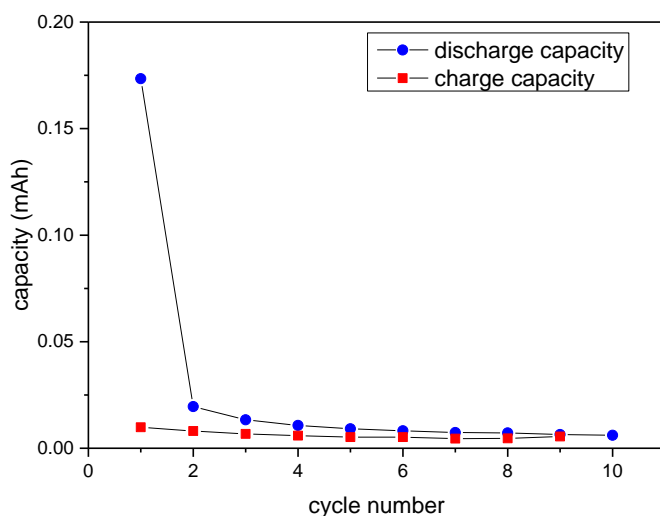


Figure 3-28: Reduced discharging voltage due to the cell internal resistance.  $U$ : the cell potential;  $R_1$ : the cell internal resistance;  $R_2$ : the external resistance;  $U_2$ : discharging voltage.



*Figure 3-29: Charge and discharge capacity of the Li-LAGP-LTO cell.*

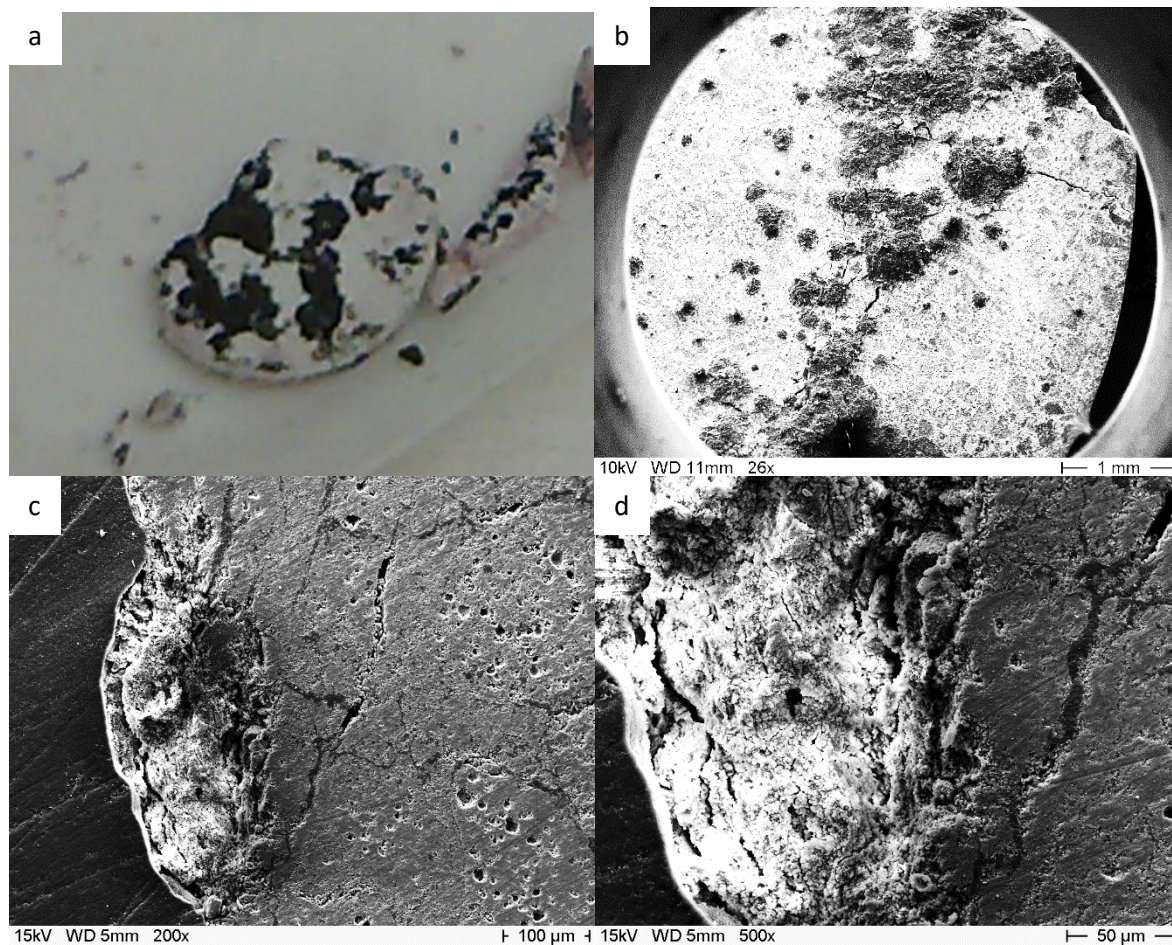
The cell was disassembled after the test. The reaction product was formed at the interface between Li anode and LAGP solid-state electrolyte (Figure 3-30-a and -b).

Figure 3-30-c and -d show the cross section of one LAGP pellet and the reaction product, which swelled out from the surface of LAGP pellet. Half of the porous reaction product is below the surface level of the LAGP pellet. The original flat LAGP surface could not be recognized. Since this area was only in contact with the Li metal anode and the LAGP electrolyte, this porous product was formed by a reaction between LAGP and Li metal and the original LAGP surface was consumed by this reaction.

The reaction zone showed a volume expansion, which can be attributed to the lithium insertion in LAGP. The volume increase induced stress in the pellet and cracks were formed. This also explains why almost all the LAGP pellets in the previous testes were fractured in the cells when a Li anode was used.

The reaction at the Li-LAGP interface resulted in the increase of internal resistance. The reaction damaged the LAGP surface and formed a new phase at the interface. The contact at the Li-LAGP interface was weakened and the ion transport in the cell was hindered, which increased the internal resistance of the test cell and hindered the charge and discharge.

### 3. Test of lithium ion cells with solid-state electrolyte



*Figure 3-30: Images of the LAGP solid-state electrolyte pellet after tested in the Li-LAGP-LTO cell. a: Photo of the LAGP pellet with the side, which was neighboring Li anode. The pellet broke apart and black reaction product was formed on the pellet; b: the SEM image of the LAGP pellet; c and d: the cross section of the reacted area on the anode side of the LAGP solid-state electrolyte (200x and 500x magnification).*

#### 3.2.2.2 Li-LAGP-LCO cell

Radio frequency magnetron sputtering was applied to deposit a  $\text{LiCoO}_2$  (LCO) layer on LAGP substrate. The procedure is described in 3.1.2. A 4- $\mu\text{m}$   $\text{LiCoO}_2$  layer was deposited on a 0.4 mm LAGP substrate. Lithium metal was applied as anode. The LAGP-LCO pellet was pressed together with a Li foil and assembled in the cell (Figure 3-31).

The cell was tested at 100°C. The galvanostatic cycling results are shown in Figure 3-32 and Figure 3-33. The capacity decreased in every cycle, which is similar to the Li-LAGP-LTO cell.

The post mortem examination showed that the LAGP pellet was fractured. On the anode side of the LAGP pellet, a black reaction product was observed and the surface of the LAGP became uneven (Figure 3-34). The cross section of the LAGP is shown on Figure 3-35. A  $\text{LiCoO}_2$  (LCO) layer with the thickness of 4  $\mu\text{m}$  was visible on the LAGP substrate. No damage on the cathode (LCO) side of the pellet was observed. On the

anode (Li) side, the reaction zone was also observed, which expanded from the LAGP surface (Figure 3-35-b). A crack was formed between the reaction area and the LAGP substrate, which separated the reaction zone from the LAGP substrate. The internal resistance of the cell increased therefore drastically and the cell could operate only for a short time.

Because of the large internal resistance, the all solid-state cells could not operate at relatively higher current (e.g. 0.1 mA). The current through the all-solid test cells were much smaller (one order of magnitude lower) compared to the cells using liquid electrolyte. The charge voltage and the discharge voltage showed significant difference, which is also attributed to the internal resistance of the cell.

In addition, the resistance at the LCO-LAGP interface has also a contribution to the resistance of the cell. As shown on the SEM photo of the cross section, the LCO layer was dense and had a good contact with the LAGP substrate. However, there could be still large resistance at the LAGP-LCO interface. The LAGP and the LCO have different lattice structures and different lattice parameters. The lattice mismatch can increase the interface resistance<sup>145</sup>: the region at the interface might be deformed and deviates from the original structure, which is unfavorable for the lithium transport<sup>146</sup>. Moreover, when the pellet was heated up, the different thermal expansion of both materials would also induce mismatch. The space charge effect can also affect the resistance at the interface<sup>147-149</sup>.

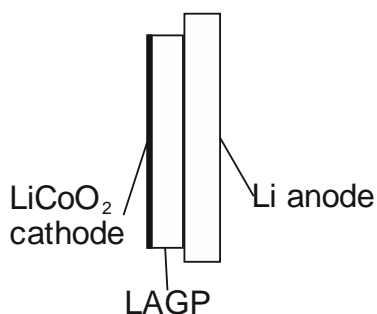


*Figure 3-31: Schematic presentation of structure of the Li-LAGP-LCO cell.*

### 3. Test of lithium ion cells with solid-state electrolyte

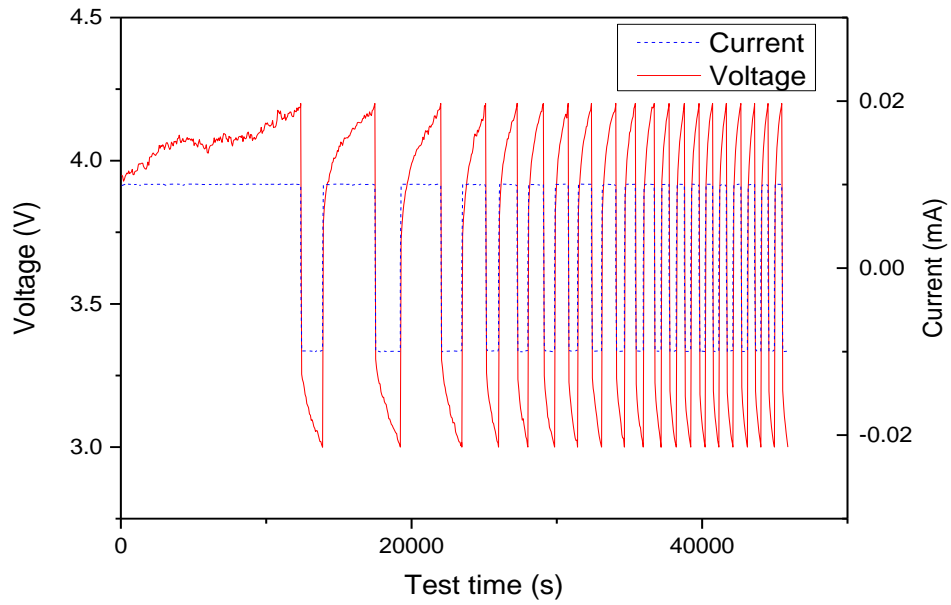


Figure 3-32: Voltage and current curves of the Li-LAGP-LCO cell during cycling.

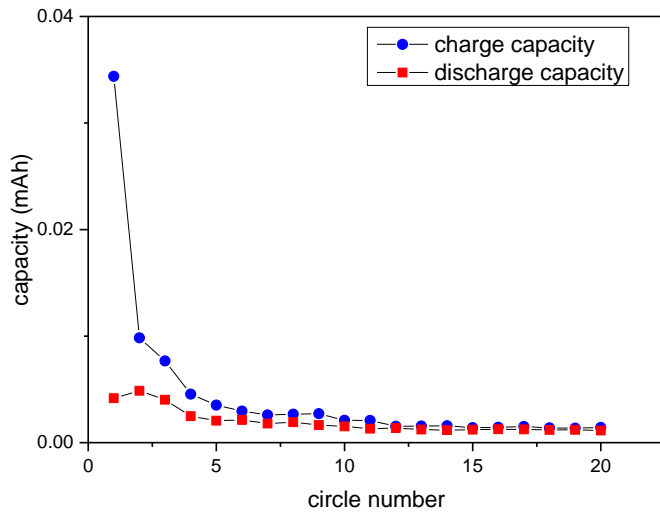


Figure 3-33: Charge and discharge capacity of the Li-LAGP-LCO cell in first 20 cycles.

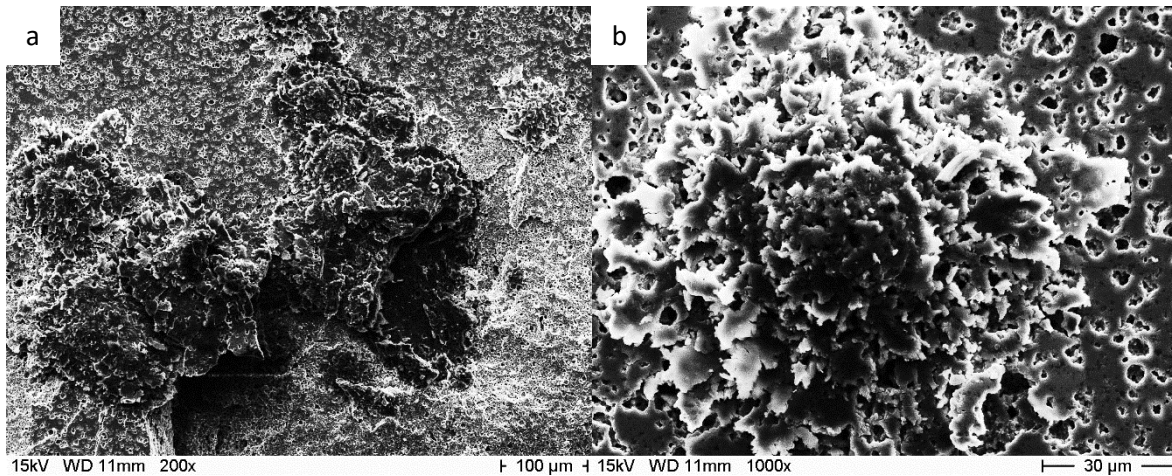


Figure 3-34: Reaction area on the LAGP-LCO pellet, which was tested in the Li-LAGP-LCO cell. a: 200x magnification; b: 1000x magnification.

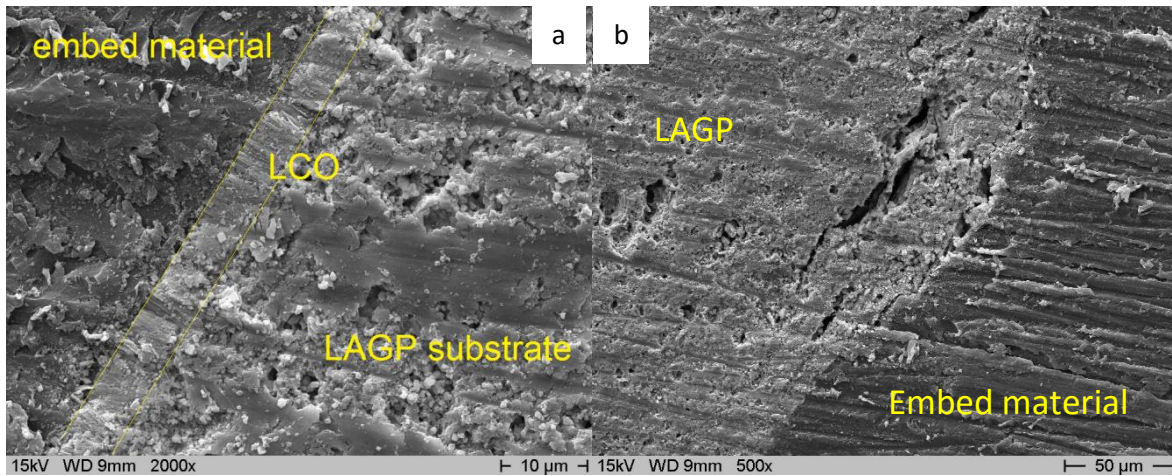


Figure 3-35: SEM image of the cross section of the LAGP-LCO pellet, which was tested in the Li-LAGP-LCO cell. a: the LAGP substrate with  $\text{LiCoO}_2$  (LCO) cathode layer; b: the anode side of the LAGP pellet with the reaction zone between LAGP and Li metal (the Li anode foil was removed).

### 3. Test of lithium ion cells with solid-state electrolyte

#### 3.3 Stability of LAGP solid-state electrolyte

The LAGP solid-state electrolyte shows instabilities in the cell tests. Therefore, cyclic voltammetry, impedance spectroscopy and LIBS were carried out to investigate the reaction on LAGP. Samples from the high lithium LAGP batch 4 fabricated through heat-treating method (800°C 6h heat-treated) were used for these tests.

##### 3.3.1 Cyclic voltammetry

Cyclic voltammetry was applied to investigate the electrochemical reaction on LAGP vs Li/Li<sup>+</sup>. The cyclic voltammetry test cells have the LAGP as working electrode and the Li metal as reference and counter electrode. A sweeping voltage is applied to the test cell. Whenever a reaction occurred in the cell, a current through the cell was registered.

###### 3.3.1.1 Li-LP30-LAGP CV-cell

The structure of the first cyclic voltammetry test cell is shown in Figure 3-36. Liquid electrolyte was applied between Li and LAGP in order to achieve a lower interface resistance. The cell was designated as Li-LP30-LAGP CV-cell. The cell can be represented schematically:

+ Al foil | Au current collector | LAGP | liquid electrolyte + separator | Li metal | Cu foil –

or simplified:

+ LAGP | liquid electrolyte + separator | Li metal –

The LAGP pellet was polished on both sides and sputtered with gold on one side, which was connected with the positive pole. A Li foil was connected to the negative pole. A separator soaked with LP30 liquid electrolyte (containing 1 M Li<sup>+</sup>) is placed between the Li foil and the LAGP pellet. The voltage of the cell is equivalent to the potential of LAGP vs. the standard potential of Li<sup>+</sup>/Li.

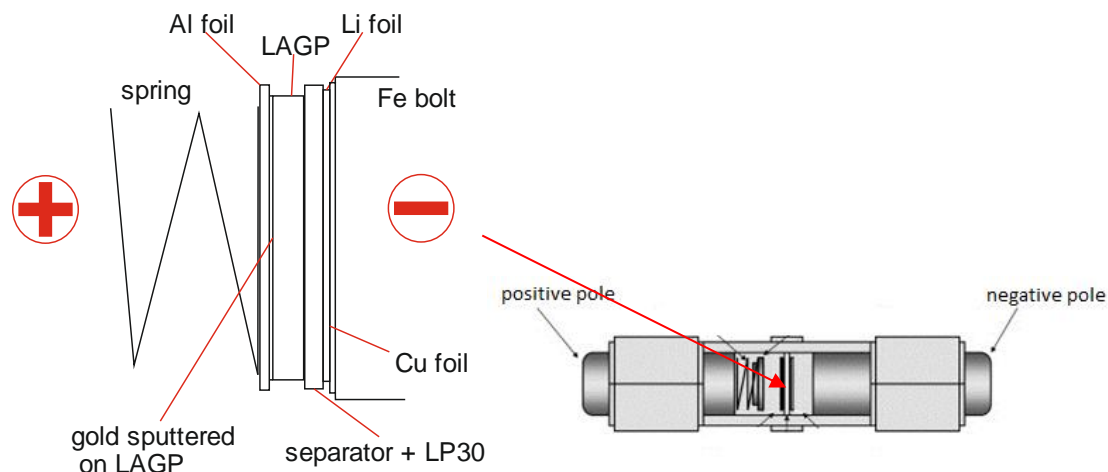


Figure 3-36: Schematic presentation of the Li-LP30-LAGP CV-cell for the cyclic voltammetry measurement of LAGP vs Li metal.

The cyclic voltammogram of the Li-LP30-LAGP cell is shown in Figure 3-37. The voltage-sweeping window was set to 0 V – 4 V. The positive current represents the current from the positive pole to the negative pole through the LAGP, which means Li<sup>+</sup> ions are transported from positive pole to the negative pole and the positive pole is oxidized. The negative current represents the Li<sup>+</sup> ion current from the negative pole to the positive pole and a reduction reaction on the positive pole.

The cell had an open circuit voltage of 1.03 V, showing that the LAGP has a positive potential vs Li<sup>+</sup>/Li and a higher electron affinity vs elemental Li. The voltage swept at the beginning in the positive direction with the rate of 5 mV/s (Figure 3-37). The current was more than 1 mA at the beginning and then dropped quickly to 0.013 mA. The relatively large current at the beginning of the test can be attributed to the charge accumulated on the LAGP due to its higher electron affinity.

The voltage sweep was inversed to the negative direction (-5 mV/s) when the voltage reached 4 V. The current became 0 mA at the voltage of 3.1V and stayed near zero. The current in the negative direction began to increase as the voltage decreased below 1.0 V, showing that a reduction reaction was taking place on LAGP. The current increased continuously until 0.42 V and showed a plateau at 0.0112 mA. The current began to increase again at 0.25 V and reached 0.102 mA at 0 V.

The voltage sweep in the negative direction shows that the LAGP is reduced between 1.0 V and 0.25 V. The plateau of the reduction current shows that the reaction reached a saturation state. The increase of the current at 0.25 V shows that another reaction was taking place, namely the reduction of Li<sup>+</sup> ions to elemental lithium.

The voltage sweep was inversed to the positive direction (5 mV/s) at 0 V. The current reached 0 mA at the voltage of 0.33 V. The current showed a peak at 0.55 V, which can be attributed to the oxidation of elemental lithium. A shoulder at 0.37 V is visible. The current has a local minimum at 0.84 V and a second peak at 1.03 V. The peak at 1.03 V represents the reverse reaction of the LAGP reduction at 0.3 V- 1.0 V.

The voltage sweep was carried out for further 2 cycles. The cell showed the same current response. Since lithium could alloy with gold<sup>150-153</sup>, gold can be lithiated between 0 V – 0.25 V and delithiated between 0.15 V – 0.45 V<sup>154</sup>. The reaction at 0 V – 0.6 V can be partially attributed to the lithiation and delithiation of the gold current collector. There could be multiple reactions taking place between 0 V – 0.6 V considering the shoulder at 0.37 V on the cyclic voltammogram. It is possible that the lithium was not only alloyed with gold, but also formed an elemental Li layer at this voltage range.

The negative current at 0.25 V – 1.0 V and the positive peak at 1.03 V can be attributed to the reduction and oxidation reaction of LAGP. These redox reactions confirm the observation in the previous cell test that the LAGP solid-state electrolyte was unstable vs Li/Li<sup>+</sup>.

### 3. Test of lithium ion cells with solid-state electrolyte

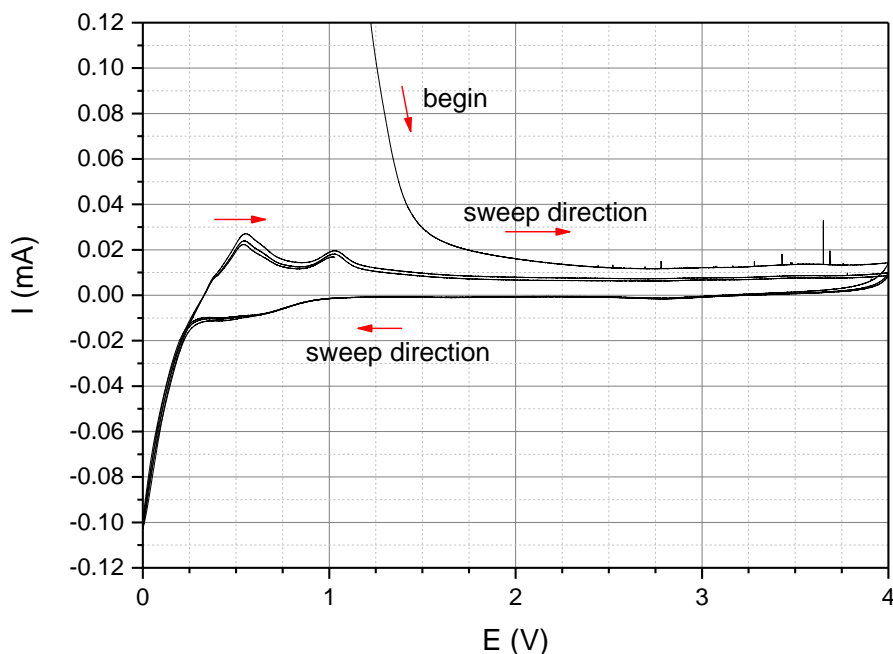


Figure 3-37: Cyclic voltammogram of the Li-LP30-LAGP cell measured with the sweeping rate of 5 mV/s. the voltage sweep started at 1.03 V in positive direction, switched to negative direction at 4.0 V and switched to positive direction at 0 V. Three sweeping cycles were carried out.

After 3 cycles with a sweeping rate of 5 mV/s, the cell was tested with the sweeping rate of 1 mV/s, 10 mV/s, 2 mV/s and 15 mV/s in succession. The results are shown in Figure 3-38. The same peaks and plateaus appeared in all these cycles.

The peaks at 0.96 V – 1.06 V showed a dependence on the sweeping rate: as the sweeping rate increased, the peak shifted to higher voltage from 0.96 V at 1 mV/s to 1.06 at 15 mV/s. In addition, the height of the peaks increased with increasing sweeping rate. The current of the corresponding reverse reaction at 0.3 V- 1.0 V increased also with increasing sweeping rate: The current plateau increased from 0.0022 mA to 0.0112 mA and 0.0255 mA as the sweeping rate increased from 1 mV/s to 5 mV/s and 15 mA/s.

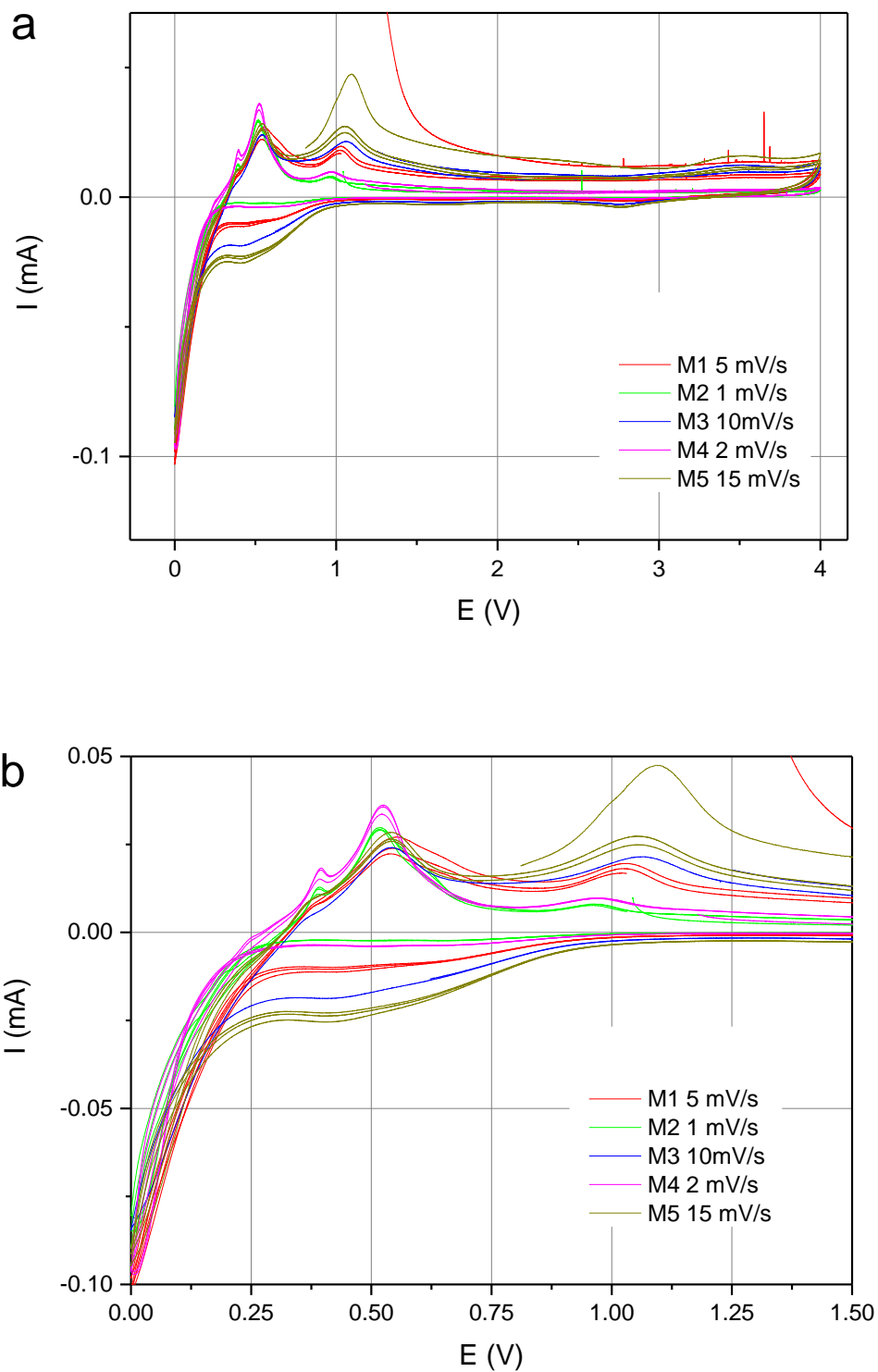


Figure 3-38: Cyclic voltammogram of the Li-LP30-LAGP cell measured with different sweeping rate from 1 mV/s up to 15 mV/s. a: the whole diagram; b: the diagram zoomed in to 0 V–1.5 V.

### 3. Test of lithium ion cells with solid-state electrolyte

Shifted peaks of the reaction at 0.3 V – 1.3 V indicate that the reaction has slower kinetics: The reaction needs higher over-potential to be accelerated. With a higher sweeping rate, the cell gets a larger over potential and hence a higher reaction rate. The highest reaction rate (the current peak) shifts to higher voltage<sup>155, 156</sup>. The reaction at 0.3 V – 1.3 V shows asymmetric behavior: The positive (oxidation) current had a peak while the negative (reduction) current showed a plateau, which also indicates an irreversible character of the reaction.

On the other hand, the peaks at around 0.53 V and the reverse reaction at 0 V – 0.3 V did not show a dependence on the sweeping rate. The sweeping with 2 mV/s rate had the highest peak at 0.52 V while the sweeping with 5 mV/s rate had the highest current at 0 V.

The Li-LP30-LAGP cell was disassembled after the test. Figure 3-39-a shows the LAGP pellet after the test. The black area on the pellet was initially sputtered with gold. After the test, this area was black colored, showing that the reaction took place at the positive pole. The other side of the LAGP pellet stayed unchanged.

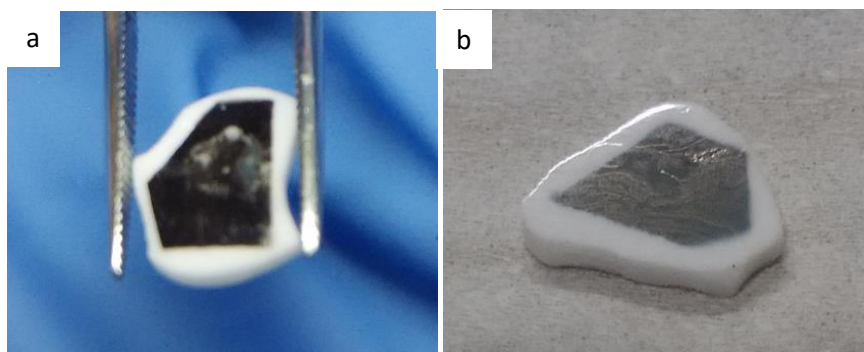


*Figure 3-39: Images of LAGP pellet sputtered with gold electrode. a: the LAGP pellet, which was tested in the Li-LP30-LAGP cell; b: the as prepared LAGP pellet for comparison.*

#### 3.3.1.2 Li-LAGP CV cell

The all-solid-state Li-LAGP CV cell without liquid electrolyte was assembled (see Figure 3-40). Since no liquid electrolyte was used in the cell, a reaction related to the liquid electrolyte could be excluded in this all solid cell. Due to the concern that aluminum might alloy with lithium, the Al foil used in the previous cell was replaced with a copper foil<sup>157</sup>. The cell can be symbolically shown as:

+ Cu foil | Au current collector | LAGP | Li metal | Cu foil –

or simplified:

+ LAGP | Li metal –

In the Li-LAGP cell, the LAGP works at the same time as electrolyte and electrode material. The reaction between LAGP and lithium metal can take place on both sides of the LAGP pellet. On the Li-LAGP interface, they react directly. On the other side of the LAGP pellet, the LAGP reacts with Li via an electrochemical reaction: The  $\text{Li}^+$  ions migrate through the LAGP electrolyte and the electrons flow through the external circuit to the Au current collector on the LAGP pellet.

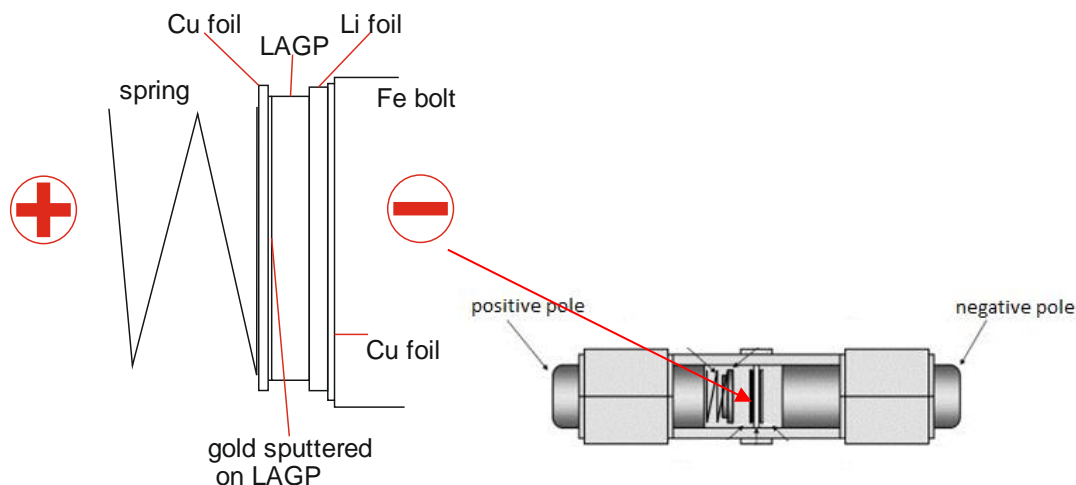


*Figure 3-40: Setup of the Li-LAGP cell for cyclic voltammetry. Gold was sputtered on one side of the LAGP pellet as positive current collector. Li foil was pressed on the other side of LAGP as negative electrode.*

Cyclic voltammetry was carried out on this Li-LAGP cell. Figure 3-41 – Figure 3-43 show the cyclic voltammograms, which were taken (i) directly after, (ii) 8 hours after and (iii) two days after the cell was assembled, respectively. Two sweeping ranges were applied on the cell. One sweeping range was 0 V – 4 V, which is the same as the previous Li-LP30-LAGP cell. The other sweeping range was 0.3 V – 4 V, in which the reduction reaction of  $\text{Li}^+$  ions would not take place.

The current in the all-solid-state cell is one order of magnitude lower as in the cell with liquid electrolyte, showing that the resistance in the all-solid-state cell is much larger. That can be attributed to a higher resistance at the interface: The liquid electrolyte can wet the whole interface. The interface between two solids (LAGP and lithium metal) is not well connected at each point, which reduces the interface area and increases the resistance. In addition, the reaction between Li and LAGP can damage the interface and hinder the ion transport.

The measurements carried out at different times showed change over time (Figure 3-41 - Figure 3-43): The current corresponding to the reaction at 0 V - 0.6 V decays over time, while the current of the reaction at 0.3 V – 1.3 V did not change.

### 3. Test of lithium ion cells with solid-state electrolyte

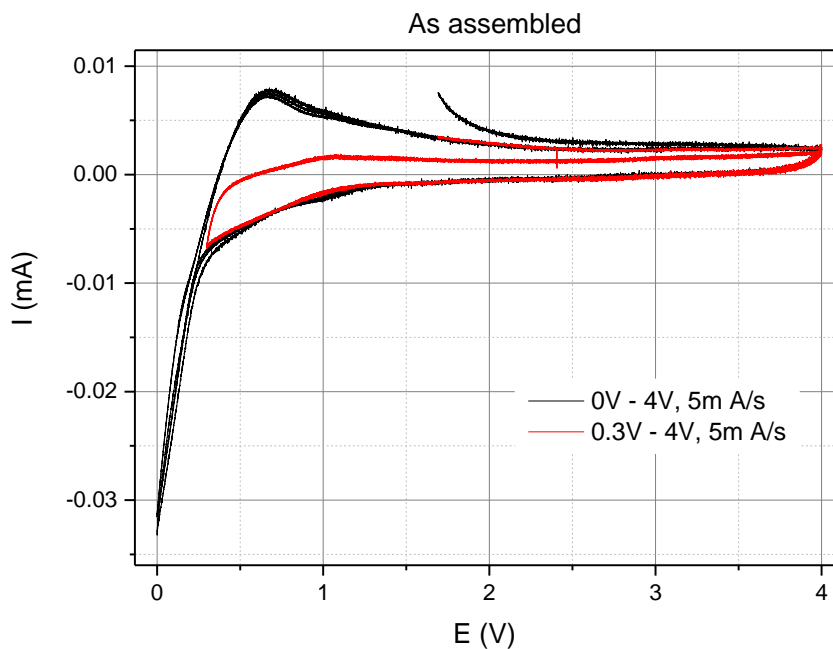


Figure 3-41: Cyclic voltammogram of the Li-LAGP cell measured with the sweeping rate from 5 mV/s directly after the cell was assembled (i).

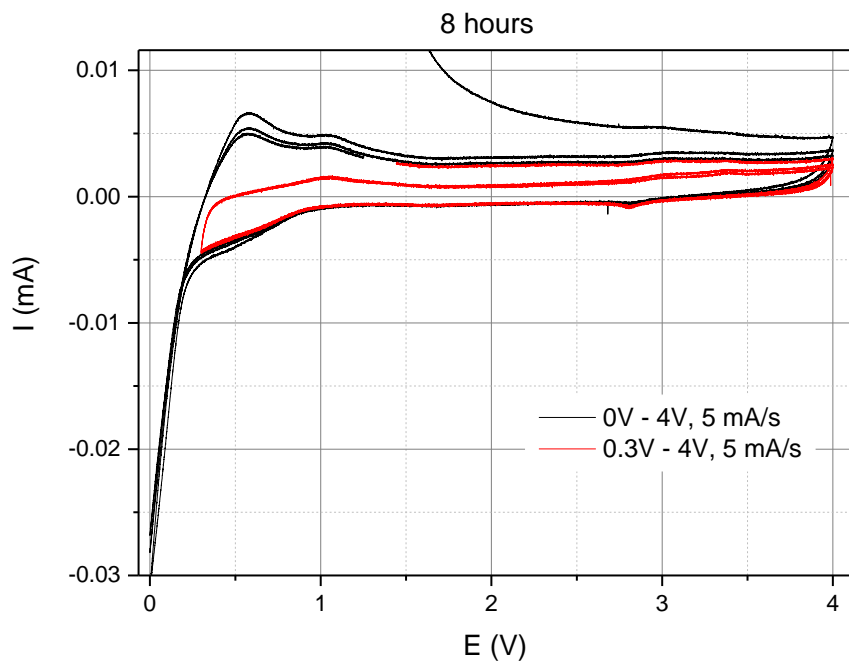


Figure 3-42: Cyclic voltammogram of the Li-LAGP cell measured with the sweeping rate from 5 mV/s 8 hours after the cell was assembled (ii).

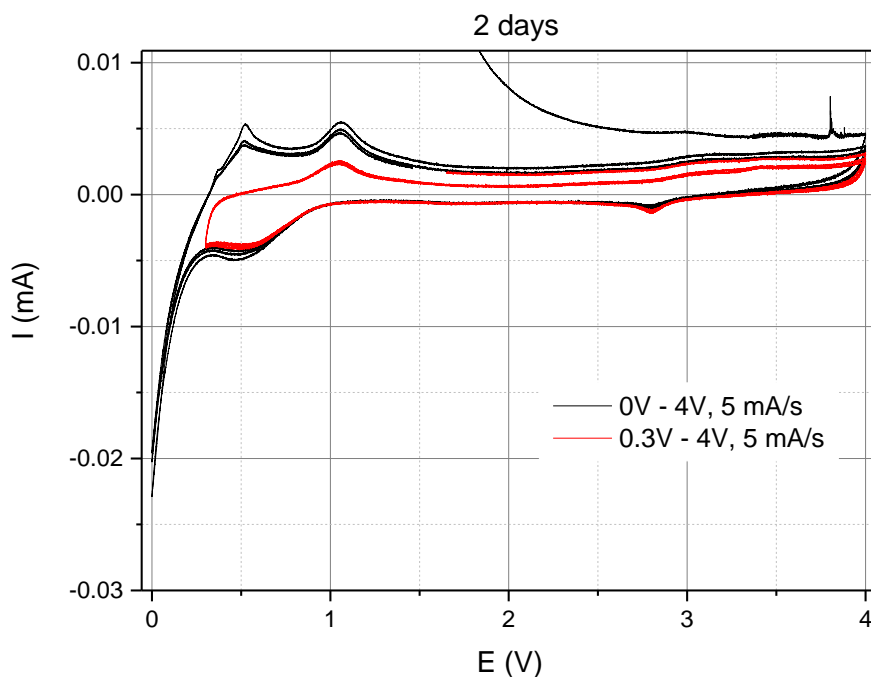


Figure 3-43: Cyclic voltammogram of the Li-LAGP cell measured with the sweeping rate from 5 mV/s 2 days after the cell was assembled (iii).

By the sweeping range of 0 – 4 V, the cells with and without liquid electrolyte showed the same peaks and plateaus on the CV-diagrams (Figure 3-37 and Figure 3-43), showing that the liquid electrolyte had not affected the reaction between Li and LAGP. The aluminum and copper foil used in the two electrolysis cells did not cause any difference. The redox reaction on LAGP at 0.3 V – 1.3 V took place in both cells with and without liquid electrolyte.

### 3.3.1.3 Discussion

The cyclic voltammetry showed that redox reactions took place on the LAGP. The LAGP was reduced at the voltage below 1 V vs Li/Li<sup>+</sup> and oxidized at the voltage above 1 V vs Li/Li<sup>+</sup>.

The Ge<sup>4+</sup> in GeO<sub>2</sub> can be reduced by elemental Li. According to the thermodynamic calculation, the reaction



and



have negative free reaction enthalpy, which means these reactions take place spontaneously<sup>158</sup>.

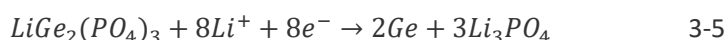
### 3. Test of lithium ion cells with solid-state electrolyte

In the work of Peña et. al, Yoon et.al and Hwang et. al, The CV diagram of GeO<sub>2</sub> was measured vs Li/Li<sup>+</sup> <sup>159–161</sup>. The GeO<sub>2</sub> showed several reduction peaks at the voltage lower than 1 V, which were attributed to the reduction of Ge<sup>4+</sup> ions and the reduction of Li<sup>+</sup> ions: the GeO<sub>2</sub> was reduced to Ge and lithium alloyed with germanium. On the sweeping in positive direction, an oxidation peak appeared at 0.4 V - 0.5 V, which was due to the oxidation of Li (delithiation of germanium). An oxidation peak also appeared at 1.2 V, which was attributed to the oxidation of the germanium, which was formed in the reduction reaction at the voltage lower than 1 V.

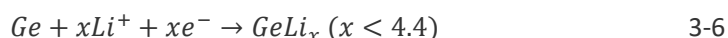
The CV-diagram of LAGP showed similarity to the CV-diagrams of GeO<sub>2</sub> in the literature<sup>159, 162, 161</sup>. Those CV-diagrams showed peaks at similar positions, showing that the Ge<sup>4+</sup> in LAGP was reduced. The minor difference between those CV-diagrams could be attributed to the different potential of Ge<sup>4+</sup> in LAGP and in GeO<sub>2</sub>. Other parameters such as the sweeping rate and the kind of electrolyte solvent could also influence the position of the peaks in the CV-diagram.

In the work of Hartmann et. al, the reaction of LAGP (Li<sub>1.6</sub>Al<sub>0.5</sub>Ge<sub>1.5</sub>P<sub>3</sub>O<sub>12</sub>) and LATGP (Ohara-glass, a commercial solid-state electrolyte containing Li, Al, Ge, Ti, Si and P) vs lithium has been investigated<sup>158</sup>. Metallic lithium was deposited on the sample surface using Ar ion sputtering. The lithium diffused into the LAGP before it could form a metallic lithium layer. XPS measurement was carried out on the lithiated samples. On the LATGP sample, the binding energy of titanium and germanium shifted partially to lower value, showing that the Ti<sup>4+</sup> and Ge<sup>4+</sup> were reduced. Moreover, the peak for the binding energy split into two, indicating that the germanium has multiple oxidation states. On the LAGP sample, the Ge(4+) was reduced to Ge(0) on the top layer. Peaks of germanium with intermediate oxidation state (between Ge(4+) and Ge(0)) emerged when the top layer was sputtered away.

In the work of Feng et. al, LiGe<sub>2</sub>(PO<sub>4</sub>)<sub>3</sub> was used as a cathode material<sup>163</sup>. The cell using a lithium metal anode and a LiGe<sub>2</sub>(PO<sub>4</sub>)<sub>3</sub> cathode could operate with a reaction between the LiGe<sub>2</sub>(PO<sub>4</sub>)<sub>3</sub> and metallic lithium:



The reduced germanium could further alloy with lithium



The LAGP had a similar reaction with metallic lithium. The reaction product might be Li<sub>3</sub>PO<sub>4</sub>, AlPO<sub>4</sub> and elemental germanium. In this work, the reaction product was analyzed with X-ray diffraction (XRD). However, metallic germanium was not identified. That can be attributed to a too small amount of the product or the amorphous state of the germanium. In addition, as shown in the work of Hartmann et. al, there are intermediate oxidation states of germanium in LAGP<sup>158</sup>. The germanium was not fully reduced to elemental Ge. The Ge<sup>4+</sup> in the LAGP crystal could be reduced to an intermediate oxidation state without destroying the lattice structure of the LAGP. The reduction reaction caused a charge deficit in the LAGP lattice and extra Li<sup>+</sup> ions could be incorporated in the LAGP lattice.

The reduction reaction on LAGP can take place as follows: The  $\text{Ge}^{4+}$  ions are reduced as the LAGP is brought into contact with a reducing agent, which has a potential lower as 1 V vs  $\text{Li}/\text{Li}^+$ . The  $\text{Ge}^{4+}$  ions are reduced to an intermediate oxidation state between  $\text{Ge}(4+)$  and  $\text{Ge}(0)$  and extra  $\text{Li}^+$  ions are incorporated in the LAGP lattice for the charge neutrality. When only a small fraction of Ge ions is reduced, the LAGP lattice retains its structure, which was observed in the test cell using graphite anode (the C-LAGP+LP30-LCO cell, 3.2.1.3). However, the LAGP decomposes when a large amount of germanium is reduced. The volume of the reaction area on the LAGP expands and breaks the LAGP pellet, which was observed in the cells using Li metal anode.

### 3.3.2 Impedance spectroscopy

Impedance spectroscopy measurement was carried out on the Li-LAGP cell tested in 3.3.1.2 (Figure 3-40) at room temperature 8 hours, 24 hours and 32 hours after the cell was assembled. Figure 3-44 shows the Nyquist-diagram of the measurements. The curves can be roughly considered as a semicircle in the high frequency area plus a spike in the low frequency area. The diameter of the semicircle represents the resistance. The sample showed a resistance of 17 k $\Omega$  8 hours after it was assembled. The resistance increased to 34 k $\Omega$  in the measurement of 24 hours. The 32h curve showed a similar resistance.

After the tests at room temperature, the cell was further tested at 150°C (Figure 3-45). The IS curve of the measurement 1 hour and 5 hours at 150°C did not show any semicircle. That is because the tester has a maximum frequency of 10 kHz, which does not cover the frequency range of the semicircle. In this case, the resistance of the cell is smaller than the intersection of the spike on the x-axis (428  $\Omega$ ). When the cell was heated up to 150°C, its internal resistance reduced was from 34 k $\Omega$  to less than 428  $\Omega$ . That is due to the decreasing resistance of LAGP electrolyte at higher temperatures. In addition, an improved contact between lithium metal and LAGP pellet also reduces the interface resistance.

As shown in Figure 3-45, the resistance was smaller than 428  $\Omega$  at 1 h and 1776  $\Omega$  at 5 h. The resistance increased to 16 k $\Omega$  after 24 hours at 150°C and to 29 k $\Omega$  after 4 days at 150°C. The resistance of the cell increased with the time.

The internal resistance of the cell consists of the resistance at the interface between the gold current collector and the LAGP pellet, the resistance of the LAGP pellet and the resistance at the interface between lithium metal and LAGP pellet. The resistances of the electron conducting materials such as the gold current collector, lithium metal and copper foil can be considered as negligible. As the reaction between Li and LAGP occurred, the LAGP pellet and the Li-LAGP interfaces were damaged, which resulted in an increasing resistance of the cell.

### 3. Test of lithium ion cells with solid-state electrolyte

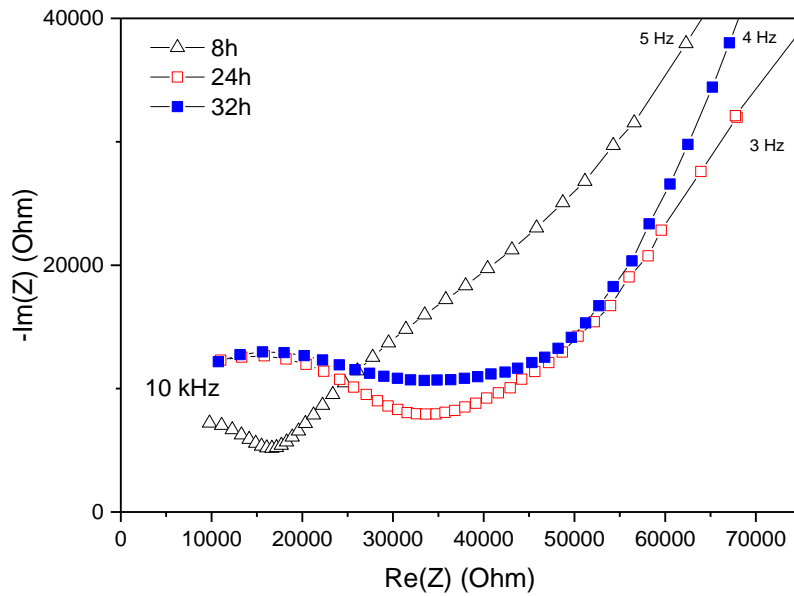


Figure 3-44: Nyquist diagram of the Li-LAGP cell at room temperature for different time after the cell was assembled.

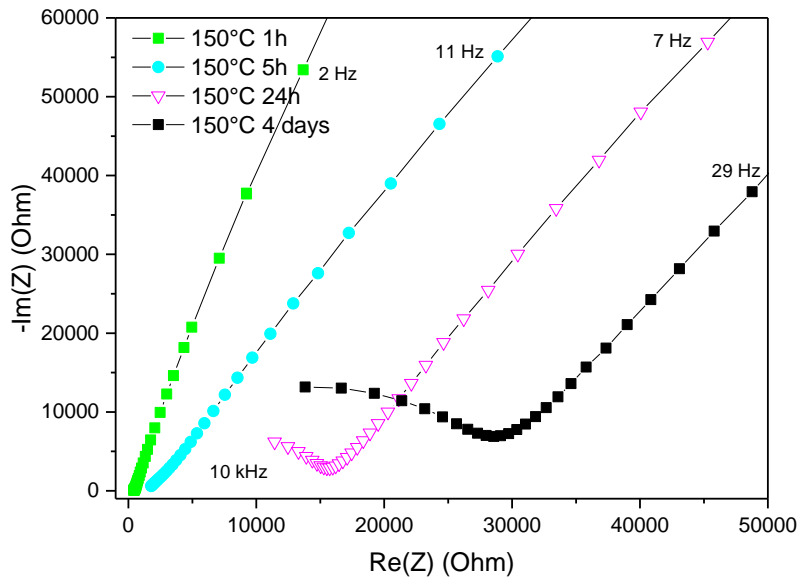
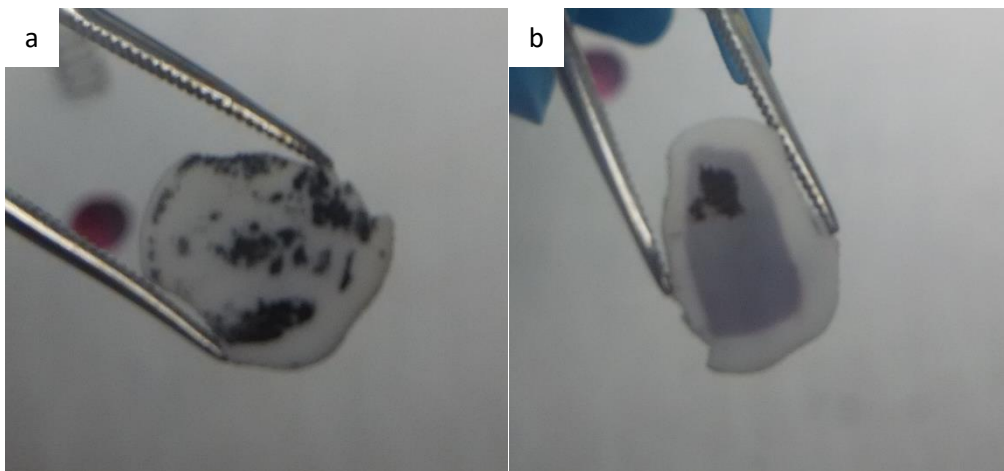


Figure 3-45: Nyquist diagram of the Li-LAGP cell at 150°C for different time.



*Figure 3-46: Images of LAGP pellet, which was tested in the Li-LAGP cell. a: the side which was in contact with Li metal; b: the side which was sputtered with gold.*

The cell was disassembled after the test. As shown in Figure 3-46, a reaction product was formed on both side of the LAGP pellet. The product on the Li side was formed by a direct reaction between Li and LAGP. On the other side of the LAGP pellet, the reaction product was formed by the electrochemical reaction, which was measured in the cyclic voltammogram.

### 3.3.3 Laser-induced breakdown spectroscopy

Laser-induced breakdown spectroscopy (LIBS) was carried out to analyze the reaction product of LAGP with Li. Laser pulses ablate the sample surface layer by layer. The material below the surface is exposed and measured. The diagram represents a depth profile of each element. However, the ablation rate is different for different materials.

A LAGP pellet was pressed together with a lithium foil and stored in argon atmosphere for two weeks. A reaction layer was formed on the LAGP pellet. Figure 3-47 shows the LIBS result of the reacted area on the LAGP pellet. For comparison, the intact unreacted surface area of the LAGP pellet was also analyzed and shown in Figure 3-48.

The LIBS analysis has confirmed the reaction between lithium and LAGP. The diagrams show that the reaction area had a similar elementary composition as the not reacted area with a higher content of lithium than the pristine area. The lithium content in the reaction layer was 60% higher compared that in unreacted LAGP. The lithium content stayed constant in the reaction layer, showing that only a limited amount of lithium can be incorporated into the LAGP lattice.

The Li signal had a clear drop at the 76th scan and the Li content jumped to the level of the pristine area, indicating that the reacted layer ended at this position.

### 3. Test of lithium ion cells with solid-state electrolyte

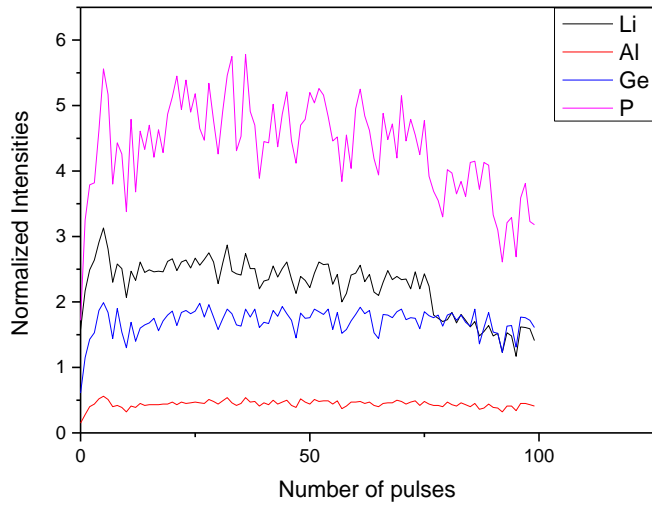


Figure 3-47: LIBS analysis of the reaction area on LAGP pellet. The normalized intensities of each element were plotted vs. the number of the laser pulse, which represents the depth into the sample.

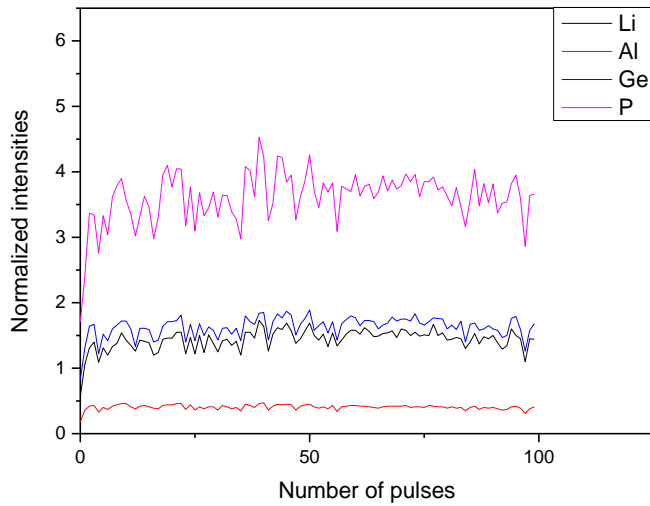


Figure 3-48: LIBS analysis of the pristine surface of the LAGP pellet. The normalized intensities of each element were plotted vs. the number of the laser pulse, which represents the depth into the sample.

## 4 Summary and conclusion

### 4.1 Material developments

For the search of optimized ionic conductivity, lithium aluminum germanium phosphates (LAGP) with different compositions ( $x = 0.3 - 0.7$  in the general formula of  $\text{Li}_{1+x}\text{Al}_x\text{Ge}_{2-x}\text{P}_3\text{O}_{12}$ ) were fabricated and ceramic LAGP samples were prepared via different processing routes with different parameters.

Samples of a high lithium LAGP batch were prepared via the sintering route. The samples showed an expansion at the temperature higher than  $670^\circ\text{C}$ , which resulted from a gas release of the samples. This gas release might be attributed to the decomposition of the  $\text{Al}(\text{PO}_3)_3$  minor secondary phase and the formation of gaseous  $\text{P}_2\text{O}_5$ . The LAGP powder was therefore calcined. The optimized sintering temperature and sintering time were found at  $800^\circ\text{C}$  for 6 hours. The samples had insufficient densification at lower sintering temperature and an expansion at higher temperature.  $\text{AlPO}_4$  and  $\text{GeO}_2$  minor phases were observed in the samples and their size increased with increasing sintering temperature.

Multiple batches of LAGP glasses were fabricated via the heat-treating route. The optimized heat-treating temperature was found to be  $800^\circ\text{C}$ . The ionic conductivity increased as the heat-treating time increased at  $800^\circ\text{C}$ . By a lower heat-treating temperature, there was relatively larger porosity in the sample. By a higher heat-treating temperature, larger amount of the  $\text{AlPO}_4$  minor phase was formed at the grain boundary, which blocked the ion transport in the LAGP matrix. Different as in the sintering route, the  $\text{GeO}_2$  phase was not formed in the heat-treated samples.

Among the LAGP samples of different compositions, which were heat-treated with the same process, the lithium rich LAGP exhibited higher ionic conductivity than the medium lithium LAGP. The sample of the low lithium LAGP exhibited a significant lower ionic conductivity than the medium Li LAGP, showing that a higher Li content is profitable for improving the  $\text{Li}^+$  ionic conductivity.

The ionic conductivity achieved in this work is not the highest among the literature values. However, this work provides a systematic investigation of the influence of different factors on the ionic conductivity, such as the composition, the formation of minor phases and the porosity, which were not completely revealed in former investigations.

The glass transition temperature of the LAGP with different compositions varied between  $504^\circ\text{C} - 535^\circ\text{C}$  and the crystallization temperature varied between  $596^\circ\text{C} - 649^\circ\text{C}$ . The glass transition and crystallization temperature increased with decreasing lithium content in LAGP samples. The DSC measurements showed a reversible phase transition in the Li rich LAGP at  $757^\circ\text{C}$ , which was not reported in other publications before. The hot stage XRD measurements showed that the lattice parameter  $a$  &  $b$  exhibit an abrupt change at  $750^\circ\text{C} - 800^\circ\text{C}$ , which also indicates a phase transition of the LAGP phase.

## 4. Summary and conclusion

The relation between the thermal conductivity and ionic conductivity was investigated. The sample with higher ionic conductivity showed higher thermal conductivity among the samples of the same composition. However, between the samples of different composition, the sample with highest thermal conductivity (sample of low Li LAGP) showed lower ionic conductivity, which can be attributed to the stronger scattering of the phonons (which carry the thermal energy) by increasing doping level. The relation between the thermal conductivity and the ionic conductivity of LAGP was investigated for the first time and it was revealed that these materials do not obey the Wiedemann-Franz law, which indicates that there is no significant contribution of the mobile ions to the thermal conductivity.

The ionic conductivity of LAMP ceramic was also investigated. Samples were prepared using sintering method. The optimized sinter process parameter was found to be “1000°C for 6 hours”, which was resulting from a combined effect of the sintering property and the formation of a minor secondary phase. Similar as for LAGP, the sintering process was too slow and the densification was insufficient at lower temperature. At higher temperature, larger amount of the secondary phase was formed, which blocked the ion transport in the LAMP matrix.

### 4.2 Cell tests

The LAGP and LAMP solid-state electrolyte were tested in lithium ion cells. Cells with different electrodes combinations and different structures were assembled and tested.

The liquid electrolyte was used in the first cells to improve the ion transport through the solid-solid interface. In the cell using Li metal anode, a reaction took place at the LAGP-Li interface. Cracks were formed on the LAGP solid-state electrolyte pellet due to the reaction between LAGP and lithium anode. In the cell using graphite anode, a reaction on the LAGP pellet was also observed.

On the other hand, the cells with lithium titanate ( $\text{Li}_4\text{Ti}_5\text{O}_{12}$ ) anode could operate properly. No sign of reaction between LTO and LAGP was observed. LAGP solid-state electrolyte is stable vs lithium titanate, which is because the lithium titanate is less reductive than the lithium metal anode.

The LAMP solid-state electrolyte showed also instability. The  $\text{Ti}^{4+}$  in LAMP was reduced to  $\text{Ti}^{3+}$  both in the cell using lithium metal anode and in the cell using lithium titanate (LTO) anode.

All solid-state cells using LAGP solid-state electrolyte without liquid electrolyte were tested. However, since lithium metal was used as anode, a reaction between lithium and LAGP had taken place. The reaction damaged the LAGP-Li interface and inhibited the ion transport in the cells. The resistance of the LAGP-Li interface increased significantly as the reaction took place.

Cyclic voltammetry measurements showed that the  $\text{Ge}^{4+}$  in LAGP was reduced at the voltage of lower than 1 V vs.  $\text{Li}/\text{Li}^+$ , which means that the LAGP would be reduced first before  $\text{Li}^+$  ions start to be reduced. The LAGP pellets used for this test showed black coloring.

Summarizing the results of the cell tests, the  $\text{Ge}^{4+}$  are reduced as the LAGP is brought in contact with a reducing agent, which has a potential lower than 1 V vs  $\text{Li}/\text{Li}^+$ . The  $\text{Ge}^{4+}$  ions are reduced at first to an intermediate oxidation state between  $\text{Ge}(4+)$  and  $\text{Ge}(0)$ . Extra  $\text{Li}^+$  ions are incorporated in the LAGP lattice for the charge neutrality. The LAGP decomposes as large amount of germanium is reduced. The volume of the reaction area on the LAGP expands and breaks the LAGP pellet. On the other hand, the lithium titanate (LTO) has a potential of 1.5 V vs  $\text{Li}/\text{Li}^+$ , which is higher than the redox potential of LAGP. The LAGP is therefore stable in the cell using LTO anode.

However, the attempt to identify the reaction product was not successful. The product could hardly be separated from the LAGP substrate. The amount was also too small. The XRD measurement, the XPS measurement and chemical analysis did not deliver useful results about the kind of the substance in the reaction product.

For the application as solid-state electrolyte in lithium ion cells, the LAGP and LATP solid-state electrolyte need improvements and modifications. The solid-state electrolytes need to be protected against the anode with lower redox potential or their composition needs to be modified to improve the chemical stability. An anode with higher redox potential (such as LTO) can also be a solution.

#### 4. Summary and conclusion

## References

1. Chen, H.; Cong, T. N.; Yang, W.; Tan, C.; Li, Y.; Ding, Y. Progress in electrical energy storage system: A critical review. *Progress in Natural Science* **2009**, *19* (3), 291–312.
2. Fergus, J. W. Ceramic and polymeric solid electrolytes for lithium-ion batteries. *J. Power Sources* **2010**, *195* (15), 4554–4569.
3. Mizushima, K.; Jones, P. C.; Wiseman, P. J.; Goodenough, J. B.  $\text{Li}_x\text{CoO}_2$ : ( $0 < x < 1$ ) A new cathode material for batteries of high energy density. *Mater. Res. Bull.* **1980**, *15* (6), 783–789.
4. Orman, H. J.; Wiseman, P. J. Cobalt(III) lithium oxide,  $\text{CoLiO}_2$ : Structure refinement by powder neutron diffraction. *Acta Crystallogr. C Cryst. Struct. Commun.* **1984**, *40* (1), 12–14.
5. Steiger, J. *Mechanisms of Dendrite Growth in Lithium Metal Batteries*. PhD thesis; Karlsruher Institut für Technologie (KIT): Karlsruhe, **2015**.
6. Yamaki, J. Thermal stability of graphite anode with electrolyte in lithium-ion cells. *Solid State Ionics* **2002**, *148* (3-4), 241–245.
7. Bak, S.-M.; Hu, E.; Zhou, Y.; Yu, X.; Senanayake, S. D.; Cho, S.-J.; Kim, K.-B.; Chung, K. Y.; Yang, X.-Q.; Nam, K.-W. Structural changes and thermal stability of charged  $\text{LiNi}_x\text{Mn}_y\text{Co}_z\text{O}_2$  cathode materials studied by combined in situ time-resolved XRD and mass spectroscopy. *ACS Appl. Mater. Interfaces* **2014**, *6* (24), 22594–22601.
8. Thackeray, M. M.; David, W.; Bruce, P. G.; Goodenough, J. B. Lithium insertion into manganese spinels. *Mater. Res. Bull.* **1983**, *18* (4), 461–472.
9. Jugović, D.; Uskoković, D. A review of recent developments in the synthesis procedures of lithium iron phosphate powders. *J. Power Sources* **2009**, *190* (2), 538–544.
10. Kanamura, K.; Umegaki, T.; Naito, H.; Takehara, Z.; Yao, T. Structural and electrochemical characteristics of  $\text{Li}_{4/3}\text{Ti}_{5/3}\text{O}_4$  as an anode material for rechargeable lithium batteries. *J. Appl. Electrochem.* **2001**, *31* (1), 73–78.
11. Ronci, F.; Reale, P.; Scrosati, B.; Panero, S.; Rossi Albertini, V.; Perfetti, P.; Di Michiel, M.; Merino, J. M. High-Resolution In-Situ Structural Measurements of the  $\text{Li}_{4/3}\text{Ti}_{5/3}\text{O}_4$  “Zero-Strain” Insertion Material. *J. Phys. Chem. B* **2002**, *106* (12), 3082–3086.
12. Omar, N.; Daowd, M.; van Bossche, P. d.; Hegazy, O.; Smekens, J.; Coosemans, T.; van Mierlo, J. Rechargeable Energy Storage Systems for Plug-in Hybrid Electric Vehicles—Assessment of Electrical Characteristics. *Energies* **2012**, *5* (8), 2952–2988.
13. Aurbach, D.; Talyosef, Y.; Markovsky, B.; Markevich, E.; Zinigrad, E.; Asraf, L.; Gnanaraj, J. S.; Kim, H.-J. Design of electrolyte solutions for Li and Li-ion batteries: A review. *Electrochim. Acta* **2004**, *50* (2-3), 247–254.
14. Younesi, R.; Veith, G. M.; Johansson, P.; Edstrom, K.; Vegge, T. Lithium salts for advanced lithium batteries: Li-metal, Li-O<sub>2</sub>, and Li-S. *Energy Environ. Sci.* **2015**, *8* (7), 1905–1922.

15. Xu, K. Nonaqueous Liquid Electrolytes for Lithium-Based Rechargeable Batteries. *Chem. Rev.* **2004**, *104* (10), 4303–4418.
16. National Center for Biotechnology Information. PubChem Compound Database. <https://pubchem.ncbi.nlm.nih.gov/compound/7303> (accessed August 11, 2016).
17. An, S. J.; Li, J.; Daniel, C.; Mohanty, D.; Nagpure, S.; Wood, D. L. The state of understanding of the lithium-ion-battery graphite solid electrolyte interphase (SEI) and its relationship to formation cycling. *Carbon* **2016**, *105*, 52–76.
18. Verma, P.; Maire, P.; Novák, P. A review of the features and analyses of the solid electrolyte interphase in Li-ion batteries. *Electrochimica Acta* **2010**, *55* (22), 6332–6341.
19. Tasaki, K. Solvent Decompositions and Physical Properties of Decomposition Compounds in Li-Ion Battery Electrolytes Studied by DFT Calculations and Molecular Dynamics Simulations. *J. Phys. Chem. B* **2005**, *109* (7), 2920–2933.
20. Yang, H.; Zhuang, G. V.; Ross, P. N. Thermal stability of LiPF<sub>6</sub> salt and Li-ion battery electrolytes containing LiPF<sub>6</sub>. *J. Power Sources* **2006**, *161* (1), 573–579.
21. Furushima, Y.; Yanagisawa, C.; Nakagawa, T.; Aoki, Y.; Muraki, N. Thermal stability and kinetics of delithiated LiCoO<sub>2</sub>. *J. Power Sources* **2011**, *196* (4), 2260–2263.
22. Doughty, D.; Roth, E. P. A General Discussion of Li Ion Battery Safety. *Electrochem. Soc. Interface* **2012**, 37.
23. Maleki, H. Thermal Stability Studies of Li-Ion Cells and Components. *J. Electrochem. Soc.* **1999**, *146* (9), 3224.
24. Monroe, C.; Newman, J. The Impact of Elastic Deformation on Deposition Kinetics at Lithium/Polymer Interfaces. *J. Electrochem. Soc.* **2005**, *152* (2), A396.
25. Zugmann, S.; Fleischmann, M.; Amereller, M.; Gschwind, R. M.; Wiemhöfer, H. D.; Gores, H. J. Measurement of transference numbers for lithium ion electrolytes via four different methods, a comparative study. *Electrochim. Acta* **2011**, *56* (11), 3926–3933.
26. Smart, L.; Moore, E. *Solid state chemistry. An introduction*, 4th ed.; CRC Press, **2016**.
27. Dieterich, W.; Peschel, I. Superionenleiter. *Phys. Bl.* **1980**, *36* (12), 354–357.
28. Dieterich, W. Superionic conductors. *J. Stat. Phys.* **1985**, *39* (5-6), 583–596.
29. Rickert, H. Solid Ionic Conductors: Principles and Applications. *Angew. Chem. Int. Ed. Engl.* **1978**, *17* (1), 37–46.
30. Kamaya, N.; Homma, K.; Yamakawa, Y.; Hirayama, M.; Kanno, R.; Yonemura, M.; Kamiyama, T.; Kato, Y.; Hama, S.; Kawamoto, K.; Mitsui, A. A lithium superionic conductor. *Nat. Mater.* **2011**, *10* (9), 682–686.
31. Ren, Y.; Chen, K.; Chen, R.; Liu, T.; Zhang, Y.; Nan, C.-W.; Vyas, B. Oxide Electrolytes for Lithium Batteries. *J. Am. Ceram. Soc.* **2015**, *98* (12), 3603–3623.

32. Thangadurai, V.; Kaack, H.; Weppner, W. J. F. Novel Fast Lithium Ion Conduction in Garnet-Type  $\text{Li}_5\text{La}_3\text{M}_2\text{O}_{12}$  (M = Nb, Ta). *J. Am. Ceram. Soc.* **2003**, *86* (3), 437–440.
33. Thangadurai, V.; Weppner, W.  $\text{Li}_6\text{A}\text{La}_2\text{Nb}_2\text{O}_{12}$  (A=Ca, Sr, Ba): A New Class of Fast Lithium Ion Conductors with Garnet-Like Structure. *J. Am. Ceram. Soc.* **2005**, *88* (2), 411–418.
34. Robertson, A.; West, A.; Ritchie, A. Review of crystalline lithium-ion conductors suitable for high temperature battery applications. *Solid State Ionics* **1997**, *104* (1-2), 1–11.
35. Kong, Y.; Li, Y.; Lu, J.; Hu, C. Conductivity and electrochemical stability of perovskite-structured lithium–strontium–niobium–hafnium-oxide solid Li-ion conductors. *J. Mater. Sci.: Mater. Electron.* **2017**, *28* (12), 8621–8629.
36. Huang, B.; Xu, B.; Li, Y.; Zhou, W.; You, Y.; Zhong, S.; Wang, C.-A.; Goodenough, J. B. Li-Ion Conduction and Stability of Perovskite  $\text{Li}_{3/8}\text{Sr}_{7/16}\text{Hf}_{1/4}\text{Ta}_{3/4}\text{O}_3$ . *ACS Appl. Mater. Interfaces* **2016**, *8* (23), 14552–14557.
37. Tatsumisago, M.; Nagao, M.; Hayashi, A. Recent development of sulfide solid electrolytes and interfacial modification for all-solid-state rechargeable lithium batteries. *J. Asian Ceram. Soc.* **2013**, *1* (1), 17–25.
38. Kanno, R.; Murayama, M. Lithium Ionic Conductor Thio-LISICON: The  $\text{Li}_2\text{S-GeS}_2\text{-P}_2\text{S}_5$  System. *J. Electrochem. Soc.* **2001**, *148* (7), A742.
39. Seino, Y.; Ota, T.; Takada, K.; Hayashi, A.; Tatsumisago, M. A sulphide lithium super ion conductor is superior to liquid ion conductors for use in rechargeable batteries. *Energy Environ. Sci.* **2014**, *7* (2), 627–631.
40. Knauth, P. Inorganic solid Li ion conductors: An overview. *Solid State Ionics* **2009**, *180* (14-16), 911–916.
41. Schroeder, M.; Glatthaar, S.; Binder, J. R. Influence of spray granulation on the properties of wet chemically synthesized  $\text{Li}_{1.3}\text{Ti}_{1.7}\text{Al}_{0.3}(\text{PO}_4)_3$  (LATP) powders. *Solid State Ionics* **2011**, *201* (1), 49–53.
42. Thokchom, J. S.; Gupta, N.; Kumar, B. Superionic Conductivity in a Lithium Aluminum Germanium Phosphate Glass–Ceramic. *J. Electrochem. Soc.* **2008**, *155* (12), A915-A920.
43. Soman, S.; Iwai, Y.; Kawamura, J.; Kulkarni, A. Crystalline phase content and ionic conductivity correlation in LATP glass–ceramic. *J. Solid State Electrochem.* **2012**, *16* (5), 1761–1766.
44. Goodenough, J. B.; Hong, H.-P.; Kafalas, J. A. Fast  $\text{Na}^+$ -ion transport in skeleton structures. *Mater. Res. Bull.* **1976**, *11* (2), 203–220.
45. Hong, H.-P. Crystal structures and crystal chemistry in the system  $\text{Na}_{1+x}\text{Zr}_2\text{Si}_x\text{P}_{3-x}\text{O}_{12}$ . *Mater. Res. Bull.* **1976**, *11* (2), 173–182.
46. Adachi, G.-y.; Imanaka, N.; Aono, H. Fast  $\text{Li}^+$  Conducting Ceramic Electrolytes. *Advanced Materials* **1996**, *8* (2), 127–135.
47. Anantharamulu, N.; Koteswara Rao, K.; Rambabu, G.; Vijaya Kumar, B.; Radha, V.; Vithal, M. A wide-ranging review on Nasion type materials. *J. Mater. Sci.* **2011**, *46* (9), 2821–2837.

48. Pang, G.; Yuan, C.; Nie, P.; Ding, B.; Zhu, J.; Zhang, X. Synthesis of NASICON-type structured  $\text{NaTi}_2(\text{PO}_4)_3$ -graphene nanocomposite as an anode for aqueous rechargeable Na-ion batteries. *Nanoscale* **2014**, *6* (12), 6328–6334.
49. Pet'kov, V. I.; Dorokhova, G. I.; Orlova, A. I. Architecture of phosphates with  $\{[\text{L}_2(\text{PO}_4)_3]^{P-}\}_3 \infty$  frameworks. *Crystallogr. Reports*, *46* (1), 69–74.
50. Krimi, S.; Mansouri, I.; El Jazouli, A.; Chaminade, J. P.; Gravereau, P.; Le Flem, G. The Structure of  $\text{Na}_5\text{Ti}(\text{PO}_4)_3$ . *J. Solid State Chem.* **1993**, *105* (2), 561–566.
51. Key, B.; Schroeder, D. J.; Ingram, B. J.; Vaughey, J. T. Solution-Based Synthesis and Characterization of Lithium-Ion Conducting Phosphate Ceramics for Lithium Metal Batteries. *Chem. Mater.* **2012**, *24* (2), 287–293.
52. París, M. A.; Sanz, J. Structural changes in the compounds  $\text{LiM}^{\text{IV}}_2(\text{PO}_4)_3$  ( $\text{M}^{\text{IV}} = \text{Ge, Ti, Sn, and Hf}$ ) as followed by  $\text{P}^{31}$  and  $\text{Li}^7$  NMR. *Phys. Rev. B* **1997**, *55* (21), 14270–14278.
53. Leo, C. J.; Chowdari, B. V. R.; Rao, G. V. S.; Souquet, J. L. Lithium conducting glass ceramic with Nasicon structure. *Mater. Res. Bull.* **2002**, *37* (8), 1419–1430.
54. Maldonado-Manso, P.; Losilla, E. R.; Martínez-Lara, M.; Aranda, M. A. G.; Bruque, S.; Mouahid, F. E.; Zahir, M. High Lithium Ionic Conductivity in the  $\text{Li}_{1+x}\text{Al}_x\text{Ge}_y\text{Ti}_{2-x-y}(\text{PO}_4)_3$  NASICON Series. *Chem. Mater.* **2003**, *15* (9), 1879–1885.
55. Nuspl, G.; Takeuchi, T.; Weiss, A.; Kageyama, H.; Yoshizawa, K.; Yamabe, T. Lithium ion migration pathways in  $\text{LiTi}_2(\text{PO}_4)_3$  and related materials. *J. Appl. Phys.* **1999**, *86* (10), 5484–5491.
56. Alami, M.; Brochu, R.; Soubeyroux, J. L.; Gravereau, P.; Le Flem, G.; Hagenmuller, P. Structure and thermal expansion of  $\text{LiGe}_2(\text{PO}_4)_3$ . *J. Solid State Chem.* **1991**, *90* (2), 185–193.
57. Lang, B.; Ziebarth, B.; Elsässer, C. Lithium Ion Conduction in  $\text{LiTi}_2(\text{PO}_4)_3$  and Related Compounds Based on the NASICON Structure: A First-Principles Study. *Chem. Mater.* **2015**, *27* (14), 5040–5048.
58. Thokchom, J. S.; Gupta, N.; Kumar, B. Superionic Conductivity in a Lithium Aluminum Germanium Phosphate Glass–Ceramic. *J. Electrochem. Soc.* **2008**, *155* (12), A915.
59. Kumar, B. Heterogeneous electrolytes: Variables for and uncertainty in conductivity measurements. *J. Power Sources* **2008**, *179* (1), 401–406.
60. Mariappan, C. R.; Gellert, M.; Yada, C.; Rosciano, F.; Roling, B. Grain boundary resistance of fast lithium ion conductors: Comparison between a lithium-ion conductive Li–Al–Ti–P–O-type glass ceramic and a  $\text{Li}_{1.5}\text{Al}_{0.5}\text{Ge}_{1.5}\text{P}_3\text{O}_{12}$  ceramic. *Electrochem. Commun.* **2012**, *14* (1), 25–28.
61. Best, A. Stoichiometric changes in lithium conducting materials based on  $\text{Li}_{1+x}\text{Al}_x\text{Ti}_{2-x}(\text{PO}_4)_3$ : Impedance, X-ray and NMR studies. *Solid State Ionics* **2000**, *136-137* (1-2), 339–344.
62. Xu, X.; Wen, Z.; Wu, X.; Yang, X.; Gu, Z. Lithium Ion-Conducting Glass–Ceramics of  $\text{Li}_{1.5}\text{Al}_{0.5}\text{Ge}_{1.5}(\text{PO}_4)_3-x\text{Li}_2\text{O}$  ( $x=0.0-0.20$ ) with Good Electrical and Electrochemical Properties. *J. Am. Ceram. Soc.* **2007**, *90* (9), 2802–2806.

63. Mariappan, C. R.; Yada, C.; Rosciano, F.; Roling, B. Correlation between micro-structural properties and ionic conductivity of  $\text{Li}_{1.5}\text{Al}_{0.5}\text{Ge}_{1.5}(\text{PO}_4)_3$  ceramics. *J. Power Sources* **2011**, *196* (15), 6456–6464.
64. Fleig, J.; Maier, J. The impedance of ceramics with highly resistive grain boundaries: Validity and limits of the brick layer model. *J. Eur. Ceram. Soc.* **1999**, *19* (6-7), 693–696.
65. Kidner, N. J.; Homrighaus, Z. J.; Ingram, B. J.; Mason, T. O.; Garboczi, E. J. Impedance/Dielectric Spectroscopy of Electroceramics: Part 1: Evaluation of Composite Models for Polycrystalline Ceramics. *J Electroceram* **2005**, *14* (3), 283–291.
66. Kumar, J.; Rodrigues, S. J.; Kumar, B. Interface-mediated electrochemical effects in lithium/polymer-ceramic cells. *J. Power Sources* **2010**, *195* (1), 327–334.
67. Berkemeier, F. H. *Ionenleitende Borat- und Silikatglasschichten*. PhD thesis; University Münster: Münster, **2007**.
68. Brug, G. J.; van den Eeden, A.; Sluyters-Rehbach, M.; Sluyters, J. H. The analysis of electrode impedances complicated by the presence of a constant phase element. *J. electroanal. chem. interfacial electrochem.* **1984**, *176* (1-2), 275–295.
69. Hodge, I. M.; Ingram, M. D.; West, A. R. Impedance and modulus spectroscopy of polycrystalline solid electrolytes. *J. electroanal. chem. interfacial electrochem.* **1976**, *74* (2), 125–143.
70. Armstrong, R. D.; Burnham, R. A. The effect of roughness on the impedance of the interface between a solid electrolyte and a blocking electrode. *J. electroanal. chem. interfacial electrochem.* **1976**, *72* (3), 257–266.
71. Liu. Fractal model for the ac response of a rough interface. *Phys. Rev. Lett.* **1985**, *55* (5), 529–532.
72. Kim, C.-H.; Pyun, S.-I.; Kim, J.-H. An investigation of the capacitance dispersion on the fractal carbon electrode with edge and basal orientations. *Electrochim. Acta* **2003**, *48* (23), 3455–3463.
73. Oldham, K. The RC time “constant” at a disk electrode. *Electrochem. Commun.* **2004**, *6* (2), 210–214.
74. Ghosh, A.; Sural, M. Conductivity spectra of sodium fluorozirconate glasses. *J. Chem. Phys.* **2001**, *114* (7), 3243.
75. K. Funke. Impedanzspektroskopie: Apparative Methoden in der Physikalischen Chemie. [https://www.uni-muenster.de/imperia/md/content/physikalische\\_chemie/app\\_impedanz.pdf](https://www.uni-muenster.de/imperia/md/content/physikalische_chemie/app_impedanz.pdf).
76. Aono, H. Ionic Conductivity of the Lithium Titanium Phosphate ( $\text{Li}_{1+x}\text{M}_x\text{Ti}_{2-x}(\text{PO}_4)_3$ , M = Al, Sc, Y, and La) Systems. *J. Electrochem. Soc.* **1989**, *136* (2), 590.
77. Aono, H. The Electrical Properties of Ceramic Electrolytes for  $\text{LiM}_x\text{Ti}_{2-x}(\text{PO}_4)_3 + y\text{Li}_2\text{O}$ , M = Ge, Sn, Hf, and Zr Systems. *J. Electrochem. Soc.* **1993**, *140* (7), 1827.
78. AONO, H. Ionic conductivity and sinterability of lithium titanium phosphate system. *Solid State Ionics* **1990**, *40-41*, 38–42.
79. Fu, J. Superionic conductivity of glass-ceramics in the system  $\text{Li}_2\text{O} \cdot \text{Al}_2\text{O}_3 \cdot \text{TiO}_2 \cdot \text{P}_2\text{O}_5$ . *Solid State Ionics* **1997**, *96* (3–4), 195–200.

80. Wong, S.; Newman, P. J.; Best, A. S.; Nairn, K. M.; Macfarlane, D. R.; Forsyth, M. Towards elucidating microscopic structural changes in Li-ion conductors  $\text{Li}_{1+y}\text{Ti}_{2-y}\text{Al}_y[\text{PO}_4]_3$  and  $\text{Li}_{1+y}\text{Ti}_{2-y}\text{Al}_y[\text{PO}_4]_{3-x}[\text{MO}_4]_x$  (M=V and Nb): X-ray and  $^{27}\text{Al}$  and  $^{31}\text{P}$  NMR studies. *J. Mater. Chem.* **1998**, *8* (10), 2199–2203.
81. KATOH, T.; INDA, Y.; BABA, M.; YE, R. Lithium-ion conductive glass-ceramics with composition ratio control and their electrochemical characteristics. *J. Ceram. Soc. Jpn.* **2010**, *118* (1384), 1159–1162.
82. Kubanska, A.; Castro, L.; Tortet, L.; Schäf, O.; Dollé, M.; Bouchet, R. Elaboration of controlled size  $\text{Li}_{1.5}\text{Al}_{0.5}\text{Ge}_{1.5}(\text{PO}_4)_3$  crystallites from glass-ceramics. *Solid State Ionics* **2014**, *266*, 44–50.
83. Arbi, K.; Bucheli, W.; Jiménez, R.; Sanz, J. High lithium ion conducting solid electrolytes based on NASICON  $\text{Li}_{1+x}\text{Al}_x\text{M}_{2-x}(\text{PO}_4)_3$  materials (M = Ti, Ge and  $0 \leq x \leq 0.5$ ). *J. Eur. Ceram. Soc.* **2015**, *35* (5), 1477–1484.
84. Fu, J. Fast  $\text{Li}^+$  ion conducting glass-ceramics in the system  $\text{Li}_2\text{O}-\text{Al}_2\text{O}_3-\text{GeO}_2-\text{P}_2\text{O}_5$ . *Solid State Ionics* **1997**, *104* (3–4), 191–194.
85. Kotobuki, M.; Koishi, M. Sol-gel synthesis of  $\text{Li}_{1.5}\text{Al}_{0.5}\text{Ge}_{1.5}(\text{PO}_4)_3$  solid electrolyte. *Ceram. Int.* **2015**, *41* (7), 8562–8567.
86. Kichambare, P. D.; Howell, T.; Rodrigues, S. Sol-Gel-Derived Lithium Superionic Conductor  $\text{Li}_{1.5}\text{Al}_{0.5}\text{Ge}_{1.5}(\text{PO}_4)_3$  Electrolyte for Solid-State Lithium-Oxygen Batteries. *Energy Technol.* **2014**, *2* (4), 391–396.
87. Zhang, M.; Huang, Z.; Cheng, J.; Yamamoto, O.; Imanishi, N.; Chi, B.; Pu, J.; Li, J. Solid state lithium ionic conducting thin film  $\text{Li}_{1.4}\text{Al}_{0.4}\text{Ge}_{1.6}(\text{PO}_4)_3$  prepared by tape casting. *J. Alloys Compd.* **2014**, *590*, 147–152.
88. Robertson, A. D.; West, A. R.; Ritchie, A. G. Review of crystalline lithium-ion conductors suitable for high temperature battery applications. *Solid State Ionics* **1997**, *104* (1–2), 1–11.
89. Thokchom, J. S.; Kumar, B. The effects of crystallization parameters on the ionic conductivity of a lithium aluminum germanium phosphate glass-ceramic. *J. Power Sources* **2010**, *195* (9), 2870–2876.
90. Thokchom, J. S.; Kumar, B. Composite effect in superionically conducting lithium aluminium germanium phosphate based glass-ceramic. *J. Power Sources* **2008**, *185* (1), 480–485.
91. NETZSCH-Gerätebau GmbH. Laser Flash Analysis – LFA. [https://www.netzsch-thermal-analysis.com/media/thermal-analysis/brochures/LFA\\_427\\_E\\_0913.pdf](https://www.netzsch-thermal-analysis.com/media/thermal-analysis/brochures/LFA_427_E_0913.pdf) (accessed September 5, 2016).
92. NETZSCH-Gerätebau GmbH. Principle of the LFA Method. <https://www.netzsch-thermal-analysis.com/en/landing-pages/principle-of-the-lfa-method/> (accessed September 5, 2016).
93. Gellert, M.; Gries, K. I.; Yada, C.; Rosciano, F.; Volz, K.; Roling, B. Grain Boundaries in a Lithium Aluminum Titanium Phosphate-Type Fast Lithium Ion Conducting Glass Ceramic: Microstructure and Nonlinear Ion Transport Properties. *J. Phys. Chem. C* **2012**, *116* (43), 22675–22678.
94. Kothari, D. H.; Kanchan, D. K.; Sharma, P. Electrical properties of Li-based NASICON compounds doped with yttrium oxide. *Ionics* **2014**, *20* (10), 1385–1390.

95. Bouchet, R.; Knauth, P.; Laugier, J.-M. Theoretical Analysis of IS of Polycrystalline Materials with Blocking or Conducting Grain Boundaries: From Microcrystals to Nanocrystals. *J. Electrochem. Soc.* **2003**, *150* (7), E348.
96. Chiou, J.-M.; Chung, D. D. L. Improvement of the temperature resistance of aluminium-matrix composites using an acid phosphate binder. *J. Mater. Sci.* **1993**, *28* (6), 1435–1446.
97. Langlet, M.; Saltzberg, M.; Shannon, R. D. Aluminium metaphosphate glass-ceramics. *J. Mater. Sci.* **1992**, *27* (4), 972–982.
98. van der Meer, H. The crystal structure of a monoclinic form of aluminium metaphosphate,  $\text{Al}(\text{PO}_3)_3$ . *Acta Crystallogr B Struct Crystallogr Cryst Chem* **1976**, *32* (8), 2423–2426.
99. Durif, A. *Crystal chemistry of condensed phosphates*; Springer, **2013**.
100. Thokchom, J. S.; Kumar, B. The effects of crystallization parameters on the ionic conductivity of a lithium aluminum germanium phosphate glass–ceramic. *J. Power Sources* **2010**, *195* (9), 2870–2876.
101. Kichambare, P. D.; Howell, T.; Rodrigues, S. Sol-Gel-Derived Lithium Superionic Conductor  $\text{Li}_{1.5}\text{Al}_{0.5}\text{Ge}_{1.5}(\text{PO}_4)_3$  Electrolyte for Solid-State Lithium-Oxygen Batteries. *Energy Technology* **2014**, *2* (4), 391–396.
102. Leo, C. Effect of MgO addition on the ionic conductivity of  $\text{LiGe}_2(\text{PO}_4)_3$  ceramics. *Solid State Ionics* **2003**, *159* (3-4), 357–367.
103. Safanama, D.; Sharma, N.; Rao, R. P.; Brand, H. E. A.; Adams, S. Structural evolution of NASICON-type  $\text{Li}_{1+x}\text{Al}_x\text{Ge}_{2-x}(\text{PO}_4)_3$  using in situ synchrotron X-ray powder diffraction. *J. Mater. Chem. A* **2016**, *4* (20), 7718–7726.
104. Liu, Z.; Venkatachalam, S.; van Wüllen, L. Structure, phase separation and Li dynamics in sol–gel-derived  $\text{Li}_{1+x}\text{Al}_x\text{Ge}_{2-x}(\text{PO}_4)_3$ . *Solid State Ionics* **2015**, *276*, 47–55.
105. Kun, H.; Yanhang, W.; Chengkui, Z.; Huifeng, Z.; Yonghua, L.; Jiang, C.; Bin, H.; Juanrong, M. Influence of  $\text{Al}_2\text{O}_3$  additions on crystallization mechanism and conductivity of  $\text{Li}_2\text{O}-\text{Ge}_2\text{O}-\text{P}_2\text{O}_5$  glass–ceramics. *Physica B: Condensed Matter*. **2011**, *406* (20), 3947–3950.
106. Yamamoto, H.; Tabuchi, M.; Takeuchi, T.; Kageyama, H.; Nakamura, O. Ionic conductivity enhancement in  $\text{LiGe}_2(\text{PO}_4)_3$  solid electrolyte. *J. Power Sources* **1997**, *68* (2), 397–401.
107. Tien, T. Y.; Hummel, F. A. Studies in Lithium Oxide Systems: X, Lithium Phosphate Compounds. *J. Am. Ceram. Soc.* **1961**, *44* (5), 206–208.
108. Sudreau, F.; Petit, D.; Boilot, J. P. Dimorphism, phase transitions, and transport properties in  $\text{LiZr}_2(\text{PO}_4)_3$ . *J. Solid State Chem.* **1989**, *83* (1), 78–90.
109. Nomura, K.; Ikeda, S.; Ito, K.; Einaga, H. Framework Structure, Phase Transition, and Transport Properties in  $\text{M}^{\text{II}}\text{Zr}_4(\text{PO}_4)_6$  Compounds ( $\text{M}^{\text{II}}=\text{Mg}, \text{Ca}, \text{Sr}, \text{Ba}, \text{Mn}, \text{Co}, \text{Ni}, \text{Zn}, \text{Cd},$  and  $\text{Pb}$ ). *Bull. Chem. Soc. Jpn.* **1992**, *65* (12), 3221–3227.

110. Pet'kov, V. I.; Asabina, E. A.; Markin, A. V.; Smirnova, N. N. Synthesis, characterization and thermodynamic data of compounds with NZP structure. *J. Therm. Anal. Calorim.* **2008**, *91* (1), 155–161.
111. Pet'kov, V. I.; Asabina, E. A.; Markin, A. V.; Kir'yanov, K. V. Calorimetric study of sodium-rich zirconium phosphate. *Thermochim. Acta* **2003**, *403* (2), 185–196.
112. Boilot, J. P.; Collin, G.; Comes, R. Zirconium deficiency in nasicon-type compounds: Crystal structure of  $\text{Na}_5\text{Zr}(\text{PO}_4)_3$ . *J. Solid State Chem.* **1983**, *50* (1), 91–99.
113. Boilot, J.; Collin, G.; Comes, R. Stoichiometry and phase transitions in NASICON type compounds. *Solid State Ionics* **1983**, *9-10*, 829–833.
114. Boilot, J. P.; Collin, G.; Comès, R. Evidence of a relation between structural defects and phase transitions in NASICON type compounds. *Solid State Commun.* **1983**, *45* (3), 231–236.
115. Franz, R.; Wiedemann, G. Ueber die Wärme-Leitungsfähigkeit der Metalle. *Ann. Phys. Chem.* **1853**, *165* (8), 497–531.
116. Mizutani, U. *Introduction to the electron theory of metals*; EBL-Schweitzer; Cambridge University Press: Cambridge, **2001**.
117. Tritt, T. M. *Thermal conductivity. Theory, properties, and applications / edited by Terry M. Tritt*; Physics of solids and liquids; Kluwer Academic/Plenum: New York, London, **2004**.
118. LOEB, A. L. Thermal Conductivity: VIII, A Theory of Thermal Conductivity of Porous Materials. *J. Am. Ceram. Soc.* **1954**, *37* (2), 96–99.
119. Kabayabaya, T.; Yu, F.; Zhang, X. Thermal diffusivity measurement of glass at high temperature by using flash method. *J. of Therm. Sci.* **2004**, *13* (1), 91–96.
120. Klemens, P. G. Heat conduction in solids by phonons. *Thermochim. Acta* **1993**, *218*, 247–255.
121. Rohde, M.; Schulz, B. The effect of the exposure to different irradiation sources on the thermal conductivity of  $\text{Al}_2\text{O}_3$ . *J. Nucl. Mater.* **1990**, *173* (3), 289–293.
122. Klemens, P. G. Theory of thermal conduction in dielectric solids: Effects of radiation damage. *Nucl. Instrum. Methods Phys. Res.* **1984**, *1* (2-3), 204–208.
123. Kotobuki, M.; Koishi, M.; Kato, Y. Preparation of  $\text{Li}_{1.5}\text{Al}_{0.5}\text{Ti}_{1.5}(\text{PO}_4)_3$  solid electrolyte via a co-precipitation method. *Ionics* **2013**, *19* (12), 1945–1948.
124. Chowdari, B. V. R.; Subba Rao, G. V.; Lee, G. Y. H. XPS and ionic conductivity studies on  $\text{Li}_2\text{O}-\text{Al}_2\text{O}_3-(\text{TiO}_2 \text{ or } \text{GeO}_2)-\text{P}_2\text{O}_5$  glass–ceramics. *Solid State Ionics* **2000**, *136-137* (0), 1067–1075.
125. Aono, H.; Imanaka, N.; Adachi, G.-y. High  $\text{Li}^+$  Conducting Ceramics. *Acc. Chem. Res.* **1994**, *27* (9), 265–270.
126. Saruwatari, H.; Kuboki, T.; Kishi, T.; Mikoshiba, S.; Takami, N. Imidazolium ionic liquids containing LiBOB electrolyte for lithium battery. *J. Power Sources* **2010**, *195* (5), 1495–1499.

127. Li, Q.; Chen, J.; Fan, L.; Kong, X.; Lu, Y. Progress in electrolytes for rechargeable Li-based batteries and beyond. *Green Energy & Environment* **2016**, *1* (1), 18–42.
128. Kim, D.-W.; Ryoo, B.-K.; Park, J.-K.; Maeng, K.-S.; Hwang, T.-S. Study on the Ionic Conductivity and Mobility of Liquid Polymer Electrolytes Containing Lithium Salts. *Polym. J.* **1992**, *24* (6), 509–518.
129. Mabbott, G. A. An introduction to cyclic voltammetry. *J. Chem. Educ.* **1983**, *60* (9), 697.
130. Nicholson, R. S. Theory and Application of Cyclic Voltammetry for Measurement of Electrode Reaction Kinetics. *Anal. Chem.* **1965**, *37* (11), 1351–1355.
131. Takahashi, Y.; Tode, S.; Kinoshita, A.; Fujimoto, H.; Nakane, I.; Fujitani, S. Development of Lithium-Ion Batteries with a LiCoO<sub>2</sub> Cathode Toward High Capacity by Elevating Charging Potential. *J. Electrochem. Soc.* **2008**, *155* (7), A537.
132. Kazda, T.; Vondrak, J.; Sedlarikova, M.; Cech, O. Comparison of Material Properties of LiCoO<sub>2</sub> Doped with Sodium and Potassium. *Port. Electrochim. Acta* **2013**, *31* (6), 331–336.
133. Subramanian, V.; Chen, C. L.; Chou, H. S.; Fey, G. T. K. Microwave-assisted solid-state synthesis of LiCoO<sub>2</sub> and its electrochemical properties as a cathode material for lithium batteries. *J. Mater. Chem.* **2001**, *11* (12), 3348–3353.
134. Ohzuku, T. Solid-State Redox Reactions of LiCoO<sub>2</sub> (R3m) for 4 Volt Secondary Lithium Cells. *J. Electrochem. Soc.* **1994**, *141* (11), 2972.
135. Zhang, J.-G.; Xu, W.; Henderson, W. A. *Lithium Metal Anodes and Rechargeable Lithium Metal Batteries* 249; Springer International Publishing: Cham, **2017**.
136. Meister, P.; Jia, H.; Li, J.; Kloepsch, R.; Winter, M.; Placke, T. Best Practice: Performance and Cost Evaluation of Lithium Ion Battery Active Materials with Special Emphasis on Energy Efficiency. *Chem. Mater.* **2016**, *28* (20), 7203–7217.
137. Delmas, C.; Nadiri, A.; Soubeyroux, J. L. The nasicon-type titanium phosphates Ati<sub>2</sub>(PO<sub>4</sub>)<sub>3</sub> (A=Li, Na) as electrode materials. *Solid State Ionics* **1988**, *28–30, Part 1* (0), 419–423.
138. Xu, X.; Wen, Z.; Yang, X.; Zhang, J.; Gu, Z. High lithium ion conductivity glass-ceramics in Li<sub>2</sub>O–Al<sub>2</sub>O<sub>3</sub>–TiO<sub>2</sub>–P<sub>2</sub>O<sub>5</sub> from nanoscaled glassy powders by mechanical milling. *Solid State Ionics* **2006**, *177* (26–32), 2611–2615.
139. Amiki, Y.; Sagane, F.; Yamamoto, K.; Hirayama, T.; Sudoh, M.; Motoyama, M.; Iriyama, Y. Electrochemical properties of an all-solid-state lithium-ion battery with an in-situ formed electrode material grown from a lithium conductive glass ceramics sheet. *J. Power Sources* **2013**, *241*, 583–588.
140. Birke, P.; Salam, F.; Döring, S.; Weppner, W. A first approach to a monolithic all solid state inorganic lithium battery. *Solid State Ionics* **1999**, *118* (1–2), 149–157.
141. Dahn, J.; Fuller, E.; Obrovac, M.; Vonsacken, U. Thermal stability of Li<sub>x</sub>CoO<sub>2</sub>, Li<sub>x</sub>NiO<sub>2</sub> and λ-MnO<sub>2</sub> and consequences for the safety of Li-ion cells. *Solid State Ionics* **1994**, *69* (3–4), 265–270.

142. IUPAC. Properties of the elements: elements symbols, atomic weights, atomic numbers, densities, melting points and boiling points (pressure 101.325 kN m<sup>-2</sup>) of the elements. [http://www.kayelaby.npl.co.uk/chemistry/3\\_1/3\\_1\\_2.html](http://www.kayelaby.npl.co.uk/chemistry/3_1/3_1_2.html) (accessed March 20, 2017).
143. Liu, T.; Ni, H.; Song, W.-L.; Fan, L.-Z. Enhanced electrochemical performance of Li<sub>4</sub>Ti<sub>5</sub>O<sub>12</sub> as anode material for lithium-ion batteries with different carbons as support. *J. Alloys Compd.* **2015**, *646*, 189–194.
144. Xu, H.; Tian, Q.; Huang, J.; Bao, D.; Zhang, Z.; Yang, L. Elaborate strategy for preparing Li<sub>4</sub>Ti<sub>5</sub>O<sub>12</sub>-based anode materials with significantly improved lithium storage: TiO<sub>2</sub> nanodots in-situ decoration and hierarchical structure construction. *J. Phys. Chem. Solids* **2017**, *110*, 49–57.
145. Wu, B.; Wang, S.; Evans IV, W. J.; Deng, D. Z.; Yang, J.; Xiao, J. Interfacial behaviours between lithium ion conductors and electrode materials in various battery systems. *J. Mater. Chem. A* **2016**, *4* (40), 15266–15280.
146. Ma, C.; Chen, K.; Liang, C.; Nan, C.-W.; Ishikawa, R.; More, K.; Chi, M. Atomic-scale origin of the large grain-boundary resistance in perovskite Li-ion-conducting solid electrolytes. *Energy Environ. Sci.* **2014**, *7* (5), 1638.
147. Takada, K. Interfacial nanoarchitectonics for solid-state lithium batteries. *Langmuir* **2013**, *29* (24), 7538–7541.
148. Takada, K.; Ohta, N.; Zhang, L.; Xu, X.; Hang, B. T.; Ohnishi, T.; Osada, M.; Sasaki, T. Interfacial phenomena in solid-state lithium battery with sulfide solid electrolyte. *Solid State Ionics* **2012**, *225*, 594–597.
149. Haruyama, J.; Sodeyama, K.; Han, L.; Takada, K.; Tateyama, Y. Space Charge Layer Effect at Interface between Oxide Cathode and Sulfide Electrolyte in All-Solid-State Lithium-Ion Battery. *Chem. Mater.* **2014**, *26* (14), 4248–4255.
150. Zeng, Z.; Liang, W.-I.; Chu, Y.-H.; Zheng, H. In situ TEM study of the Li-Au reaction in an electrochemical liquid cell. *Faraday discussions* **2014**, *176*, 95–107.
151. Taillades, G. Metal-based very thin film anodes for lithium ion microbatteries. *Solid State Ionics* **2002**, *152-153*, 119–124.
152. Bach, P.; Valencia-Jaime, I.; Rütt, U.; Gutowski, O.; Romero, A. H.; Renner, F. U. Electrochemical Lithiation Cycles of Gold Anodes Observed by In Situ High-Energy X-ray Diffraction. *Chem. Mater.* **2016**, *28* (9), 2941–2948.
153. Obrovac, M. N.; Chevrier, V. L. Alloy negative electrodes for Li-ion batteries. *Chemical reviews* **2014**, *114* (23), 11444–11502.
154. Yuan, L.; Liu, H.; Maaroo, A.; Konstantinov, K.; Liu, J.; Cortie, M. Mesoporous gold as anode material for lithium-ion cells. *J. New Mater. Electrochem. Syst.* **2007**, *10*.
155. Brownson, D. A. C.; Banks, C. E. Interpreting Electrochemistry. In *The Handbook of Graphene Electrochemistry*; Brownson, D. A. C., Banks, C. E., Eds.; Springer London: London, **2014**; pp 23–77.

156. Nicholson, R. S. Theory and Application of Cyclic Voltammetry for Measurement of Electrode Reaction Kinetics. *Anal. Chem.* **1965**, *37* (11), 1351–1355.
157. Kasajima, T.; Nishikiori, T.; Nohira, T.; Ito, Y. Electrochemical Window and the Characteristics of ( $\alpha$  +  $\beta$ ) Al-Li Alloy Reference Electrode for a LiBr-KBr-CsBr Eutectic Melt. *J. Electrochem. Soc.* **2004**, *151* (11), E335.
158. Hartmann, P.; Leichtweiss, T.; Busche, M. R.; Schneider, M.; Reich, M.; Sann, J.; Adelhelm, P.; Janek, J. Degradation of NASICON-Type Materials in Contact with Lithium Metal: Formation of Mixed Conducting Interphases (MCI) on Solid Electrolytes. *J. Phys. Chem. C* **2013**, *117* (41), 21064–21074.
159. Peña, J. S.; Sandu, I.; Joubert, O.; Pascual, F. S.; Areán, C. O.; Brousse, T. Electrochemical Reaction Between Lithium and  $\beta$ -Quartz GeO<sub>2</sub>. *Electrochem. Solid-State Lett.* **2004**, *7* (9), A278.
160. Yoon, S.; Jung, S.-H.; Jung, K.-N.; Woo, S.-G.; Cho, W.; Jo, Y.-N.; Cho, K. Y. Preparation of nanostructured Ge/GeO<sub>2</sub> composite in carbon matrix as an anode material for lithium-ion batteries. *Electrochimica Acta* **2016**, *188*, 120–125.
161. Hwang, J.; Jo, C.; Kim, M. G.; Chun, J.; Lim, E.; Kim, S.; Jeong, S.; Kim, Y.; Lee, J. Mesoporous Ge/GeO<sub>2</sub>/Carbon Lithium-Ion Battery Anodes with High Capacity and High Reversibility. *ACS nano* **2015**, *9* (5), 5299–5309.
162. Yoon, S.; Jung, S.-H.; Jung, K.-N.; Woo, S.-G.; Cho, W.; Jo, Y.-N.; Cho, K. Y. Preparation of nanostructured Ge/GeO<sub>2</sub> composite in carbon matrix as an anode material for lithium-ion batteries. *Electrochimica Acta* **2016**, *188*, 120–125.
163. Feng, J.; Xia, H.; Lai, M. O.; Lu, L. NASICON-Structured LiGe<sub>2</sub>(PO<sub>4</sub>)<sub>3</sub> with Improved Cyclability for High-Performance Lithium Batteries. *J. Phys. Chem. C* **2009**, *113* (47), 20514–20520.

## Appendix

### Ionic conductivity of the LAGP and LATP samples

Table A- 1

LAGP batch 1 Sample #2: 900°C 6h sintered using not calcined powder			
Temperature (°C)	1000/T (1/K)	Ionic conductivity (S/cm)	Error of ionic conductivity (S/cm)
25	3.36	7.0E-05	1.0E-05
55	3.05	2.2E-04	4.0E-05
102	2.67	1.0E-03	6.0E-05
151	2.36	3.2E-03	1.5E-04
200	2.11	7.7E-03	6.0E-04
250	1.91	1.5E-02	1.5E-03

Table A- 2

LAGP batch 1 Sample #4: 750°C 6h sintered using calcined powder			
Temperature (°C)	1000/T(1/K)	Ionic conductivity (S/cm)	Error of ionic conductivity (S/cm)
25	3.36	3.2E-05	3.8E-06
50	3.10	9.2E-05	1.8E-05
100	2.68	5.0E-04	1.2E-04
150	2.36	1.8E-03	5.8E-04
200	2.11	4.9E-03	1.6E-03
253	1.90	1.0E-02	1.8E-03

Table A- 3

LAGP batch 1 Sample #5: 800°C 6h sintered using calcined powder			
Temperature (°C)	1000/T (1/K)	Ionic conductivity (S/cm)	Error of ionic conductivity (S/cm)
25	3.36	1.5E-04	1.4E-5
51	3.09	5.1E-04	6.0E-5
101	2.67	3.0E-03	3.0E-4
151	2.36	9.8E-03	1.0E-3
200	2.11	2.2E-02	1.0E-3

Table A- 4

LAGP batch 1 Sample #6: 900°C 6h sintered using calcined powder			
Temperature (°C)	1000/T (1/K)	Ionic conductivity (S/cm)	Error of ionic conductivity (S/cm)
25	3.36	8.4E-05	7.0E-06
50	3.10	2.2E-04	2.1E-05
100	2.68	1.2E-03	1.4E-04
150	2.36	2.9E-03	3.7E-04
200	2.11	8.3E-03	9.9E-04
250	1.91	1.5E-02	1.9E-03

Table A- 5

LAGP batch 1 Sample #7: 850°C 6h sintered using calcined powder			
Temperature (°C)	1000/T (1/K)	Ionic conductivity (S/cm)	Error of ionic conductivity (S/cm)
28	3.32	7.7E-05	8.0E-06
50	3.10	2.5E-04	2.6E-05
103	2.66	1.6E-03	2.1E-04
150	2.36	6.0E-03	4.5E-04
202	2.11	1.1E-02	9.0E-04
250	1.91	2.6E-02	2.0E-03

Table A- 6

LAGP batch 1 Sample #8: 800°C 3h sintered using calcined powder			
Temperature (°C)	1000/T (1/K)	Ionic conductivity (S/cm)	Error of ionic conductivity (S/cm)
25	3.36	1.3E-04	2.4E-05
50	3.10	4.3E-04	7.0E-05
100	2.68	2.3E-03	2.9E-04
150	2.36	6.6E-03	1.2E-03
200	2.11	1.5E-02	2.4E-03

Table A- 7

LAGP batch 1 Sample #9: 800°C 9h sintered using calcined powder			
Temperature (°C)	1000/T (1/K)	Ionic conductivity (S/cm)	Error of ionic conductivity (S/cm)
25	3.36	8.6E-05	9.0E-06
50	3.10	2.8E-04	2.9E-05
100	2.68	1.9E-03	1.9E-04
153	2.35	7.2E-03	4.7E-04
200	2.11	1.7E-02	1.1E-03

Table A- 8

LAGP batch 2 Sample #2: 660°C 3h heat-treated			
Temperature (°C)	1000/T (1/K)	Ionic conductivity (S/cm)	Error of ionic conductivity (S/cm)
24	3.37	4.6E-06	2.0E-06
48	3.12	1.6E-05	6.0E-06
97	2.70	1.4E-04	4.0E-05
140	2.42	6.3E-04	6.0E-05
232	1.98	4.1E-03	6.0E-04

Table A- 9

LAGP batch 2 Sample #3: 800°C 3h heat-treated			
Temperature (°C)	1000/T (1/K)	Ionic conductivity (S/cm)	Error of ionic conductivity (S/cm)
24	3.37	4.1E-05	1.0E-05
48	3.12	1.3E-04	7.0E-05
130	2.48	1.5E-03	2.9E-04
184	2.19	3.7E-03	1.2E-03
230	1.99	7.0E-03	2.4E-03

Table A- 10

LAGP batch 2 Sample #3: 800°C 3h + 6h heat-treated			
Temperature (°C)	1000/T (1/K)	Ionic conductivity (S/cm)	Error of ionic conductivity (S/cm)
27	3.33	1.2E-04	8.5E-06
48	3.12	2.6E-04	3.5E-05
95	2.72	1.1E-03	3.5E-04
116	2.57	2.4E-03	5.2E-04
150	2.36	4.9E-03	1.1E-03
203	2.10	1.1E-02	2.4E-03

Table A- 11

LAGP batch 2 Sample #4: 800°C 6h heat-treated			
Temperature (°C)	1000/T (1/K)	Ionic conductivity (S/cm)	Error of ionic conductivity (S/cm)
24	3.37	6.3E-05	7.8E-06
49	3.11	1.9E-04	2.6E-05
95	2.72	1.0E-03	1.5E-04
148	2.38	4.1E-03	6.1E-04
192	2.15	9.7E-03	1.1E-03

Table A- 12

LAGP batch 3 Sample #1: 800°C 6h heat-treated			
Temperature (°C)	1000/T (1/K)	Ionic conductivity (S/cm)	Error of ionic conductivity (S/cm)
22	3.39	1.7E-04	8.0E-06
48	3.12	5.2E-04	1.8E-05
93	2.73	2.4E-03	4.2E-04
140	2.42	7.4E-03	1.8E-03
196	2.13	1.9E-02	3.6E-03
221	2.02	2.6E-02	3.8E-03

Table A- 13

LAGP batch 3 Sample #2: 550°C 10min + 650°C 2h heat-treated			
Temperature (°C)	1000/T (1/K)	Ionic conductivity (S/cm)	Error of ionic conductivity (S/cm)
25	3.36	2.6E-05	4.7E-06
45	3.14	7.0E-05	1.6E-05
92	2.74	4.4E-04	1.1E-04
140	2.42	1.2E-03	2.9E-04

Table A- 14

LAGP batch 3 Sample #3: 800°C 6h sintered from glass powder			
Temperature (°C)	1000/T (1/K)	Ionic conductivity (S/cm)	Error of ionic conductivity (S/cm)
24	3.37	2.8E-05	2.6E-06
47	3.13	9.4E-05	9.8E-06
93	2.73	6.5E-04	7.3E-05
142	2.41	2.8E-03	3.4E-04
193	2.15	4.3E-03	3.7E-04

Table A- 15

LAGP batch 4 Sample #1: 800°C 6h heat-treated			
Temperature (°C)	1000/T (1/K)	Ionic conductivity (S/cm)	Error of ionic conductivity (S/cm)
26	3.34	2.1E-04	3.1E-05
60	3.00	1.3E-03	3.0E-04
119	2.55	5.3E-03	1.3E-03
149	2.37	9.0E-03	1.3E-03
254	1.90	6.2E-02	7.0E-03

Table A- 16

LAGP batch 4 Sample #2: 550°C-630°C-800°C each 1h heat-treated			
Temperature (°C)	1000/T (1/K)	Ionic conductivity (S/cm)	Error of ionic conductivity (S/cm)
23	3.38	7.5E-05	3.8E-06
53	3.07	2.4E-04	6.8E-06
99	2.69	1.1E-03	1.2E-04
152	2.35	4.1E-03	5.8E-04
205	2.09	9.4E-03	1.6E-03

Table A- 17

LAGP batch 4 Sample #3: 600°C 2h + 800°C 6h heat-treated			
Temperature (°C)	1000/T (1/K)	Ionic conductivity (S/cm)	Error of ionic conductivity (S/cm)
24	3.37	2.3E-04	2.0E-05
48	3.12	6.9E-04	6.7E-05
120	2.54	7.7E-03	8.0E-04
144	2.40	1.4E-02	1.3E-03
210	2.07	4.3E-02	8.0E-03

Table A- 18

LAGP batch 4 Sample #4: 900°C 6h heat-treated			
Temperature (°C)	1000/T (1/K)	Ionic conductivity (S/cm)	Error of ionic conductivity (S/cm)
22	3.39	1.5E-04	2.5E-05
72	2.90	1.1E-03	2.8E-04
106	2.64	3.7E-03	1.1E-03
168	2.27	1.0E-02	7.0E-04
211	2.07	2.6E-02	7.0E-03
256	1.89	5.3E-02	9.0E-03

Table A- 19

LAGP batch 4 Sample #5: 800°C 12h heat-treated			
Temperature (°C)	1000/T (1/K)	Ionic conductivity (S/cm)	Error of ionic conductivity (S/cm)
25	3.36	3.3E-04	4.7E-05
47	3.13	9.5E-04	1.5E-04
99	2.69	5.2E-03	1.2E-03
149	2.37	9.8E-03	2.8E-03
182	2.20	2.6E-02	7.0E-03
221	2.02	4.4E-02	1.0E-02

Table A- 20

LATP Sample #1: 1200°C 6h sintered			
Temperature (°C)	1000/T (1/K)	Ionic conductivity (S/cm)	Error of ionic conductivity (S/cm)
25	3.36	1.7E-04	1.0E-05
50	3.10	3.4E-04	1.0E-05
100	2.68	1.1E-03	7.0E-05
150	2.36	2.7E-03	1.6E-04
200	2.11	5.1E-03	3.1E-04
250	1.91	8.8E-03	4.4E-04

Table A- 21

LATP Sample #2: 1100°C 6h sintered			
Temperature (°C)	1000/T (1/K)	Ionic conductivity (S/cm)	Error of ionic conductivity (S/cm)
25	3.36	1.4E-04	2.5E-05
50	3.10	2.4E-04	4.8E-05
100	2.68	9.1E-04	1.8E-04
150	2.36	2.4E-03	4.0E-04
200	2.11	4.2E-03	8.2E-04
250	1.91	6.7E-03	7.5E-04

Table A- 22

LATP Sample #3: 1000°C 6h sintered			
Temperature (°C)	1000/T (1/K)	Ionic conductivity (S/cm)	Error of ionic conductivity (S/cm)
25	3.36	6.2E-04	2.5E-05
50	3.10	1.3E-03	7.0E-05
100	2.68	4.9E-03	3.5E-04
150	2.36	1.2E-02	8.0E-04
200	2.11	2.2E-02	1.4E-03
250	1.91	3.5E-02	1.2E-03

Table A- 23

LATP Sample #4: 900°C 6h sintered			
Temperature (°C)	1000/T (1/K)	Ionic conductivity (S/cm)	Error of ionic conductivity (S/cm)
25	3.36	3.4E-04	1.6E-05
50	3.10	8.2E-04	4.0E-05
100	2.68	3.2E-03	2.1E-04
150	2.36	8.7E-03	5.7E-04
200	2.11	1.7E-02	6.0E-04
250	1.91	2.5E-02	2.4E-03

Table A- 24

LATP Sample #5: 950°C 6h sintered			
Temperature (°C)	1000/T (1/K)	Ionic conductivity (S/cm)	Error of ionic conductivity (S/cm)
25	3.36	4.2E-04	7.0E-06
50	3.10	7.8E-04	2.1E-05
100	2.68	2.8E-03	8.0E-05
150	2.36	7.0E-03	2.7E-04
200	2.11	1.3E-02	5.2E-04
250	1.91	2.2E-02	8.0E-04

Table A- 25

LATP Sample #6: 1000°C 3h sintered			
Temperature (°C)	1000/T (1/K)	Ionic conductivity (S/cm)	Error of ionic conductivity (S/cm)
25	3.36	2.9E-04	1.4E-05
50	3.10	6.7E-04	4.5E-05
100	2.68	2.3E-03	1.5E-04
150	2.36	5.7E-03	5.6E-04
200	2.11	1.0E-02	9.4E-04
250	1.91	1.7E-02	1.2E-03

Table A- 26

LATP Sample #7: 1000°C 6h + 900°C 6h sintered			
Temperature (°C)	1000/T (1/K)	Ionic conductivity (S/cm)	Error of ionic conductivity (S/cm)
25	3.36	2.4E-04	4.1E-05
50	3.10	5.0E-04	9.0E-05
104	2.65	1.8E-03	2.6E-04
150	2.36	3.3E-03	8.2E-04
200	2.11	6.1E-03	1.8E-03
250	1.91	1.4E-02	9.5E-04

Table A- 27

LATP Sample #8: 900°C 12h sintered			
Temperature (°C)	1000/T (1/K)	Ionic conductivity (S/cm)	Error of ionic conductivity (S/cm)
25	3.36	2.5E-04	2.1E-05
50	3.10	5.2E-04	4.9E-05
100	2.68	1.6E-03	1.4E-04
150	2.36	3.1E-03	2.5E-04
200	2.11	4.3E-03	5.3E-04
250	1.91	7.7E-03	6.9E-04

## Thermal diffusivity and thermal conductivity of the LAGP samples

Table A- 28

LAGP batch 2 sample #2: 660°C 3h heat-treated					
T(°C)	Thermal diffusivity (cm <sup>2</sup> /s)	Error (cm <sup>2</sup> /s)	Thermal conductivity (W/cm K)	Error (W/cm K)	
27	5.67E-03	1.8E-04	1.22E-02	6.4E-04	
100	5.45E-03	1.7E-04	1.33E-02	6.9E-04	
200	5.16E-03	7.0E-05	1.40E-02	4.8E-04	
300	4.91E-03	9.7E-05	1.41E-02	5.7E-04	
400	4.91E-03	4.7E-05	1.47E-02	4.5E-04	
500	4.78E-03	9.6E-05	1.46E-02	6.0E-04	

Table A- 29

LAGP batch 2 sample #3: 800°C 3h + 6h heat-treated					
T(°C)	Thermal diffusivity (cm <sup>2</sup> /s)	Error (cm <sup>2</sup> /s)	Thermal conductivity (W/cm K)	Error (W/cm K)	
27	7.07E-03	3.5E-04	1.63E-02	1.1E-03	
100	6.88E-03	1.9E-04	1.80E-02	8.8E-04	
200	6.38E-03	2.0E-04	1.85E-02	9.6E-04	
300	6.27E-03	9.8E-05	1.92E-02	7.0E-04	
400	6.26E-03	1.1E-04	2.00E-02	7.7E-04	
500	6.15E-03	3.0E-04	2.01E-02	1.4E-03	

Table A- 30

LAGP batch 2 sample #4: 800°C 6h heat-treated, first measurement					
T(°C)	Thermal diffusivity (cm <sup>2</sup> /s)	Error (cm <sup>2</sup> /s)	Thermal conductivity (W/cm K)	Error (W/cm K)	
27	6.87E-03	4.6E-04	1.56E-02	1.4E-03	
100	6.43E-03	2.5E-04	1.66E-02	1.0E-03	
201	6.03E-03	9.3E-05	1.73E-02	6.3E-04	
299	5.82E-03	5.5E-05	1.76E-02	5.3E-04	
400	5.66E-03	3.5E-04	1.79E-02	1.5E-03	
500	5.65E-03	1.2E-04	1.82E-02	7.8E-04	
Second measurement					
T(°C)	Thermal diffusivity (cm <sup>2</sup> /s)	Error (cm <sup>2</sup> /s)	Thermal conductivity (W/cm K)	Error (W/cm K)	
25	7.38E-03	7.0E-05	1.68E-02	5.1E-04	
100	6.62E-03	7.0E-05	1.71E-02	5.4E-04	
200	6.17E-03	4.0E-05	1.77E-02	4.8E-04	

300	5.98E-03	3.7E-04	1.80E-02	1.5E-03
400	5.60E-03	2.6E-04	1.77E-02	1.8E-03
500	5.36E-03	1.8E-04	1.73E-02	1.1E-03
600	5.49E-03	3.1E-04	1.79E-02	1.3E-03
700	5.41E-03	2.6E-04	1.78E-02	1.2E-03
Third measurement				
T(°C)	Thermal diffusivity (cm <sup>2</sup> /s)	Error (cm <sup>2</sup> /s)	Thermal conductivity (W/cm K)	Error (W/cm K)
25	7.00E-03	1.7E-04	1.59E-02	7.1E-04
50	6.50E-03	2.3E-04	1.55E-02	8.8E-04
100	6.43E-03	6.7E-05	1.66E-02	5.2E-04
150	6.14E-03	6.2E-05	1.71E-02	5.3E-04
200	5.96E-03	8.9E-06	1.70E-02	3.8E-04
250	5.90E-03	5.9E-05	1.74E-02	5.4E-04
300	5.81E-03	4.9E-05	1.75E-02	5.1E-04
350	5.70E-03	8.2E-05	1.78E-02	6.3E-04
400	5.66E-03	4.4E-05	1.79E-02	5.1E-04
450	5.55E-03	5.8E-06	1.77E-02	3.9E-04
500	5.49E-03	4.6E-05	1.77E-02	5.2E-04
550	5.45E-03	1.1E-04	1.77E-02	7.2E-04
600	5.48E-03	9.6E-05	1.79E-02	6.9E-04
650	5.60E-03	1.5E-04	1.84E-02	8.7E-04
700	5.38E-03	1.5E-04	1.77E-02	8.6E-04
750	5.44E-03	1.1E-04	1.80E-02	7.2E-04

Table A- 31

LAGP batch 2 sample #5: glass				
T(°C)	Thermal diffusivity (cm <sup>2</sup> /s)	Error (cm <sup>2</sup> /s)	Thermal conductivity (W/cm K)	Error (W/cm K)
27	3.43E-03	9.1E-04	6.45E-03	1.9E-03
100	3.90E-03	4.1E-04	8.76E-03	1.1E-03
200	4.15E-03	1.5E-04	1.04E-02	6.0E-04
299	4.23E-03	1.7E-04	1.12E-02	6.8E-04
400	4.32E-03	2.0E-04	1.22E-02	8.2E-04
500	4.62E-03	2.1E-04	1.31E-02	8.7E-04

Table A- 32

LAGP batch 3 sample #1: 800°C 6h heat-treated, first measurement					
T(°C)	Thermal diffusivity (cm <sup>2</sup> /s)	Error (cm <sup>2</sup> /s)	Thermal conductivity (W/cm K)	Error (W/cm K)	
26	5.75E-03	3.5E-04	1.33E-02	1.1E-03	
100	5.88E-03	1.7E-04	1.54E-02	7.7E-04	
200	5.41E-03	1.9E-04	1.42E-02	8.0E-04	
300	5.24E-03	1.6E-04	1.42E-02	7.3E-04	
400	5.12E-03	8.0E-05	1.41E-02	5.1E-04	
500	4.93E-03	3.4E-04	1.37E-02	1.2E-03	
600	4.83E-03	3.7E-04	1.35E-02	1.3E-03	
700	4.87E-03	3.2E-04	1.48E-02	1.3E-03	
Second measurement					
T(°C)	Thermal diffusivity (cm <sup>2</sup> /s)	Error (cm <sup>2</sup> /s)	Thermal conductivity (W/cm K)	Error (W/cm K)	
24	6.17E-03	3.1E-04	1.42E-02	1.0E-03	
100	5.94E-03	1.9E-04	1.55E-02	8.1E-04	
200	5.51E-03	3.6E-05	1.45E-02	4.0E-04	
300	5.42E-03	7.7E-05	1.47E-02	5.2E-04	
Third measurement					
T(°C)	Thermal diffusivity (cm <sup>2</sup> /s)	Error (cm <sup>2</sup> /s)	Thermal conductivity (W/cm K)	Error (W/cm K)	
24	6.25E-03	1.8E-04	1.44E-02	7.2E-04	
50	5.90E-03	2.1E-04	1.42E-02	8.2E-04	
100	5.67E-03	1.2E-04	1.48E-02	6.1E-04	
150	5.51E-03	3.8E-05	1.43E-02	4.0E-04	
200	5.35E-03	4.0E-05	1.41E-02	4.0E-04	
250	5.31E-03	2.5E-05	1.42E-02	3.7E-04	
300	5.20E-03	3.0E-05	1.41E-02	3.8E-04	
350	5.24E-03	7.0E-05	1.43E-02	4.9E-04	
400	5.24E-03	4.7E-05	1.44E-02	4.3E-04	
450	5.14E-03	1.2E-04	1.42E-02	6.4E-04	
500	5.04E-03	9.5E-05	1.40E-02	5.6E-04	
550	5.09E-03	2.5E-05	1.44E-02	3.7E-04	
600	5.01E-03	5.9E-05	1.40E-02	4.6E-04	
650	5.16E-03	1.4E-04	1.48E-02	7.2E-04	
700	5.02E-03	2.5E-04	1.52E-02	1.1E-03	
750	4.99E-03	2.5E-04	1.50E-02	1.1E-03	

Table A- 33

LAGP batch 4 sample #7: 800°C 6h heat-treated, first measurement					
T(°C)	Thermal diffusivity (cm <sup>2</sup> /s)	Error (cm <sup>2</sup> /s)	Thermal conductivity (W/cm K)	Error (W/cm K)	
26	5.52E-03	3.0E-04	1.25E-02	9.4E-04	
100	5.57E-03	2.9E-04	1.42E-02	1.0E-03	
200	5.30E-03	1.9E-04	1.43E-02	8.1E-04	
300	4.99E-03	2.1E-04	1.39E-02	8.8E-04	
400	5.17E-03	2.7E-04	1.47E-02	1.1E-03	
500	4.85E-03	1.9E-04	1.41E-02	8.5E-04	
600	4.87E-03	1.4E-04	1.47E-02	7.3E-04	
700	5.02E-03	3.3E-04	1.57E-02	1.4E-03	
Second measurement					
T(°C)	Thermal diffusivity (cm <sup>2</sup> /s)	Error (cm <sup>2</sup> /s)	Thermal conductivity (W/cm K)	Error (W/cm K)	
25	6.01E-03	1.7E-04	1.36E-02	8.9E-04	
100	5.54E-03	7.0E-05	1.41E-02	4.7E-04	
200	5.05E-03	1.4E-04	1.36E-02	6.6E-04	
300	5.22E-03	3.1E-04	1.46E-02	1.4E-03	
400	4.80E-03	4.0E-04	1.36E-02	1.6E-03	
500	4.55E-03	2.0E-04	1.32E-02	1.7E-03	
600	4.92E-03	3.2E-04	1.49E-02	1.3E-03	
700	4.67E-03	3.5E-04	1.46E-02	1.4E-03	
Third measurement					
T(°C)	Thermal diffusivity (cm <sup>2</sup> /s)	Error (cm <sup>2</sup> /s)	Thermal conductivity (W/cm K)	Error (W/cm K)	
25	5.70E-03	3.0E-04	1.29E-02	9.4E-04	
50	5.43E-03	2.1E-04	1.28E-02	7.6E-04	
100	5.19E-03	4.7E-05	1.32E-02	4.0E-04	
150	4.95E-03	4.1E-05	1.31E-02	3.9E-04	
200	4.84E-03	5.1E-05	1.31E-02	4.1E-04	
250	4.69E-03	4.8E-05	1.29E-02	4.0E-04	
300	4.72E-03	3.8E-05	1.32E-02	3.8E-04	
350	4.68E-03	7.3E-05	1.32E-02	4.8E-04	
375	4.67E-03	3.1E-05	1.32E-02	3.6E-04	
400	4.66E-03	1.1E-04	1.32E-02	5.8E-04	
425	4.59E-03	3.8E-05	1.31E-02	3.8E-04	
450	4.59E-03	5.1E-05	1.31E-02	4.2E-04	
475	4.68E-03	8.9E-05	1.35E-02	5.4E-04	
500	4.56E-03	6.3E-05	1.33E-02	4.6E-04	
525	4.59E-03	5.3E-05	1.35E-02	4.4E-04	

550	4.58E-03	2.0E-04	1.35E-02	8.9E-04
575	4.54E-03	6.4E-05	1.35E-02	4.7E-04
600	4.51E-03	1.1E-04	1.36E-02	6.3E-04
625	4.47E-03	2.3E-05	1.38E-02	3.6E-04
650	4.54E-03	3.1E-05	1.41E-02	3.9E-04
700	4.41E-03	3.1E-05	1.38E-02	3.9E-04
750	4.42E-03	1.7E-04	1.38E-02	8.3E-04